SAPIENZA
UNIVERSITÀ DI ROMA

Multidimensional nonlinear THz spectroscopies in superconductors

Scuola Dottorale in Scienze Astronomiche, Chimiche, Fisiche, Matematiche e della Terra "Vito Volterra"
Dottorato di Ricerca in Fisica (XXXVII cycle)

Jacopo Fiore
ID number 1751766

Advisor
Prof.ssa Lara Benfatto

Academic Year 2023/24

Multidimensional nonlinear THz spectroscopies in superconductors
Sapienza University of Rome

This thesis has been typeset by LaTeX and the Sapthesis class.

Author's email: jacopo.fiore@uniroma1.it

This is the third time;
I hope good luck lies in odd numbers.

Abstract

This thesis presents an in-depth analysis of the nonlinear optical response in superconductors exposed to intense THz pulses, using a quasi-equilibrium approach rooted in many-body perturbation theory. By establishing connections between nonlinear response functions and experimentally measurable quantities, we investigate how superconducting systems respond to single-pulse and two-pulse (multidimensional) protocols. Special focus is given to understanding how diverse light-matter coupling mechanisms and electronic excitations shape the observable outcomes across different experimental setups. We examine, for instance, the role of phase fluctuations in single-layer and bilayer cuprates, which show marked differences in third harmonic generation (THG) along the CuO_2 stacking direction due to the combined action of their momentum dispersion and light polarization. Our work then moves to two-dimensional (2D) THz spectroscopy, which offers unique capabilities to distinguish various nonlinear pathways in quantum materials. We begin with a simplified semiconductor model where we can explicitly compute different light-matter interaction processes and analyze two applications in superconducting systems, applying insights from the THG analysis. We then examine 2D THz spectroscopy of cuprates, where internal screening effects present challenges in disentangling distinct contributions, and subsequently turn to NbN thin films. In the latter case, we demonstrate how specific nonlinear pathways can be uniquely sensitive to amplitude fluctuations, revealing a fresh perspective on the analysis of superconducting dynamics.

Contents

Introduction

Understanding and controlling the emergence and temporal evolution of quantum phases following external perturbations provides critical insights into the roles of charge, spin, orbital, and lattice degrees of freedom in shaping the macroscopic, functional properties of materials. This endeavor is not only of substantial fundamental interest but also represents a foundational step toward realizing a range of future quantum technologies, including quantum sensing, high-speed data processing, and storage solutions. Recent advances in laser technology have enabled the use of optical pulses to externally drive quantum materials, either through impulsive interactions or sustained perturbations, to induce transient states that reveal novel physical phenomena[48, 11, 138, 51].

The strength of the perturbation serves as a primary control parameter for the range of phenomena emerging from the interaction of a light pulse with a quantum material characterized by a complex phase diagram with multiple, intertwined degrees of freedom[27]. In the weak-pulse regime, optical driving can transiently activate collective oscillations of underlying order parameters, and by monitoring these modes in the time domain, one can disentangle distinct microscopic excitations and their interactions[98, 113, 50]. In some materials, photoexcitation can induce transitions to alternative low-energy or hidden states that are unfavored or metastable in thermal equilibrium. Under carefully controlled excitation conditions, ultrafast changes in the free energy landscape may also trigger nonequilibrium phase transitions, providing insights into nonthermal critical behavior[37, 101]. At even higher excitation strengths, the system can enter nonlinear regimes where effective microscopic couplings dynamically evolve, modifying the quantum many-body wave function and revealing emergent phenomena without equilibrium analogs[41, 64].

Given these distinctions, a primary theoretical challenge lies in adapting many-body methodologies, typically formulated in the frequency domain, to time-resolved protocols. In a fully nonequilibrium setup, these approximation schemes are more complex than in equilibrium, as time translational invariance cannot be exploited and, generally, two time variables instead of one energy variable must be managed. Consequently, significant theoretical work has been devoted to either perturbative calculations of the nonlinear response, applicable in the weak-pump regime including many-body effects, or to incorporating periodic drive effects in frameworks for weakly correlated materials, such as Floquet formalism and time-dependent density functional theory, suited to the strong-pump regime [132, 8, 27].

In this thesis, we employ a quasi-equilibrium perturbative approach, which restricts the range of field strengths and phenomena that can be described but nevertheless captures a wide array of experimental findings in various quantum materials[142].

More specifically, we apply the standard diagrammatic theory in an effective-action formalism, which allows to handle the dynamics of the various degrees of freedom at play in a compact way[108, 25]. To motivate the need for our effective-action approach, we will start in **Chapter 1** by recalling the limitations of the time-dependent Ginzburg-Landau framework applied to superconducting excitations, emphasizing the necessity of a many-body Hamiltonian that treats fermions as dynamic degrees of freedom[21, 128]. This method is particularly relevant under the non-adiabatic conditions encountered with THz waveforms and the electronic response in superconductors, a distinctive feature that sets superconducting excitations apart from other collective modes, such as phonons in wide-band insulators. In our case, in fact, the typical energy scale associated with the collective amplitude mode of the order parameter coincides with the scale of the fermionic excitations, ultimately mediating the coupling between light and matter.

Having clarified the limitations and strengths of our methodology, we proceed by reviewing the link between microscopically derived response functions–defined at nonlinear order in the spirit of the Kubo formula for linear response–and the experimental observables accessed in measurements. We will examine the reasoning that connects the measured quantities in the case-study experiment of Third Harmonic Generation (THG) to a microscopic response function derived from a theoretical description of the superconducting state. A central theme of this thesis will be determining the conditions under which the above-mentioned connection can be applied across a range of superconducting (and other) systems, experimental geometries, and increasingly complex time-resolved protocols that generate nonlinear signals. In several key cases discussed in the following chapters, we will examine how this link can–and sometimes must–be refined and expanded to accurately capture the mechanisms underlying nonlinear current generation. Chapter 1 ends by introducing a compact yet versatile tool for describing the outcomes of THz experiments in both single-pulse and multi-pulse protocols, based on the perturbative solution of Maxwell's equation in presence of a non-linearly generated current, a framework that will be applied in subsequent chapters to various experimental scenarios to capture the effects of light propagation.

In **Chapter 2**, we examine the case of third harmonic generation (THG) in layered superconductors, specifically focusing on cuprates[39]. The weak coupling between CuO_2 planes induces strong anisotropy between the in-plane plasma frequency ω_{xy} and the out-of-plane plasma frequency ω_z in the long-wavelength limit. While ω_{xy} lies at an energy scale largely unaffected by the superconducting transition, the softer ω_z plasmon becomes undamped with the opening of the superconducting gap below T_c, manifesting as a sharp plasma edge in c-axis reflectivity at a temperature-dependent scale, $\omega_z(T)$ [137]. In cuprates, pair tunneling dominates inter-layer hopping below T_c, justifying a Josephson-like description for out-of-plane plasma/phase modes. The intrinsic anharmonicity of this model serves as a primary source of nonlinear optical response below T_c, encoded in the minimal coupling of the phase gradient to the gauge field [118].

Analogous to nonlinear phononics [41], the primary THG mechanism can be understood as a sum-frequency process in which two photons of the THz pulse, centered at frequency Ω, simultaneously excite two plasma waves with opposite 3D momenta[45]. As a result, while linear reflectivity is sensitive only to the long-wavelength plasma frequencies ω_{xy} and ω_z, nonlinear optics probes a convolution of plasma excitations at finite momenta, which shows marked differences between single-layer and bilayer structures.

In single-layer systems, the light polarization fully projects the plasmon dispersion toward the lower energy ω_z value measured by linear optics. In bilayer superconductors, however, the modulation of intra-bilayer (J_{z1}) and inter-bilayer (J_{z2}) Josephson couplings along the stacking direction–with $J_{z1} \gg J_{z2}$–leads to a doubling of the Josephson plasmon branches, producing two scales in the long-wavelength limit: $\omega_{z1} \gg \omega_{z2}$. The smaller scale, $\omega_{z2} \propto \sqrt{J_{z2}}$, determines the lower, sharper reflectivity edge at zero momentum. By calculating the THG in the bilayer case, we show that the dominant contributions to THG originate from intra-bilayer phase fluctuations, which scale conversely with the larger Josephson stiffness, J_{z1}. Consequently, in bilayer systems, momentum integration shifts the THG spectral weight towards a higher energy scale, accounting for the absence of any resonance associated with the lower Josephson plasmon seen in linear optics[73].

In the remaining part of the thesis, we delve into two-dimensional coherent spectroscopy (2DCS), a powerful nonlinear spectroscopic technique that tracks system dynamics by exciting a sample with two time-delayed pulses [26]. The resulting spectra, mapped over two independent time axes and Fourier-transformed, provide a comprehensive view of the nonlinear response, capturing specific four-wave mixing processes and revealing the underlying interactions within the system. Initially developed for molecular and semiconductor systems, 2DCS has now been extended into the THz range to investigate collective modes and interactions in quantum materials, including superconductors[92, 75, 72, 89].

The two-dimensional nature of this protocol makes it uniquely suited for identifying coupled modes and interaction mechanisms by resolving different nonlinear pathways that are otherwise challenging to disentangle in single-pulse experiments. In **Chapter 3** we establish a basic theoretical framework to model THz 2D experiments across various electronic system having as core ingredient the third-order response function. These are characterized by two ingredients making them different from previously studied molecular systems: (i) a continuum of electronic excitations and (ii) the existence of paramagnetic and diamagnetic microscopic couplings to light. An application to a model semiconductor demonstrates how these two different types of coupling yield different signatures in the 2D spectral maps, showcasing the technique's potential to reveal subtle distinctions between nonlinear processes.

In **Chapter 4**, the focus narrows to two applications of two-dimensional spectroscopy on superconductors. The first example investigates the *c*-axis response in single-layer cuprates [89], combining insights from previous analyses of THG discussed in Chapter 2 within the 2DCS framework developed in Chapter 3. Emphasis is placed on understanding how the linear response of the system influences the resulting 2D spectral map. A key challenge in this case is disentangling contributions from the two-plasmon processes–characteristic nonlinear pathways in these systems–from simpler, instantaneous processes [52]. This complexity is further compounded by disorder-related effects, which add yet another layer of difficulty in isolating the nonlinear signatures of the two-plasmon response. This example underscores the challenges and the critical refinements needed for effective analysis of 2D spectra in superconducting materials.

We then report the results of our work [72], conducted in collaboration with N. Peter Armitage's experimental group, which used THz-2DCS to examine the properties of superconducting thin films of niobium nitride (NbN). Specifically, we focused on measurements using narrowband THz pulses with an angular frequency Ω, collected at zero-time delay between the two pulses. The intrinsic subtraction method in 2DCS enabled us to isolate two prominent peaks in the power spectrum, observed at Ω and 3Ω, corresponding to first harmonic (FH) and third harmonic (TH) of the pump. Notably, both FH and TH intensities scaled with the third power of the field strength, confirming these as third-order nonlinear responses. The TH signal exhibited a temperature-dependent peak intensity when 2Ω matched twice the superconducting (SC) gap energy, 2Δ, consistent with previous reports [98]. Meanwhile, the FH signal showed a resonance when the driving frequency equaled 2Δ, a behavior that was consistently observed across NbN samples with varying critical temperatures T_c. This FH signal, usually masked by the dominant first harmonic from linear transmission in single-pulse experiments, was distinctly resolved here due to the unique difference-signal analysis encoded in 2DCS.

To better understand the experimental observations, we employed the diagrammatic approach to analyze the different nonlinear processes occurring in the superconducting state, which arise from the combination of diamagnetic (quadratic) and paramagnetic (linear) couplings between electronic excitations and the electromagnetic field. Our findings indicate that the enhancement of the first harmonic (FH) signal observed when $\Omega = 2\Delta$ can only be explained by incorporating paramagnetic processes that are activated by disorder. We investigated these expectations through numerical simulations performed on the attractive Hubbard model on a square lattice, incorporating Anderson-type impurities to account for disorder, in collaboration with G. Seibold, separating the contributions from quasiparticle excitations and amplitude fluctuations of the superconducting order parameter. The results for the third harmonic (TH) signal revealed that the relative ratio of these contributions aligns with previous studies, indicating that the amplitude mode gains significant spectral weight in the presence of strong disorder. Conversely, the FH resonance was found to be predominantly influenced by the amplitude mode across all levels of disorder examined, suggesting a consistent dominance of this mode in shaping the resonance behavior in the superconducting state.

To offer analytical insight that supports our numerical findings, we finally compute with a semi-analytical treatment of disorder the process identified in our simulations as the primary contributor to the enhancement of the amplitude-mode contribution to the non-linearly generated FH current. We demonstrate that the enhancement of the fundamental harmonic can be readily understood as a result of two key features influencing this specific four-wave-mixing process. The first is the Eliashberg effect, which describes how the value of the order parameter is modified when the system is irradiated by an electromagnetic field [55, 29]. The second feature is the presence of a sharp absorptive threshold at the spectral gap, 2Δ, leading to a divergence in the derivative of the current-current response function with respect to the order parameter at $\Omega = 2\Delta$. Consequently, the FH signal offers a distinct channel through which the amplitude fluctuations couple quadratically to light.

List of publications

The candidate reports here a list of the publications in which he was involved during the three years of the Ph.D. program:

- Sellati N., Fiore J., Villani S. P., Benfatto L. and Udina M. *Phonon-Polaritons in Non-Centrosymmetric Systems: Theory of Terahertz Pump-Optical Probe Spectroscopy.* Preprint under review (2024). URL: arxiv.org/abs/2411.10160.

- Fiore J., Sellati N., Gabriele F., Castellani C., Seibold G., Udina M. and Benfatto L. *Investigating Josephson plasmons in layered cuprates via non-linear terahertz spectroscopy.* In Phys. Rev. B 110, L060504 (2024). DOI: 10.1103/PhysRevB.110.L060504.

- Katsumi K., Fiore J., Udina M., Romero R., Barbalas D., Jesudasan J., Raychaudhuri P., Seibold G., Benfatto L. and Armitage N. P. *Revealing Novel Aspects of Light-Matter Coupling by Terahertz Two-Dimensional Coherent Spectroscopy: The Case of the Amplitude Mode in Superconductors.* In Phys. Rev. Lett. 132, 256903 (2024). DOI: 10.1103/PhysRevLett.132.256903.

- Sellati N., Fiore J., Castellani C. and Benfatto L. *Optical Absorption in Tilted Geometries as an Indirect Measurement of Longitudinal Plasma Waves in Layered Cuprates.* In Nanomaterials 14, 1021 (2024). DOI: 10.3390/nano14121021.

- Fiore J., Udina M., Marciani M., Seibold G. and Benfatto L. *Contribution of collective excitations to third harmonic generation in two-band superconductors: The case of* MgB_2. In Phys. Rev. B 106, 094515 (2022). DOI: 10.1103/PhysRevB.106.094515.

- Udina M., Fiore J., Cea T., Castellani C., Seibold G. and Benfatto L. *THz non-linear optical response in cuprates: predominance of the BCS response over the Higgs mode.* In Faraday Discuss. 237, 168-285 (2022). DOI: 10.1039/D2FD00016D.

Chapter 1

Nonlinear THz response in superconductors: a short overview

Part of the contents of this chapter has been published or used in Refs. [143, 40, 124, 39, 72].

1.1 Introduction

Light-matter interaction has represented for a long time a preferential tool to gain information on the physical mechanisms underlying macroscopic properties of materials. Well-established experimental protocols like infrared absorption or Raman scattering have relied on the excitation of the material through a weak, frequency-tuned probe to measure microscopically specific correlation functions in the linear response regime. The advent of more intense, coherent and ultrashort laser pulses, spanning now most of the electromagnetic spectrum relevant for condensed matter systems, has paved the way to access the nonlinear response regime, hosting a richer dynamics involving several intertwined degrees of freedom, with the ultimate purpose to drive the system through non-thermal states inaccessible at equilibrium [48, 27].

Accessing this high-intensity regime for the THz region of the electromagnetic spectrum has represented for years a holy grail for the experimental community, since the generation of such light pulses presented more challenging difficulties with respect to the optical or X-ray region [83]. The interest in this spectral range is driven by the possibility to access the low-energy excitations of emergent states of matter, like in the case of superconductivity. Indeed, collective excitations in superconductors have usually a scalar coupling with the electromagnetic field, being unaccessible to the conventional linear spectroscopies that only probe excitations with a dipolar-like coupling. The relatively recent availability of these THz sources has thus enabled the possibility to probe nonlinear phenomena induced by the interaction of the sample with such intense electric fields[70, 109, 150].

In this view, we start by examining a prototypical experimental technique which in the last ten years has been widely used to access the nonlinear response in

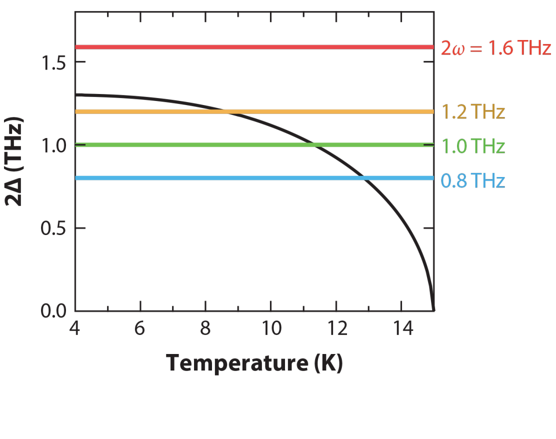

Figure 1.1. The experimental results on NbN obtained in Ref. [98]. Four narrowband THz pulses at various central frequencies Ω resonates at different temperatures with the superconducting optical gap $2\Delta(T)$ of NbN (left panel). The THG intensity at 3Ω increases below the superconducting transition and it is maximised at the temperature T^* such that $2\Omega = 2\Delta(T^*)$ (right panel).

superconducting systems, Third Harmonic Generation (THG). This process is a four-wave mixing which occurs when an intense electric field oscillating at frequency Ω impinging on a sample induces an outgoing electric field at three times the incident frequency, 3Ω. By studying the characteristics of the outgoing radiation, such as its intensity and polarization dependence as a function of Ω or the temperature, it is possible to gain information on the nonlinear processes that occurred inside the system to generate the observed higher harmonic.

We report in Fig. 1.1 the results of one of the first experiments that studied THG from superconductors, led by Shimano's group in Tokyo [98]. A thin film of niobium nitride (NbN) is illuminated by an intense THz field, in this case a multicycle pulse with a temporal envelope of the order of ten picoseconds with a tunable central frequency. The transmitted THz signal is then filtered through band pass filters and in this case also the polarization dependence is analyzed. As it possible to see in Fig. 1.1, there are two experimental facts that must be explained. First, there is an enhancement of the THG signal going below the critical temperature T_c of the sample, signaling that the phenomenon is intimately related to the onset of the superconducting state. Second, we notice that the THG intensity is maximum when the frequency of the incident field is resonant with the gap amplitude at the temperature considered, as can be seen from the corresponding color cuts in the gap vs temperature plot.

In the past ten years, a significant amount of experimental work has then focused on capturing the dynamics of superconducting excitations in various classes of materials using several non-linear THz spectroscopy setups, changing field strength, spectral content, and acquisition protocols. For instance, we mention the observation collective modes in iron-based and MgB_2 multiband superconductors. Measurements have revealed amplitude modes related to order parameters opening at different Fermi surface sheets [145, 77, 56], as well as the Leggett mode associated with oscillations of their relative phase [50], with the activation of harmonics higher than third-order at strong fields [115, 92]. Another important research line, inspired by early predictions in the context of Raman spectroscopy [87, 88], examines the dynamic interplay between amplitude excitations associated with charge density waves and superconducting order, as reported in $NbSe_2$ [38] and various cuprate classes [23, 24, 152]. From a theoretical perspective, explaining these phenomena has been a source of ongoing debate, with various groups contributing to the discussion. Several studies have emphasized the crucial roles of light-matter coupling, impurities, and the polarization of incoming light [139, 21, 20, 99, 19, 105, 130, 123, 143] in shaping the contribution of collective modes to the non-linearly generated signal. Furthermore, different investigations have highlighted the importance of the nature of the pairing interaction, reflected in the momentum-dependence of the order parameter [121, 119, 120, 14], the presence of two or more superconducting gaps at the Fermi level [106, 105, 57, 40], and the transition to non-perturbative regimes under strong fields [103, 102] in determining the non-linear response of superconducting systems.

We then start by following the line of reasoning which allowed to connect the measured quantities of the case-study NbN experiment mentioned above to a microscopic response function derived from a theoretical description of the superconducting state. Indeed, one of the common thread of this thesis is to understand under which conditions it is possible to apply this relatively intuitive procedure to situations where one studies different superconducting systems, probes them in various experimental geometries and collects the nonlinear signal generated by more complicated time-resolved protocols. In some paradigmatic cases which will be illustrated in the following chapters, we will then appreciate how it is possible, and sometimes necessary, to refine and extend the procedure to get the right clue on what is happening during the nonlinear current generation.

1.2 Third Harmonic Generation: from experiments to theory

In conventional linear spectroscopy the experimental findings are usually described through response functions, like the dielectric function ϵ or the conductivity σ, that relate an observable of the physical system under exam, for instance the current $J^{(1)}$, to the perturbation represented by the experimental probe. Introducing the linear electromagnetic kernel $K^{(1)}$ one usually writes the current as a function of the gauge field $A(t)$

$$J^{(1)}_\alpha(t) \sim \int dt' K_{\alpha\beta}(t-t') A_\beta(t'), \tag{1.1}$$

where greek indices stand for the cartesian components. The phenomenon of third harmonic generation is a third-order process, in a diagrammatic approach one would then need three photon lines, or three fields, to interact and produce the measured nonlinear current. In this view, we can place THG inside the wider class of four-wave-mixing (FWM) processes, with three photons incoming and one photon outcoming. Extending the previous formalism we can then introduce a nonlinear electromagnetic kernel such that

$$J^{(3)}_\alpha \sim K^{(3)}_{\alpha\beta\gamma\delta} A_\beta A_\gamma A_\delta, \tag{1.2}$$

where for simplicity we subtended the time dependences of the kernel, the current and the fields, that have to be properly convoluted. What is important at this point is to give a form to this response function through the microscopic description underpinning our system. In linear-response theory, for instance, one treats perturbatively the coupling between some internal degree of freedom of the system and the external perturbation to derive the response of the observable of interest. This is exactly the mechanism underlying the Kubo formula [79, 2].

Let us now extend naively this approach to the nonlinear case and explain how THG can be used to detect collective excitations of the system. Suppose in general to have in the hamiltonian a quadratic coupling of the gauge field with some internal degree of freedom $\delta\psi$ of the system

$$\delta H \sim \Gamma \delta\psi A^2(t), \tag{1.3}$$

where Γ is a suitable coefficient taken for simplicity constant. Here $\delta\psi$ can represent a Raman-active phonon, or a collective electronic excitation as the ones that we will discuss in the rest of the thesis. The current generated by this term reads

$$J^{(3)}(t) = \frac{\delta H}{\delta A(t)} \sim \Gamma A(t)\delta\psi(t). \tag{1.4}$$

The dynamics of $\delta\psi(t)$ under the action of the perturbation in Eq. 1.3 can be evaluated through a two-point, Kubo-like response function, which allows one to find the induced current as

$$J^{(3)}(t) \sim \Gamma^2 A(t) \int_{-\infty}^{t} dt' \langle[\delta\psi(t), \delta\psi(t')]\rangle A^2(t') \equiv A(t) \int dt' K_\psi^{(3)}(t-t') A^2(t'). \tag{1.5}$$

As one expects, the all important quantity that determines the response of the system is the propagator of the fluctuations $\delta\psi$, i.e. $\langle[\delta\psi(t), \delta\psi(t')]\rangle$. Let us now consider a monochromatic perturbation like $A(t) \sim \bar{A}\cos(\Omega t)$ and replace the corresponding terms in the previous expression. One can find two harmonic contributions to the non-linearly generated current

$$J^{(3)}(t) \sim \bar{A}^3 \left[2K_\psi^{(3)}(0) + K_\psi^{(3)}(2\Omega)\right] e^{i\Omega t} + \bar{A}^3 K_\psi^{(3)}(2\Omega) e^{i3\Omega t} + (\Omega \to -\Omega). \tag{1.6}$$

The term oscillating at Ω will represent the nonlinear contribution to the first harmonic Ω of the field: since usually linear response effects are orders of magnitude larger than nonlinear ones, one expects this contribution to be negligible unless, as we will see in Chapter 4, one devises a specific experimental scheme to isolate it. The third harmonic contribution at 3Ω is instead a genuine signature of the four-wave-mixing process described above, and it is connected to the nonlinear response kernel evaluated at 2Ω.

We want at this point to relate the induced current $J^{(3)}$, that can be theoretically derived through some microscopic model, to the electric field E measured for instance in a transmission experiment on a thin film of thickness d. This can be done, and we will provide a general treatment at the end of the chapter, thorugh a perturbative solution of Maxwell equations in presence of a nonlinear source current. If the film is in vacuo, one can write for the third harmonic field[17]

$$E_t(3\Omega) = -\frac{2\pi d}{c} J^{(3)}(3\Omega), \tag{1.7}$$

where we put ourselves in the approximation of $d \ll \lambda$, i.e. the thickness of the film is much shorter than the wavelength λ of the incident field. In the experiment one uses a band pass filter to select the third harmonic 3Ω in the transmitted field, getting

$$I_{\mathrm{THG}} \sim \bar{A}^6 |K^{(3)}(2\Omega)|^2. \tag{1.8}$$

All we have to do, and it is not an easy task, is to give a form to the nonlinear response function $K^{(3)}(2\Omega)$ of the system. In the scheme mentioned above, if $\delta\psi$ is a propagating mode of the system with mass ω_ψ, we could expect the resulting propagator to acquire the typical form

$$\langle \delta\psi^2 \rangle(\omega) \sim \frac{1}{\omega^2 - \omega_\psi^2}. \tag{1.9}$$

This is for instance the case of lattice vibrations, where ω_ψ coincides with the oscillation frequency of the corresponding phonon mode. But then, using Eq. 1.9 in the previous Eq. 1.6 we observe that we end up with a resonance in the third harmonic response when $2\Omega = \omega_\psi$, since

$$K^{(3)}(2\Omega) \sim \Gamma^2 \langle \delta\psi^2 \rangle(2\Omega). \tag{1.10}$$

It is tempting now to interpret the the results of the experiment in Fig. 1.1 in light of what we have just illustrated. The enahncement is observed when $2\Omega = 2\Delta$ and the amplitude mode, as we will recall in the next section, has exactly that mass. Nonetheless, what we observe in the previous equation is not only the dependence of the third-harmonic kernel on the spectrum of the collective mode, but also on the coupling Γ between light and $\delta\psi$. In the case of a Raman-active phonon, one can compute Γ e.g. through ab-initio methods, tipically by calculating the phonon Raman tensor in the adiabatic approximation [18]. In the case of superconducting collective modes, which have an electronic nature, one nonetheless violates the requirements of adiabaticity, since the fermionic quasiparticle dispersion, ultimately coupling light and amplitude fluctuations, has a typical energy scale of exactly 2Δ. One then needs to compute the coupling Γ starting from a microscopic model which treats on equal footing the two ingredients entering Eq. 1.10.

1.3 Phenomenology of collective modes inside a superconductor

In order to understand why THG experiments on superconductors triggered an intense discussion on the role of collective modes, it is useful to start with a phenomenological description stemming from an approximate expression of the free energy. In 1950 Ginzburg and Landau developed a phenomenological theory of superconductivity based on the concept of spontaneous symmetry breaking occurring at a phase transition [49]. The key quantity in their theory was the expansion of the free energy of the system below the critical temperature T_c as a function of a complex order parameter ψ

$$\mathcal{F}[\psi] = \mathcal{F}_{\mathrm{n}} + \alpha|\psi|^2 + \frac{\beta}{2}|\psi|^4 + \frac{1}{2m}|\nabla\psi|^2, \tag{1.11}$$

where $\mathcal{F}_{\rm n}$ is the free energy in the normal state and $\alpha \sim T - T_c$. In this picture, ψ is zero above T_c and acquires a finite complex value by lowering the temperature below the superconducting transition, signaling the realization of a specific value of the order parameter. The ground state of the system is characterized by a homogeneous value $\psi_0 = |\psi_0| e^{i\theta_0}$ upon which one can consider fluctuations $\delta\psi(\mathbf{r})$ both in the amplitude and in the phase of the order parameter, namely

$$\psi(\mathbf{r}) = |\psi_0 + \delta\psi(\mathbf{r})| e^{i(\theta_0 + \delta\theta(\mathbf{r}))}. \tag{1.12}$$

We rewrite then $\mathcal{F}[\psi] = \mathcal{F}_{\rm mf}[\psi_0, \theta_0] + \mathcal{F}_{\rm fl}[\delta\psi, \delta\theta]$, where the first part depends only on the constant part of the order parameter, while the second one contains the contribution from the fluctuations. Minimizing $\mathcal{F}_{\rm mf}$ with respect to ψ_0 and θ_0 and choosing $\theta_0 = 0$ in the mean-field order parameter, as allowed by the $U(1)$ global gauge symmetry of $\mathcal{F}_{\rm mf}$, we get at second order in the fluctuations

$$\mathcal{F}_{\rm fl} = 2\psi_0(\alpha + \beta\psi_0^2)\delta\psi + (\alpha + 3\beta\psi_0^2)\delta\psi^2 + \frac{1}{2m}|\nabla\delta\psi|^2 + \frac{\psi_0^2}{2m}|\nabla\delta\theta|^2. \tag{1.13}$$

Naturally, since the minimum of $\mathcal{F}_{\rm mf}$ occurs for $\psi_0^2 = -\alpha/\beta$, the linear coefficient of $\delta\psi$ in the first row vanishes. As a result, we notice that the phase fluctuations are massless, since there are not terms at order $\delta\theta^2$, while the amplitude fluctuations are massive since the coefficient of the $\delta\psi^2$ term is $-2\alpha > 0$. Introducing $m_H^2 = -2\alpha$ we rewrite then

$$\mathcal{F}_{\rm fl} = m_H^2\delta\psi^2 + \frac{1}{2m}|\nabla\delta\psi|^2 + \frac{\psi_0^2}{2m}|\nabla\delta\theta|^2. \tag{1.14}$$

The description so far employed lacks any dynamical information. A possible extension is a Lorentz invariant model that preserves the $U(1)$ symmetry of the classical free energy. Even though this is not appropriate for superconductors [21] we discuss it here just to give a first account of the role of fluctuations. We try to consider then a time dependence in the order parameter $\psi(\mathbf{r}, t)$ and rewrite

$$\mathcal{F}[\psi, \theta] \to \mathcal{F}[\psi(\mathbf{r}, t), \theta(\mathbf{r}, t)] - |\partial_t\psi(\mathbf{r}, t)|^2, \tag{1.15}$$

where the contribution of the fluctuations will be given now by

$$\mathcal{F}_{\rm fl} \to \mathcal{F}_{\rm fl} - |\partial_t\delta\psi|^2 - \psi_0^2|\partial_t\delta\theta|^2. \tag{1.16}$$

At this point it is possible to write the correlation function of the amplitude and phase fluctuations of the order parameter, since the theory so far is gaussian and we can read the corresponding quantities from the coefficient fo $\delta\psi^2$ and $\delta\theta^2$, respectively. We have for the amplitude fluctuactions, or Higgs mode,

$$\langle\delta\psi^2\rangle \sim \frac{1}{m_H^2 + v_s^2|\mathbf{q}|^2 - \omega^2}, \tag{1.17}$$

The propagator for the phase fluctuations, or Goldstone mode, is instead

$$\langle\delta\theta^2\rangle \sim \frac{\psi_0^{-2}}{v_s^2|\mathbf{q}|^2 - \omega^2}, \tag{1.18}$$

manifestly displaying a massless character, where we have denoted as v_s the sound velocity. A picture of the situation is reported in Figure 1.2.

At this point one would be tempted to couple somehow the system to the gauge potential that is the experimental probe at our disposal. In the gauge invariant theory so far developed we could add the free energy of the electromagnetic field and perform a minimal coupling substitution sending $-i\nabla \to -i\nabla - 2e\mathbf{A}/c$ and $i\partial_t \to i\partial_t - 2e\phi$. Indeed, as one can check by performing the above mentioned replacement in Eq. 1.11 and proceeding as in Ref. [128], one would obtain a coupling $\sim \psi_0^2 \delta\psi A^2$ between the amplitude fluctuations $\delta\psi$ and the square of the gauge field A^2 scaling with ψ_0^2, predicting then a substantial contribution to THG according to Eq. 1.10. Nonetheless, we still miss an important part of the problem, due to the fact that at microscopic level the gauge field couples to the fermionic degrees of freedom of our superconductor, i.e. the electrons.

As we know from the Landau theory of Fermi liquids, for instance, fermionic systems are characterized not only by collective excitations, like those described by the above Lorentz invariant generalization 1.15 of the Ginzburg-Landau expression, but also by particle-hole excitations, a true fingerprint of the realization of the Pauli exclusion principle. These latter are overlooked in the previous formalism and have to be taken into account by introducing a proper microscopic model involving the electrons [21].

We then proceed by introducing the Bardeen, Cooper and Schrieffer [9] (BCS) hamiltonian, that in 1957 succeeded in describing the superconducting behaviour through the formation and scattering of the so-called Cooper pairs, formed by electrons with opposite momenta and spins in proximity of the Fermi surface through an effective attractive interaction. Their celebrated result was originally obtained by a mean-field treatment of the hamiltonian

$$H = \sum_{\mathbf{k}\sigma} \xi_{\mathbf{k}} c^\dagger_{\mathbf{k}\sigma} c_{\mathbf{k}\sigma} - \sum_{\mathbf{k}\mathbf{k}'} V_{\mathbf{k}\mathbf{k}'} c^\dagger_{\mathbf{k}\uparrow} c^\dagger_{-\mathbf{k}\downarrow} c_{-\mathbf{k}'\downarrow} c_{\mathbf{k}'\uparrow}, \tag{1.19}$$

where $\xi_{\mathbf{k}} = \epsilon_{\mathbf{k}} - \mu$ is the band dispersion of the metallic state and $V_{\mathbf{k}\mathbf{k}'}$ is the effective attractive interaction originated from the interplay between the electronic and lattice degrees of freedom. Assuming a momentum independent $V_{\mathbf{k}\mathbf{k}'} \sim U$, one can diagonalize at mean-field level the previous hamiltonian and get the eigenvalues

$$\pm E_{\mathbf{k}} = \pm\sqrt{\xi_{\mathbf{k}}^2 + \Delta^2}, \tag{1.20}$$

where Δ can be determined self-consistently through the weel-known gap equation. We can immediately notice that the fingerprint of the superconducting state in the band structure is the opening of a gap 2Δ at the Fermi level, that determines the spectrum of the possible particle-hole excitations in the BCS model.

The bridge between the BCS and Ginzburg-Landau theories was built by Gor'kov [53], who showed how the Ginzburg-Landau equations could be obtained from the response of the BCS model to a transverse electromagnetic field near the critical temperature. Notably this naturally required the identification of the gap amplitude with the order parameter introduced by Landau. This is the key point: being $-\alpha = 2\Delta$, the mass of the amplitude fluctuations becomes 2Δ at $|\mathbf{q}|= 0$, the same threshold for the creation of particle-hole pairs. This spoils irremediably the

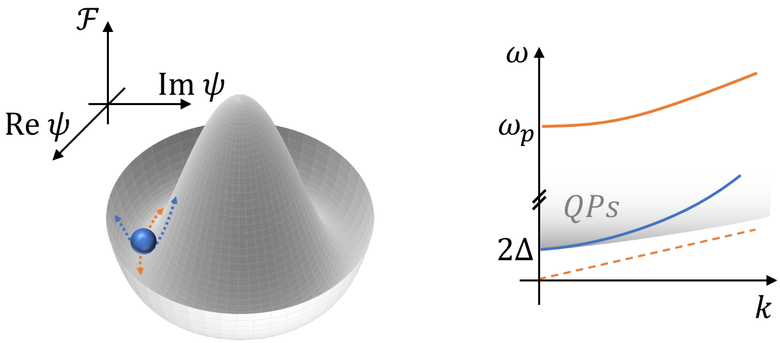

Figure 1.2. Left: the Ginzburg-Landau free-energy profile at $T < T_c$. Right: the dispersion of the phase (orange) and amplitude (blue) fluctuations [128]. Massless phase fluctuations are lifted to the scale of the plasma energy due to the Anderson-Higgs mechanism.

relativistic nature, see 1.17, of the amplitude fluctuations predicted through the phenomenological model devised before. In the microscopic BCS model we will see how the spectrum of the Higgs fluctuations immediately acquires a finite lifetime above 2Δ due to the proliferation of Cooper pairs. In addition, this result made the interpretation of THG experiments problematic: the enhancement of THG at $2\Omega = 2\Delta$ can be due both to purely quasiparticle and Higgs contributions.

1.4 Coupling between light and collective modes

Having at our disposal a microscopic model for the superconducting system, we can now illustrate a general procedure that allows one to clarify the mechanisms of light-matter coupling involving the various degrees of freedom at play.

In a minimal coupling scheme, light-matter coupling enters the hamiltonian of the system through a modification of the kinetic term. Introducing appropriate fermionic operators Ψ and $\Psi^\dagger$, in a continuum model the kinetic term H_{kin} of the hamiltonian would be replaced by

$$H_{\text{kin}} = \frac{1}{2m}\int \Psi^\dagger \left(-i\nabla - \frac{e}{c}\mathbf{A}\right)^2 \Psi, \tag{1.21}$$

where from now on we set $\hbar = k_B = 1$ unless explicitly stated. Expanding this expression one finds two terms beyond the non interacting piece, namely

$$\delta H = \frac{e}{2mic}\int [(\nabla\Psi^\dagger)\Psi - \Psi^\dagger(\nabla\Psi)]\cdot\mathbf{A} + \frac{e^2}{2mc^2}\int \Psi^\dagger\Psi A^2. \tag{1.22}$$

Assuming a uniform ($|\mathbf{q}| = 0$) gauge potential $\mathbf{A}$, one can rewrite the first term in momentum space as

$$\delta H_{\text{para}} = -\frac{e}{c}\sum_{\mathbf{k},\sigma}\frac{\partial\xi_{\mathbf{k}}}{\partial k_\alpha}c^\dagger_{\mathbf{k}\sigma}c_{\mathbf{k}\sigma}A_\alpha \sim -j_\alpha A_\alpha, \tag{1.23}$$

where j_α defines the α cartesian component of the paramagnetic current operator. Here we generalized the coupling to lattice models with band dispersion $\epsilon_{\mathbf{k}}$, with

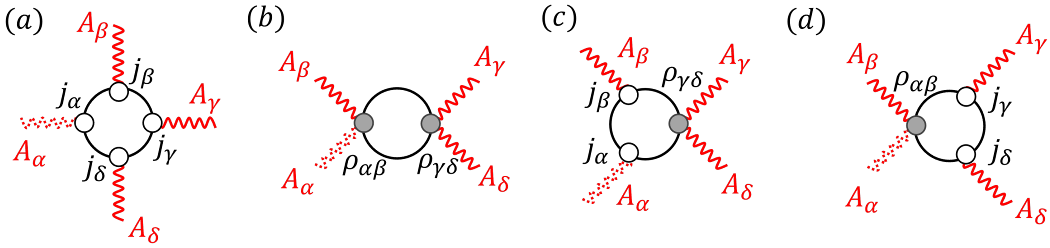

Figure 1.3. Diagrammatic representation of the contribution from the fully-paramagnetic (a), full-diamagnetic (b) and mixed (c)-(d) processes to the third-order current in Eq. 1.27. The dashed line is the field vertex on which one is performing the derivative in Eq. 1.27.

$\xi_{\mathbf{k}} = \epsilon_{\mathbf{k}} - \mu$ and μ the chemical potential. The second term reads instead

$$\delta H_{\text{dia}} = \frac{1}{2}\left(\frac{e}{c}\right)^2 \sum_{\mathbf{k},\sigma} \frac{\partial^2 \xi_{\mathbf{k}}}{\partial k_\alpha \partial k_\beta} c^\dagger_{\mathbf{k}\sigma} c_{\mathbf{k}\sigma} A_\alpha A_\beta \sim \rho_{\alpha\beta} A_\alpha A_\beta, \tag{1.24}$$

where $\rho_{\alpha\beta}$ reduces to $\rho/m\delta_{\alpha\beta}$ for parabolic bands, i.e. is proportional to the density operator, while for lattice models it is related to the inverse mass tensor. To find the current induced by the external field one should integrate out both in the kinetic and in interacting part the matter degrees of freedom, represented here by the fermionic operators [108, 25]. This can be efficiently done by introducing the action

$$S[c, \bar{c}, \mathbf{A}] = \int_0^\beta d\tau \, \left(\bar{c}\partial_\tau c + H[c, \bar{c}] + \delta H[c, \bar{c}, \mathbf{A}]\right), \tag{1.25}$$

where we separated in H the hamiltonian in absence of the external gauge field and in δH the part containing the ligh-matter coupling. After integration of the fermionic variables one is left with an effective action $S[\mathbf{A}]$ where terms at all orders in A^n are present. Proceeding schematically, one can construct a perturbative theory in powers of the gauge field $\mathbf{A}$, such that the value of the $n-$th order induced current $J^{(n)}$ can be obtained through a functional derivatives of the resulting action expanded at order A^{n+1}. For the linear response one gets

$$J^{(1)}_\alpha \sim \frac{\partial S[A^2]}{\partial A_\alpha} \sim \left(-\langle j_\alpha j_\beta \rangle + \langle \rho_{\alpha\beta} \rangle\right) A_\beta \equiv K^{(1)}_{\alpha\beta} A_\beta, \tag{1.26}$$

where $\langle j_\alpha j_\beta \rangle$ is the two-point current-current response function and $\langle \rho_{\alpha\beta} \rangle$ in a continuum model is just proportional to the electron density. For the third-order response one has instead

$$\begin{aligned} J^{(3)}_\alpha \sim \frac{\partial S[A^4]}{\partial A_\alpha} &\sim \left(\langle j_\alpha j_\beta j_\gamma j_\delta \rangle + \langle \rho_{\alpha\beta} \rho_{\gamma\delta} \rangle + \langle j_\alpha j_\beta \rho_{\gamma\delta} \rangle + \langle \rho_{\alpha\beta} j_\gamma j_\delta \rangle\right) A_\beta A_\gamma A_\delta \\ &\equiv K^{(3)}_{\alpha\beta\gamma\delta} A_\beta A_\gamma A_\delta, \end{aligned} \tag{1.27}$$

where the four types of contribution, for the continuum model, are displayed in Fig. 1.3.

As one can see, at third order both four-point, three-point and two-point response functions need to be calculated, and we will do this calculation for a toy-model

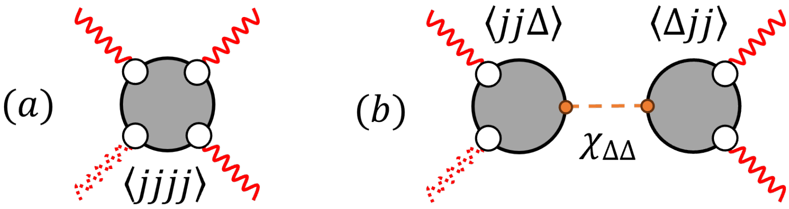

Figure 1.4. Sketch of the paramagnetic processes, where the paramagnetic vertex is represented as a white dot. In the clean case the fermionic bubbles are exactly zero, while in presence of disorder they are finite due to self-energy and vertex corrections (grey shading). (a) The paramagnetic process involving only quasiparticle excitations, $\langle jjjj\rangle$ in Eq. 1.29. (b) The diagram in Eq. 1.30 involving an intermediate amplitude excitation $\chi_{\Delta\Delta}$ (orange dashed line), where the amplitude vertex is the orange dot.

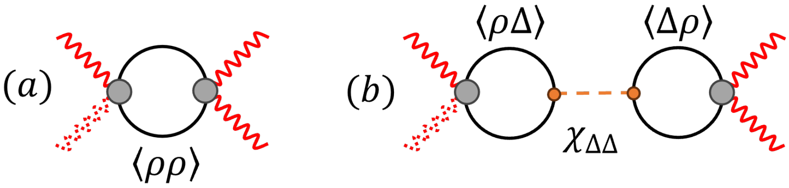

Figure 1.5. Sketch of the diamagnetic processes, where the diamagnetic vertex is represented as a grey dot. (a) The diamagnetic process involving only quasiparticle excitations, $\langle\rho\rho\rangle$ in Eq. 1.31, which dominates in the clean limit. (b) The diagram in Eq. 1.32 involving an intermediate amplitude excitation $\chi_{\Delta\Delta}$ (orange dashed line), where the amplitude vertex is the orange dot, which is suppressed in the clean limit.

semiconductor in Chapter 3. Up to now, we have left aside the contribution of collective excitations, which can be actually included in this scheme using the Hubbard-Stratonovich decoupling [4]. The procedure is similar to the mean field decoupling, that is usually accomplished by replacing the interacting term in the BCS hamiltonian by

$$-U\sum_{\mathbf{k},\mathbf{k}'}\bar{c}_{\mathbf{k}\uparrow}\bar{c}_{-\mathbf{k}\downarrow}c_{-\mathbf{k}'\downarrow}c_{\mathbf{k}'\uparrow}\to\frac{1}{U}\bar{\Delta}\Delta+\sum_{\mathbf{k}}\bar{\Delta}c_{-\mathbf{k}\downarrow}c_{\mathbf{k}\uparrow}+\sum_{\mathbf{k}}\Delta\bar{c}_{\mathbf{k}\uparrow}\bar{c}_{-\mathbf{k}\downarrow}, \tag{1.28}$$

so that one is left with a quadratic action in the fermionic operators at the price of including new Δ and $\bar{\Delta}$ to be determined self-consistently. To include fluctuations, one promotes them to new dynamical variables $\Delta(\mathbf{q},\tau)$ and $\bar{\Delta}(\mathbf{q},\tau)$, in the same spirit of Eq. 1.14 and Eq. 1.15 but within a microscopic framework. After integrating out the fermionic variables c and $\bar{c}$, one still is left with $S[\Delta,\bar{\Delta},\mathbf{A}]$, where now Δ and $\bar{\Delta}$ can be mapped into amplitude ($\delta\Delta$) and phase ($\delta\theta$) fluctuations of the order parameter, which can be as well integrated out. We refer for details to previous studies [20], for our purposes the all important news is that now one can identify in the response function pieces where intermediate excitations of the collective mode can be explicitly taken into account.

For instance, in a clean superconductor one can verify that the paramagnetic processes involving purely quasiparticle excitations

$$K^{(3),\mathrm{para}}_{\mathrm{BCS}}\sim\langle jjjj\rangle, \tag{1.29}$$

or intermediate amplitude fluctuations

$$K^{(3),\text{para}}_{\text{Higgs}} \sim \frac{\langle jj\delta\Delta\rangle\langle\delta\Delta jj\rangle}{\frac{1}{U} + \langle\delta\Delta^2\rangle} \equiv \langle jj\delta\Delta\rangle\langle\delta\Delta jj\rangle\chi_{\Delta\Delta}, \tag{1.30}$$

are suppressed, where we adopted the same notation used above and included the amplitude fluctuations, see Fig. 1.5 and Fig. 1.4. In this view, $\langle jj\delta\Delta\rangle$ represent the coupling of light to the amplitude mode via paramagnetic processes, i.e. it has the role of the Γ parameter in the phenomenological coupling 1.3, while the $\chi_{\Delta\Delta}$ part contains the spectrum of the amplitude fluctuations, corresponding thus to $\langle\delta\psi^2\rangle$ in the derivation presented at the beginning of the chapter. For the diamagnetic processes, instead, one finds out that in the clean limit

$$K^{(3),\text{dia}}_{\text{BCS}} \sim \langle\rho\rho\rangle, \tag{1.31}$$

far outweight the contribution coming from

$$K^{(3),\text{dia}}_{\text{Higgs}} \sim \langle\rho\delta\Delta\rangle\langle\delta\Delta\rho\rangle\chi_{\Delta\Delta}. \tag{1.32}$$

This example illustrates how the phenomenological description presented above through the Ginzburg-Landau approach can give spurious results if it is not substantiated by a microscopic calculation involving fermionic degrees of freedom. For what concerns the diamagnetic contribution, the spectral content of $K^{(3),\text{dia}}_{\text{BCS}}$ and $K^{(3),\text{dia}}_{\text{Higgs}}$ is very similar [20], so that only by performing the computation, or looking at the experimental polarization dependence of the THG signal, one can determine which process is playing the major role in the nonlinear current generation.

We notice here that the situation is radically different when disorder is included. Both analytical calculations in self-consistent Born approximation [105, 130] and numerically exact computations on finite size systems [123] have shown that a considerable paramagnetic contribution is to be expected already at a small level of disorder, parametrized as $\gamma/(2\Delta)$, where γ is the impurity scattering rate that determines the width of the Drude peak in the optical conductivity. The paramagnetic response almost immediately overcomes the diamagnetic contribution of the clean case in every fluctuation channel. Most importantly, one finds a larger contribution of collective modes to the THG intensity increases as disorder increases, eventually becoming bigger than the purely quasiparticle one in the $\gamma \gg 2\Delta$ limit. In 1.6 we report a brief overview of the numerical results in the disordered case from [123]. We notice also that numerical simulations show that the spectral content of paramagnetic and diamagnetic contributions are similar in the s-wave case, as was also shown in Ref. [130, 105], making it difficult to disentangle the two in the THG signal. The situation can substantially change when one for instance includes disorder in d-wave superconductors [14], which show a different frequency dependence of $K^{(3),\text{dia}}$ and $K^{(3),\text{para}}$ that would be witnessed by THG experiments. Finally, in Chapter 4 we will analyze in more detail how can hope to get distinct signatures from the various processes by looking at other experimentally accessible quantities, such as the non-linearly generated first harmonic or to the map extracted from a two-dimensional spectroscopy.

We end this section by noticing that the general scheme outlined above can be extended to several situations. Multiband superconductors, for instance, can

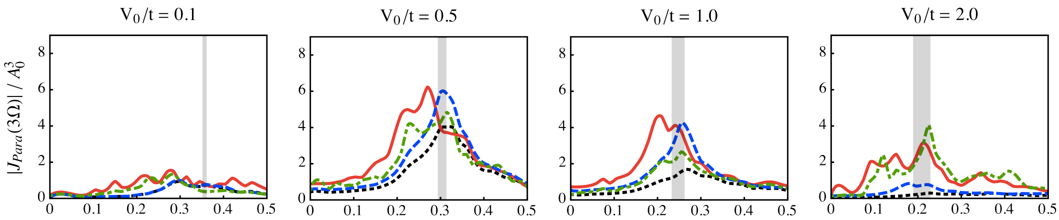

Figure 1.6. Third harmonic paramagnetic current at various disorder levels from [123]. In terms of the disorder parameter $\gamma/(2\Delta)$ from the left to the right we have 0.035, 0.68, 2.86, 18.87. The black line is the quasiparticle only contribution, the blue line includes amplitude fluctuations, the green line includes charge and phase fluctuations, the red line includes every collective mode. The grey stripe signals the range of variation of half the spectral gap in the different configurations.

host collective excitations with marked differences with respect to their single-band counterpart. In a recent work [40], which will not be discussed in the thesis, we first studied the spectrum of collective amplitude fluctuations in a clean two-band superconductor, showing that the spectral weight of the Higgs mode rapidly deviates from the naive extension of the single band case as the interband coupling is turned on, focusing in this perspective on the zoology of the possible fluctuations present in this kind of systems as shown in Fig. 1.7. These results were then used to critically analyze the nonlinear optical response in MgB_2, providing an explanation for the apparently contradictory results of recent experiments, pointing towards a selective relevance either of the Leggett mode [50], associated with the relative phase fluctuations between the two order parameters, or of the amplitude fluctuations at twice the lower gap[77]. By using numerical simulations and realistic estimates of disorder we computed the relative contribution of the quasiparticle, amplitude, and phase fluctuations to the nonlinear optical response by modelling the coupling of these latter with light. We showed that at low pumping frequency only the resonance at twice the smaller gap emerges, as due to the BCS response, while the Leggett mode dominates only in a narrow range of higher pumping frequencies matching its low-temperature value.

1.5 Comparing experiments and theory: a generalized Fresnel approach

The following chapters of the thesis will analyze in detail the outcome of some measurements carried out on superconducting systems with different experimental geometries and protocols, that we want to use as benchmark for the theoretical predictions that we try to make. We want then to understand whether the relation that we have presented above, Eq. 1.7, to connect the transmitted third-harmonic electric field, collected via electro-optic sampling, to the third-order nonlinear current, calculated theoretically, can be extended without further effort. What we want to understand, in particular, is wheter the connection

$$E^{\rm out} \leftrightarrow J^{(3)} \propto K^{(3)}(E^{\rm ext})^3, \tag{1.33}$$

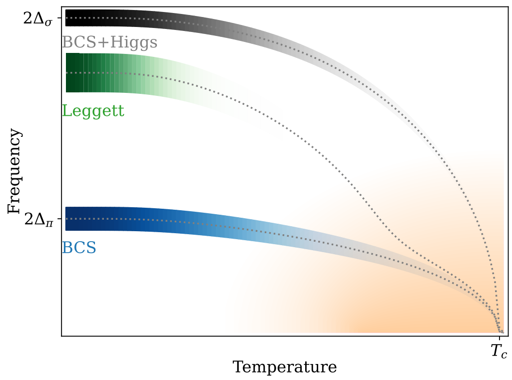

Figure 1.7. The zoology of collective excitations in MgB_2 analyzed in Ref. [40]. Dotted lines denote the temperature dependence of the two order parameters and of the Leggett mode, while shaded areas mark the typical frequency broadening of the corresponding resonances in the nonlinear optical kernel. Around $2\Delta_\sigma$ both the BCS and Higgs fluctuations have a sizable weight, while around $2\Delta_\pi$ BCS fluctuations dominate. The orange shade covers the region of the plot where BCS/Higgs resonances are smeared out and damped by thermal fluctuations.

can always be made, clearly having verified experimentally that the collected signal still depends on the incoming external field as $E^{\text{out}} \propto (E^{\text{ext}})^3$. Indeed, a substantial amount of experimental and theoretical works in this field have clarified the necessity to take care of the so-called screening, or propagation effects, of the incoming radiation inside the superconducting sample. A common procedure that is for instance adopted in the case of transmission experiments with monochromatic THz light [147, 115, 24, 152], is to connect the outgoing radiation with the internal, screened field E^{in}, modifying the previous relation to something like

$$E^{\text{out}} \leftrightarrow J^{(3)} \propto K^{(3)}(E^{\text{in}})^3, \tag{1.34}$$

where E^{in} is either approximated by the transmitted field in linear response regime or calculated thorugh Fabry-Pérot-like formulas. This of course changes in some cases significantly the temperature dependence of the THG signal, since the transmissivity of thin superconducting films strongly depends on temperature [32]. A similar procedure was for instance adopted by us in Ref. [40] discussing MgB_2. In reflection configuration a similar calculation can be made with minimal modifications to take into account the modified Fresnel-like coefficients due to the changing geometry [153, 73].

In order to present under a unified and versatile formalism a possible solution to this issue, in this section we set up a general framework which allows one to compute the outcome of a nonlinear spectroscopy experiment on some prototypical systems, exploring how varying the protocol and the geometry one can relate the measured quantities to the nonlinear response kernel $K^{(3)}$. The procedure will then be applicable to any spectral content of the incoming field, overcoming the limitation of the commonly used Fresnel formulas for the monochromatic limit, and to a generic form of $K^{(3)}(\omega_1, \omega_2, \omega_3)$, which can be the outcome of a numerical simulation or some analytical result from a specific model. Clearly, the result can be used also for computing the outcome of experiments in non-superconducting systems or generalized to second-order non-linearities, as we have done in a forthcoming work for non-centrosymmetric polar insulators.

From the theory point of view, what we have in our hand up to now is a recipe to compute the nonlinear current having as a given, external source the gauge field **A**. What we are missing is the dynamics of this field, which is determined by the Maxwell equations or, equivalently, by the free action of the electromagnetic field. One can then treat on equal footing the light and matter degrees of freedom by solving a coupled system of equations for the two.

1.5.1 Perturbative solution of Maxwell equations

We consider then a nonlinear material in the region of space $0 < z < d$ characterized by a uniform ($z-$independent) nonlinear third order susceptibility $K^{(3)}(\omega_1, \omega_2, \omega_3)$ sandwiched by vacuum, on which we shine the transverse field $\mathbf{A} = (A_x(z, \omega), 0, 0)$. The non-linearly induced current reads in the most general case

$$J_x^{(3)}(z, \omega) = \int d\omega_i\, K^{(3)}(\omega_1, \omega_2, \omega_3) A_x(z, \omega_1) A_x(z, \omega_2) A_x(z, \omega_3) \delta\left(\omega - \sum_i \omega_i\right). \tag{1.35}$$

This source term will enter the Maxwell equations resulting in the following Helmholtz equations

$$\begin{cases} \partial_z^2 A(z, \omega) + \frac{\omega^2}{c^2} A(z, \omega) = 0 & (z < 0, z > d) \\ \partial_z^2 A(z, \omega) + \frac{n^2(\omega)\omega^2}{c^2} A(z, \omega) = -\frac{4\pi}{c} J^{(3)}(z, \omega) & (0 < z < d), \end{cases} \tag{1.36}$$

where we now omit the x pedix everywhere. In principle one has to solve self-consistently the two equations since there is a dependence on the vector potential in the source term of the right hand side. As nonlinear effects are usually smaller with respect to linear ones, which are already taken into account by $n(\omega)$, it is possible to solve with a perturbative approach the previous differential equation. Let us introduce a fictitious small parameter η in order to keep track of this perturbative expansion, such that

$$K^{(3)}(\omega_1, \omega_2, \omega_3) \equiv \eta \tilde{K}^{(3)}(\omega_1, \omega_2, \omega_3). \tag{1.37}$$

Then we suppose

$$A(z, \omega) = \sum_m \eta^m A^{(m)}(z, \omega), \tag{1.38}$$

and replace these expressions in Eq. 1.35

$$J^{(3)}(z, \omega) = \sum_{p,q,r} \eta^{p+q+r+1} \int d\omega_i\, K^{(3)}(\omega_1, \omega_2, \omega_3) A^{(p)}(z, \omega_1) A^{(q)}(z, \omega_2) A^{(r)}(z, \omega_3) \times \\ \times \delta\left(\omega - \sum_i \omega_i\right). \tag{1.39}$$

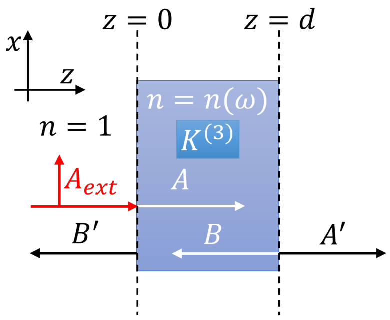

Figure 1.8. A film of thickness d with refractive index $n(\omega)$ and nonlinear response kernel $K^{(3)}$ is sandwiched by vacuum at $z = 0$ and $z = d$. The gauge potential $A_{\text{ext}}(\omega)$ impinges from $z < 0$ and generates the fields $A^{(0)}(z,\omega)$, containing linear effects, and $A^{(1)}(z,\omega)$, containing nonlinear effects. The latter depends on the coefficients A, B for $0 < z < d$, and A', B' for $z > d$ and $z < 0$, respectively, which enter the system for the boundary conditions in Eq. 1.50.

We can solve the Eq. 1.36 order by order in η, collecting the corresponding terms in the two sides of the equation. For η^0 we have

$$\begin{cases} \partial_z^2 A^{(0)}(z,\omega) + \frac{\omega^2}{c^2} A^{(0)}(z,\omega) = 0 & (z < 0, z > d) \\ \partial_z^2 A^{(0)}(z,\omega) + \frac{n^2(\omega)\omega^2}{c^2} A^{(0)}(z,\omega) = 0 & (0 < z < d), \end{cases} \tag{1.40}$$

which is the usual propagation of waves in a slab of thickness d in the linear regime. The solution to the system for the linear response in the region $0 < z < d$ reads

$$A^{(0)}(z,\omega) = A_t(\omega) e^{i\omega n(\omega) z/c} + A_r(\omega) e^{-i\omega n(\omega) z/c}. \tag{1.41}$$

Here we have

$$A_t(\omega) = A_{\text{ext}}(\omega) t(\omega) f(\omega), \tag{1.42}$$

$$A_r(\omega) = A_{\text{ext}}(\omega) t(\omega) e^{i2\omega n(\omega) d/c} r(\omega) f(\omega), \tag{1.43}$$

in terms of the spectrum of the incident field $A_{\text{ext}}(\omega)$, the usual vacuum-material transmission and reflection coefficients

$$t(\omega) = \frac{2}{n(\omega) + 1}, \tag{1.44}$$

$$r(\omega) = \frac{n(\omega) - 1}{n(\omega) + 1}, \tag{1.45}$$

and the Fabry-Pérot factor

$$f(\omega) = \frac{1}{1 - r(\omega)^2 e^{i2\omega n(\omega) d/c}}. \tag{1.46}$$

Due to the linearity of Maxwell equations in absence of source terms, one can in principle extend by superposition the previous solution for arbitrary frequency spectrum of the incident field. For η^1 we obtain

$$\begin{cases} \partial_z^2 A^{(1)}(z,\omega) + \frac{\omega^2}{c^2} A^{(1)}(z,\omega) = 0 & (z < 0, z > d) \\ \partial_z^2 A^{(1)}(z,\omega) + \frac{n^2(\omega)\omega^2}{c^2} A^{(1)}(z,\omega) = -\frac{4\pi}{c} J^{(3)}_{\eta^1}(z,\omega) & (0 < z < d), \end{cases} \tag{1.47}$$

where

$$J^{(3)}_{\eta^1}(z,\omega) = \int d\omega_i\, K^{(3)}(\omega_1,\omega_2,\omega_3)A^{(0)}(z,\omega_1)A^{(0)}(z,\omega_2)A^{(0)}(z,\omega_3)\times \\ \times\delta\left(\omega - \sum_i \omega_i\right). \tag{1.48}$$

The solution to the last equation of the previous system reads as usual

$$A^{(1)}(z,\omega) = A_p(z) + Ae^{i\omega n(\omega)z/c} + Be^{-i\omega n(\omega)z/c}, \tag{1.49}$$

where we denote as $A_p(z)$ the particular solution. Considering the outgoing nonlinear signal in free space, $A^{(1)}(z<0,\omega) = B'e^{-i\omega z/c}$ and $A^{(1)}(z>d,\omega) = A'e^{i\omega z/c}$, the boundary conditions read,

$$\begin{cases} B' & = A_p(0) + A + B \\ -\frac{i\omega}{c}B' & = A'_p(0) + \frac{in(\omega)\omega}{c}(A-B) \\ A'e^{i\omega d/c} & = A_p(d) + Ae^{in(\omega)\omega d/c} + Be^{-in(\omega)\omega d/c} \\ \frac{i\omega}{c}A'e^{i\omega d/c} & = A'_p(d) + \frac{in(\omega)\omega}{c}(Ae^{in(\omega)\omega d/c} - Be^{-in(\omega)\omega d/c}). \end{cases} \tag{1.50}$$

If one is interested in finding the nonlinear signal detected in reflection configuration, the all important coefficient is B', while in transmission the relevant quantity is A'; both of them can be found by inverting the linear system written before in terms of the values of the particular solution A_p and its first derivative A'_p at the two ends of the slab.

We now focus on the expression for A', which is the relevant quantity to derive the expression for the electric field right beyond the sample in the standard THG experiments in transmission configuration. If one uses a reflection geometry, one analogously computes the B' coefficient, as we will see later in the limit of bulk samples. Redefining now A' to include the pure phase factor $e^{i\omega d/c}$, it reads explicitly

$$A' = -\frac{f(\omega)}{(n(\omega)+1)^2}\Bigg[2n(\omega)e^{in(\omega)\omega d/c}\left(A_p(0) - \frac{ic}{\omega}A'_p(0)\right) \\ +(n(\omega)-1)e^{i2n(\omega)\omega d/c}\left(n(\omega)A_p(d) + \frac{ic}{\omega}A'_p(d)\right) \\ -(n(\omega)+1)\left(n(\omega)A_p(d) - \frac{ic}{\omega}A'_p(d)\right)\Bigg]. \tag{1.51}$$

In order to compute the transmission one should then evaluate the particular solution and its derivative. One can use for instance Fourier transforms and consider the following expression of the particular solution

$$A_p(z,\omega) = \frac{4\pi}{c}\frac{1}{2\pi}\int dk\, \frac{e^{-ikz}}{k^2 - n^2(\omega)\omega^2/c^2}J^{(3)}_{\eta^1}(k,\omega), \tag{1.52}$$

where $J^{(3)}_{\eta^1}(k,\omega)$ is the Fourier transform of the non-linearly induced current, Eq. 1.48, that we rewrite as

$$J^{(3)}_{\eta^1}(k,\omega) = \sum_{\{\alpha_i\}}\int_0^d dz \int d\omega_i\, e^{i(k+\sum_i \alpha_i n(\omega_i)\omega_i/c)z}K^{(3)}(\omega_1,\omega_2,\omega_3)\times \\ \times A_{\alpha_1}(\omega_1)A_{\alpha_2}(\omega_2)A_{\alpha_3}(\omega_3)\delta\left(\omega - \sum_i \omega_i\right). \tag{1.53}$$

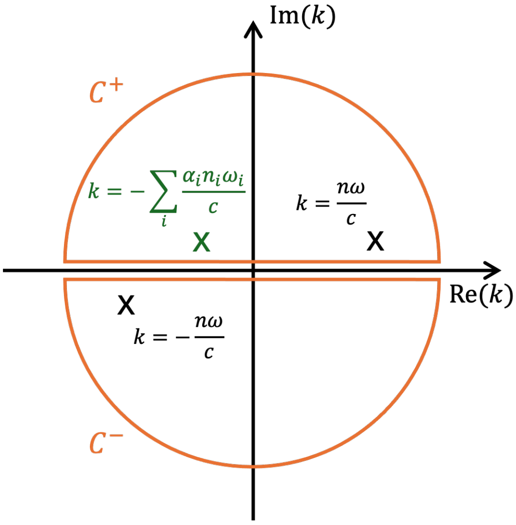

Figure 1.9. The integration contours used in Eq. 1.55. The green pole lies in the upper or lower half-plane according to the signs of α_i.

Here we used the z-dependence of the field inside the material given by Eq. 1.41, separating the (eight) contributions according to the number of forward ($\propto A_t$) or backward ($\propto A_r$) propagating fields appearing in the triple $A^{(0)}$ product. This amounts to sum over the possible $\{\alpha_i\} = (\alpha_1, \alpha_2, \alpha_3)$ combinations where $\alpha_i = +1$ for A_t terms and $\alpha_i = -1$ for A_r terms. The integral over z can be performed immediately and one gets

$$\begin{aligned} J^{(3)}_{\eta^1}(k,\omega) = \sum_{\{\alpha_i\}} \int d\omega_i \, \frac{e^{i(k+\sum_i \alpha_i n(\omega_i)\omega_i/c)d} - 1}{i(k + \sum_i \alpha_i n(\omega_i)\omega_i/c)} K^{(3)}(\omega_1,\omega_2,\omega_3)\times \\ \times A_{\alpha_1}(\omega_1) A_{\alpha_2}(\omega_2) A_{\alpha_3}(\omega_3) \delta\left(\omega - \sum_i \omega_i\right). \end{aligned} \tag{1.54}$$

Plugging the last expression in $A_p(z)$ we get

$$\begin{aligned} A_p(z,\omega) = \frac{4\pi}{c} \sum_{\{\alpha_i\}} \int d\omega_i \, K^{(3)}(\omega_1,\omega_2,\omega_3) A_{\alpha_1}(\omega_1) A_{\alpha_2}(\omega_2) A_{\alpha_3}(\omega_3) \delta\left(\omega - \sum_i \omega_i\right) \times \\ \times \frac{1}{2\pi} \int dk \, \frac{e^{-ikz}}{k^2 - n^2(\omega)\omega^2/c^2} \frac{e^{i(k+\sum_i \alpha_i n(\omega_i)\omega_i/c)d} - 1}{i(k + \sum_i \alpha_i n(\omega_i)\omega_i/c)}. \end{aligned} \tag{1.55}$$

The k-integral can then be computed through residues. Since we are interested in the particular solution for $z \to 0^+$ and $z \to d^-$, we need to choose the integration contour accordingly. For the first term in the k-integral ($\propto e^{-ik(z-d)}$), we should close the contour in the upper half plane, since $z - d < 0$, while for the second term

($\propto e^{-ikz}$) we should close in the lower half plane, since $z > 0$. Explicitly we have

$$\begin{aligned}
&\frac{1}{2\pi}\int dk\, \frac{e^{-ikz}}{k^2 - n^2(\omega)\omega^2/c^2}\,\frac{e^{i(k+\sum_i \alpha_i n(\omega_i)\omega_i/c)d} - 1}{i(k + \sum_i \alpha_i n(\omega_i)\omega_i/c)} = \\
&= \int_{\mathcal{C}^+} dk\, \frac{e^{-ik(z-d)}e^{i\sum_i \alpha_i n(\omega_i)\omega_i d/c}}{(k^2 - n^2(\omega)\omega^2/c^2)(k + \sum_i \alpha_i n(\omega_i)\omega_i/c)} \\
&+ \int_{\mathcal{C}^-} dk\, \frac{e^{-ikz}}{(k^2 - n^2(\omega)\omega^2/c^2)(k + \sum_i \alpha_i n(\omega_i)\omega_i/c).}
\end{aligned} \tag{1.56}$$

In both contours we will have one pole determining the (forward or backward) Maxwell-like propagation of the non-linearly generated radiation ($k = \pm n(\omega)\omega/c$) and the one(s) corresponding to the propagation of the internal fields generating the nonlinear signal ($k = -\sum_i \alpha_i n(\omega_i)\omega_i/c$). According to the overall sign of $\sum_i \alpha_i n''(\omega_i)\omega_i/c$ the corresponding pole(s) will lie in the lower or upper half complex plane, thus being enclosed in one or the other integration contour. Denoting for brevity $n = n(\omega)$ and $n_i = n(\omega_i)$, in the end we get, for $0 < z < d$,

$$\begin{aligned}
&\frac{1}{2\pi}\int dk\, \frac{e^{-ikz}}{k^2 - n^2\omega^2/c^2}\,\frac{e^{i(k+\sum_i \alpha_i n_i\omega_i/c)d} - 1}{i(k + \sum_i \alpha_i n_i\omega_i/c)} = \\
&= \frac{e^{in\omega z/c}}{(-n\omega/c + \sum_i \alpha_i n_i\omega_i/c)(2n\omega/c)} - \frac{e^{-in\omega z/c}e^{i\left(n\omega + \sum_i \alpha_i n_i \omega_i\right)d/c}}{(n\omega/c + \sum_i \alpha_i n_i\omega_i/c)(2n\omega/c)} \\
&- \frac{e^{i\sum_i \alpha_i n_i \omega_i z/c}}{(n\omega/c)^2 - \left(\sum_i \alpha_i n_i\omega_i/c\right)^2}.
\end{aligned} \tag{1.57}$$

Using this result in Eq. 1.55 we are able to compute the values of the particular solution and its first derivative at the boundaries of the slab. The A' coefficient then reads

$$\begin{aligned}
A' = &\frac{4\pi i}{\omega}\frac{f e^{in\omega d/c}}{n+1}\sum_{\{\alpha_i\}}\int d\omega_i\, K^{(3)}(\omega_1,\omega_2,\omega_3)A_{\alpha_1}(\omega_1)A_{\alpha_2}(\omega_2)A_{\alpha_3}(\omega_3)\times \\
&\times\left(\frac{n-1}{n+1}\frac{e^{i\left(\sum_i \alpha_i n_i\omega_i + n\omega\right)d/c} - 1}{i\left(\sum_i \alpha_i n_i\omega_i + n\omega\right)/c} + \frac{e^{i\left(\sum_i \alpha_i n_i\omega_i - n\omega\right)d/c} - 1}{i\left(\sum_i \alpha_i n_i\omega_i - n\omega\right)/c}\right)\delta\left(\omega - \sum_i \omega_i\right).
\end{aligned} \tag{1.58}$$

This result is valid for any value of the thickness of the film and takes into account all the propagation effects inside the material. We recognize in the second line the phase matching conditions between the non-linearly generated radiation and the internal fields, which appear with both minus and plus signs according to the specific combinations of forward or backward propagating waves that we can consider. Clearly, in non-dispersive media the phase-matching condition coincides with the energy conservation, while here it strongly depends on $n(\omega)$. As a final remark we point out that a similar result has been obtained in Ref. [65], where the effects of phase-mismatch between THz-pump and eV-probe have been studied in the context of ultrafast Kerr effect, i.e. considering an instantaneous $K^{(3)}$. A minor difference is just that here we looked for a solution to the full second-order Maxwell equation in

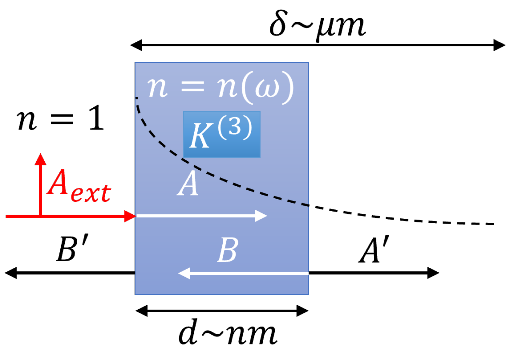

Figure 1.10. Scheme for the approximation used in trasmission experiments on thin films, where the thickness is the smallest lengthscale at play. The crudest approximation in Eq. 1.60 amounts to consider the profile of the field constant inside the material, while in Eq. 1.62 one keeps the effect of screening.

the second line of Eq. 1.47, while in Ref. [65] the authors explicilty integrate the $z-$dependence of the nonlinear polarizarion by using the slowly-varying amplitude approximation.

1.5.2 Approximate expressions for limiting cases

It is useful to derive an approximate expression of Eq. 1.58 to be used in some limiting cases. For very thin films with thickness d much shorter than wavelength $\lambda = c/(n'\omega)$ and the penetration depth $\delta = c/(n''\omega)$ of the radiation inside the material, one can expand the term in round brackets at the second line of Eq. 1.58 using $e^{i\alpha} \sim 1 + i\alpha$ for $\alpha \ll 1$, obtaining

$$\frac{n-1}{n+1}\frac{e^{i\alpha d}-1}{i\alpha} + \frac{e^{i\alpha' d}-1}{i\alpha'} \sim \frac{2nd}{n+1}. \tag{1.59}$$

If one is interested in the electric field at leading order in d, one must set $d = 0$ in all other pieces of Eq. 1.58. Using the relation $E(\omega) = i\omega A(\omega)/c$, one recovers the expression

$$E(z = d^+, \omega) = E^{(0)}(z = d^+, \omega) - \frac{2\pi d}{c} J^{(3)}_{\eta^1}(z = 0, \omega), \tag{1.60}$$

where now, since for $d = 0$ one has $A^{(0)}(z = 0, \omega) = A_{\text{ext}}(\omega)$ in Eq. 1.48, the nonlinear current becomes

$$J^{(3)}_{\eta^1}(z = 0, \omega) = \int d\omega_i\, K^{(3)}(\omega_1, \omega_2, \omega_3) A_{\text{ext}}(\omega_1) A_{\text{ext}}(\omega_2) A_{\text{ext}}(\omega_3) \delta\left(\omega - \sum_i \omega_i\right). \tag{1.61}$$

This result is not surprising: in the approximation $d \to 0$ neither the non-linearly generated current nor the field generating it are sensitive to any propagation effect. We stress that this is exactly the result presented at the beginning of the chapter to connect the transmitted third-harmonic field to the corresponding harmonic of the nonlinear current.

A less crude approximation is instead obtained if one consistently takes into account the screening of the incoming field inside the material. Assuming nonetheless

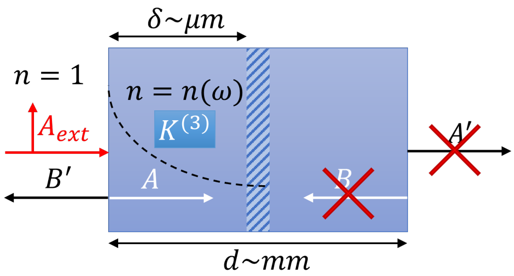

Figure 1.11. Scheme to approximate the reflection from bulk samples as a process of reflection from a semi-infinite medium. Since the field penetrates just in a small fraction of the sample, one can neglect in 1.50 both the transmitted field outside the material and the back-propagating internal one.

that $|n|\omega d/c \ll 1$, one can rewrite the previous Eq. 1.58 as

$$A' = \frac{2\pi i d}{\omega} T(\omega) \int d\omega_i \, K^{(3)}(\omega_1, \omega_2, \omega_3) A_{\text{in}}(\omega_1) A_{\text{in}}(\omega_2) A_{\text{in}}(\omega_3) \delta \left(\omega - \sum_i \omega_i \right), \tag{1.62}$$

where we defined

$$T(\omega) = \frac{2n}{2n \cos(n\omega d/c) - i(n^2+1) \sin(n\omega d/c)} \approx \frac{1}{1 - i(n^2+1)\omega d/(2c)}, \tag{1.63}$$

which is the transmissivity of the vacuum-film-vacuum sandwich, and the internal field $A_{\text{in}}(\omega) = A^{(0)}(z=0, \omega)$ appearing in Eq. 1.48

$$\begin{aligned} A_{\text{in}}(\omega) &= A_{\text{ext}}(\omega) \frac{2n \cos(n\omega d/c) - 2i \sin(n\omega d/c)}{2n \cos(n\omega d/c) - i(n^2+1) \sin(n\omega d/c)} \\ &\approx A_{\text{ext}}(\omega) \frac{1 - i\omega d/c}{1 - i(n^2+1)\omega d/(2c)}. \end{aligned} \tag{1.64}$$

Since $\omega d/c \ll 1$, comparing the last two equations one can also approximate the internal field with the transmitted one, i.e. one can take $A_{\text{in}}(\omega) \approx T(\omega) A_{\text{ext}}(\omega)$. This result validates then the common approximation presented at the beginning of this section for THG experiments, see Eq. 1.34, where $E_{\text{in}}(\omega) = T(\omega) E_{\text{out}}(\omega)$.

On the other hand, we can consider reflection from bulk systems, considering the opposite limit when $d \gg \lambda, \delta$, as it usually happens for experiments with $c-$axis polarized electric fields on cuprate samples[153, 73]. One gets from an equivalent system of Eq. 1.50 including only the boundary conditions at $z = 0$

$$B' = \frac{1}{n(\omega)+1} \left(n(\omega) A_p(0) + \frac{ic}{\omega} A_p'(0) \right). \tag{1.65}$$

Considering the expression of the particular solution

$$A_p(z, \omega) = \frac{4\pi}{c} \frac{1}{2\pi} \int dk \, \frac{e^{-ikz}}{k^2 - n^2(\omega)\omega^2/c^2} J^{(3)}_{\eta^1}(k, \omega), \tag{1.66}$$

we should compute the Fourier transform of the non-linearly induced current. We notice that in the bulk limit, i.e. for samples much thicker than the penetration depth of the radiation inside the material, the backward propagating internal fields entering $A^{(0)}(z,\omega)$ in Eq. 1.41 thorugh $A_r(\omega)$ are exponentially suppressed. Thus only forward propagating internal fields ($\propto A'_t$) contribute, giving

$$\begin{aligned} J^{(3)}_{\eta^1}(k,\omega) = \int_0^\infty dz \int d\omega_i \, e^{i(k+\sum_i n(\omega_i)\omega_i/c)z} K^{(3)}(\omega_1,\omega_2,\omega_3)\times \\ \times A_{\rm ext}(\omega_1)t(\omega_1)A_{\rm ext}(\omega_2)t(\omega_2)A_{\rm ext}(\omega_3)t(\omega_3)\delta\left(\omega-\sum_i\omega_i\right). \end{aligned} \tag{1.67}$$

Here we extend the upper limit of integration to infinity since the thickness is the largest lengthscale at play here. We can nevertheless assure the convergence of the integral in z since i) $\omega n''(\omega)$ is positive-definite for any frequency and ii) the field has a finite cutoff in frequency given by the incident radiation. Then one gets

$$\begin{aligned} J^{(3)}_{\eta^1}(k,\omega) = i \int d\omega_i \, K^{(3)}(\omega_1,\omega_2,\omega_3)\frac{A_{\rm ext}(\omega_1)t(\omega_1)A_{\rm ext}(\omega_2)t(\omega_2)A_{\rm ext}(\omega_3)t(\omega_3)}{k+\sum_i n(\omega_i)\omega_i/c}\times \\ \times\delta\left(\omega-\sum_i\omega_i\right). \end{aligned} \tag{1.68}$$

Plugging the latter expression in Eq. 1.66 to find the particular solution and computing the coefficient B' from Eq. 1.65, one gets finally

$$\begin{aligned} B' = \frac{4\pi}{\omega}\frac{1}{1+n(\omega)}\int d\omega_i \, K^{(3)}(\omega_1,\omega_2,\omega_3)A_{\rm ext}(\omega_1)A_{\rm ext}(\omega_2)A_{\rm ext}(\omega_3)\times \\ \times\frac{t(\omega_1)t(\omega_2)t(\omega_3)}{n(\omega)\omega/c+\sum_i n(\omega_i)\omega_i/c}\delta\left(\omega-\sum_i\omega_i\right). \end{aligned} \tag{1.69}$$

The reflected electric field, using again the relation $E(\omega) = i\omega A(\omega)/c$, reads in this case

$$\begin{aligned} E(z<0,\omega) &= E^{(0)}(z<0,\omega) \\ &+ 2\pi i t(\omega)\int d\omega_i \, K^{(3)}(\omega_1,\omega_2,\omega_3)\frac{A_{\rm in}(\omega_1)A_{\rm in}(\omega_2)A_{\rm in}(\omega_3)}{n(\omega)\omega+\sum_i n(\omega_i)\omega_i}\delta\left(\omega-\sum_i\omega_i\right), \end{aligned} \tag{1.70}$$

where the internal field is in this case given by $A_{\rm in}(\omega) = A_{\rm ext}(\omega)t(\omega)$. This result, specialized for a monochromatic incoming field and focusing on the third harmonic, has been used in Ref. [39] to compare the experimental measurements of Ref. [73] to the computed two-plasmon kernel, as we will see in Chapter 2. We stress also that an analogous expression was obtained by a similar perturbative calculation in Ref. [52]. In that case, however, the obtained expression was specialized to the case of the sine-Gordon model, which is used to describe the $c-$axis response of superconducting cuprates mediated by Josephson plasmons, while the result presented here is valid for a generic third-order optical kernel. In Ref. [153] as well a similar procedure is presented to simulate the two-dimensional THz map of cuprate LBCO.

Chapter 2

Phase excitations in cuprates: the case of $c-$axis Josephson plasmons

The content of this chapter has been published in Ref. [39].

2.1 Introduction

Plasma modes describe the propagation of longitudinal electromagnetic waves in metals, hybridized with electronic charge fluctuations. As such, they can be detected via density-sensitive probes, like inelastic X-ray scattering[5] (RIXS) or electron energy-loss spectroscopy[46] (EELS). Whenever the metal becomes superconductor the fluctuations of the superconducting phase, canonically conjugate to the density, bring up the information on the plasma mode[108].

In layered superconductors, as e.g. cuprates, the weak coupling between CuO_2 planes induces a marked anisotropy between in-plane ω_{xy} and out-of-plane ω_z long-wavelength plasma frequencies. While ω_{xy} lies at an energy scale where no appreciable change occurs across the superconducting transition, the soft ω_z plasmon becomes undamped by the opening of the superconducting gap below T_c, as evidenced by the emergence of a sharp plasma edge in the c-axis reflectivity at a temperature-dependent scale $\omega_z(T)$[137, 63, 74, 12, 144, 104, 69, 33, 64, 31]. At finite momentum the two energy scales ω_{xy} and ω_z get mixed, and the energy-momentum dispersion of the layered three-dimensional (3D) plasmon, shown in Fig. 2.1(a), acquires acoustic-like branches at fixed k_z, see Fig. 2.1(b), due to the reduced screening between neighboring layers. RIXS and EELS can probe such a dispersion both in the normal and superconducting states, see Fig. 2.1(b) and (c), even though they cannot access the long-wavelength limit due to charge conservation[61, 86, 107, 13].

In cuprates pair tunnelling is the dominant inter-layer hopping mechanism below T_c, justifying a Josephson-like description for the out-of-plane phase modes[118, 117]. The excitation energy of superconducting Josephson plasmon scales with the cosine of the superconducting phase gradient. Such an intrinsic anharmonicity turns in a primary source of nonlinear optical response below T_c, thanks to the minimal coupling of the phase gradient to the gauge field[118, 117]. A typical hallmark of

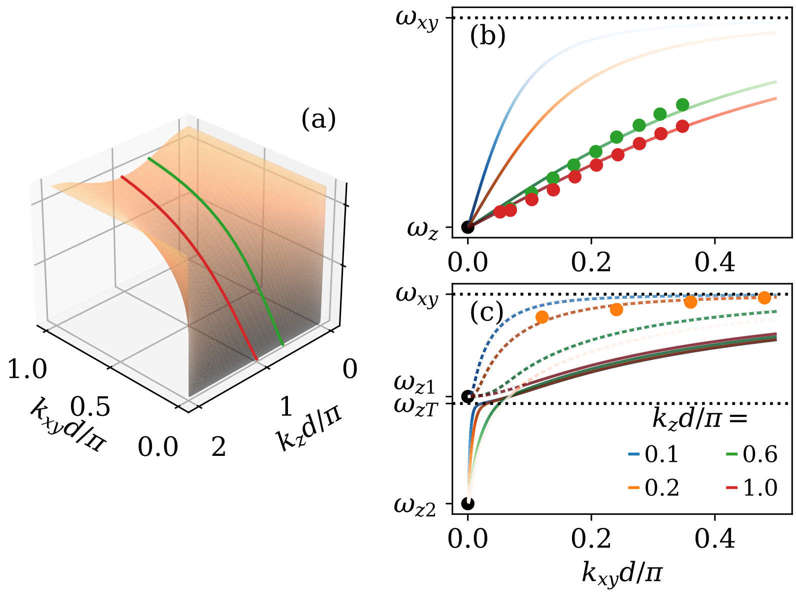

Figure 2.1. (a) Plasmon dispersion in a layered superconductor from Eq. 2.3. Red and green solid lines highlight cuts at fixed k_z. (b) RIXS measurements (dots) from Ref. [107] superimposed to plasmon branches plotted with a line intensity proportional to the THG polarization weight. In the bilayer case (c) the plasmon branches (shown in log scale) double, the upper one (dashed line) being the analogous of the single-layer mode. The lower branch, which rapidly approaches the ω_T scale seen in absorption (see text), is not visible in RIXS measurements [13]. The momentum scale and color codes are the same in panels (b) and (c).

nonlinear response is THz Third Harmonic Generation (THG). THG from Josephson plasmons[114, 73, 68, 153], as well as additional effects connected to their nonlinear response[81, 42, 89], have been experimentally proven in cuprates. In analogy with nonlinear phononics[67, 146, 41, 133, 84, 10], the main THG process can be understood as a sum-frequency process where two photons of the THz pulse centered at Ω excite simultaneously two plasma waves[45] with opposite 3D momenta. As a consequence, while linear reflectivity is only sensitive to the long-wavelength limits ω_{xy}, ω_z of the plasmon dispersion, nonlinear optics is sensitive to the convolution of plasmon excitations at *finite* momenta. This process retrieves the density of states of plasma excitations in a momentum region complementary to the one measured by RIXS, see Fig. 2.1(b) and (c), providing in principle a mechanism to selectively tune the resonance energy for THz THG in a layered heterostructure.

In this chapter we demonstrate this principle by comparing single- and bi-layer structures. In single-layer systems, with a single plane per unit cell in the stacking direction, the light polarization projects out the full plasmon dispersion towards the low-energy ω_z value measured by linear optics. Since experiments are performed at a fixed pump frequency Ω as a function of temperature, the largest THG is expected at $\bar{T}$ where $\Omega = \omega_z(\bar{T})$. Such a prediction, qualitatively similar to what obtained[45] by neglecting the plasmon dispersion, is consistent with experiments [114, 68].

In bilayer superconductors the modulation of intra-bilayer J_{z1} and inter-bilayer J_{z2} Josephson couplings along the stacking direction, with $J_{z1} \gg J_{z2}$, leads to a doubling of the Josephson plasmon branches, as originally explained in Ref. [144], giving in the long-wavelength limit two scales $\omega_{z1} \gg \omega_{z2}$. The lower one $\omega_{z2} \propto \sqrt{J_{z2}}$ controls the lower and sharper reflectivity edge at zero momentum[63, 74, 12, 144, 69, 33, 64], while the upper Josephson branch has been recently measured by RIXS[13], that turns out to be insensitive to the lower plasmon branch, see Fig. 2.1(c). By computing the THG for the bilayer case we show that the dominant contributions of plasma modes to the THG arise from intra-bilayer phase fluctuations, scaling with the larger Josephson stiffness. As a consequence, in the bilayer system the momentum integration moves the THG spectral weight towards a higher energy scale $\omega_{zT} \approx \omega_{z1}$, explaining the lack of any resonance at the temperature $\bar{T}$ where $\Omega = \omega_{z2}(\bar{T})$ in the measurements of Ref. [73].

2.2 Single-layer case

The contribution of plasma waves to the nonlinear optical response can be qualitatively understood within a simplified anisotropic Josephson-like model for the superconducting phase. Labelling with θ_n the superconducting phase in the n-th layer one can write an effective classical Hamiltonian:

$$H = \frac{1}{8}\int d^2r\, d \sum_n \Big[D_{xy}(\nabla_{xy}\theta)^2 - 8J_z \cos(\theta_{n+1} - \theta_n) \Big], \tag{2.1}$$

where the in-plane phase difference has been already promoted to a continuum phase gradient, D_{xy} is the in-plane stiffness (equivalent to $\hbar^2 n_s/m$ in the continuum, isotropic limit) and J_z is an energy density defining the superfluid stiffness as $D_z = 4J_z d^2$ along the out-of-plane z direction, d being the interlayer distance. Henceforth, unless explicitly displayed, we set $\hbar = k_B = 1$. The classical model in Eq. 2.1 is promoted to a quantum equivalent by including dynamical effects related to the phase gradient in time, scaling as $\kappa_0(\partial_\tau\theta_n)^2$, with κ_0 the charge compressibility. Once that Coulomb effects are included, κ_0 is replaced by the RPA charge compressibility[15, 134]. By retaining only the quadratic term in the expansion of the cosine in Eq. 2.1 we obtain the following Gaussian quantum action[110, 28]:

$$S_G = \frac{1}{32\pi e^2} \sum_{i\omega_m, \mathbf{k}} |\mathbf{k}|^2 \left(-(i\omega_m)^2 + \omega_L^2(\mathbf{k}) \right) |\theta(i\omega_m, \mathbf{k})|^2, \tag{2.2}$$

where $i\omega_m = 2\pi m T$ are bosonic Matsubara frequencies, and $\omega_L(\mathbf{k})$ includes the full momentum dependence of the layered Josephson plasma mode (JPM):

$$\omega_L^2(\mathbf{k}) = \omega_{xy}^2 \frac{k_{xy}^2}{|\mathbf{k}|^2} + \omega_z^2 \frac{q_z^2}{|\mathbf{k}|^2}, \tag{2.3}$$

where $\omega_{xy,z}^2 = 4\pi e^2 D_{xy,z}$, $q_z = (2/d)\sin(k_z d/2)$ and $|\mathbf{k}|^2 = k_{xy}^2 + q_z^2$. An external gauge field A_z polarized along the z direction enters the model in Eq. 2.1 via the minimal coupling substitution $\theta_{n+1} - \theta_n \to \theta_{n+1} - \theta_n - 2edA_z/c$. As detailed in the following Section 2.2.1, the third-order current $J^{NL} \sim KA_z^3$ can be obtained by expanding the cosine Josephson interaction in Eq. 2.1 beyond second order in the gauge-invariant phase gradient along z, and integrating out the phase degrees

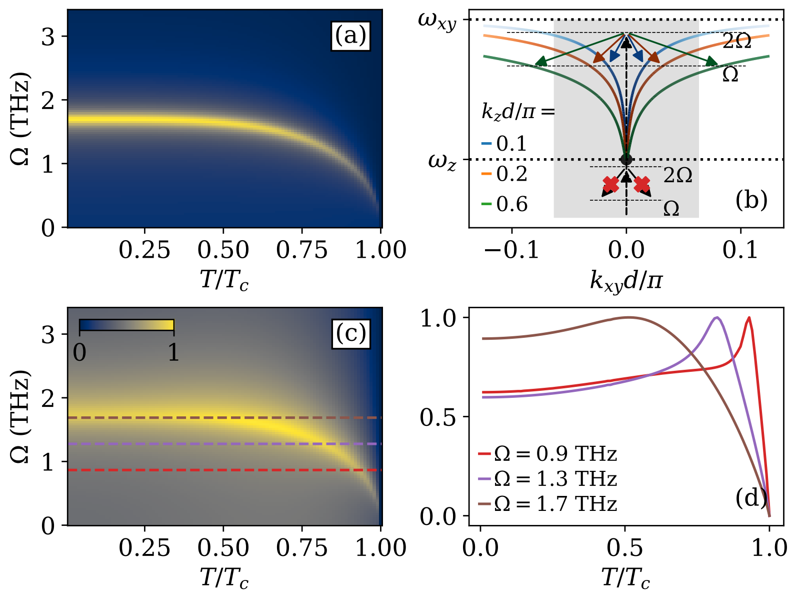

Figure 2.2. Comparison between the nonlinear kernel $|K(2\Omega, T)|$ of Eq. 2.4 for (a) non-dispersive plasmon, corresponding to replacing $\omega_L(\mathbf{k})$ with ω_z, and (c) the dispersive plasmon. (b) Sketch of the THG process. The $\omega_L(\mathbf{k})$ dispersion from Eq. 2.3 is plotted in log scale, with a line intensity weighted with the spectral weight of the two-plasmon process from Eq. 2.4. Only for $\Omega > \omega_z$ two light pulses at Ω can decay in two plasmons with opposite momenta. At larger energies the number of available states increases, but these correspond to a region with smaller spectral weight (see text and). The shaded area corresponds to the region $k_{xy} < 1/\xi$ of allowed in-plane momenta. (d) $|K(2\Omega)|$ from panel (c) as a function of temperature for three selected pump frequencies (dashed lines in panel (c)), where each curve is normalized to its maximum.

of freedom[45]. For a monochromatic incident field $A_z = A_0 \cos(\Omega t)$ the resulting THG intensity is proportional[20, 142, 123] to $I_{THG} \propto |K(2\Omega)|^2$. The resonant part of the nonlinear kernel K accounts for the density-of-states of the process involving the generation of two JPMs with opposite momenta, see Fig. 2.2(b), and it is given explicitly by:

$$K(\Omega) \propto J_z^2 \frac{1}{V} \sum_{\mathbf{k}} \frac{q_z^4}{|\mathbf{k}|^4} \frac{\coth\left(\frac{\beta\omega_L(\mathbf{k})}{2}\right)}{\omega_L(\mathbf{k})(4\omega_L^2(\mathbf{k}) - (\Omega + i\delta)^2)}, \tag{2.4}$$

where $i\omega_m \to \Omega + i\delta$. Within the Josephson model in Eq. 2.1 the coupling J_z controls both the stiffness and the anharmonic interaction terms. Thus we will adopt the same experimental temperature-dependent stiffness $D_z(T)$, $D_{xy}(T)$ both in the plasmon dispersion in Eq. 2.3 and in the effective anharmonic couplings, see[127].

In Fig. 2.2 we show the nonlinear kernel K as a function of temperature and frequency, by setting $\omega_{xy}(T = 0) = 250$ THz and $\omega_z(T = 0) = 1.7$ THz, as appropriate for optimally-doped LSCO samples ($T_c = 38$ K)[68]. We compare the case where the full plasmon dispersion in Eq. 2.3 is included (panel c) with the case, considered previously[45], where $\omega_L(\mathbf{k})$ is assumed to be non dispersive (panel a). The latter case is equivalent to setting $\omega_L(\mathbf{k}) = \omega_z$ in Eq. 2.4, which results in a resonance at $\Omega = \omega_z$ of the kernel $K(2\Omega)$. As one can see, even though the

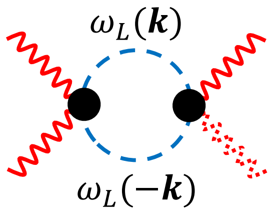

Figure 2.3. Diagram corresponding to the nonlinear current in Eq. 2.17 excited through the the two-plasmon nonlinear kernel in Eq. 2.20. Wavy lines represent the incoming field exciting a plasmon pair with opposite momenta $\mathbf{k}$ and $-\mathbf{k}$ and energy $\omega_L(\mathbf{k})$, represented with dahed lines. The interaction vertex is in this model represented by the out-of-plane superfluid stiffness, pictured as the black bullet.

dispersive case leads to a smearing of such a sharp resonance, the nonlinear kernel shows nonetheless a marked maximum around ω_z, see panel (c). The reasons are the following. As detailed in Section 2.5.3, the spectral weight of the two-plasmon process is zero when $\Omega < \omega_z$, with a discontinuity at the edge, which consequently causes a singularity in $|K(2\Omega = 2\omega_z)|$. Secondly, the overall factor $q_z^4/|\mathbf{k}|^4$ in Eq. 2.4, which accounts for the polarization of the light in the z direction, projects out the full dispersion 2.3 on the phase space where $q_z/|\mathbf{k}|$ is large, that corresponds to an energy around ω_z. In addition, the resonance at ω_L in Eq. 2.4 scales overall as $1/\omega_L^2$, highlighting further low-momentum processes, i.e. those less relevant for RIXS[61, 86, 107], see Fig. 2.1(b). The combined action of these effects is visualized in Fig. 2.2(b), where the intensity of each plasmon line is proportional to its contribution to the nonlinear kernel in Eq. 2.4. The overall enhancement of the kernel at energies around ω_z leads to a non-monotonic T dependence of the THG measured at a fixed pump frequency $\Omega < \omega_z(T=0)$, see Fig. 2.2(d), maximum at $\bar{T}$ where $\Omega = \omega_z(\bar{T})$, in qualitative agreement with the result obtained for a non-dispersive plasmon[45]. Notice that even if the two-plasmon process is only possible above $2\omega_z$, the real part of the optical kernel in Eq. 2.4 is finite below it, giving THG even when the pump frequency is below $\omega_z(T)$.

2.2.1 Derivation of THG from phase-only action

In this section we give an extended derivation of the THG kernel presented in Eq. 2.4 starting from the Josephson model. We start by recalling that the superconducting phase-only action in the isotropic case reads [43, 110, 28]

$$S = \frac{1}{8}\int_0^\beta d\tau \int d^3r\,[\kappa_0(\partial_\tau\theta)^2 + D(\nabla\theta)^2], \tag{2.5}$$

where κ_0 is the bare charge compressibility and D is the superfluid stiffness. In layered systems one can modify the previous expression in order o account for the anisotropy of the superfluid stiffness in the following way

$$S = \frac{1}{8}\int_0^\beta d\tau \int d^3r\,[\kappa_0(\partial_\tau\theta)^2 + D_{xy}(\nabla_{xy}\theta)^2 + D_z(\nabla_z\theta)^2]. \tag{2.6}$$

The phase-only model in Eq. 2.5 is assumed to be a coarse-grained model on the scale of the superconducting coherence length ξ. Since in-plane phase variations appear usually on a scale $\xi_{xy} \gg a$, where a is the in-plane lattice constant, we can retain a continuum description for the in-plane phase gradient, as already done in Eq. 2.5. On the other hand, the weak coupling among layers make $\xi_z \sim d$, with d interlayer distance, calling for a discretization of the model in the stacking direction. We can then describe the system as a stack of weakly Josephson-coupled superconducting layers, placed at a distance d, such that the superconducting phase takes a defined value θ_n in each plane. The phase interactions along the z direction can then be described by a Josephson-like model

$$H_z = -\mathcal{J}_z \sum_n \cos(\theta_{n+1}(\mathbf{r}_{xy}) - \theta_n(\mathbf{r}_{xy})), \tag{2.7}$$

where $\mathcal{J}_z$ is the Josephson coupling among neighboring layers. In this description, the model of Eq. 2.7 is modified to

$$H = \frac{1}{8} \int d^2r\, d \sum_n \left[D_{xy}(\nabla_{xy}\theta)^2 - \frac{2D_z}{d^2} \cos(\theta_{n+1} - \theta_n) \right], \tag{2.8}$$

where the relation $D_z = 4J_z d^2$ holds, having defined the energy density $J_z = \mathcal{J}_z/(a^2 d)$ and given $a^2 d$ the volume of the unit cell. When only the quadratic term of the cosine is considered, this hamiltonian leads to the following action in Fourier space

$$S_G = \frac{1}{8} \sum_{\mathbf{k}, i\omega_n} [-\kappa_0 (i\omega_n)^2 + D_{xy} k_{xy}^2 + D_z q_z^2] |\theta(\mathbf{k}, i\omega_n)|^2, \tag{2.9}$$

where $\mathbf{k} = (\mathbf{k}_{xy}, k_z)$, with $q_z = (2/d)\sin(k_z d/2)$ due to the discretization, and $i\omega_n = 2\pi nT$ are the bosonic Matsubara frequencies. To account for Coulomb interactions one can follow the standard procedure used in the isotropic case[15, 134], that amounts to dress at RPA level the charge compressibility with the three-dimensional Coulomb potential $V(\mathbf{k}) = 4\pi e^2/|\mathbf{k}|^2$, i.e. $\kappa_0 \to \kappa_0/(1 + V(\mathbf{k})\kappa_0)$. As a consequence at long wavelengths, and neglecting plasma dispersion scaling with the Debye screening length $\lambda^2 \sim 1/(4\pi e^2 \kappa_0)$[43], as appropriate in the momentum region we are interested in, this leads to the action

$$S_G = \frac{1}{32\pi e^2} \sum_{\mathbf{k}, i\omega_n} |\mathbf{k}|^2 \left[-(i\omega_n)^2 + \omega_{xy}^2 \frac{k_{xy}^2}{|\mathbf{k}|^2} + \omega_z^2 \frac{q_z^2}{|\mathbf{k}|^2} \right] |\theta(\mathbf{k}, i\omega_n)|^2, \tag{2.10}$$

where we defined $\omega_{xy}^2 = 4\pi e^2 D_{xy}$ and $\omega_z^2 = 4\pi e^2 D_z$ the in- and out-of-plane plasma frequencies, respectively. One can at this point introduce the coupling with a uniform external gauge field polarized along the c-axis, i.e. $\mathbf{A}_z(t) \equiv A_z(t)\hat{z}$. This will enter Eq. 2.7 via

$$H_z = -\mathcal{J}_z \sum_n \cos\left(\theta_{n+1}(\mathbf{r}_{xy}) - \theta_n(\mathbf{r}_{xy}) + \frac{2e}{c} A_z d \right), \tag{2.11}$$

with $e > 0$. In the spirit of Ref. [45], we model the nonlinear coupling between the phase degree of freedom and the gauge field as the one coming from the fourth-order expansion of the cosine in Eq. 2.11. Even though it is known that the quantum Josephson model is just an approximation for the microscopically-derived anharmonic phase model[15], such an approximation already captures the main experimental findings, as we will discuss below. This amount to add to the Gaussian action (2.10) the term

$$\Delta S = \frac{1}{16}\left(\frac{2e}{c}\right)^2 D_z d^2 \sqrt{T} \sum_{\mathbf{k}, i\omega_n, i\omega_m} q_z^2 \theta(-\mathbf{k}, -i\omega_n)\theta(\mathbf{k}, i\omega_m) A_z^2(i\omega_n - i\omega_m), \quad (2.12)$$

where $A_z^2(i\omega_n)$ is the Fourier component of the squared gauge field $A_z^2(t)$. By denoting $k = (\mathbf{k}, i\omega_n)$ and $k' = (\mathbf{k}', i\omega_m)$ we can rewrite the total action as:

$$S_{\text{tot}}[\theta, A_z] = S_G[\theta] + \Delta S[\theta, A_z] = \sum_{kk'} \theta(-k)[M(k,k') + R(k,k')]\theta(k'), \quad (2.13)$$

where

$$M(k,k') = \frac{1}{32\pi e^2}|\mathbf{k}|^2 \left[-(i\omega_n)^2 + \omega_{xy}^2 \frac{k_{xy}^2}{|\mathbf{k}|^2} + \omega_z^2 \frac{q_z^2}{|\mathbf{k}|^2}\right] \delta_{kk'}, \quad (2.14)$$

and

$$R(k,k') = \frac{1}{16}\left(\frac{2e}{c}\right)^2 D_z d^2 \sqrt{T} k_z^2 A_z^2(i\omega_n - i\omega_m)\delta_{\mathbf{kk}'}. \quad (2.15)$$

It is then immediate to integrate out the phase variables obtaining the effective action of the gauge field written formally as $S[A_z] = \operatorname{Tr}\log(1 + M^{-1}R)$, where the trace Tr acts on momenta indexes. The induced current density for a uniform gauge field reads

$$J(i\Omega) = -\frac{c}{2V}\frac{\partial S[A_z]}{\partial A_z(-i\Omega)} = -\frac{c}{2V}\frac{\partial}{\partial A_z(-i\Omega)} \operatorname{Tr}\log(1 + M^{-1}R). \quad (2.16)$$

In order to obtain the third-harmonic current, we should keep terms up to fourth order in the gauge field. Thus, by expanding the logarithm we get,

$$J^{(3)}(i\Omega) = \frac{c}{2V}\frac{\partial}{\partial A_z(-i\Omega)}\frac{1}{2}\operatorname{Tr}(M^{-1}R)^2 \equiv \sum_{i\omega_n} A_z(i\Omega - i\omega_n)K(i\omega_n)A_z^2(i\omega_n), \quad (2.17)$$

where the nonlinear kernel K is, see also Fig. 2.3,

$$K(i\omega_n) = \frac{c}{4}\left(\frac{2e}{c}\right)^4 \omega_z^4 d^4 \frac{T}{V} \sum_{\mathbf{k}, i\omega_m} \left(\frac{q_z^2}{|\mathbf{k}|^2}\right)^2 \frac{1}{(i\omega_m)^2 - \omega_L^2(\mathbf{k})} \frac{1}{(i\omega_m + i\omega_n)^2 - \omega_L^2(\mathbf{k})}, \quad (2.18)$$

and we defined again the plasmon dispersion as

$$\omega_L^2(\mathbf{k}) = \omega_{xy}^2 k_{xy}^2/|\mathbf{k}|^2 + \omega_z^2 q_z^2/|\mathbf{k}|^2. \quad (2.19)$$

Considering monochromatic incident field $A_z(\omega)$ centered at frequency Ω in Eq. 2.17, the third harmonic nonlinear current reads $J^{(3)}(3\Omega) = K(2\Omega)A(\Omega)^3$. Thus, summing over the Matsubara frequencies and after analytic continuation $i\omega_n \to \Omega + i\delta$, the kernel reads

$$K(\Omega) = \frac{c}{4}\left(\frac{2e}{c}\right)^4 \omega_z^4 d^4 \frac{1}{V}\sum_{\mathbf{k}} \left(\frac{q_z^2}{|\mathbf{k}|^2}\right)^2 \frac{\coth\left(\frac{\beta\omega_L(\mathbf{k})}{2}\right)}{\omega_L(\mathbf{k})((\Omega + i\delta)^2 - (2\omega_L(\mathbf{k}))^2)}, \quad (2.20)$$

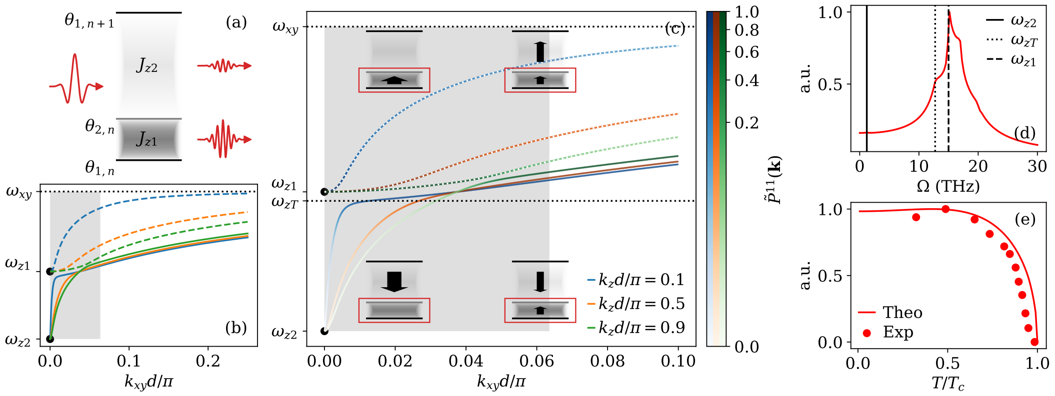

Figure 2.4. (a) Sketch of the c-axis nonlinear response for the YBCO bilayer system. Since $J_{z1} \gg J_{z2}$ the THG signal is mainly determined by the intra-bilayer phase fluctuations. (b) Plasmon branches $\omega_1(\mathbf{k})$ (dotted lines) and $\omega_2(\mathbf{k})$ (solid lines) at selected k_z for a wide range of k_{xy} value. (c) Zoom-in of panel (c) in the region of integration relevant for the THG, as denoted by the grey shaded area. Here the line intensity is rescaled according to the relative weight of intra-bilayer phase fluctuations $\tilde{\mathcal{P}}^{11}_{\sigma}$ of each mode, shown as a color-bar on the right of the panel. A sketch of the corresponding polarizations of the modes[126] in each momenta region is also reported. (d) Frequency dependence of the nonlinear kernel $|K(2\Omega)|$ at $T = 0$. Vertical bars denote the position of ω_{z1}, ω_{zT} and ω_{z2}. (e) Temperature dependence of the nonlinear kernel $|K(2\Omega)|$ (solid line) for fixed pump frequency $\Omega = 0.5$ THz. The dots represents the experimental data from Ref. [73].

which coincides with Eq. 2.4 and whose behavior is shown in Fig. 2.2 above. In order to compute the response, we choose to model the temperature dependence of the in- and out-of-plane stiffness as $D_z(T) = D_z(T = 0)(1 - (T/T_c)^4)$ and $D_{xy}(T) = D_{xy}(T = 0)(1 - T/T_c)e^{T/T_c}$, fitting data of Ref. [127]. We explicitly integrate Eq. 2.20 over a cylindric region in momentum space with height $k_z = 2\pi/d$, where d the distance between planes, and radius $k_{xy} = 1/\xi$, with $\xi = 5d$ the in-plane coherence length[7, 135], that is the $\mathbf{k}$-region where a phase-only model can be defined.

2.3 Bilayer case

In the bilayer case one has two planes denoted as $\lambda = 1, 2$ per unit cell, so that one introduces two phase variables $\theta_{\lambda,n}$. The out-of-plane hamiltonian density is

$$\mathcal{H}^{\perp}_n = -J_{z1}\cos(\theta_{1,n} - \theta_{2,n}) - J_{z2}\cos(\theta_{1,n+1} - \theta_{2,n}), \tag{2.21}$$

in close analogy with Eq. 2.1, while the in-plane part has the same form. Here we introduced two different Josephson couplings J_{z1} and J_{z2}, with $J_{z1} \gg J_{z2}$, corresponding to a phase difference between the two nearest planes within the same unit cell (at distance $d_1 = 3.2$ Å for YBCO) or in neighboring cells (at distance $d_2 = 8.2$ Å for YBCO), $d = d_1 + d_2$ being the periodicity in the z direction[126, 3, 144], see Fig. 2.4(a). The corresponding stiffnesses $D_{z\lambda} = 4J_{z\lambda}d^2_{\lambda}$ are also modulated. By introducing the spinor $\bar{\theta} = (\theta_1, \theta_2)$ the generalization of the Gaussian quantum action in Eq. 2.2 to the bilayer case reads

$$S_G = \frac{1}{64\pi e^2} \sum_{i\omega_m, \mathbf{k}} \bar{\theta}(-k)\mathcal{K}^2 \left(-(i\omega_m)^2 \mathbb{1} + \Omega_L^2(\mathbf{k})\right) \bar{\theta}(k). \tag{2.22}$$

Here we introduced the 2×2 matrix $\mathcal{K}^2 = k_{xy}^2 \mathbb{1} + \mathcal{K}_z^\dagger \mathcal{K}_z$ which generalizes the quadratic term in momentum, where

$$\mathcal{K}_z = \frac{\sqrt{2}}{d} \begin{pmatrix} -\frac{e^{-ik_z d_1/2}}{\sqrt{d_1/d}} & \frac{e^{ik_z d_1/2}}{\sqrt{d_1/d}} \\ \frac{e^{ik_z d_2/2}}{\sqrt{d_2/d}} & -\frac{e^{-ik_z d_2/2}}{\sqrt{d_2/d}} \end{pmatrix}, \tag{2.23}$$

keeps track of the discretization of the phase variables along the z direction. Analogously $\Omega_L^2(\mathbf{k})$ generalizes the plasma dispersion in Eq. 2.3, with $\Omega_L^2(\mathbf{k}) = (\mathcal{K}^2)^{-1}(\omega_{xy}^2 k_{xy}^2 \mathbb{1} + \mathcal{K}_z^\dagger \Omega_z^2 \mathcal{K}_z)$, where $(\Omega_z^2)_{\lambda\mu} = \delta_{\lambda\mu}\omega_{z\lambda}^2$ and $\omega_{z\lambda}^2 = 4\pi e^2 D_{z\lambda}$. From the structure of Eq. 2.22 one readily sees that the doubling of the layers per unit cell leads to a doubling of the JPMs, defined as the square-root of the eigenvalues of the matrix $\Omega_L^2(\mathbf{k})$, and shown in Fig. 2.4(b). The upper plasmon $\omega_1(\mathbf{k})$, dispersing between ω_{z1} and ω_{xy}, is the equivalent of the single-layer plasmon $\omega_L(\mathbf{k})$, while the additional low-energy out-of-plane plasmon $\omega_2(\mathbf{k})$, dispersing away from ω_{z2}, is characteristic of the bilayer case. For increasing in-plane momentum $\omega_2(\mathbf{k})$ evolves rapidly towards an energy scale $\omega_{zT} = \sqrt{(\omega_{z1}^2 d_2 + \omega_{z2}^2 d_1)/d} \approx \omega_{z1}$ for $J_{z1} \gg J_{z2}$, usually named *transverse* plasmon in the literature because it identifies the scale of a resonance peak in the c-axis optical conductivity [144, 104, 64]. For even larger values of k_{xy} $\omega_2(\mathbf{k})$ grows slowly towards the in-plane frequency ω_{xy}.

The computation of the nonlinear kernel follows the same steps as before, with both plasmon branches contributing to the out-of-plane response, so that $K(\Omega) = K_+(\Omega) + K_-(\Omega)$, where

$$K_\pm(\Omega) = \sum_{\sigma\sigma', \mathbf{k}} W_{\sigma\sigma'} \frac{\omega_\sigma \pm \omega_{\sigma'}}{4\omega_\sigma \omega_{\sigma'}} \frac{\coth\left(\frac{\beta\omega_\sigma}{2}\right) \pm \coth\left(\frac{\beta\omega_{\sigma'}}{2}\right)}{(\omega_\sigma \pm \omega_{\sigma'})^2 - (\Omega + i\delta)^2} \tag{2.24}$$

combines two JPMs from the same ($\sigma = \sigma'$) or from different ($\sigma \neq \sigma'$) plasmon branches, with $\sigma, \sigma' = 1, 2$, weighted by the $\mathbf{k}$-dependent $W_{\sigma\sigma'}$ prefactors, which project out the contribution of each mode to selected region of momenta. A full numerical computation of the kernel 2.24 at $T = 0$ for parameter values appropriate for YBCO is shown in Fig. 2.4(d). We set $T_c = 61$ K, $\omega_{z1}(T = 0) = 15$ THz and $\omega_{z2}(T = 0) = 1.2$ THz[73, 64], that gives a peak in the transverse conductivity at $\omega_{zT}(T = 0) = 11$ THz, in agreement with the experiments[64]. As one can see, $|K(2\Omega)|$ shows a marked resonance near the value $\Omega \approx \omega_{z1} \sim 15$ THz, without any signature at the lower plasmon $\omega_{z2} \sim 1.2$ THz, that is the energy scale defining instead the sharp plasma edge in the c-axis reflectivity below T_c[63, 12, 144, 64].

A better insight into this result can be obtained by introducing a new sets of phase variables, corresponding to the intra-bilayer $\tilde{\theta}_1 \sim \theta_{2,n} - \theta_{1,n}$ and inter-bilayer $\tilde{\theta}_2 \sim \theta_{1,n+1} - \theta_{2,n}$ phase gradient in the n-th unit cell, respectively. As manifest from Eq. 2.21, the larger scale J_{z1} couples the gauge field A_z to $\tilde{\theta}_1$, while J_{z2} controls its coupling to $\tilde{\theta}_2$. By changing basis from (θ_1, θ_2) to $(\tilde{\theta}_1, \tilde{\theta}_2)$ one can write the projectors as $W_{\sigma\sigma'} \propto \mathrm{Tr}\,(\tilde{\mathcal{P}}_\sigma \mathcal{C} \tilde{\mathcal{P}}_{\sigma'} \mathcal{C})$, where the diagonal matrix $(\mathcal{C})_{\lambda\mu} = D_{z\lambda} d_\lambda^2 \delta_{\lambda\mu}$ comes from the coupling with the gauge field ($\sim D_{z\lambda} A_z^2 d_\lambda{}^2$) and the matrix $\tilde{\mathcal{P}}_\sigma$ weights each plasmon branch according to its projection onto inter-bilayer (11 element) and intra-bilayer (22 element) phase fluctuations. Since $D_{z1} \gg D_{z2}$, one finds that plasmon branches contribute to THG in the momentum region where they have a large intra-bilayer component, $\tilde{\mathcal{P}}_\sigma^{11}(\mathbf{k})$. This effect is highlighted in Fig. 2.4(c), where the line intensity for each plasmon dispersion, plotted at fixed k_z, scales with its $\tilde{P}_\sigma^{11}(\mathbf{k})$ intra-bilayer weight. The upper plasmon branch $\omega_1(\mathbf{k})$ is purely intra-bilayer for $k_{xy} = 0$, and gradually acquires an inter-bilayer component as k_{xy} increases. Thus, it contributes to THG in the low-momenta region where $\omega_1(\mathbf{k}) \approx \omega_{z1}$, as already observed for the $\omega_L(\mathbf{k})$ in the single-layer case. Conversely, the lower plasmon branch $\omega_2(\mathbf{k})$ has exactly zero intra-bilayer projection at $k_{xy} = 0$, where it is associated with purely inter-bilayer phase fluctuations[126], while it acquires intra-bilayer character as it approaches the ω_{zT} energy scale. The suppression of spectral weight at low energy comes from the deep entanglement between the momentum dependence of the plasmon energies and of the polarization weights, which would not be captured if the system were described neglecting the dispersion of the plasmon branches. These two ingredients explain the lack on any signature at ω_{z2} in the numerical result of Fig. 2.4(d) at $T = 0$, and the absence of a THG enhancement at $\Omega = \omega_{z2}(T)$ in the THG measurements Ref. [73], performed with fixed $\Omega \sim 0.5$ THz. At the same time the condition $\Omega = \omega_{z1}(\bar{T})$ is achieved at a temperature $\bar{T}$ so close to T_c that the resonance itself is washed out by the thermal depletion of the stiffness. Thus the computed THG, given by the solid line in Fig. 2.4(e), increases monotonically in temperature, in remarkable agreement with the experimental THG of Ref. [73], extracted by the measured reflected electric field E_r. The latter is obtained by using the results presented in the previous Chapter 1, in particular Eq. 1.70 where we computed the reflected electric field from a bulk sample. Computing the expression in the monochromatic case we have

$$E_r \propto K(2\Omega)\Big(\frac{2}{n(\Omega)+1}\Big)^3 \frac{1}{n(3\Omega)+n(\Omega)} \frac{1}{n(3\Omega)+1} E_0^3, \tag{2.25}$$

where $n(\Omega)$ ($n(3\Omega)$) is the experimentally-measured index of refraction at Ω (3Ω).

2.3.1 Derivation of the RPA dressing of κ_0 in the bilayer case

In this section we explicitly derive the gaussian action in Eq. 2.22 by computing the RPA dressing of the bare compressibility with the scalar potential in the case of a bilayer system. We consider a model for the bilayer crystal in which each unit cell (label n) contains two planes (label $1, 2$). We consider plane $2, n$ separated by a distance d_1 from plane $1, n$ and by a distance d_2 from plane $1, n+1$. The Josephson-like couplings in the same unit cell are considered different, as well, being $\mathcal{J}_{z1}$ between plane $2, n$ and plane $1, n$ and $\mathcal{J}_{z2}$ between plane $2, n$ and plane $1, n+1$. The hamiltonian in the out-of-plane direction is then a straightforward modification of Eq. 2.7, namely

$$H_\perp = -\mathcal{J}_{z1} \sum_n \cos\left(\theta_{1,n}(\mathbf{r}_{xy}) - \theta_{2,n}(\mathbf{r}_{xy})\right) - \mathcal{J}_{z2} \sum_n \cos\left(\theta_{1,n+1}(\mathbf{r}_{xy}) - \theta_{2,n}(\mathbf{r}_{xy})\right). \tag{2.26}$$

By expanding the cosines up to second order in the phase fluctuations the action can be written as

$$S_G[\theta] = \frac{1}{8}\int_0^\beta d\tau \int d^2r\, \frac{d}{2}\sum_n \Big[\kappa_0(|\partial_\tau\theta_{1,n}|^2 + |\partial_\tau\theta_{2,n}|^2) + D_{xy}(\nabla_{xy}\theta_{1,n})^2 \\ + D_{xy}(\nabla_{xy}\theta_{2,n})^2 + 2D_{z1}z_1(\Delta_{z1}\theta_{1,n})^2 + 2D_{z2}z_2(\Delta_{z2}\theta_{2,n})^2\Big], \tag{2.27}$$

where we defined $z_\lambda = d_\lambda/d$ and $d = d_1 + d_2$ is the length of the unit cell along the z direction. Analogously to the single layer case we defined the stiffnesses $D_{z\lambda} = 4J_\lambda d_\lambda^2$, with the two out-of-plane values scaling as $D_{z\lambda}(T) = D_{z\lambda}(T=0)(1-(T/T_c)^4)$, while for the in-plane values we retained the same single-layer plasma frequency. For the sake of notation we also introduced the discrete derivative in the out-of-plane direction as:

$$\Delta_{z\lambda} f_{\lambda,n} = \begin{cases} \frac{f_{2,n}-f_{1,n}}{d_1} & \text{if } \lambda = 1 \\ \frac{f_{1,n+1}-f_{2,n}}{d_2} & \text{if } \lambda = 2 \end{cases}. \tag{2.28}$$

We want now to obtain the expression of the action in the Fourier space, following the procedure used in Ref. [126]. Adopting the notation $k = (i\omega_n, \mathbf{k})$, we have

$$\begin{aligned} S_G = \frac{1}{16}\sum_k \Bigg[&\left(-(i\omega_n)^2\kappa_0 + k_{xy}^2 D_{xy} + \frac{2D_{z1}}{d^2 z_1} + \frac{2D_{z2}}{d^2 z_2}\right)(|\theta_1(k)|^2 + |\theta_2(k)|^2) \\ &-\frac{2D_{z1}}{d^2 z_1}(\theta_1(k)\theta_2(-k)e^{-ik_z d_1} + \theta_1(-k)\theta_2(k)e^{ik_z d_1}) \\ &-\frac{2D_{z2}}{d^2 z_2}(\theta_1(k)\theta_2(-k)e^{ik_z d_2} + \theta_1(-k)\theta_2(k)e^{-ik_z d_2})\Bigg]. \end{aligned} \tag{2.29}$$

Defining now

$$\mathcal{K}_z = \frac{\sqrt{2}}{d}\begin{pmatrix} -\frac{e^{-ik_z d_1/2}}{\sqrt{z_1}} & \frac{e^{ik_z d_1/2}}{\sqrt{z_1}} \\ \frac{e^{ik_z d_2/2}}{\sqrt{z_2}} & -\frac{e^{-ik_z d_2/2}}{\sqrt{z_2}} \end{pmatrix}, \tag{2.30}$$

the out-of-plane plasma frequencies $\omega_{z\lambda}^2 = 4\pi e^2 D_{z\lambda}$ and the matrix

$$\Omega_z^2 = \begin{pmatrix} \omega_{z1}^2 & 0 \\ 0 & \omega_{z2}^2 \end{pmatrix}, \tag{2.31}$$

we can rewrite the action simply as

$$S_G[\theta] = \frac{1}{64\pi e^2}\sum_k \bar\theta^T(-k)\left[-\frac{(i\omega_n)^2}{\alpha}\mathbb{1} + \omega_{xy}^2 k_{xy}^2\mathbb{1} + \mathcal{K}_z^\dagger\Omega_z^2\mathcal{K}_z\right]\bar\theta(k), \tag{2.32}$$

where we defined $\bar\theta = (\theta_1, \theta_2)$ and $\alpha = 1/(4\pi e^2\kappa_0)$. The coupling to the electromagnetic field can be straightforwardly obtained via the minimal-coupling substitution:

$$\begin{cases} i\partial_\tau\theta_{\lambda,n} & \to i\partial_\tau\theta_{\lambda,n} - 2e\phi_{\lambda,n} \\ \nabla_{xy}\theta_{\lambda,n} & \to \nabla_{xy}\theta_{\lambda,n} + 2e\mathrm{A}_{xy\lambda,n}/c \\ \Delta_z\theta_{\lambda,n} & \to \Delta_z\theta_{\lambda,n} + 2e\mathrm{A}_{z\lambda,n}/c \end{cases}. \tag{2.33}$$

As detailed in Ref. [126] for the bilayer case, in the layered systems one cannot achieve a decoupling of the phase to the vector potential. However, as we show explicitly in the single layer case in Sections 2.5.1 and 2.5.2, this effect is irrelevant for the THG and one can retain only the coupling to the scalar potential ϕ. By adding the free electromagnetic action for the electromagnetic field, one is thus left with an action for θ and ϕ that reads

$$\begin{aligned} S[\phi,\theta] = S_G[\theta] - \frac{1}{16\pi}\sum_k \bar{\phi}^T(-k)\left(\frac{1}{\alpha}\mathbb{1} + k_{xy}^2\mathbb{1} + \mathcal{K}_z^\dagger\mathcal{K}_z\right)\bar{\phi}(k) \\ + \frac{i}{32\pi e}\sum_k \frac{i\omega_n}{\alpha}\bar{\theta}^T(-k)\bar{\phi}(k). \end{aligned} \tag{2.34}$$

After integrating out the scalar potential, the action reads

$$\begin{aligned} S[\theta] = \frac{1}{64\pi e^2}\sum_k \bar{\theta}^T(-k)\Bigg[-\frac{(i\omega_n)^2}{\alpha}\mathbb{1} + \omega_{xy}^2 k_{xy}^2\mathbb{1} + \mathcal{K}_z^\dagger\Omega_z^2\mathcal{K}_z \\ + \frac{(i\omega_n)^2}{\alpha}(\mathbb{1} + \alpha k_{xy}^2\mathbb{1} + \alpha\mathcal{K}_z^\dagger\mathcal{K}_z)^{-1}\Bigg]\bar{\theta}(k). \end{aligned} \tag{2.35}$$

By defining the matrix $\mathcal{K}^2$ as

$$\mathcal{K}^2 = k_{xy}^2\mathbb{1} + \mathcal{K}_z^\dagger\mathcal{K}_z, \tag{2.36}$$

the effective action for the superconducting phase fluctuations can be rewritten as

$$\begin{aligned} S[\theta] = \frac{1}{64\pi e^2}\sum_k \bar{\theta}^T(-k)(\mathbb{1} + \alpha\mathcal{K}^2)^{-1}\times \\ \times\left[-\frac{(i\omega_n)^2}{\alpha}(\mathbb{1} + \alpha\mathcal{K}^2) + \mathcal{K}^2\Omega_L^2(\mathbf{k})(\mathbb{1} + \alpha\mathcal{K}^2) + \frac{(i\omega_n)^2}{\alpha}\mathbb{1}\right]\bar{\theta}(k). \end{aligned} \tag{2.37}$$

Here we introduced the generalization of the single-layer plasma frequency in Eq. 2.19 as the matrix

$$\Omega_L^2(\mathbf{k}) = (\mathcal{K}^2)^{-1}(\omega_{xy}^2 k_{xy}^2\mathbb{1} + \mathcal{K}_z^\dagger\Omega_z^2\mathcal{K}_z). \tag{2.38}$$

By taking the limit for $\alpha \to 0$, as appropriate for cuprates, we finally get

$$S[\theta] = \frac{1}{64\pi e^2}\sum_k \bar{\theta}^T(-k)\mathcal{K}^2[-(i\omega_n)^2\mathbb{1} + \Omega_L^2(\mathbf{k})]\bar{\theta}(k). \tag{2.39}$$

By comparing Eq. 2.39 with the bare phase action in Eq. 2.32 one sees that, in full analogy with the single-layer case, also here the coupling to the scalar potential dresses the bare compressibility as

$$\kappa_0\mathbb{1} \to \kappa_0(\mathbb{1} + 4\pi e^2(\mathcal{K}^2)^{-1}\kappa_0)^{-1}, \tag{2.40}$$

with the latter term being dominant at small momenta. Eq. 2.39 shows that the dispersions $\omega_{1,2}(\mathbf{k})$ of the two Josephson plasma modes of a bilayer superconductor, plotted in Fig. 2.4(b) above, are found as roots of the determinant of $-(i\omega_n)^2\mathbb{1} + \Omega_L^2(\mathbf{k})$. As mentioned above, these modes do not include the coupling between the phase fluctuations and the vector potential, but are nonetheless good approximations of the exact modes, derived e.g. in Ref. [126], at momenta $k \gtrsim k_c$. As discussed in Ref. [126], $\omega_2(\mathbf{k})$ can be intuitively understood (for $d_1 = d_2 = d/2$) as a back-folding of the $q_z = \pi/(d/2)$ soft plasmon of the single-layer, due to the breaking of the periodicity along z when $J_{z1} \neq J_{z2}$, as evidenced by the fact that it describes out-of-phase oscillations of the intra-cell phases. As such, it always has virtually a large q_z component, making it a longitudinal out-of-plane phase fluctuation in the usual sense.

2.3.2 Derivation THG in bilayer superconductors

In this section we derive in detail the THG kernel in the bilayer system, considering again a z-polarized external field incident on a bilayer superconductor, introduced by means of a minimal coupling substitution in the Josephson-like model in Eq. 2.26. In the spirit of what was done for the single-layer case, the total action of the system is written as

$$S[\theta, \mathbf{A}_z] = S[\theta] + \Delta S[\theta, \mathbf{A}_z] = \sum_{k,k'} \bar{\theta}^T(-k)\left[\mathcal{M}(k,k') + \mathcal{R}(k,k')\right]\bar{\theta}(k'), \tag{2.41}$$

where the matrix $\mathcal{M}(k,k')$ of the Gaussian phase fluctuations is defined by Eq. 2.39:

$$\mathcal{M}(k,k') = \frac{1}{64\pi e^2}\mathcal{K}^2[-(i\omega_n)^2\mathbb{1} + \Omega_L^2(\mathbf{k})]\delta_{kk'}, \tag{2.42}$$

while the coupling matrix $\mathcal{R}(k,k')$ reads

$$\mathcal{R}(k,k') = \frac{1}{32}\left(\frac{2e}{c}\right)^2 \sqrt{T}\mathcal{K}_z^\dagger \mathcal{C}\mathcal{K}_z A_z^2(i\omega_m - i\omega_n)\delta_{\mathbf{k}\mathbf{k}'}. \tag{2.43}$$

Here we defined $(\mathcal{C})_{\lambda\mu} = D_{z\lambda} d_\lambda^2 \delta_{\lambda\mu}$, which comes from the nonlinear coupling between the external gauge field A_z and the phase variables ($\sim D_{z\lambda}A_z^2 d_\lambda^2$). Here $\mathcal{M}$ and $\mathcal{R}$ are the straightforward extension to the bilayer case of the matrices M and R introduced for the single-layer case in Eq. 2.14 and Eq. 2.15, respectively. After integration of the phase degrees of freedom we obtain the third-order nonlinear kernel which reads

$$K(i\Omega) = \frac{c}{4}\left(\frac{2e}{c}\right)^4 \frac{T}{V}\sum_{\mathbf{k}, i\omega_n} \mathrm{Tr}[\tilde{\mathcal{M}}^{-1}(\mathbf{k}, i\omega_n)\mathcal{P}_z\tilde{\mathcal{M}}^{-1}(\mathbf{k}, i\omega_n + i\Omega)\mathcal{P}_z]. \tag{2.44}$$

The matrix

$$\mathcal{P}_z = (\mathcal{K}^2)^{-1}\mathcal{K}_z^\dagger 4\pi e^2 \mathcal{C}\mathcal{K}_z \tag{2.45}$$

plays the same role of the factor $\sim \omega_z^2 d^2 k_z^2/|\mathbf{k}|^2$ in the single-layer case, i.e. it projects the phase fluctuations on the polarization direction of the external probe. In Eq. 2.44 we introduced the matrix $\tilde{\mathcal{M}} = -(i\omega_n)^2\mathbb{1} + \Omega_L^2(\mathbf{k})$, whose inverse can be decomposed in terms of the two plasmon branches in the usual way

$$\tilde{\mathcal{M}}^{-1}(\mathbf{k}, i\omega_n) = \frac{\mathcal{P}_1(\mathbf{k})}{(i\omega_n)^2 - \omega_1^2(\mathbf{k})} + \frac{\mathcal{P}_2(\mathbf{k})}{(i\omega_n^2) - \omega_2^2(\mathbf{k})}, \tag{2.46}$$

having defined

$$\mathcal{P}_\sigma(\mathbf{k}) = (-1)^\sigma \frac{\omega_\sigma^2(\mathbf{k})\mathbb{1} - \det\left(\Omega_L^2\right)\left(\Omega_L^2\right)^{-1}}{\omega_2^2(\mathbf{k}) - \omega_1^2(\mathbf{k})}. \tag{2.47}$$

By performing the Matsubara summation as in Eq. 2.64 above we obtain:

$$\begin{aligned} K(i\Omega) = &\frac{c}{4}\left(\frac{2e}{c}\right)^4 \sum_{\sigma,\sigma'} \frac{1}{V}\sum_{\mathbf{k}} \mathrm{Tr}(\mathcal{P}_\sigma \mathcal{P}_z \mathcal{P}_{\sigma'} \mathcal{P}_z) \\ &\times \left[\frac{\omega_\sigma + \omega_{\sigma'}}{4\omega_\sigma \omega_{\sigma'}} \frac{\coth\left(\frac{\beta\omega_\sigma}{2}\right) + \coth\left(\frac{\beta\omega_{\sigma'}}{2}\right)}{(\omega_\sigma + \omega_{\sigma'})^2 - (\Omega + i\delta)^2} + \frac{\omega_\sigma - \omega_{\sigma'}}{4\omega_\sigma \omega_{\sigma'}} \frac{\coth\left(\frac{\beta\omega_\sigma}{2}\right) - \coth\left(\frac{\beta\omega_{\sigma'}}{2}\right)}{(\omega_\sigma - \omega_{\sigma'})^2 - (\Omega + i\delta)^2}\right]. \end{aligned} \tag{2.48}$$

In order to better visualize the role of the projectors $\mathcal{P}_z$ and $\mathcal{P}_\sigma$, let us make a change of basis from the spinorial representation in the layer index $\bar{\theta}^T = \begin{pmatrix}\theta_1 & \theta_2\end{pmatrix}$ to a new one $\bar{\theta}^T = \begin{pmatrix}\tilde{\theta}_1 & \tilde{\theta}_2\end{pmatrix}$ defined from

$$\begin{pmatrix}\tilde{\theta}_1 \\ \tilde{\theta}_2\end{pmatrix} = d\mathcal{K}_z \begin{pmatrix}\theta_1 \\ \theta_2\end{pmatrix}. \tag{2.49}$$

One can indeed show that the new spinorial basis reads in real space

$$\begin{cases} \tilde{\theta}_{1,n} &= \sqrt{\frac{2}{z_1}}\,(\theta_{2,n} - \theta_{1,n}) \\ \tilde{\theta}_{2,n} &= \sqrt{\frac{2}{z_2}}\,(\theta_{1,n+1} - \theta_{2,n}) \end{cases}, \tag{2.50}$$

i.e. its basis elements correspond to (rescaled) intra-bilayer ($\tilde{\theta}_1$) and inter-bilayer ($\tilde{\theta}_2$) phase differences. In this new basis the coupling to the gauge field is diagonal, namely we can rewrite

$$\mathcal{R}(k,k') = \frac{1}{d^2}\frac{1}{32}\left(\frac{2e}{c}\right)^2 \sqrt{T}\mathcal{C}A_z^2(i\omega_m - i\omega_n)\delta_{\mathbf{k}\mathbf{k}'}, \tag{2.51}$$

This is expected since the the Josephson couplings J_{z1} and J_{z2} are indeed coupled to phase differences $\tilde{\theta}_1$ and $\tilde{\theta}_2$ in the real-space hamiltonian in Eq. 2.26. Notice that, as compared to the expression in Eq. 2.15 of the single-layer case, the equivalent of the $k_z^2 \to \mathcal{K}_z^\dagger \mathcal{K}_z$ term does not appear in Eq. 2.51 since it has been included in the definition of the new phase variables in Eq. 2.50, that scale actually as a discrete phase gradient along z. For the same reason they appear instead in the definition of the phase-fluctuation matrix that is rewritten as

$$\mathcal{M}(k,k') = \frac{1}{64\pi e^2 d^2}(\mathcal{K}_z^\dagger)^{-1}\mathcal{K}^2[-(i\omega_n)^2\mathbb{1} + \Omega_L^2(\mathbf{k})]\mathcal{K}_z^{-1}\delta_{kk'}. \tag{2.52}$$

As before the kernel is proportional to the trace of the product $(\mathcal{M}^{-1}\mathcal{R})^2$, so we decompose again $[-(i\omega_n)^2\mathbb{1} + \Omega_L^2(\mathbf{k})]^{-1}$ in terms of the projections over the two plasmonic branches $\omega_{1,2}(\mathbf{k})$, as in Eq. 2.46, so that

$$\begin{aligned} \mathcal{M}^{-1}(k,k') &= 64\pi e^2 d^2 \sum_\sigma \frac{1}{(i\omega_n)^2 - \omega_\sigma^2}\mathcal{K}_z \mathcal{P}_\sigma (\mathcal{K}^2)^{-1}\mathcal{K}_z^\dagger \delta_{kk'} \\ &\equiv 64\pi e^2 d^2 \sum_\sigma \begin{pmatrix}\tilde{\mathcal{P}}_\sigma^{11} & \tilde{\mathcal{P}}_\sigma^{12} \\ \tilde{\mathcal{P}}_\sigma^{21} & \tilde{\mathcal{P}}_\sigma^{22}\end{pmatrix} \frac{1}{(i\omega_n)^2 - \omega_\sigma^2}, \end{aligned} \tag{2.53}$$

where the matrix elements of $\tilde{\mathcal{P}}_\sigma$ determine the amount of intra-bilayer (11 element) or inter-bilayer (22 element) or mixed character of the two plasmonic branches as a function of momentum. We notice that in the end the kernel is written in the same way as before, since we have only reshuffled the matrices appearing in the trace of Eq. 2.48 due to the change of basis, but the physical meaning is now more clear. Indeed, the projector $\mathrm{Tr}(\mathcal{P}_\sigma \mathcal{P}_z \mathcal{P}_{\sigma'} \mathcal{P}_z)$ appearing in Eq. 2.48 reads in terms of the new matrices as:

$$\mathrm{Tr}(\mathcal{P}_\sigma \mathcal{P}_z \mathcal{P}_{\sigma'} \mathcal{P}_z) = \mathrm{Tr}(\tilde{\mathcal{P}}_\sigma \mathcal{C} \tilde{\mathcal{P}}_{\sigma'} \mathcal{C}). \tag{2.54}$$

Being $\mathcal{C}$ diagonal, it is easier to disentangle the various contributions. Since $J_{z1} \gg J_{z2}$ and given d_1, d_2, one realizes $\omega_{z1}^4 d_1^4 \gg \omega_{z2}^4 d_2^4$, then the leading contribution to the THG kernel will be the one proportional to $\omega_{z1}^4 d_1^4$. Thus, working out the previous trace, one has

$$\mathrm{Tr}(\tilde{\mathcal{P}}_\sigma \mathcal{C} \tilde{\mathcal{P}}_{\sigma'} \mathcal{C}) = \omega_{z1}^4 d_1^4 \left[(\tilde{\mathcal{P}}_\sigma^{11})^2 + (\tilde{\mathcal{P}}_{\sigma'}^{11})^2 + 2\tilde{\mathcal{P}}_\sigma^{11} \tilde{\mathcal{P}}_{\sigma'}^{11} \right] + \dots, \tag{2.55}$$

where we neglected terms proportional to $\omega_{z1}^2 d_1^2$ or less. Hence, Eq. 2.55 proves that the leading contribution to the THG kernel come from the plasmonic branch having the largest projection onto the intra-layer phase fluctuations, which are controlled by a larger stiffness J_{z1}. One could then approximate the nonlinear kernel in Eq. 2.48 as

$$K(i\Omega) \sim \frac{c}{4} \left(\frac{2e}{c} \right)^4 \omega_{z1}^4 d_1^4 \sum_\sigma \frac{1}{V} \sum_{\mathbf{k}} (\tilde{\mathcal{P}}_\sigma^{11}(\mathbf{k}))^2 \frac{\coth\left(\frac{\beta \omega_\sigma(\mathbf{k})}{2}\right)}{\omega_\sigma(\mathbf{k})((i\Omega)^2 - (2\omega_\sigma(\mathbf{k}))^2)}. \tag{2.56}$$

In this expression we neglected the mixed process involving the excitation of two plasmons in different branches since as a function of momentum $\tilde{\mathcal{P}}_1^{11} \tilde{\mathcal{P}}_2^{11} \sim 0$, see Fig. 2.5. Indeed, the numerical results presented in Fig. 2.4 above can be then understood by computing numerically the projections $\tilde{\mathcal{P}}_{1,2}^{11}$ of the two plasma branches $\omega_{1,2}(\mathbf{k})$ onto the intra-layer fluctuations. As one can see in Fig. 2.5, for $k_{xy} = 0$ one always obtains $\tilde{\mathcal{P}}_1^{11} = 1$ and $\tilde{\mathcal{P}}_2^{11} = 0$: this is a direct consequence of the fact that for zero in-plane momentum the upper plasmon branch (located at ω_{z1}) and the lower branch (located at ω_{z2}) describe purely intra-bilayer and inter-bilayer phase fluctuations, respectively. Nevertheless, as k_{xy} increases, the lower plasmon branch acquires a sizeable intra-bilayer component, dominating the kernel. Since in this momenta region $\omega_2(\mathbf{k})$ evolves towards the value $\omega_{zT} = \sqrt{\omega_{z1}^2 d_2^2 + \omega_{z2}^2 d_1^2/d}$, this is the dominant frequency contribution to the nonlinear response, while the region of $\omega \simeq \omega_{z2}$ is essentially projected out from the THG response. Analogously, since the spectral weight of the ω_1 branch is suppressed for increasing k_{xy}, that corresponds to the region of momenta where ω_1 disperses towards ω_{xy}, such a high-energy part of the plasma mode does not contribute significantly to the kernel, leaving most of its spectral content around $\omega \simeq \omega_{z1}$. This analysis accounts then for the peaked structure around ω_{z1} reported in Fig. 2.4(d) above.

2.4 Conclusions

The present results for the two-plasmon contribution to the nonlinear response reconcile experiments in single-layer and bilayer cuprates. The combined effect of the

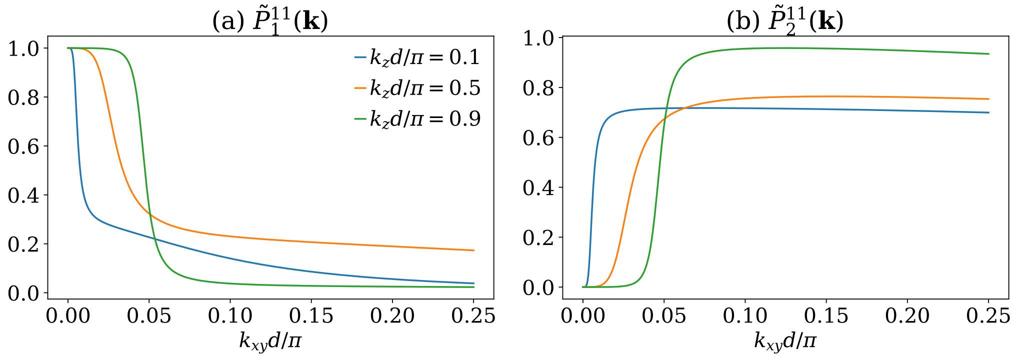

Figure 2.5. The projectors over the intra-bilayer phase fluctuations (11 element) of the upper ω_1 (a) and lower ω_2 (b) plasmonic branches.

light polarization and the plasmon dispersion explains a resonant THG for pumping frequency matching the plasma edge in single-layer materials, while it accounts for a shift of the resonance frequency towards the larger out-of-plane plasma mode for bilayer structures. It turns out that in those systems THG is sensitive exactly to the part of the plasmon branches that are hidden to RIXS, as shown in Fig 2.1(c), where recent RIXS measurements from Ref. [13] have been reported. Even though such a dichotomy is not yet understood theoretically[13], we expect that it should come from different selection rules at play for the plasma-mode contribution to the current (probed by THG) or to the density (probed by RIXS) response.

On a more general perspective, the present results can serve as a guide to engineer artificial heterostructures for the generation of THz pulses via THG up-conversion, using the plasmon dispersion to tune the enhancement of the nonlinear response for pumping THz field polarized along the layer stacking direction in cuprate superconductors. In the last few years giant progresses have been made in the realization of stable superconducting films of Bi-based cuprates, down to the dimensions of few unit cells[151, 155, 111]. It is now possible to realize efficient and tunable Josephson junctions by twisting neighbouring films, thanks to the angle-dependence of the pair tunnelling in a d-wave superconductor[154, 82, 95]. Even though the present technology is still limited to single junctions, in the near future the realisation of Junction arrays could lead to controllable artificial bilayer lattices, with a tunable resonance frequency. At the same time, the full quantum description of the nonlinear Josephson response is the starting point for the understanding of the multidimensional spectrum obtained in two-dimensional THz protocols[89], and to assess its potential for disentangling the intrinsic thermal effects from inhomogeneity broadening in unconventional cuprates, as we will see in Chapter 4.

2.5 Supplementary calculations

2.5.1 Role of polaritons in the THG response

As recently discussed in Ref. [43], the expression in Eq. 2.19 provides the correct description of the plasma modes only for momenta larger than a crossover scale

$k_c \sim \sqrt{\omega_{xy}^2 - \omega_z^2}/c$ set by the plasma-frequency anisotropy. At smaller momenta one cannot define two separate longitudinal (plasmon) and a transverse (polariton) electromagnetic modes, being their character mixed (see also discussion in Ref. [44]). This effect is a consequence of retardation (or relativistic) effects, that are relevant at $k < k_c$ and modify the dispersion itself of the electromagnetic modes as compared to the RPA-like result in Eq. 2.19, obtained by including only the effects of the instantaneous Coulomb potential. The longitudinal/transverse mixing can be rephrased in the language of Eq. 2.9 by noticing that for a layered system one cannot eliminate the coupling of the superconducting phase to the vector potential $\mathbf{A}$, even in the Coulomb gauge. In other words, the effect of the e.m. interactions is not exhausted by including the RPA resummation of the Coulomb potential, corresponding to Eq. 2.10, since also the retardation effects connected to the coupling to $\mathbf{A}$ must be included. This has a twofold consequence: (i) at low momenta the plasma modes have a mixed plasmon-polariton character and (ii) the external field couples also to the transverse modes, so that one should add in principle also the contribution of polariton-polariton and mixed plasmon-polariton corrections to the THG. However, as we will show here, item (i) is relevant in the regime $k \lesssim k_c$ that has a negligible phase-space contribution to the momentum summation in Eq. 2.20, and the additional corrections (ii) are quantitatively irrelevant, since the $c^2|\mathbf{k}|^2$ dispersion in the polarition rapidly suppresses its contribution as compared to the plasmon one as momentum increases.

To provide a general derivation of the generalized modes and their contribution to the THG, it is convenient to use the same approach of Ref. [43]. We then write the coupling between the phase and the electromagnetic potential in the Weyl gauge, where the potential vanishes and all the components of the (internal) vector potential are retained. The action is then better expressed in terms of the gauge invariant variables $\boldsymbol{\psi} = \nabla\theta + 2e/c\mathbf{A}$, and after integration of the θ field it reads, defining $k = (\mathbf{k}, i\omega_n)$,

$$S_G[\boldsymbol{\psi}] = \frac{1}{32\pi e^2} \sum_{i\omega_n, \mathbf{k}} \boldsymbol{\psi}^T(-k) \begin{pmatrix} -(i\omega_n)^2 + \omega_{xy}^2 + c^2k_z^2 & -c^2k_{xy}k_z \\ -c^2k_{xy}k_z & -(i\omega_n)^2 + \omega_z^2 + c^2k_{xy}^2 \end{pmatrix} \boldsymbol{\psi}(k), \tag{2.57}$$

where $\boldsymbol{\psi} = (\psi_{xy}, \psi_z)$ and $(i\omega_n)^2\mathbb{1} - \Omega^2(\mathbf{k}) \equiv \tilde{M}(\mathbf{k}, i\omega_n)$. In this section we further consider the continuum limit, since we are interested in the region of momenta $k_z \ll \pi/d$ where $q_z \to k_z$. As one can see, for fluctuations fully polarized in plane ($k_z = 0$) or out-of-plane ($k_{xy} = 0$) one recovers the same dispersion of Eq. 2.19, but at generica momenta the full electromagnetic modes will be defined by the square root $\omega_+(\mathbf{k})$ and $\omega_-(\mathbf{k})$ of the eigenvalues of the $\Omega^2(\mathbf{k})$ matrix, that are in general different from the expression 2.19

$$\omega_\pm^2(\mathbf{k}) = \frac{\omega_{xy}^2 + \omega_z^2 + c^2|\mathbf{k}|^2 \pm \sqrt{(\omega_{xy}^2 - \omega_z^2)^2 + c^4|\mathbf{k}|^4 - 2c^2(k_{xy}^2 - k_z^2)(\omega_{xy}^2 - \omega_z^2)}}{2}. \tag{2.58}$$

The mixing among plasmon and polariton modes arising from the coupling between θ and the (internal) $\mathbf{A}$ in the layered system leads also to a coupling between the external field and the transverse modes. In the presence of a given external $z-$polarized gauge field $\mathbf{A}_z = A_z\hat{z}$ the gauge-invariant phase along the z

direction should be rescaled as $\tilde{\psi}_z = \psi_z - 2e/cA_z$. As a consequence, the quadratic coupling to the A_z obtained in the same spirit of Eq. 2.12 reads:

$$\begin{aligned}\Delta S &= \frac{1}{16}\left(\frac{2e}{c}\right)^2 D_z d^2 \sqrt{T} \sum_{\mathbf{k}, i\omega_n, i\omega_m} \psi_z(-\mathbf{k}, -i\omega_n)\psi_z(\mathbf{k}, i\omega_m) A_z^2(i\omega_m - i\omega_n) \\ &= \frac{1}{16}\left(\frac{2e}{c}\right)^2 D_z d^2 \sqrt{T} \sum_{\mathbf{k}, i\omega_n, i\omega_m} \boldsymbol{\psi}^T(-\mathbf{k}, -i\omega_n) \begin{pmatrix} 0 & 0 \\ 0 & 1 \end{pmatrix} \boldsymbol{\psi}(\mathbf{k}, i\omega_m) A_z^2(i\omega_m - i\omega_n) \\ &\equiv \sum_{k,k'} \bar{\boldsymbol{\psi}}^T(-k)\tilde{R}(k,k')\boldsymbol{\psi}(k').\end{aligned} \tag{2.59}$$

Rewriting, as before, the total action in the form

$$S = \sum_{k,k'} \bar{\boldsymbol{\psi}}^T(-k)[\tilde{M}(k,k') + \tilde{R}(k,k')]\boldsymbol{\psi}(k'), \tag{2.60}$$

and integrating out the gauge-invariant variables, we are left with the kernel

$$K(i\Omega) = \frac{c}{4}\left(\frac{2e}{c}\right)^4 \omega_z^4 d^4 \frac{T}{V} \sum_{\mathbf{k}, i\omega_n} \tilde{M}_{zz}^{-1}(\mathbf{k}, i\omega_n)\tilde{M}_{zz}^{-1}(\mathbf{k}, i\omega_n + i\Omega). \tag{2.61}$$

where $\tilde{M}_{zz}^{-1}$ denotes the 22 term of the inverse matrix $\tilde{M}^{-1}$, and it accounts for the contribution of each mode in Eq. 2.58 to the final response, weighted by the projection onto the external field. We can indeed rewrite

$$\begin{aligned}\tilde{M}_{zz}^{-1}(\mathbf{k}, i\omega_n) &= \frac{\omega_+^2(\mathbf{k}) - \omega_{xy}^2 - c^2k_z^2}{\omega_+^2(\mathbf{k}) - \omega_-^2(\mathbf{k})} \frac{1}{(i\omega_n)^2 - \omega_+^2(\mathbf{k})} \\ &+ \frac{\omega_-^2(\mathbf{k}) - \omega_{xy}^2 - c^2k_z^2}{\omega_-^2(\mathbf{k}) - \omega_+^2(\mathbf{k})} \frac{1}{(i\omega_n)^2 - \omega_-^2(\mathbf{k})} \\ &\equiv \mathcal{P}_+(\mathbf{k})\frac{1}{(i\omega_n)^2 - \omega_+^2(\mathbf{k})} + \mathcal{P}_-(\mathbf{k})\frac{1}{(i\omega_n)^2 - \omega_-^2(\mathbf{k})},\end{aligned} \tag{2.62}$$

where $\mathcal{P}_{+,-}(\mathbf{k})$ represent the projectors on the z-direction of the two eigenmodes. The nonlinear kernel can then be rewritten, for $\sigma, \sigma' = +, -$, as

$$\begin{aligned}K(i\Omega) &= \sum_{\sigma,\sigma'} K_{\sigma\sigma'}(i\Omega) \\ &= \frac{c}{4}\left(\frac{2e}{c}\right)^4 \omega_z^4 d^4 \sum_{\sigma,\sigma'} \frac{1}{V}\sum_{\mathbf{k}} \mathcal{P}_\sigma(\mathbf{k})\mathcal{P}_{\sigma'}(\mathbf{k}) T \sum_{i\omega_n} \frac{1}{(i\omega_n)^2 - \omega_\sigma^2} \frac{1}{(i\omega_n + i\Omega)^2 - \omega_{\sigma'}^2}.\end{aligned} \tag{2.63}$$

The result of the Matsubara summation after analytic continuation $i\Omega \to \Omega + i\delta$ is finally

$$\begin{aligned}T\sum_{i\omega_n} \frac{1}{(i\omega_n)^2 - \omega_\sigma^2}\frac{1}{(i\omega_n + i\Omega)^2 - \omega_{\sigma'}^2} &= \frac{\omega_\sigma + \omega_{\sigma'}}{4\omega_\sigma\omega_{\sigma'}} \frac{\coth\left(\frac{\beta\omega_\sigma}{2}\right) + \coth\left(\frac{\beta\omega_{\sigma'}}{2}\right)}{(\omega_\sigma + \omega_{\sigma'})^2 - (\Omega + i\delta)^2} \\ &+ \frac{\omega_\sigma - \omega_{\sigma'}}{4\omega_\sigma\omega_{\sigma'}} \frac{\coth\left(\frac{\beta\omega_\sigma}{2}\right) - \coth\left(\frac{\beta\omega_{\sigma'}}{2}\right)}{(\omega_\sigma - \omega_{\sigma'})^2 - (\Omega + i\delta)^2}.\end{aligned} \tag{2.64}$$

Proceeding in terms of gauge invariant variables, we have shown that the plasmon and polariton branches are indeed coupled and in principle, with a third order process, one should consider mixed plasmon-polariton and two-polariton processes contributing to the overall third harmonic signal. However the explicit numerical computation of Eq. 2.64 shows that the contributions arising from the polariton are several orders of magnitude smaller than the plasmon one. In order to provide an analytical understanding of this finding, in the next section we estimate the relative order of magnitude of the various processes.

2.5.2 Estimate of the DOS for plasmon-like and polariton-like contributions to the THG

In order to perform the integration over momenta and obtain the nonlinear kernel, we introduce the quantity akin to a joint density of states

$$\rho_{\sigma\sigma'}(z,z') = \frac{1}{V}\sum_{\mathbf{k}} \mathcal{P}_\sigma(\mathbf{k})\mathcal{P}_{\sigma'}(\mathbf{k})\delta(z-\omega_\sigma(\mathbf{k}))\delta(z'-\omega_{\sigma'}(\mathbf{k})), \tag{2.65}$$

through which we rewrite

$$\begin{aligned} K(\Omega) = \frac{c}{4}\left(\frac{2e}{c}\right)^4 \omega_z^4 d^4 \sum_{\sigma,\sigma'} \int dz\, dz'\, \rho_{\sigma\sigma'}(z,z') \Bigg[& \frac{z+z'}{4zz'} \frac{\coth\left(\frac{\beta z}{2}\right)+\coth\left(\frac{\beta z'}{2}\right)}{(z+z')^2-(\Omega+i\delta)^2} \\ & + \frac{z-z'}{4zz'} \frac{\coth\left(\frac{\beta z}{2}\right)-\coth\left(\frac{\beta z'}{2}\right)}{(z-z')^2-(\Omega+i\delta)^2} \Bigg]. \end{aligned} \tag{2.66}$$

In the case of the plasmon-plasmon and polariton-polariton processes ($\sigma=\sigma'$), one can define $\rho_{\sigma\sigma}(z,z') \equiv \rho_{\sigma\sigma}(z)\delta(z-z')$ and the following kernel is obtained

$$K_{\sigma\sigma}(\Omega) \propto \int dz\, \rho_{\sigma\sigma}(z) \frac{1}{z} \frac{\coth\left(\frac{\beta z}{2}\right)}{(2z)^2-(\Omega+i\delta)^2}, \tag{2.67}$$

from which it is straightforward to obtain the imaginary part in the limit $\delta \to 0$, which reads

$$\begin{aligned} \mathrm{Im} K_{\sigma\sigma}(\Omega) &\propto \pi \int dz\, \rho_{\sigma\sigma}(z) \frac{\coth\left(\frac{\beta z}{2}\right)}{4z^2}[\delta(2z-\Omega)-\delta(2z+\Omega)] \\ &= \frac{\pi}{\Omega^2}\rho_{\sigma\sigma}\left(\frac{|\Omega|}{2}\right)\coth\left(\frac{\beta\Omega}{4}\right). \end{aligned} \tag{2.68}$$

From the imaginary part of the kernel it is possible to evaluate the real part through the Kramers-Kronig relation. Since the nonlinear signal is related to the modulus of the kernel [20], it is worth computing explicitly the density of states to estimate the contribution of the various processes to the nonlinear response.

As a first step we evaluate the density of states associated with the plasmon-plasmon and polariton-polariton. We notice that the summation over the momenta $\mathbf{k}$ extends over a region $k_z \lesssim 1/d$ and $k_{xy} \lesssim 1/\xi$. Both these limiting values are orders of magnitude larger than the value $k_c = \sqrt{\omega_{xy}^2-\omega_z^2}/c \sim \omega_{xy}/c$ [43] beyond which the mixing of the $\omega_+(\mathbf{k})$ and $\omega_-(\mathbf{k})$ modes is relevant. In particular, one can consider that the volume of the phase space interested by the mixing is $\sim k_c^3$, that compared to the total integration region gives $\sim \omega_{xy}^3 d\xi^2/c^3 \ll 1$, since for cuprates $\omega_{xy} \sim 1$ eV, $d \sim 1$ nm, $\xi \sim 5$ nm, so that $c/(d\xi^2)^{1/3} \sim 425$ eV. Thus, as confirmed by numerical simulations with the full relativistic dispersion, it is absolutely safe to consider the $k \gg k_c$ limit of the expressions for the projectors and for the modes in Eq. 2.58, such that the $\omega_-(\mathbf{k})$ solution tends to the longitudinal plasmon-like excitation $\omega_L(\mathbf{k})$ of Eq. 2.19, while the $\omega_+(\mathbf{k})$ solution tends to the RPA-value of the transverse polariton-like excitation $\omega_T(\mathbf{k})$, with

$$\omega_T^2(\mathbf{k}) = \omega_{xy}^2 \frac{k_z^2}{|\mathbf{k}|^2} + \omega_z^2 \frac{k_{xy}^2}{|\mathbf{k}|^2} + c^2|\mathbf{k}|^2. \tag{2.69}$$

We can show that the projectors over the two eigenvalues then read

$$\mathcal{P}_+(|\mathbf{k}| \gg k_c) \equiv \mathcal{P}_T = \frac{k_{xy}^2}{|\mathbf{k}|^2} = \sin^2\eta, \quad \mathcal{P}_-(|\mathbf{k}| \gg k_c) \equiv \mathcal{P}_L = \frac{k_z^2}{|\mathbf{k}|^2} = \cos^2\eta, \tag{2.70}$$

with η being the angle of the momentum $\mathbf{k}$ with the z direction. To get an analytical expressions for $\rho_{LL}(z)$ and $\rho_{TT}(z)$ we first consider the case where the $\mathbf{k}$-summation is extended over a sphere of radius $k_0 \sim 1/(d\xi^2)^{1/3}$, that allows one to get at least the correct order of magnitude of the three processes. We have for the plasmon part

$$\rho_{LL}(\omega_z < z < \omega_{xy}) \equiv \rho_{LL}^0 \frac{4\pi}{3} \frac{z}{\sqrt{\omega_{xy}^2 - \omega_z^2}} \left(\frac{\omega_{xy}^2 - z^2}{\omega_{xy}^2 - \omega_z^2}\right)^{\frac{3}{2}}, \tag{2.71}$$

and zero elsewhere, where we defined $\rho_{LL}^0 = k_0^3/\sqrt{\omega_{xy}^2 - \omega_z^2}$. For the polariton part we can instead evaluate, in the region $\omega_z < z < \omega_{xy}$,

$$\begin{aligned}\rho_{TT}(\omega_z < z < \omega_{xy}) \equiv \rho_{TT}^0 \frac{\pi}{32} \frac{z}{\sqrt{\omega_{xy}^2 - \omega_z^2}} \frac{z^2 - \omega_z^2}{\omega_{xy}^2 - \omega_z^2} \times \\ \times \left[\left(\frac{z^2 - \omega_z^2}{\omega_{xy}^2 - \omega_z^2}\right)^2 - 4\left(\frac{z^2 - \omega_z^2}{\omega_{xy}^2 - \omega_z^2}\right) + 8\right].\end{aligned} \tag{2.72}$$

where $\rho_{TT}^0 = (\omega_{xy}^2 - \omega_z^2)/c^3$. From Eq. 2.71 we observe that ρ_{LL} jumps from zero to a finite value in correspondence of $\Omega = \omega_z$. Since $\mathrm{Im}K_{LL}(2\Omega) \propto \rho_{LL}(\Omega)$, the imaginary part of the two-plasmon kernel has the same discontinuity at ω_z, that leads by Kramers-Kronig to a logarithmic divergence in its real part. In contrast the ρ_{TT} is zero at ω_z, so that the imaginary part of the two-polariton kernel is continuous at $\Omega = \omega_z$, and we do not expect anomalies in its real part, making the nonlinear kernel dominated by the logarythmic divergence coming from the plasmon-plasmon part. An additional observation is that the relative strength between the polariton-polariton and plasmon-plasmon processes is determined by the ratio $\rho_{TT}^0/\rho_{LL}^0 \sim (\omega_{xy}^2 - \omega_z^2)^{\frac{3}{2}}/c^3k_0^3 \sim (\omega_{xy}/ck_0)^3$, being $\omega_{xy} \gg \omega_z$. As recalled before, this ratio is extremely small and thus further suppresses the two-polariton contribution.

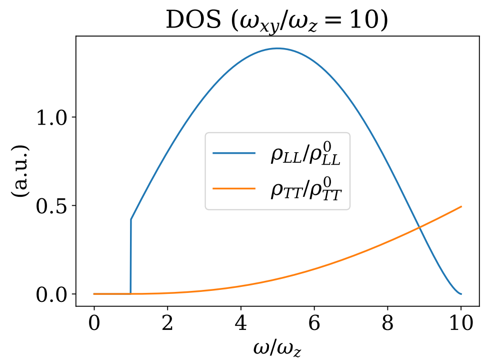

Figure 2.6. Graph for the plasmon-plasmon and polariton-polariton excitations coming from Eq. 2.71 and Eq. 2.72, respectively, where we set $\omega_{xy}/\omega_z = 10$ to better visualize the overall behavior. Notice that both densities of states are zero for $\omega < \omega_z$, but while $\rho_{LL}(\omega)$ jumps from zero to a finite value at $\omega = \omega_z$, $\rho_{TT}(\omega)$ is continuous at $\omega = \omega_z$.

The mixed plasmon-polariton process, as well, is suppressed by a similar prefactor. Indeed, the relative joint density of states $\rho_{LT}(z, z')$ is different from zero in the region $\omega_z < z < \omega_{xy}$ and $\sqrt{\omega_z^2 + \omega_{xy}^2 - z^2} < z' < \sqrt{\omega_z^2 + \omega_{xy}^2 + c^2 k_0^2 - z^2}$, reading

$$\rho_{LT}(z, z') = \frac{2\sqrt{\omega_{xy}^2 - \omega_z^2}}{c^3} \frac{z z'}{\omega_{xy}^2 - \omega_z^2} \sqrt{\frac{z'^2 + z^2 - \omega_{xy}^2 - \omega_z^2}{\omega_{xy}^2 - \omega_z^2} \frac{z^2 - \omega_z^2}{\omega_{xy}^2 - \omega_z^2} \sqrt{\frac{\omega_{xy}^2 - z^2}{\omega_{xy}^2 - \omega_z^2}}}. \tag{2.73}$$

In this latter case, from Eq. 2.66, one gets for the imaginary part of the kernel a more involved expression

$$\begin{aligned} \mathrm{Im} K_{LT}(2\Omega) \propto \int dz \, & \frac{\coth\left(\beta(z+\Omega)/2\right) - \coth\left(\beta(z-\Omega)/2\right)}{8(z^2 - \Omega^2)} \times \\ & \times \left[\rho_{LT}(z+\Omega, \Omega - z) + \rho_{LT}(-z-\Omega, z+\Omega) \right. \\ & \left. - \rho_{LT}(z+\Omega, z-\Omega) - \rho_{LT}(-z-\Omega, -z+\Omega)\right]. \end{aligned} \tag{2.74}$$

We notice that the singular denominator in the integral cancels out with an analogous term at the numerator coming from ρ_{LT}, thus the integrand is regular. One can easily check that also $\rho_{LT}(z, z')$ is continuous as a function of z, z', hence one does not expect discontinuities in $\mathrm{Im}K_{LT}(\Omega)$. Indeed, one can analytically compute at $T = 0$

$$\begin{aligned} \mathrm{Im} K_{LT}(2\Omega) \propto \int_0^\Omega dz \, & \left[\frac{\rho_{LT}(z+\Omega, \Omega - z) + \rho_{LT}(-z-\Omega, z+\Omega)}{4(z^2 - \Omega^2)} \right. \\ & \left. - \frac{\rho_{LT}(z+\Omega, z-\Omega) + \rho_{LT}(-z-\Omega, -z+\Omega)}{4(z^2 - \Omega^2)} \right]. \end{aligned} \tag{2.75}$$

For $\Omega < \omega_{xy}$, replacing Eq. 2.73 in the previous expression, one can find that $\mathrm{Im}K_{LT}(2\Omega)$ is zero, since the region of integration lies into the support of the function ρ_{LT}. It is then safe to neglect the polariton-polariton and the plasmon-polariton processes and proceed with the standard RPA-like result used above, where the phase variable is only dressed by the Coulomb potential and in the bilayer case one works directly with the superconducting phase variables.

As a last point we notice that this suppression of the plasmon-polariton and polariton-polariton contribution is obtained even in the case when the external field is polarized along the in-plane direction. In that case, the corresponding plasmon-plasmon process would produce a logarythmic divergence at $\Omega = \omega_{xy}$, while the processes involving the excitation of polaritons would be again suppressed by the relativistic part $\sim c^2|\mathbf{k}|^2$ of their dispersion.

2.5.3 Estimate of the DOS in the anisotropic case

In this section we give the full analytical expression of the density of states associated with the single-layer plasmon, when the discretization along the z-axis is retained and the integration range is anisotropic, which allows us to calculate the kernel shown in Fig. 2.2 above. Although the DOS is different from what we calculated for a spherical volume in the previous section, we want to show here explicitly that there are no further singularities originating in the nonlinear kernel and the overall signal is dominated by the logarythmic singularity at $\Omega = \omega_z$.

We start from Eq. 2.65 where we set $\sigma = \sigma' = L$ and instead of expressing the dispersion and the projector in terms of the angle η we retain the dependence on k_z, k_{xy}. In cylindric coordinates the density of states reads

$$\rho_{LL}(z) = 2\pi \int_{-\bar{k}_z}^{\bar{k}_z} dk_z \int_0^{\bar{k}_{xy}} dk_{xy}\, k_{xy} \left(\frac{k_z^2}{k_z^2 + k_{xy}^2}\right)^2 \delta\left(z - \sqrt{\frac{\omega_{xy}^2 k_{xy}^2 + \omega_z^2 k_z^2}{k_{xy}^2 + k_z^2}}\right). \tag{2.76}$$

In this case one integrates at first the k_{xy} variable, obtaining

$$\rho_{LL}(z) = 2\pi \frac{z}{\omega_{xy}^2 - \omega_z^2}\theta(z-\omega_z) \int_{-\bar{k}_z}^{\bar{k}_z} dk_z\, k_z^2 \theta\left(\sqrt{\frac{\omega_{xy}^2 \bar{k}_{xy}^2 + \omega_z^2 k_z^2}{\bar{k}_{xy}^2 + k_z^2}} - z\right) \tag{2.77}$$

The case with the discretization along z is treated by replacing $k_z \to (2/d)\sin(k_z d/2)$ and considering $\bar{k}_z = \pi/d$, which does not affect the integration of the in-plane momentum that we have just performed. The Heaviside function depends on k_z and bounds the upper extreme of the integral as a function of z, namely using the fact that $z < \omega_{xy}$ we rewrite

$$\rho_{LL}(z) = 4\pi \frac{z}{\omega_{xy}^2 - \omega_z^2}\theta(z-\omega_z)\theta(\omega_{xy} - z) \int_0^{\bar{k}_z} dk_z\, k_z^2 \theta\left(\bar{k}_{xy}\sqrt{\frac{\omega_{xy}^2 - z^2}{z^2 - \omega_z^2}} - k_z\right). \tag{2.78}$$

The integral can be now performed and has a piecewise but *continuous* behavior

$$\rho_{LL}(\omega_z < z < \omega_{xy}) = 4\pi \frac{z}{\omega_{xy}^2 - \omega_z^2}\bar{k}_{xy}^3 \chi^3 \times \\ \times \begin{cases} \frac{1}{3} & \text{if}\, \omega_z < z < \sqrt{\frac{\omega_{xy}^2 + \omega_z^2\chi^2}{1+\chi^2}} \\ \frac{1}{3\chi^3}\left(\frac{\omega_{xy}^2 - z^2}{z^2 - \omega_z^2}\right)^{\frac{3}{2}} & \text{if}\, \sqrt{\frac{\omega_{xy}^2 + \omega_z^2\chi^2}{1+\chi^2}} < z < \omega_{xy} \end{cases}, \tag{2.79}$$

where we defined $\chi = \bar{k}_z/\bar{k}_{xy}$ the anisotropy ratio between the out-of-plane and in-plane cutoffs for the momenta. Since the function is monotonically increasing in the first region and monotonically decreasing in the second one, the peak of the density of states is located exactly at energy

$$\bar{\omega} = \sqrt{\frac{\omega_{xy}^2 + \omega_z^2\chi^2}{1+\chi^2}} = \omega_z\sqrt{\frac{\alpha^2+\chi^2}{1+\chi^2}}, \tag{2.80}$$

whose value is determined by the interplay between the out-of-plane and in-plane anisotropies of both the plasma frequencies ($\alpha = \omega_{xy}/\omega_z$) and the cutoff momenta (χ). In our case, being $\alpha \sim 100$ and $\chi \sim 5$ we have $\bar{\omega} \sim (\alpha/\chi)\omega_z \sim 5\omega_z$. The non-dispersive case of Ref. [45] is instead recovered in the $\chi \to \infty$ limit, since in that case $\bar{\omega} \to \omega_z$ irrespectively on α and the peak shifts towards the out-of-plane plasma frequency.

When the discretization is considered, the computations are performed in the same fashion and the result is only slightly modified

$$\begin{aligned}\rho_{LL}(z) &= 4\pi\frac{z}{\omega_{xy}^2-\omega_z^2}\bar{k}_{xy}^3\chi^3\times \\ &\times\begin{cases}\frac{\pi}{2} & \text{if}\, \omega_z < z < \bar{\omega} \\ \arcsin\left(\frac{1}{\chi}\sqrt{\frac{\omega_{xy}^2-z^2}{z^2-\omega_z^2}}\right) - \frac{1}{\chi}\sqrt{\frac{\omega_{xy}^2-z^2}{z^2-\omega_z^2}}\sqrt{1-\frac{1}{\chi^2}\frac{\omega_{xy}^2-z^2}{z^2-\omega_z^2}} & \text{if}\, \bar{\omega} < z < \omega_{xy}\end{cases},\end{aligned} \tag{2.81}$$

where now we redefined the anisotropy parameter $\chi = 2/(\bar{k}_{xy}d)$ and $\bar{\omega}$ is the same of Eq. 2.80. Also in this latter case the DOS is continuous and the kernel is dominated by the logarythmic singularity at ω_z.

2.5.4 Comparison between instantaneous response and two-plasmon process

When expanding at fourth order the cosine in Eq. 2.11 one should consider in principle also the instantaneous process $\sim A^4(t)$ together with the two-plasmon excitation mediated by $\sim A^2(\Delta_z\theta)^2$. Indeed, it has been recently proposed [153] that this term by itself could provide a justification for the experimental nonlinear signal, since the sharp plasma edge at $\Omega = \omega_z$ filters the incoming field at linear order. Here we show explicitly that, in the Josephson model, both intantaneous K_{inst} and two-plasmon K_{2p} contributions have a comparable weight in the nonlinear kernel $K(2\Omega)$ in the THz region $\Omega \sim \omega_z$. Indeed, one can immediately evaluate from Eq. 2.11 the instantaneous part

$$K_{\text{inst}}(2\Omega) = \frac{c}{24}\left(\frac{2e}{c}\right)^4 D_z d^2 = \frac{c}{24}\left(\frac{2e}{c}\right)^4\frac{\omega_z^2 d}{4\pi e^2/d} \sim \frac{c}{24}\left(\frac{2e}{c}\right)^4\frac{\omega_z^2 d}{\omega_{xy}}, \tag{2.82}$$

where in the last passage we approximated $4\pi e^2/d \sim \omega_{xy}$, as appropriate for the cuprate case. From Eq. 2.68 we can instead immediately evaluate

$$\text{Im}K_{\text{2p}}(2\Omega) = \frac{c}{4}\left(\frac{2e}{c}\right)^4\omega_z^4 d^4\frac{\pi}{4\Omega^2}\coth\left(\frac{\beta\Omega}{2}\right)\rho_{LL}(|\Omega|). \tag{2.83}$$

We can now use the analytical expression found in Eq. 2.81 to evaluate the plasmon-plasmon density of states at $\Omega = \omega_z^+$, i.e. right above the discontinuity

$$\rho_{LL}(\omega_z) = \frac{16\pi^2\omega_z}{d^3(\omega_{xy}^2 - \omega_z^2)} \sim \frac{16\pi^2\omega_z}{d^3\omega_{xy}^2}. \tag{2.84}$$

Using this value in the previous expression we can evaluate in the end

$$\frac{\mathrm{Im}K_{2\mathrm{p}}(2\Omega \sim 2\omega_z)}{K_{\mathrm{inst}}(2\omega_z)} \sim \frac{24\pi^3\omega_z}{\omega_{xy}}, \tag{2.85}$$

from which we see that the imaginary part of the two-plasmon process and the instantaneous contribution have a similar order of magnitude when the typical values $\omega_z \sim 1$ THz and $\omega_{xy} \sim 1$ eV for cuprates are considered. As recalled before, in the real part of the two-plasmon contribution there is a logarithmic singularity at $\Omega \sim \omega_z$ which dominates the nonlinear response, being the latter proportional to $|K(2\Omega)|$ for monochromatic pulses. Nevertheless, if the resonance is broadened by a finite plasmon damping into Eq. 2.67 for the kernel, the instantaneous processes could lead to a smoothening of the temperature dependence when the resonance condition is crossed.

To conclude, we stress that the relative contribution of the two parts has been computed so far within the framework of an effective Josephson Hamiltionian, which is used here as an approximation of a more realistic microscopic model in order to get a qualitative behaviour of the nonlinear response. As discussed recently within the context of the nonlinear response appropriate for in-plane polarized field[123], the microscopic coupling of the superconducting collective modes to light is mediated in general by fermionic susceptibilities that will scale differently from the the effective ω_z appearing in Eq. 2.82 and Eq. 2.83. As a consequence, a quantitative estimate of the two relative contributions requires a more microscopic approach, that is beyond the scope of the present thesis.

Chapter 3

Two-dimensional spectroscopy in electronic systems

Part of the contents of this chapter has been published in Ref. [39]. The rest of the chapter will be submitted soon for publication.

3.1 Introduction

Among the nonlinear spectroscopies developed in the years, 2DCS is capable to monitor the real-time dynamic of a system following the excitation by two time-delayed pulses [26, 131]. The spectrum is acquired as a function of i) the time following the excitation and ii) the inter-pulse delay, producing 2D Fourier spectra which allow one to directly access the nonlinear optical response function of the system through a four-wave mixing process. These two control knobs were originally employed shining IR-visible pulses on molecules and semiconducting quantum wells to clarify the mutual coupling and relaxation dynamics of different excitation channels, with only few applications to situations where many-body effects are relevant [71]. More recently, this technique has been extended to the THz region, where the phenomenology connected with collective degrees of freedom of materials plays a significant role.

As an example, 2D-THz spectroscopy has been then used to clarify the dynamical interplay between spin and/or lattice excitations, being particularly useful in disentangling the different nonlinear pathways connecting them in complex free energy landscapes where anharmonicities come into action [91, 96, 85]. Indeed, thanks to the intrinsic dependency on two independent timescales, the corresponding Fourier-transformed 2D frequency map presents unique signatures when two or more modes of the system are coupled, being particularly sensitive to the nature of the interaction processes between light and matter [66, 16].

For what concerns electronic degrees of freedom, this technique was proposed to distinguish between different types of line-broadening in concomitance of phase transitions, whether related to the formation of structures in real space leading to inhomogeneities over nano- or mesoscopic length scales or to intrinsic broadening effects connected to the lifetime of the excitation. The power of the 2D technique comes also here into help due to its unique separation between the former, leading to a distribution of electronic resonances, or the latter, producing a homogeneous broadening of their linewidth [94, 89].

These two peculiarities of 2D coherent spectroscopy have recently found a common playground in superconducting systems. On the one hand, multiple and intertwined electronic and lattice excitation channels are available in the THz region, where the superconducting gap lies [136, 75]; on the other, unconventional systems such as cuprates offer the ideal phase diagram to host competition between different types of electronic order, producing the inhomogeneous picture mentioned above [89].

Although we are experiencing a flourishing period for experimental applications of 2D-THz spectroscopy to quantum materials where many-body dynamics is important, the theoretical modeling of this spectroscopic tool for those systems is still at its infancy [58]. For what concerns superconductors, theoretical advances have been made to simulate 2D dynamics in isotropic systems as well as layered ones, with particular attention to the role of collective modes [92, 52, 75]. With this respect, we show how the previously developed insight into the basic mechanisms underlying nonlinear optical response of superconductors, such as the role of disorder, anisotropy, gap nature, in determining the properties of the system can be applied to discuss the results of multidimensional experiments[102, 112].

In this chapter, we first introduce a general framework that allows one to compute theoretically the result of a 2D experiment, having as key ingredient the nonlinear third-order optical response function of the system, $K^{(3)}$. We will put forward the idea that this protocol is a convenient experimental strategy to extract detailed information on the nature of the nonlinear processes occurring in the system, taking advantage of the intrinsic dependence of the protocol on two independent time delays. We will explicitly see that there is no conceptual difference, from the theory point of view, between the computation of the nonlinear response function for a 2D protocol and the simulation of simpler single-pulse experiments such as Third Harmonic Generation (THG). Nonetheless, numerical simulations can be more time consuming, calling for a semi-analyitical approach to the problem.

Secondly, we apply the developed formalism to compute the 2D response in some specific cases. We analyze the response of a model semiconductor with a direct bandgap, for which we compute the contributions to $K^{(3)}$ stemming from different nonlinear processes involving paramagnetic-like or diamagnetic-like light-matter couplings. We will show that the two give very different signatures in the 2D experimental map, as opposed to the more ambiguous signal that is collected as a function of a single time delay. Although the computation is here performed for a clean semiconductor, we provide some analogies with the case of a disordered superconductor, which will be analyzed more in depth in the following chapter, where we discuss and extend the results that we published in Ref. [72] on superconducting NbN.

A further application is again to cuprate superconductors, where as discussed previously the strong anisotropy of the superconducting stiffness in the in-plane and out-of-plane directions gives rise to an undamped low-energy out-of-plane plasma mode (ω_z), the Josephson plasmon, which is relevant both in linear [43, 126, 124] and nonlinear c-axis response of the system [45, 39]. This mode directly affects the refractive index of the superconductor, providing a soft plasma edge in the c-axis reflectivity, which acts to reshape the spectral content of the incoming pulse at low temperatures. Moreover, inhomogeneity and disorder within the superconducting planes were proposed to effectively produce a distribution of out-of-plane plasma frequencies [144, 31], whose width is hard to extract in standard spectroscopic analysis. The 2D protocol, instead, has recently been proposed as a tool to distinguish the latter contribution from the usual quasiparticle broadening by looking at the Josephson Echo, i.e. the $(\omega_z, -\omega_z)$ peak [89, 52] in the Fourier-transformed frequency map. The extraction of the degree of inhomogeneity with this method requires the implementation of all the effects that influence the 2D spectrum, like the screening of the plasmon and the presence of a nonlinear kernel, possibly with contributions from the same two-plasmon process discussed in the preceding chapter.

We conclude by noticing how, as happens for single-pulse nonlinear spectroscopies [142], the formalism is flexible enough to establish a parallel between the multiphoton excitation of electronic degrees of freedom and phononic ones, providing a natural extension to situations where diverse hybrid light-matter polaritons become important, such as the phonon-polariton [90, 125].

3.2 General framework

We begin by considering a system in which a general third-order response function $K^{(3)}$ is present, such that the nonlinear signal reads

$$J^{(3)}(t) = \int dt_i \, K^{(3)}(t; t_1, t_2, t_3) A(t_1) A(t_2) A(t_3). \tag{3.1}$$

where $K^{(3)}(t; t_1, t_2, t_3) = \theta(t-t_1)\theta(t_1-t_2)\theta(t_2-t_3)\tilde{K}^{(3)}(t-t_1, t_1-t_2, t_2-t_3)$ under the general assumptions of invariance under time translation and causality, which are fulfilled in a quasi-equilibrium perturbative approach [36, 116]. To be concise, here we also assumed a specific time ordering $t_3 < t_2 < t_1 < t$, but symmetry under exchange of t_i can be always assured. Let us imagine to have at disposal three delta-like pulses A_0, A_τ, $A_{\tau'}$ delayed in time as in Fig. 3.1, i.e. $A_0(s) = \bar{A}\delta(s)$, $A_\tau(s) = \bar{A}\delta(s+\tau)$ and $A_{\tau+\tau'}(s) = \bar{A}\delta(s+\tau+\tau')$ and to collect the nonlinear signal generated at time t, with the possibility of sweeping τ and τ'. Let us imagine to register at first the nonlinear current generated by the total field

$$A(s) = A_0(s) + A_\tau(s) + A_{\tau+\tau'}(s), \tag{3.2}$$

that we denote as $J^{(3)}_{0,\tau,\tau+\tau'}(t)$, as a function of the three time delays (t, τ, τ'). Then imagine to repeat the experiment when only two pulses at a time are present, collecting the current $J^{(3)}_{0,\tau}(t)$, $J^{(3)}_{\tau,\tau+\tau'}(t)$, $J^{(3)}_{0,\tau+\tau'}(t)$. To conclude we sample the current when only one pulse is switched on, obtaining $J^{(3)}_0(t)$, $J^{(3)}_\tau(t)$, $J^{(3)}_{\tau+\tau'}(t)$. If we calculate through Eq. 3.1

$$J^{(3)}_{3D} = J^{(3)}_{0,\tau,\tau+\tau'} - J^{(3)}_{0,\tau} - J^{(3)}_{\tau,\tau+\tau'} - J^{(3)}_{0,\tau+\tau'} + J^{(3)}_0 + J^{(3)}_\tau + J^{(3)}_{\tau+\tau'}, \tag{3.3}$$

then we get, replacing for each term the corresponding sum of delta-like $A(t)$,

$$J^{(3)}_{3D}(t, \tau, \tau') \sim \theta(t)\theta(\tau)\theta(\tau')\tilde{K}^{(3)}(t, \tau, \tau')\bar{A}^3. \tag{3.4}$$

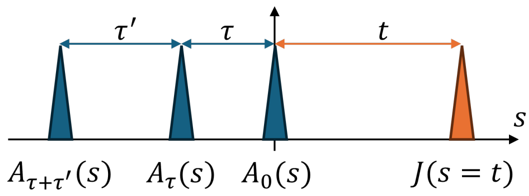

Figure 3.1. The time ordering of the fields in the ideal multidimensional experiment described above. For the 2D protocol the field $A_{\tau+\tau'}$ is absent and one collects the signal as a function of the times (t,τ). We notice by examining the scheme that in case of identical envelopes, i.e. $A_\tau(s) = A_0(t+\tau)$, the time-domain 2D map for $\tau < 0$ is related to the one at $\tau > 0$ by the relation $J^{(3)}_{2D}(t,-|\tau|) = J^{(3)}_{2D}(t-|\tau|,|\tau|)$.

We notice at first that this procedure completely eliminates the response generated by the linear response kernel $K^{(1)}$, as one can check by direct computation of $J^{(1)}_{3D}$ by means of the first-order equivalent of Eq. 3.3. Most importantly, with such an experimental setup one then directly characterizes the full time-dependence of the nonlinear third-order response function of the system, thus eliminating the integrations over time delays which are involved in a standard single-pulse setup. A two-pulse protocol is then an intermediate platform between the ideal experiment just described, which was for instance employed in multi-dimensional spectroscopies of molecules [30] or quantum wells [141], and the setups commonly used in spectroscopies of solid state systems. As we shall see, 2D THz spectroscopy can be used to discriminate among different possible nonlinear pathways that would lead to similar single-pulse signals but very different 2D maps.

In the rest of the chapter we will consider a simplified 2D protocol where two time-delayed copies of the same pulse $A_0(t) = A(t)$ and $A_\tau(t) = A(t+\tau)$ are applied on the system. The non-linearly generated signal

$$J^{(3)}_{2D}(t,\tau) = J^{(3)}_{0,\tau}(t,\tau) - J^{(3)}_{0}(t) - J^{(3)}_{\tau}(t,\tau), \tag{3.5}$$

is detected and a 2D Fourier transform $(t,\tau) \to (\omega_t,\omega_\tau)$ is performed. As detailed in the following, we will consider explicitly the effects of the experimental configuration on the collected signal, by explicitly taking into account the spatial propagation of the external field A in the sample and of the non-linearly generated polarization $J^{(3)}$, making use of the results presented in Chapter 1. To fix the ideas we will start by focusing on the effects of the spectral content of the incoming pulse on $J^{(3)}_{2D}(\omega_t,\omega_\tau)$, by considering realistic pulse shapes $A(t)$.

Let us consider at first the simplest nonlinear third-order kernel, an instantaneous one, i.e.

$$K^{(3)}(t;t_1,t_2,t_3) \sim \delta(t-t_1)\delta(t_1-t_2)\delta(t_2-t_3), \tag{3.6}$$

such that the corresponding nonlinear current is simply given by $J^{(3)}(t) \sim A^3(t)$. Replacing the latter in Eq. 3.5 one is left with

$$J^{(3)}_{2D}(t,\tau) \sim A^2(t)A(t+\tau) + A(t)A^2(t+\tau). \tag{3.7}$$

The first term corresponds to a double interaction with the field $A_0(t)$, i.e. the one whose temporal envelope is centered at zero time delay, and a single interaction with

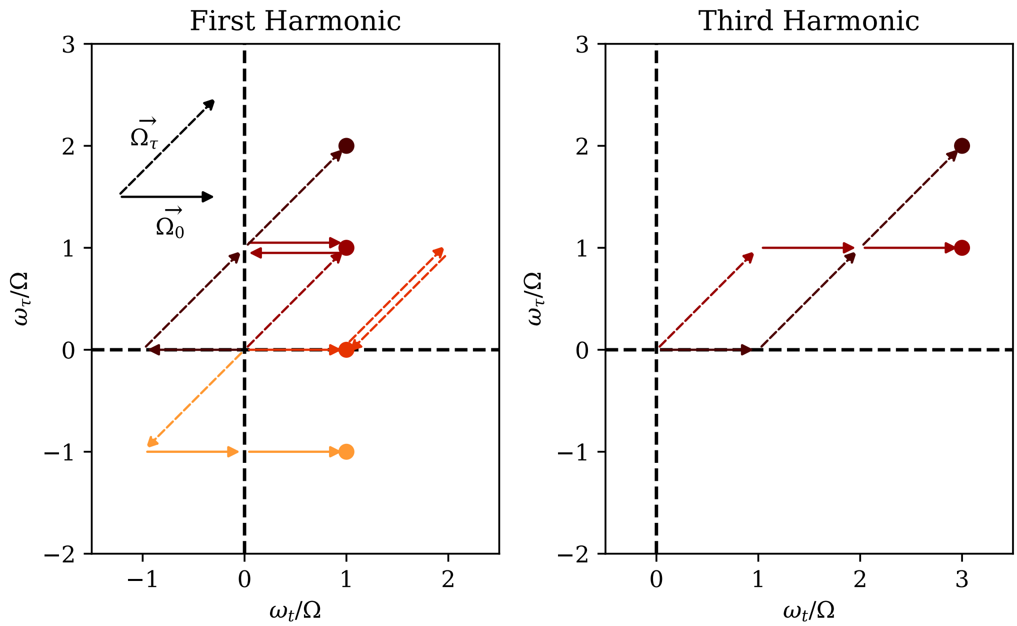

Figure 3.2. Frequency-vector representation of the 2D map for the instantaneous response, which is valid for the monochromatic limit also for general form of the third-order kernel. The various combinations produce four spots aligned along the direction of the first harmonic Ω (left panel) and two for the third harmonic 3Ω (right panel).

$A_\tau(t)$, which is delayed by τ from the former. The second term is analogous but the roles of $A_0(t)$ and $A_\tau(t)$ are switched. In order to understand how the 2D map in frequency domain looks like, let us assume that the spectral content of the field is centered around frequency $\pm\Omega$, namely $A(t) \sim \bar{A}e^{-t^2/(2\tau_p^2)}\cos(\Omega t)$. One can then collect the oscillating components in the time domain and represent them as arrows in the Fourier conjugated (ω_t, ω_τ) plane. Their orientation and length will depend on whether they come from the $+\Omega$ or $-\Omega$ frequency component of pulse $A_0(t)$ or $A_\tau(t)$, which are depicted as $\pm\overrightarrow{\Omega_0}$ and $\pm\overrightarrow{\Omega_\tau}$, respectively, see Fig. 3.2. Expression 3.7 can be then pictorially computed by the vectorial sum of two $\pm\overrightarrow{\Omega_0}$ and one $\pm\overrightarrow{\Omega_\tau}$ for the $A^2(t)A(t+\tau)$ contribution, or one $\pm\overrightarrow{\Omega_0}$ and two $\pm\overrightarrow{\Omega_\tau}$ for the $A(t)A^2(t+\tau)$ piece. The possible sixteen combinations give rise to twelve dinstict spots, which are two by two symmetric with respect to the origin of the (ω_t, ω_τ) plane. We show in Fig. 3.2 the six contributions in the $\omega_t > 0$ semiplane, whose width will be related to the inverse of the parameter τ_p which determines the time duration of the pulse. We also show in Fig. 3.3a and 3.3b how different conventions to label the time-delays and the Fourier-transformed peaks are adopted in the literature, with consequently different outcomes for experiments and simulations.

We remark here that this sketchy derivation is valid for an instantaneous kernel but for general pulse spectrum. Nonetheless, one can obtain similar results for a

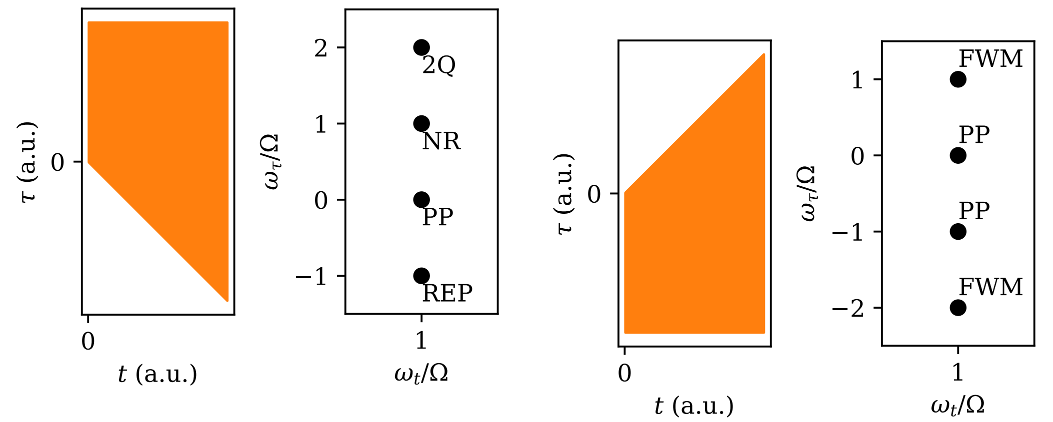

(a) Conventions used in Ref. [94, 72, 89]. Used names are 2Q (two-quantum), NR (non-rephasing), PP (pump-probe) and REP (rephasing or photon-echo).

(b) Conventions used in Ref. [92]. Used names are PP (pump-probe) and FWM (four-wave-mixing).

Figure 3.3. Comparison between various conventions adopted in the literature to label peaks and time-delays in a 2D-THz experiment. We report the region in time-domain where one consequently expects to observe non-linearly induced oscillations, i.e. when both pulses come before the detection (orange zone). Panel (a) correspond to the time-delay scheme shown in Fig. 3.1. Panel (b) shows the convention where one reverses the sign of τ with respect to panel (a). Processes are distinguished according to whether two opposite-sign photons are taken from the same pulse (PP) or from different pulses (FWM).

general form of the third-order response but considering strictly monochromatic pulses, i.e. $A(t) = \bar{A}\cos(\Omega t)$, and replacing the corresponding expression in Eq. 3.5 and Eq. 3.1. Since we find more convenient to work in Fourier space, we now abandon the time-domain representation and move to frequency representation. For identical field envelopes, indeed, the computation is simplified by noticing that the Fourier transform of $A_\tau(t)$ reads $A_\tau(\omega) = e^{-i\omega\tau}A(\omega)$, i.e. it contains a simple phase shift with respect to the Fourier transform of the pulse $A_0(t)$.

Let us then consider Eq. 3.1 in frequency domain

$$J^{(3)}(\omega_t) = \int d\omega_i\, K^{(3)}(\omega_1,\omega_2,\omega_3)A(\omega_1)A(\omega_2)A(\omega_3)\delta(\omega_t-\omega_1-\omega_2-\omega_3). \quad (3.8)$$

Since we define ω_i as the Fourier conjugate of t_i, the third order kernel entering the previous expression will explicitly depend on the incoming frequencies as[1]

$$K^{(3)}(\omega_1,\omega_2,\omega_3) = K^{(3)}(\omega_1+\omega_2+\omega_3,\omega_2+\omega_3,\omega_3). \quad (3.10)$$

[1] In order to account for intrinsic permutation symmetry with respect to the indices $m \in \{1,2,3\}$, one can explicitly introduce the symmetrized form of $K^{(3)}$,

$$K^{(3)}_{\mathcal{S}}(\omega_1,\omega_2,\omega_3) = \sum_{\pi\in\mathcal{S}} K^{(3)}\left(\omega_{\pi(1)}+\omega_{\pi(2)}+\omega_{\pi(3)},\omega_{\pi(2)}+\omega_{\pi(3)},\omega_{\pi(3)}\right), \quad (3.9)$$

where $\pi(m)$ is the action of the permutation π on the index $m \in \{1,2,3\}$, and $\mathcal{S}$ is the symmetric group over the set of time and frequency indices.

We anticipate that in a perturbative calculation, as the one we will show later, the combinations of frequencies appearing in the argument of $K^{(3)}$ are then also those running into the propagators connecting the interactions with the gauge field.

Let us now perform the Fourier transform of the 2D map written in Eq. 3.5, using Eq. 3.8. Replacing the appropriate spectra of the fields $A_0(\omega)$ and $A_\tau(\omega)$, we note that as in time domain the terms proportional to A_0^3 and A_τ^3 drop out and we have, as a function of ω_t and τ,

$$\begin{aligned} J^{(3)}_{2D}(\omega_t,\tau) = \int d\omega_i\, K^{(3)}(\omega_1,\omega_2,\omega_3)A(\omega_1)A(\omega_2)A(\omega_3)\delta(\omega_t-\omega_1-\omega_2-\omega_3)\times \\ \times\left(e^{-i\omega_1\tau}+e^{-i\omega_2\tau}+e^{-i\omega_3\tau}+e^{-i(\omega_1+\omega_2)\tau}+e^{-i(\omega_2+\omega_3)\tau}+e^{-i(\omega_2+\omega_3)\tau}\right). \end{aligned} \tag{3.11}$$

One can now identify, exactly as it happened in Eq. 3.7, two types of contributions in Eq. 3.11. The first three terms in the second line correspond to two interactions with field A_0 and one with field A_τ, that we will denote as $J^{(3)}_{00\tau}$. The other three terms correspond to two interactions with field A_τ and one with field A_0, that we will denote accordingly as $J^{(3)}_{0\tau\tau}$.

Let us focus on the first contribution, $J^{(3)}_{00\tau}(\omega_t,\omega_\tau)$. The Fourier transform $\tau\to\omega_\tau$ in Eq. 3.11 will produce a $\delta(\omega_i-\omega_\tau)$, that can be used to eliminate one integral over frequency and set one of the field frequencies as ω_τ. Since there is still the energy-conservation delta to exploit, we can use it to eliminate a further integration over an internal frequency, and we are left with only one last frequency integral to perform. We notice that this process is symmetric over the choice of the frequency ω_i, as all of them appear in Eq. 3.11, one can use the symmetrized form of the kernel $K^{(3)}_{\mathcal{S}}$ to write out

$$J^{(3)}_{00\tau}(\omega_t,\omega_\tau) = A(\omega_\tau)\int d\omega\, K^{(3)}_{\mathcal{S}}(\omega,\omega_\tau,\omega_t-\omega_\tau-\omega)A(\omega)A(\omega_t-\omega_\tau-\omega), \tag{3.12}$$

where we denoted as ω the last frequency over which we integrate, and $\omega_t-\omega_\tau-\omega$ is the one which is determined by using the energy-conservation delta.

A similar analysis can be carried out for the second contribution, $J^{(3)}_{0\tau\tau}$. In this case, one gets from the τ Fourier transform a $\delta(\omega_\tau-\omega_i-\omega_j)$, with $i\neq j$. But then the energy-conservation delta will equivalently read $\delta(\omega_t-\omega_\tau-\omega_k)$, where k is the only frequency index which is neither i nor j. We can then here saturate the ω_k-frequency integral by replacing the corresponding value with $\omega_t-\omega_\tau$. One of the remaining frequency integral can be saturated via the $\delta(\omega_\tau-\omega_i-\omega_j)$, and as before we are left with only one last integration. Invoking again the symmetry argument, one writes out

$$J^{(3)}_{0\tau\tau}(\omega_t,\omega_\tau) = A(\omega_t-\omega_\tau)\int d\omega\, K^{(3)}_{\mathcal{S}}(\omega,\omega_t-\omega_\tau,\omega_\tau-\omega)A(\omega)A(\omega_\tau-\omega). \tag{3.13}$$

We notice immediately that the two contributions can be transformed one into each other by means of the exchange $\omega_\tau\leftrightarrow\omega_t-\omega_\tau$, which is enforced thanks to the invariance under time translations of the system and the approximation of identical field envelopes.

We are now ready to show how the 2D map measured by two time-delayed copies of a monochromatic field looks like. One can replace $A(\omega) = \bar{A}\,(\delta(\omega-\Omega)+\delta(\omega+\Omega))$ in the previous Eq. 3.12, from which we get

$$\begin{aligned} J^{(3)}_{00\tau}(\omega_t>0,\omega_\tau) = \delta(\omega_t-\Omega)\,[2\delta(\omega_\tau-\Omega)+\delta(\omega_\tau+\Omega)]\,K^{(3)}_{\mathcal{S}}(\Omega,\Omega,-\Omega)\bar{A}^3 \\ +\,\delta(\omega_t-3\Omega)\delta(\omega_\tau-\Omega)K^{(3)}_{\mathcal{S}}(\Omega,\Omega,\Omega)\bar{A}^3, \end{aligned} \tag{3.14}$$

and the analogous result for $J^{(3)}_{0\tau\tau}$. The final 2D map in the $\omega_t>0$ semiplane contains then six spots, four of them aligned along the vertical direction of the first harmonic $\omega_t=\Omega$ ($\omega_\tau=-\Omega,0,\Omega,2\Omega$) and two of them aligned along the line $\omega_t=3\Omega$ ($\omega_\tau=\Omega,2\Omega$), see Fig. 3.2, which are exactly the ones presented above. We notice that in the monochromatic limit the frequency content along the ω_τ direction does not depend explicitly on the specific form of the third-order kernel, which only controls the relative weight between the first and third harmonic as one would get in the usual single-pulse setup. We finally show in Fig. 3.4 some experimental results from Kota Katsumi and N. Peter Armitage, where a narrowband pulse is used to measure the 2D-THz response of superconducting NbN and MgB_2. As one can see, there is a nice correspondence between the theoretical understanding presented above and the experimental features witnessed in this limit.

We now want to consider the opposite impulsive limit, i.e. $A(t)=\bar{A}\delta(t)$ so that $A(\omega)=\bar{A}$. In this situation the structure of the (ω_t,ω_τ) map is completely determined by the frequency structure of $K^{(3)}_{\mathcal{S}}$, which will keep track of the nonlinear dynamics of the system. In a perturbative framework, one can compute the $K^{(3)}_{\mathcal{S}}$ by using extensions of the linear-response theory, as presented e.g. in Ref. [116] in terms of exact-eigenstates representation. The result will in this view crucially depend on i) the single- or multi-photon nature of the light-matter vertices and ii) the structure of the matter propagators connecting them.

In order to substantiate what we have found so far, we now introduce a simple toy-model which allows us to obtain the form of the $K^{(3)}$ in a many-body system. Specifically, we refer to a direct bandgap semiconductor for a two-fold reason. First, it contains some analogies with the case of a superconductor: the associated bandstructure hosts the same singularities which are present in the BCS spectrum, although the particle-hole like character in the semiconducting bands is not mixed as it happens in the BCS theory. This is a crucial characteristic of the model which allows for optically-active transitions mediated by paramagnetic processes. Consequently, as a second point, we use this peculiarity to elaborate on analogies and differences between this many-body framework and the diffused two-level model [94, 80], where the light-matter interaction is represented as a single-photon, dipole-like interaction. To connect with experimental measurements, we will study how the signal evolves as a function of the spectral content of the incoming pulse $A(\omega)$, which interpolates between the monochromatic and impulsive limits described above.

3.3 Nonlinear response for a toy-model semiconductor

Let us consider a simple model for a one-dimensional semiconductor hosting a direct bandgap 2Δ. It can be obtained considering a linear chain with two atoms per unit

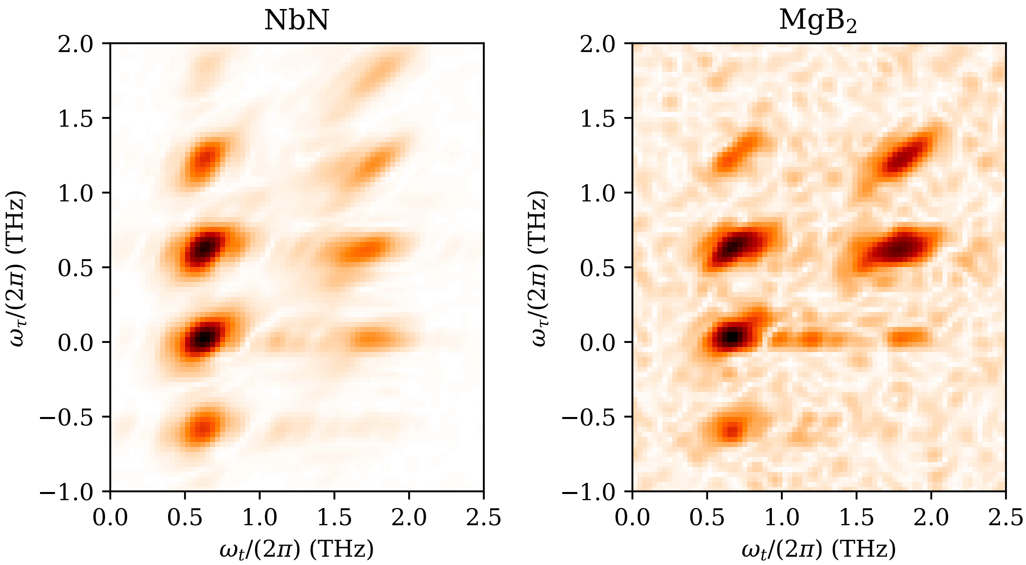

Figure 3.4. Experimental 2D-THz map of superconducting NbN (left panel) and MgB_2 (right panel) at low temperature, collected using a narrowband incoming field centered at $\Omega/(2\pi) \sim 0.6$ THz. Courtesy of Kota Katsumi and N. Peter Armitage.

cell A, B with nearest neighbor hopping t and alternating on-site potential Δ. The resulting tight-binding hamiltonian reads

$$H = -t\sum_n \left(c^\dagger_{nA}c_{nB} + c^\dagger_{nB}c_{n+1A} + \text{h.c.}\right) + \sum_n \Delta\left(c^\dagger_{nA}c_{nA} - c^\dagger_{nB}c_{nB}\right), \tag{3.15}$$

that can be written in reciprocal space as

$$H = \sum_{\mathbf{k}} \begin{pmatrix} c^\dagger_{\mathbf{k}A} & c^\dagger_{\mathbf{k}B}\end{pmatrix} \begin{pmatrix} \Delta & \epsilon_{\mathbf{k}} \\ \epsilon_{\mathbf{k}} & -\Delta \end{pmatrix} \begin{pmatrix} c_{\mathbf{k}A} \\ c_{\mathbf{k}B}\end{pmatrix}, \tag{3.16}$$

with $\epsilon_{\mathbf{k}} = -2t\cos(ka)$ and a the distance between atomic sites. In order to minimally account also for the dependence on the polarization of the incoming pulse with respect to the cristallographic directions, we need to extend the model to two spatial dimensions. We consider then a square lattice with chessboard-like disposition of the atoms A and B. The 1D dispersion is easily generalized to $\epsilon_{\mathbf{k}} = -2t\cos(k_x a) - 2t\cos(k_y a)$. The corresponding quantum action reads, setting $k = (i\omega_n, \mathbf{k})$ with $i\omega_n$ fermionic Matsubara frequency,

$$S = \sum_k \begin{pmatrix} c^\dagger_{kA} & c^\dagger_{kB}\end{pmatrix} \begin{pmatrix} i\omega_n - \Delta & -\epsilon_{\mathbf{k}} \\ -\epsilon_{\mathbf{k}} & i\omega_n + \Delta \end{pmatrix} \begin{pmatrix} c_{kA} \\ c_{kB}\end{pmatrix}. \tag{3.17}$$

The corresponding Green's function, introducting the Pauli matrices σ_i, is then

$$\begin{aligned} G_0(k) = \frac{i\omega_n\sigma_0 + \Delta\sigma_3 + \epsilon_{\mathbf{k}}\sigma_1}{(i\omega_n)^2 - E^2_{\mathbf{k}}} &\equiv \begin{pmatrix} u_{\mathbf{k}} & v_{\mathbf{k}} \\ -v_{\mathbf{k}} & u_{\mathbf{k}} \end{pmatrix} \begin{pmatrix} \frac{1}{i\omega_n - E_{\mathbf{k}}} & 0 \\ 0 & \frac{1}{i\omega_n + E_{\mathbf{k}}} \end{pmatrix} \begin{pmatrix} u_{\mathbf{k}} & -v_{\mathbf{k}} \\ v_{\mathbf{k}} & u_{\mathbf{k}} \end{pmatrix} \\ &\equiv \mathcal{U}^\dagger_{\mathbf{k}} \tilde{G}_0(k) \mathcal{U}_{\mathbf{k}}, \end{aligned} \tag{3.18}$$

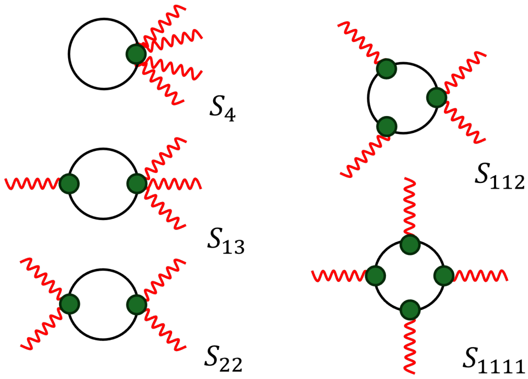

Figure 3.5. The set of diagrams presented in Eq. 3.19. Red wavy lines denote the gauge field, green bullets denote the σ_1 vertex connecting the electronic propagators in Nambu space, represented by solid black lines.

whose poles are the two (valence and conduction) bands $\pm E_{\mathbf{k}} = \pm\sqrt{\epsilon_{\mathbf{k}}^2 + \Delta^2}$, which host a direct bandgap 2Δ. Here we set for simplicity the chemical potential $\mu = 0$ and the usual unitary rotation matrix $\mathcal{U}_{\mathbf{k}}$ has been introduced, such that $u_{\mathbf{k}}^2 - v_{\mathbf{k}}^2 = \Delta/E_{\mathbf{k}}$ and $2u_{\mathbf{k}}v_{\mathbf{k}} = \epsilon_{\mathbf{k}}/E_{\mathbf{k}}$.

The coupling to a uniform gauge field is introduced as usual via the Peierls substitution, namely $\epsilon_{\mathbf{k}} \to \epsilon_{\mathbf{k}-e/c\mathbf{A}(t)}$, which upon expansion up to the fourth order in $\mathbf{A}$ provides the set of couplings between gauge field and electrons. One can then introduce the self-energy

$$\begin{aligned}\Sigma(i\Omega,\mathbf{k}) = &-\frac{e}{c}\sum_{\alpha_1}\frac{\partial\epsilon_{\mathbf{k}}}{\partial k_{\alpha_1}}A_{\alpha_1}(i\Omega)\sigma_1 + \frac{1}{2}\left(\frac{e}{c}\right)^2\sum_{\alpha_1,\alpha_2}\frac{\partial^2\epsilon_{\mathbf{k}}}{\partial k_{\alpha_1}\partial k_{\alpha_2}}A^2_{\alpha_1\alpha_2}(i\Omega)\sigma_1\\ &-\frac{1}{6}\left(\frac{e}{c}\right)^3\sum_{\alpha_1,\alpha_2,\alpha_3}\frac{\partial^3\epsilon_{\mathbf{k}}}{\partial k_{\alpha_1}\partial k_{\alpha_2}\partial k_{\alpha_3}}A^3_{\alpha_1\alpha_2\alpha_3}(i\Omega)\sigma_1\\ &+\frac{1}{24}\left(\frac{e}{c}\right)^4\sum_{\alpha_1,\alpha_2,\alpha_3,\alpha_4}\frac{\partial^4\epsilon_{\mathbf{k}}}{\partial k_{\alpha_1}\partial k_{\alpha_2}\partial k_{\alpha_3}\partial k_{\alpha_4}}A^4_{\alpha_1\alpha_2\alpha_3\alpha_4}(i\Omega)\sigma_1,\end{aligned} \tag{3.19}$$

where $A^n_{\alpha_1\ldots\alpha_n}(i\Omega)$ denotes the Fourier transform of $A_{\alpha_1}(t)\cdots A_{\alpha_n}(t)$ in imaginary time, with $\alpha_i = x, y$ cartesian components of the gauge field. Let us denote the previous four contributions to the self-energy as $\Sigma_1, \ldots, \Sigma_4$, according to the corresponding power of the gauge field. Then, after integration of the fermionic degrees of freedom one can collect several contributions to the fourth order $S[A^4]$. These can be classified according to the frequency structure of the corresponding Feynman diagram, see Fig. 3.5. There is the instantaneous contribution

$$S_4 = \sum_k \mathrm{Tr}\left[G_0(i\omega_n,\mathbf{k})\Sigma_4(0,\mathbf{k})\right], \tag{3.20}$$

then the Kubo-like responses, S_{13} and S_{22} (fully-diamagnetic), which can be written ($ij = 13, 22$) as

$$S_{ij} = \sum_k\sum_{i\Omega}\mathrm{Tr}\left[G_0(i\omega_n,\mathbf{k})\Sigma_i(i\Omega,\mathbf{k})G_0(i\omega_n+i\Omega,\mathbf{k})\Sigma_j(-i\Omega,\mathbf{k})\right], \tag{3.21}$$

the three-point response S_{112} ($i\Omega_{12} = i\Omega_1 + i\Omega_2$)

$$S_{112} = \sum_k \sum_{\{i\Omega_i\}} \mathrm{Tr}\left[\; G_0(i\omega_n, \mathbf{k})\Sigma_1(i\Omega_1, \mathbf{k})G_0(i\omega_n + i\Omega_1, \mathbf{k})\Sigma_1(i\Omega_2, \mathbf{k}) \times \right. \\ \left. \times\; G_0(i\omega_n + i\Omega_{12}, \mathbf{k})\Sigma_2(-i\Omega_{12}, \mathbf{k})\right], \tag{3.22}$$

and finally the four-point (fully-paramagnetic) response which is written ($i\Omega_{123} = i\Omega_1 + i\Omega_2 + i\Omega_3$)

$$S_{1111} = \sum_k \sum_{\{i\Omega_i\}} \mathrm{Tr}\left[\; G_0(i\omega_n, \mathbf{k})\Sigma_1(i\Omega_1, \mathbf{k})G_0(i\omega_n + i\Omega_1, \mathbf{k})\Sigma_1(i\Omega_2, \mathbf{k}) \times \right. \\ \left. \times\; G_0(i\omega_n + i\Omega_{12}, \mathbf{k})\Sigma_1(i\Omega_3, \mathbf{k})G_0(i\omega_n + i\Omega_{123}, \mathbf{k})\Sigma_1(-i\Omega_{123})\right]. \tag{3.23}$$

We notice that since every Σ_i contains a σ_1 Pauli matrix, the products in the trace actually involve multiplications of a certain number of (diagonal) $\tilde{G}_0$ matrices with $\mathcal{U}_\mathbf{k}\sigma_1\mathcal{U}_\mathbf{k}^\dagger = \Delta/E_\mathbf{k}\sigma_1 - \epsilon_\mathbf{k}/E_\mathbf{k}\sigma_3$. We also remark that, differently from the case of the superconductor where there is alternation between σ_0 and σ_3 for odd and even powers of the gauge field, in the semiconductor only σ_1 type of coupling is present. This difference is crucial in allowing optically-active transitions through paramagnetic-like couplings in the semiconductor, thanks to the off diagonal mixing between the poles at $+E_\mathbf{k}$ and $-E_\mathbf{k}$ mediated by σ_1.

In the following we will analyze in particular the contributions to the nonlinear kernel stemming from the two terms in the effective action S_{22}, (fully-diamagnetic), and S_{1111}, (fully-paramagnetic), in order to capture the differences in the 2D map due to the nature of the light-matter interaction in the two cases. We choose to analyze the fully-diamagnetic term because, as we will see, it shares its form with the corresponding process in the superconducting case[20]. Moreover, the frequency structure that we foresee in the 2D map can be extended to other cases where the intaraction between light and matter can be mapped in an effective two-photon process, as we did in the two-plasmon case in Chapter 2 or in the Raman-like excitation of a phonon [90, 10]. We also explicitly compute the fully-paramagnetic term since, as we anticipated before, it has a direct counterpart in the two-level hamiltonian, where only single-photon dipole-like transistions are allowed. It is thus possible to make a direct comparison between the many-body situation where a continuum, dispersive set of excited states is present and the discrete, non-dispersive case of the two-level system.

Eventually, since numerical simulations [123] show that in disordered superconductors the fully-paramagnetic process is the one dominating the BCS part of the nonlinear response, we can also imagine that the result obtained in the semiconducting system can be somehow extended to nonlinear spetroscopies on superconductors, given also the similarity between the BCS mean-field hamiltonian and the semiconducting system. The key issue is that in a clean superconductor, since the paramagnetic vertex is represented by a σ_0 matrix, one cannot mix poles at $E_\mathbf{k}$ and $-E_\mathbf{k}$, which would allow for optical transitions. Consequently, the corresponding S_{1111} is zero. Indeed, the role of disorder is usually described[100] as effectively relaxing momentum conservation during an optical transition, mixing responses at different wavevectors $\mathbf{k}$ and $\mathbf{k}'$. Indeed, computing the product $\mathcal{U}_{\mathbf{k}}\mathcal{U}^\dagger_{\mathbf{k}'}$, one gets

$$\mathcal{U}_{\mathbf{k}}\mathcal{U}^\dagger_{\mathbf{k}'} = \sigma_0(u_{\mathbf{k}}u_{\mathbf{k}'} + v_{\mathbf{k}}v_{\mathbf{k}'}) + i\sigma_2(u_{\mathbf{k}}v_{\mathbf{k}'} - v_{\mathbf{k}}u_{\mathbf{k}'}), \tag{3.24}$$

where $u_{\mathbf{k}}$ and $v_{\mathbf{k}}$ are related to the usual coherence factors. From this expression we see that one can then mix the two poles as soon as the there is a momentum mismatch between two G_0 propagators, thanks to the off-diagonal structure of $i\sigma_2$. Intuitively, then, one can then make a connection between the processes mediated by σ_3 and σ_1 in the clean semiconductor and those mediated by σ_0 and σ_2 in the dirty superconductor, respectively.

3.3.1 Diamagnetic term

Let us analyze now the fully-diamagnetic contribution coming from S_{22}. One can define the diamagnetic contribution to the nonlinear current by

$$J^{(3),\text{dia}}_\alpha(i\Omega) = -\frac{\partial S_{22}[A^4]}{\partial A_\alpha(-i\Omega)} \equiv \sum_{i\Omega'} K^{(3),\text{dia}}_{\alpha\beta\gamma\delta}(i\Omega')A_\beta(i\Omega - i\Omega')A^2_{\gamma\delta}(i\Omega'), \tag{3.25}$$

where we defined the $A^2_{\gamma\delta}(i\Omega)$ the transform of $A_\gamma(t)A_\delta(t)$ in imaginary time. By means of a change of variable, the previous expression can also be rewritten in the completely symmetric form

$$J^{(3),\text{dia}}_\alpha(i\Omega) = \sum_{i\Omega_i} K^{(3),\text{dia}}_{\alpha\beta\gamma\delta}(i\Omega_{ij})A_\beta(i\Omega_1)A_\gamma(i\Omega_2)A_\delta(i\Omega_3)\delta(i\Omega - i\Omega_{123}), \tag{3.26}$$

where $i\Omega_{ij}$ is the sum of two incoming frequencies. From Eq. 3.21 one can obtain

$$\begin{aligned} K^{(3),\text{dia}}_{\alpha\beta\gamma\delta}(i\Omega) = \sum_{\mathbf{k},i\omega_n} &\frac{\partial^2\epsilon_{\mathbf{k}}}{\partial k_\alpha \partial k_\beta}\frac{\partial^2\epsilon_{\mathbf{k}}}{\partial k_\gamma \partial k_\delta}\times \\ &\times \mathrm{Tr}\left[\begin{pmatrix} \frac{1}{i\omega_n - E_{\mathbf{k}}} & 0 \\ 0 & \frac{1}{i\omega_n + E_{\mathbf{k}}}\end{pmatrix}\Lambda^1_{\mathbf{k}\mathbf{k}}\begin{pmatrix} \frac{1}{i\omega_n + i\Omega - E_{\mathbf{k}}} & 0 \\ 0 & \frac{1}{i\omega_n + i\Omega + E_{\mathbf{k}}}\end{pmatrix}\Lambda^1_{\mathbf{k}\mathbf{k}}\right], \end{aligned} \tag{3.27}$$

where we defined $\Lambda^1_{\mathbf{k}\mathbf{k}} = \mathcal{U}_{\mathbf{k}}\sigma_1\mathcal{U}^\dagger_{\mathbf{k}}$. As we reported before, in Nambu space the matrix $\Lambda^1_{\mathbf{k}\mathbf{k}}$ is a linear combination of σ_3 (diagonal) or σ_1 (off-diagonal). Since the matrix $\tilde{G}_0$ is diagonal as well, one immediately finds out that the only contributions that survive in the trace are obtained from the product of the two pieces containing σ_3 or the two pieces containing σ_1, namely

$$\begin{aligned} &\mathrm{Tr}\left[\begin{pmatrix} \frac{1}{i\omega_n - E_{\mathbf{k}}} & 0 \\ 0 & \frac{1}{i\omega_n + E_{\mathbf{k}}}\end{pmatrix}\Lambda^1_{\mathbf{k}\mathbf{k}}\begin{pmatrix} \frac{1}{i\omega_n + i\Omega - E_{\mathbf{k}}} & 0 \\ 0 & \frac{1}{i\omega_n + i\Omega + E_{\mathbf{k}}}\end{pmatrix}\Lambda^1_{\mathbf{k}\mathbf{k}}\right] = \\ &= \frac{\epsilon^2_{\mathbf{k}}}{E^2_{\mathbf{k}}}\left(\frac{1}{i\omega_n - E_{\mathbf{k}}}\frac{1}{i\omega_n + i\Omega - E_{\mathbf{k}}} + \frac{1}{i\omega_n + E_{\mathbf{k}}}\frac{1}{i\omega_n + i\Omega + E_{\mathbf{k}}}\right) \\ &+ \frac{\Delta^2}{E^2_{\mathbf{k}}}\left(\frac{1}{i\omega_n + E_{\mathbf{k}}}\frac{1}{i\omega_n + i\Omega - E_{\mathbf{k}}} + \frac{1}{i\omega_n - E_{\mathbf{k}}}\frac{1}{i\omega_n + i\Omega + E_{\mathbf{k}}}\right). \end{aligned} \tag{3.28}$$

The first term in the last sum, that comes from the product $\tilde{G}_0\sigma_3\tilde{G}_0\sigma_3$, expresses scattering of electrons and holes belonging to the same band, as can be seen from the same sign of $E_{\mathbf{k}}$ in the two propagators, thus it will represent an intraband process. The second term instead, stemming from the $\tilde{G}_0\sigma_1\tilde{G}_0\sigma_1$ contribution, represents a scattering process between the valence and conduction band, since it connects propagators having opposite sign of $E_{\mathbf{k}}$, standing for an interband process. Evaluating then the Matsubara sum in Eq. 3.27, one sees that the intraband contribution vanishes, so that one is left with

$$K^{(3),\mathrm{dia}}_{\alpha\beta\gamma\delta}(i\Omega) = \sum_{\mathbf{k}} \frac{\partial^2\epsilon_{\mathbf{k}}}{\partial k_\alpha \partial k_\beta}\frac{\partial^2\epsilon_{\mathbf{k}}}{\partial k_\gamma \partial k_\delta} \tanh\left(\beta E_{\mathbf{k}}/2\right)\frac{\Delta^2}{E^2_{\mathbf{k}}}\left(\frac{1}{i\Omega - 2E_{\mathbf{k}}} - \frac{1}{i\Omega + 2E_{\mathbf{k}}}\right). \tag{3.29}$$

We can recognize in this expression the exact counterpart of the quasiparticle contribution to the third-order response in a clean superconductor [20]. To capture the effect of the continuum dispersion, we introduce the density of states associated with the diamagnetic vertex by

$$\tilde{\rho}^{\mathrm{dia}}_{\alpha\beta\gamma\delta}(\epsilon) \equiv \sum_{\mathbf{k}} \delta(\epsilon - \epsilon_{\mathbf{k}})\frac{\partial^2\epsilon_{\mathbf{k}}}{\partial k_\alpha \partial k_\beta}\frac{\partial^2\epsilon_{\mathbf{k}}}{\partial k_\gamma \partial k_\delta}, \tag{3.30}$$

so that one can rewrite,

$$K^{(3),\mathrm{dia}}_{\alpha\beta\gamma\delta}(i\Omega) = \int d\epsilon\, \tilde{\rho}^{\mathrm{dia}}_{\alpha\beta\gamma\delta}(\epsilon) \tanh\left(\beta\sqrt{\epsilon^2+\Delta^2}/2\right)\frac{\Delta^2}{\epsilon^2+\Delta^2}K^{\mathrm{dia}}\left(\sqrt{\epsilon^2+\Delta^2}, i\Omega\right). \tag{3.31}$$

Here we isolated the frequency depenent part of the response,

$$K^{\mathrm{dia}}(E, i\Omega) = \frac{1}{i\Omega - 2E} - \frac{1}{i\Omega + 2E}, \tag{3.32}$$

and we defined the function $\tilde{\rho}^{\mathrm{dia}}_{\alpha\beta\gamma\delta}$ which will encode the information about the density of states of the dispersion $\epsilon_{\mathbf{k}}$ and the tensorial structure of the response due to the two diamagnetic insertions. We consider here the case of a two-dimensional square lattice and compute explicitly the isotropic A_{1g} component of the response. For the considered symmetry it is obtained by

$$K^{(3),\mathrm{dia}}_{A_{1g}} = K^{(3),\mathrm{dia}}_{xxxx} + K^{(3),\mathrm{dia}}_{xxyy}, \tag{3.33}$$

from where it is possible to compute the associated $\tilde{\rho}^{\mathrm{dia}}_{A_{1g}}$. One can express the result in terms of the elliptic integral K, defining $x = \epsilon/(4t)$,

$$\tilde{\rho}^{\mathrm{dia}}_{A_{1g}}(x) = x^2 K\left(\sqrt{1-x^2}\right)\theta\left(1-|x|\right). \tag{3.34}$$

3.3.2 Paramagnetic term

Let us now analyze the fully-paramagnetic term, which is derived from S_{1111} as

$$\begin{aligned} J^{(3),\mathrm{para}}_{\alpha}(i\Omega) &= -\frac{\partial S_{1111}[A^4]}{\partial A_\alpha(-i\Omega)} \\ &\equiv \sum_{i\Omega_i} K^{(3),\mathrm{para}}_{\alpha\beta\gamma\delta}(i\Omega_1, i\Omega_2, i\Omega_3)A_\beta(i\Omega_1)A_\gamma(i\Omega_2)A_\delta(i\Omega_3)\delta(i\Omega - i\Omega_{123}). \end{aligned} \tag{3.35}$$

It reads

$$K^{(3),\text{para}}_{\alpha\beta\gamma\delta}(i\Omega_1, i\Omega_2, i\Omega_3) = \sum_{\mathbf{k}, i\omega_n} \frac{\partial\epsilon_\mathbf{k}}{\partial k_\alpha}\frac{\partial\epsilon_\mathbf{k}}{\partial k_\beta}\frac{\partial\epsilon_\mathbf{k}}{\partial k_\gamma}\frac{\partial\epsilon_\mathbf{k}}{\partial k_\delta}\,\mathrm{Tr}[\dots], \tag{3.36}$$

where

$$\begin{aligned}\mathrm{Tr}[\dots] = \mathrm{Tr}\Big[\, & \tilde{G}_0(\mathbf{k}, i\omega_n)\Lambda^1_{\mathbf{kk}}\tilde{G}_0(\mathbf{k}, i\omega_n + i\Omega_1)\Lambda^1_{\mathbf{kk}}\times \\ & \times \tilde{G}_0(\mathbf{k}, i\omega_n + i\Omega_{12})\Lambda^1_{\mathbf{kk}}\tilde{G}_0(\mathbf{k}, i\omega_n + i\Omega_{123})\Lambda^1_{\mathbf{kk}}\Big]\,.\end{aligned} \tag{3.37}$$

In this case one realizes that the trace will give non-zero results whenever one selects in $\Lambda^1_{\mathbf{kk}}$ four σ_3, two σ_3 and two σ_1, or four σ_1 contributions. These cases will correspond to completely intraband, mixed intraband and interband, or fully interband interactions, respectively. In order to keep track of the possible combinations and compute systematically the result, we rewrite the paramagnetic kernel as

$$K^{(3),\text{para}}_{\alpha\beta\gamma\delta}(i\Omega_1, i\Omega_2, i\Omega_3) = \sum_{\{\mu_i,\nu_i\}}\sum_{\mathbf{k}} \frac{\partial\epsilon_\mathbf{k}}{\partial k_\alpha}\frac{\partial\epsilon_\mathbf{k}}{\partial k_\beta}\frac{\partial\epsilon_\mathbf{k}}{\partial k_\gamma}\frac{\partial\epsilon_\mathbf{k}}{\partial k_\delta} f_{\{\nu_i\}}(\mathbf{k}) M_{\{\mu_i,\nu_i\}} G^{(4)}_{\{\mu_i\}}(\mathbf{k}, i\Omega_i). \tag{3.38}$$

Here $\{\mu_i\} = (\mu_0, \mu_1, \mu_2, \mu_3)$, $\mu_i = +1, -1$, denotes the valence or conduction band of the semiconductor, respectively, which is encoded in the projector structure $D_{\mu_i} = (\sigma_0 + \mu_i\sigma_3)/2$ in Nambu space; analogously $\{\nu_i\} = (\nu_0, \nu_1, \nu_2, \nu_3)$, $\nu_i = 1, 3$ encodes the possible interband or intraband transitions mediated by σ_1 or σ_3, respectively. We singled out the result of the trace in Nambu space by introducing $M_{\{\mu_i,\nu_i\}} = \mathrm{Tr}\left[D_{\mu_0}\sigma_{\nu_0}D_{\mu_1}\sigma_{\nu_1}D_{\mu_2}\sigma_{\nu_2}D_{\mu_3}\sigma_{\nu_3}\right]$, which will determine which possible combinations among the various $\{\mu_i, \nu_i\}$ indices give non-zero result. The function

$$f_{\{\nu_i\}}(\mathbf{k}) = \left(-\frac{\epsilon_\mathbf{k}}{E_\mathbf{k}}\right)^{\sum_i \delta_{\nu_i 3}} \left(\frac{\Delta}{E_\mathbf{k}}\right)^{\sum_i \delta_{\nu_i 1}} \tag{3.39}$$

keeps track of the number of σ_1 or σ_3 matrices for each choice of $\{\nu_i\}$. Finally, we also introduced the result of the Matsubara sum over $i\omega_n$ by means of

$$\begin{aligned}G^{(4)}_{\{\mu_i\}}(\mathbf{k}, i\Omega_1, i\Omega_2, i\Omega_3) = & \sum_{i\omega_n}\frac{1}{i\omega_n - \mu_0 E_\mathbf{k}}\frac{1}{i\omega_n + i\Omega_1 - \mu_1 E_\mathbf{k}}\times \\ & \times\frac{1}{i\omega_n + i\Omega_{12} - \mu_2 E_\mathbf{k}}\frac{1}{i\omega_n + i\Omega_{123} - \mu_3 E_\mathbf{k}},\end{aligned} \tag{3.40}$$

which can be carried out explicitly. By computing $M_{\{\mu_i,\nu_i\}}$, one is left with three classes of processes listed in Table 3.1 and anticipated before. The first one comes from fully intraband scattering processes mediated by four σ_3 interactions and is cancelled when computing the corresponding Matsubara sum in $G^{(4)}$, as it happened for the diamagnetic process. The second one comes from the possible terms involving two σ_3 and two σ_1, which allow for mixed interband and intraband scattering, the various processes differing in the ordering of the single scattering events. The third one is equivalent to purely interband transitions between the valence and conduction band of the semiconductor, mediated by four σ_1 vertices. After lengthy algebra, one is able to recollect the various terms in a fully symmetric fashion under the exchange of $i\Omega_i$,

Type	$\{\mu_i\}$	$\{\nu_i\}$	Tr
Intra	(+1,+1,+1,+1)	(3,3,3,3)	1
Mix	(+1,+1,+1,-1)	(3,3,1,1)	1
Mix	(+1,+1,-1,+1)	(3,1,1,3)	1
Mix	(+1,-1,+1,+1)	(1,1,3,3)	1
Mix	(+1,-1,-1,-1)	(1,3,3,1)	1
Mix	(+1,+1,-1,-1)	(3,1,3,1)	-1
Mix	(+1,-1,-1,+1)	(1,3,1,3)	-1
Inter	(+1,-1,+1,-1)	(1,1,1,1)	1

Table 3.1. Table summarizing the various contributions to the fully paramagnetic third-order response, classified according to the nature (intraband, mixed, interband) presented in the text. We explicitly report the combinations of the poles $\{\mu_i\}$ of the Green's function, valence $(+1)$ or conduction (-1) band; the combinations of the vertices for the light-matter coupling $\{\nu_i\}$, intraband (3) or interband (1); and the corresponding value of the trace entering Eq. 3.38. The same contributions are present with their particle-hole symmetric copy $E_{\mathbf{k}} \to -E_{\mathbf{k}}$, i.e. sending $\mu_i \to -\mu_i$, while ν_i and the sign of the trace remain the same.

$$\begin{aligned} K^{(3),\mathrm{para}}_{\alpha\beta\gamma\delta}(i\Omega_1, i\Omega_2, i\Omega_3) = \sum_{\mathbf{k}} \frac{\partial\epsilon_{\mathbf{k}}}{\partial k_\alpha}\frac{\partial\epsilon_{\mathbf{k}}}{\partial k_\beta}\frac{\partial\epsilon_{\mathbf{k}}}{\partial k_\gamma}\frac{\partial\epsilon_{\mathbf{k}}}{\partial k_\delta} \tanh\left(\beta E_{\mathbf{k}}/2\right) \times \\ \times \left[\frac{\Delta^4}{E^4_{\mathbf{k}}} K^{\mathrm{inter}}(E_{\mathbf{k}}, i\Omega_i) + \frac{\Delta^2\epsilon^2_{\mathbf{k}}}{E^4_{\mathbf{k}}} K^{\mathrm{mix}}(E_{\mathbf{k}}, i\Omega_i)\right]. \end{aligned} \tag{3.41}$$

Here we defined the interband contribution

$$K^{\mathrm{inter}}(E_{\mathbf{k}}, i\Omega_i) = \left(\frac{1}{i\Omega_{123} - 2E_{\mathbf{k}}} - \frac{1}{i\Omega_{123} + 2E_{\mathbf{k}}}\right)\sum_{i\neq j}\frac{1}{i\Omega_i - 2E_{\mathbf{k}}}\frac{1}{i\Omega_j + 2E_{\mathbf{k}}}, \tag{3.42}$$

and the mixed one

$$\begin{aligned} K^{\mathrm{mix}}(E_{\mathbf{k}}, i\Omega_i) = \left(\frac{1}{i\Omega_{123} - 2E_{\mathbf{k}}} - \frac{1}{i\Omega_{123}}\right)\sum_i \frac{1}{i\Omega_i - 2E_{\mathbf{k}}}\sum_{j\neq i}\frac{1}{i\Omega_{ij} - 2E_{\mathbf{k}}} \\ - \left(\frac{1}{i\Omega_{123} + 2E_{\mathbf{k}}} - \frac{1}{i\Omega_{123}}\right)\sum_i \frac{1}{i\Omega_i + 2E_{\mathbf{k}}}\sum_{j\neq i}\frac{1}{i\Omega_{ij} + 2E_{\mathbf{k}}}. \end{aligned} \tag{3.43}$$

Also for this process we introduce a function which keeps track of the continuum of excited states which is present in our system, defining in a similar fashion to the diamagnetic case

$$\tilde{\rho}^{\mathrm{para}}_{\alpha\beta\gamma\delta}(\epsilon) \equiv \sum_{\mathbf{k}} \delta(\epsilon - \epsilon_{\mathbf{k}})\frac{\partial\epsilon_{\mathbf{k}}}{\partial k_\alpha}\frac{\partial\epsilon_{\mathbf{k}}}{\partial k_\beta}\frac{\partial\epsilon_{\mathbf{k}}}{\partial k_\gamma}\frac{\partial\epsilon_{\mathbf{k}}}{\partial k_\delta}, \tag{3.44}$$

through which we rewrite

$$\begin{aligned} K^{(3),\mathrm{para}}_{\alpha\beta\gamma\delta}(i\Omega_1, i\Omega_2, i\Omega_3) = \int d\epsilon\, \tilde{\rho}^{\mathrm{para}}_{\alpha\beta\gamma\delta}(\epsilon) \tanh\left(\beta\sqrt{\epsilon^2+\Delta^2}/2\right)\times \\ \times\left[\frac{\Delta^4}{(\epsilon^2+\Delta^2)^2} K^{\mathrm{inter}}\left(\sqrt{\epsilon^2+\Delta^2}, i\Omega_i\right)\right. \\ \left. + \frac{\Delta^2\epsilon^2}{(\epsilon^2+\Delta^2)^2} K^{\mathrm{mix}}\left(\sqrt{\epsilon^2+\Delta^2}, i\Omega_i\right)\right]. \end{aligned} \tag{3.45}$$

We consider also here the case of a two-dimensional square lattice and compute explicitly the isotropic A_{1g} component of the response. The expression is as before

$$K^{(3),\mathrm{para}}_{A_{1g}} = K^{(3),\mathrm{para}}_{xxxx} + K^{(3),\mathrm{para}}_{xxyy}, \tag{3.46}$$

from where it we compute the associated $\tilde{\rho}^{\mathrm{para}}_{A_{1g}}$. We omit the details and we give the result in terms of the elliptic integrals E and K, defining $x = \epsilon/(4t)$,

$$\tilde{\rho}^{\mathrm{para}}_{A_{1g}}(x) = \left[(1-5x^2)E\left(\sqrt{1-x^2}\right) + x^2(1+3x^2)K\left(\sqrt{1-x^2}\right)\right]\theta\left(1-|x|\right). \tag{3.47}$$

3.4 Analytical continuation and 2D map

In the previous subsection we computed the nonlinear third order kernel $K^{(3)}$ in Matsubara frequency representation. Before computing the 2D map resulting from such a response function we need to perform the analytical continuation to real frequencies. In our simple non-interacting model, this can be obtained [36, 116] by sending $i\Omega_i \to \omega_i + i\eta$, with $\eta > 0$. With this choice one can assure that the causality properties of the response function in real time, i.e. the analiticity conditions in frequency space, are those presented at the beginning in Eq. 3.1. In the following expressions we assume that η, the can be thought of as the rate of adiabatic switching, is the same for all the three incoming fields, and we just denote $\eta_3 = 3\eta$, $\eta_2 = 2\eta$ and $\eta_1 = \eta$. Using then the prescription in Eq. 3.11 with the analitically continued $K^{(3)}$ it is possible to compute the 2D map for any spectral content of the incoming fields.

We start by remembering Eq. 3.12 and 3.13, that are used to obtain the 2D map as

$$\begin{aligned} J^{(3)}_{2D}(\omega_t, \omega_\tau) = A(\omega_\tau)\int d\omega\, K^{(3)}_{\mathcal{S}}(\omega, \omega_\tau, \omega_t-\omega_\tau-\omega)A(\omega)A(\omega_t-\omega_\tau-\omega) \\ + A(\omega_t-\omega_\tau)\int d\omega\, K^{(3)}_{\mathcal{S}}(\omega, \omega_t-\omega_\tau, \omega_\tau-\omega)A(\omega)A(\omega_\tau-\omega). \end{aligned} \tag{3.48}$$

Examining Eq. 3.31 for the diamagnetic contribution and Eq. 3.45 for the paramagnetic one, we notice that one can always rewrite, in a sketchy expression,

$$\begin{aligned} J^{(3)}_{2D}(\omega_t, \omega_\tau) &\sim \int dE\, w(E)\tilde{J}^{(3)}_{2D}(E, \omega_t, \omega_\tau) \\ &\sim \int dE\, w(E)\int d\omega\, K^{(3)}_{\mathcal{S}}(E, \omega, \omega_t, \omega_\tau)A^3(\omega, \omega_t, \omega_\tau). \end{aligned} \tag{3.49}$$

where $w(E)$ is the appropriate weighting function which depends solely on the energy variable spanning the continuum of possible excitations; $K^{(3)}(E,\omega,\omega_t,\omega_\tau)$ is obtained by isolating the propagators at the frequencies read out by Eq. 3.48, namely K^{inter} and K^{mix} for the paramagnetic process, K^{dia} for the diamagnetic one; $A^3(\omega,\omega_t,\omega_\tau)$ is a shorthand for the product of the three fields read at the appropriate frequencies. In order to simulate the 2D map in a convenient way, the crucial point is to first integrate over the internal frequency ω, and only later to integrate over the energy E.

3.4.1 Diamagnetic term

Let us now compute the result for the diamagnetic process, which will be also the most relevant one for the clean superconductor. In this case, the calculation is simplified due to the dependence of the nonlinear kernel only on the sum of two incoming frequencies of the field, i.e. from Eq. 3.26 one has $K^{\text{dia}}(\omega_{ij}+i\eta_2)$ as appropriate for two-photon vertices. For the $\tilde{J}^{(3)}_{00\tau}$ part of the 2D map, one needs then to write out all the possible combinations

$$K^{\text{dia}}_{\mathcal{S}}(E,\omega,\omega_\tau,\omega_t-\omega_\tau-\omega) = K^{\text{dia}}(E,\omega+\omega_\tau)+K^{\text{dia}}(E,\omega_t-\omega)+K^{\text{dia}}(E,\omega_t-\omega_\tau). \tag{3.50}$$

More explicitly, considering the structure of Eq. 3.31 one finds

$$\begin{aligned}\tilde{J}^{(3)}_{00\tau}(E,\omega_t,\omega_\tau) &= 2A(\omega_\tau)\left[F^{\text{dia}}_{00\tau}(-2E)-F^{\text{dia}}_{00\tau}(2E)\right]\\ &\quad + A(\omega_\tau)A^2(\omega_t-\omega_\tau)\left(\frac{1}{\omega_t-\omega_\tau+i\eta_2-2E}-\frac{1}{\omega_t-\omega_\tau+i\eta_2+2E}\right),\end{aligned} \tag{3.51}$$

where the function $F^{\text{dia}}_{00\tau}$ reads

$$F^{\text{dia}}_{00\tau}(2E) = \int d\omega\,\frac{A(\omega)A(\omega_t-\omega_\tau-\omega)}{\omega_\tau+\omega+i\eta_2+2E}. \tag{3.52}$$

If the spectrum of the incoming pulse is gaussian i.e. $A(t)=\bar{A}e^{-t^2/(2\tau_p^2)}\cos(\Omega t)$, the function $F^{\text{dia}}_{00\tau}$ can be reduced to a combination of Faddeeva functions, or Voigt functions, which can be straightforwardly evaluated. The factor two in the first line of Eq. 3.51 is due to the fact that the two pieces stamming from $K^{\text{dia}}(E,\omega+\omega_\tau)$ and $K^{\text{dia}}(E,\omega_t-\omega)$ can be shown to be equal by changing the intagration variable $\omega\to\omega_t-\omega_\tau-\omega$. Analogously we obtain the other contribution to the 2D map

$$\begin{aligned}\tilde{J}^{(3)}_{0\tau\tau}(E,\omega_t,\omega_\tau) &= 2A(\omega_t-\omega_\tau)\left[F^{\text{dia}}_{0\tau\tau}(-2E)-F^{\text{dia}}_{0\tau\tau}(2E)\right]\\ &\quad + A(\omega_t-\omega_\tau)A^2(\omega_\tau)\left(\frac{1}{\omega_\tau+i\eta_2-2E}-\frac{1}{\omega_\tau+i\eta_2+2E}\right),\end{aligned} \tag{3.53}$$

where $F^{\text{dia}}_{0\tau\tau}$ is obtained from $F^{\text{dia}}_{00\tau}$ by exchanging $\omega_t-\omega_\tau\leftrightarrow\omega_\tau$. The structure of the F^{dia} functions is characterized by the interplay between the spectral features of the kernel, encoded in their denominator, and the field envelopes at the numerator, which tend to redistribute the spectral weight along the lines $\omega_\tau=0,\pm2\Omega$ and $\omega_t-\omega_\tau=0,\pm2\Omega$.

To better understand these results, let us consider the impulsive limit, i.e. let us take $A(\omega) = \bar{A}$. One can note that now the $F^{\rm dia}$ functions can be evaluated through residues, from which we observe that the combination in the first line of Eq. 3.51 and 3.53 vanishes. The remaining pieces then give

$$\tilde{J}^{(3)}_{00\tau}(E,\omega_t,\omega_\tau) = \left(\frac{1}{\omega_t-\omega_\tau+i\eta_2-2E} - \frac{1}{\omega_t-\omega_\tau+i\eta_2+2E}\right)\bar{A}^3, \tag{3.54}$$

and

$$\tilde{J}^{(3)}_{0\tau\tau}(E,\omega_t,\omega_\tau) = \left(\frac{1}{\omega_\tau+i\eta_2-2E} - \frac{1}{\omega_\tau+i\eta_2+2E}\right)\bar{A}^3, \tag{3.55}$$

From this expression we notice that the spectral weight on the 2D map in the impulsive limit is spread along the lines $\omega_t-\omega_\tau = \pm 2E$ and $\omega_\tau = \pm 2E$. We simulate the resulting signal for three values of $\tau_p\Omega$, which correspond to a narrowband, intermediate or broadband incoming pulse. In order to clarify the role of the continuum of excitations we simulated two different situations. In one panel, Fig. 3.6a, we considered the $t \ll \Delta$ limit, where the bandwidth is taken much smaller than the semiconducting gap and one has almost non-dispersive bands, akin to a two level system. In this limit one can approximate $w(E) \sim \delta(E-\Delta)$ in Eq. 3.49 and can just simulate the previous expressions by sending $E \to \Delta$. In the other panel, Fig. 3.6b, we considered the $t \gg \Delta$ limit, where one needs to integrate the previous expressions over the energy E including in the function $w(E)$ all the factors foreseen in Eq. 3.31. We observe that in this case the spectral weight is more spread in the (ω_t,ω_τ) plane going towards the impulsive limit, as expected for a continuum of excitations which has an onset at the optical gap.

3.4.2 Paramagnetic term

Let us now consider the paramagnetic contribution. As done for $K^{\rm dia}$, we focus on the structures given by $K^{\rm inter}$ and $K^{\rm mix}$ when plugged into Eq. 3.49. One has for the fully-interband scattering

$$\begin{aligned} K^{\rm inter}_{\mathcal{S}}(E,\omega,\omega_\tau,\omega_t-\omega_\tau-\omega) = &\left(\frac{1}{\omega_t+i\eta_3-2E} - \frac{1}{\omega_t+i\eta_3+2E}\right)\times \\ &\times\left[\frac{1}{\omega+i\eta_1-2E}\frac{1}{\omega_\tau+i\eta_1+2E}\right. \\ &+\frac{1}{\omega_\tau+i\eta_1-2E}\frac{1}{\omega_t-\omega_\tau-\omega+i\eta_1+2E} \\ &\left.+\frac{1}{\omega_t-\omega_\tau-\omega+i\eta_1-2E}\frac{1}{\omega+i\eta_1+2E} + E\to -E\right]. \end{aligned} \tag{3.56}$$

Noticing again the symmetry $\omega \to \omega_t-\omega_\tau-\omega$ in the previous expression, one can write

$$\begin{aligned} \tilde{J}^{(3)}_{00\tau}(E,\omega_t,\omega_\tau) = A(\omega_\tau)&\left(\frac{1}{\omega_t+i\eta_3-2E} - \frac{1}{\omega_t+i\eta_3+2E}\right)\times \\ \times&\left[\frac{F^{\rm inter}_{00\tau}(2E)}{\omega_\tau+i\eta_1-2E} + \frac{F^{\rm inter}_{00\tau}(-2E)}{\omega_\tau+i\eta_1+2E} + \frac{F^{\rm inter}_{00\tau}(2E)+F^{\rm inter}_{00\tau}(-2E)}{\omega_t-\omega_\tau+i\eta_2}\right], \end{aligned} \tag{3.57}$$

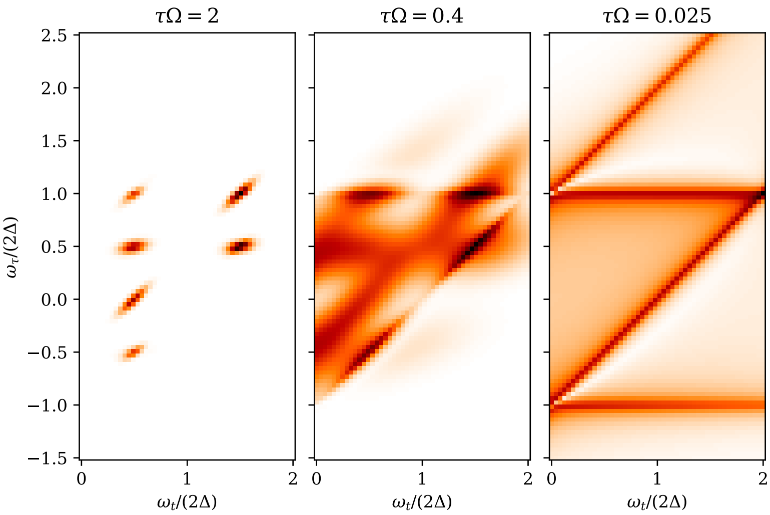

(a) The 2D map obtained in the two-level limit $t \ll \Delta$.

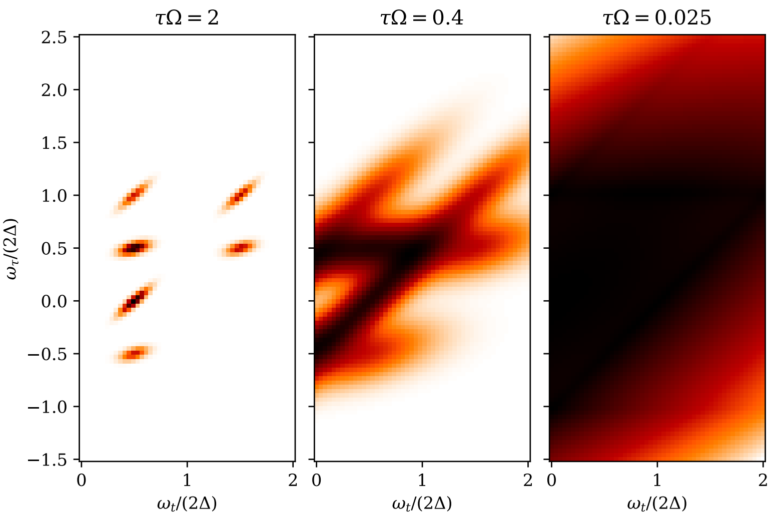

(b) The 2D map obtained for $t/\Delta = 100$.

Figure 3.6. Comparison between the 2D map obtained from the fully-diamagnetic process, computed integrating over energy E the sum of Eq. 3.51 and 3.53. In the upper panel we weight the sum by $w(E) \sim \delta(E - \Delta)$, corresponding to the two-level limit. In the lower panel we explicitly include the full form of $w(E)$ derived from Eq. 3.31. We show the dependence on the time duration of the incoming pulse, defined by $A(t) = \bar{A}e^{-t^2/(2\tau^2)}\cos(\Omega t)$, and we set $2\Omega = 2\Delta$, i.e. twice the central frequency of the pulse is resonant with the optical gap of the semiconductor.

where the function $F_{00\tau}^{\text{inter}}$ reads now

$$F_{00\tau}^{\text{inter}}(2E) = \int d\omega \, \frac{A(\omega)A(\omega_t - \omega_\tau - \omega)}{\omega_t - \omega_\tau - \omega + i\eta_1 + 2E}. \tag{3.58}$$

The contribution $\tilde{J}_{0\tau\tau}^{(3)}(E, \omega_t, \omega_\tau)$ reads as well

$$\begin{aligned} \tilde{J}_{0\tau\tau}^{(3)}(E, \omega_t, \omega_\tau) = A(\omega_t - \omega_\tau) \left(\frac{1}{\omega_t + i\eta_3 - 2E} - \frac{1}{\omega_t + i\eta_3 + 2E} \right) \times \\ \times \left[\frac{F_{0\tau\tau}^{\text{inter}}(2E)}{\omega_t - \omega_\tau + i\eta_1 - 2E} + \frac{F_{0\tau\tau}^{\text{inter}}(-2E)}{\omega_t - \omega_\tau + i\eta_1 + 2E} \right. \\ \left. + \frac{F_{0\tau\tau}^{\text{inter}}(2E) + F_{0\tau\tau}^{\text{inter}}(-2E)}{\omega_\tau + i\eta_2} \right], \end{aligned} \tag{3.59}$$

where the function $F_{0\tau\tau}^{\text{inter}}$ is obtained from $F_{00\tau}^{\text{inter}}$ by exchanging $\omega_t - \omega_\tau \leftrightarrow \omega_\tau$. Once again we analyze the impulsive limit, in which the F functions can be integrated out to constants and the resulting 2D map is characterized by

$$\begin{aligned} \tilde{J}_{00\tau}^{(3)}(E, \omega_t, \omega_\tau) = \left(\frac{1}{\omega_t + i\eta_3 - 2E} - \frac{1}{\omega_t + i\eta_3 + 2E} \right) \times \\ \times \left[\frac{1}{\omega_\tau + i\eta_1 - 2E} + \frac{1}{\omega_\tau + i\eta_1 + 2E} + \frac{2}{\omega_t - \omega_\tau + i\eta_2} \right] \bar{A}^3, \end{aligned} \tag{3.60}$$

and

$$\begin{aligned} \tilde{J}_{0\tau\tau}^{(3)}(E, \omega_t, \omega_\tau) = \left(\frac{1}{\omega_t + i\eta_3 - 2E} - \frac{1}{\omega_t + i\eta_3 + 2E} \right) \times \\ \times \left[\frac{1}{\omega_t - \omega_\tau + i\eta_1 - 2E} + \frac{1}{\omega_t - \omega_\tau + i\eta_1 + 2E} + \frac{2}{\omega_\tau + i\eta_2} \right] \bar{A}^3. \end{aligned} \tag{3.61}$$

In this case one can immediately recognize four peaked structures in the semiplane $\omega_t > 0$, which are obtained from the intersections of the Lorentzian maximized along the line $\omega_t = 2E$ with the ones in parentheses in the previous expressions, which are peaked along $\omega_\tau = 0, \pm 2E$ and $\omega_t - \omega_\tau = 0, \pm 2E$. The four spots are then located at coordinates $(2E, -2E)$, $(2E, 0)$, $(2E, 2E)$ and $(2E, 4E)$.

A similar but more involved computation can be then performed for the mixed terms in Eq. 3.43. One has for the $K_{\mathcal{S}}^{\text{mix}}(E, \omega, \omega_\tau, \omega_t - \omega_\tau - \omega)$ piece contributing to $\tilde{J}_{00\tau}^{(3)}(E, \omega_t, \omega_\tau)$

$$\begin{aligned} K_{\mathcal{S}}^{\text{mix}}(\dots) = \left(\frac{1}{\omega_t + i\eta_3 - 2E} - \frac{1}{\omega_t + i\eta_3} \right) \times \\ \times \left[\frac{1}{\omega + i\eta_1 - 2E} \left(\frac{1}{\omega + \omega_\tau + i\eta_2 - 2E} + \frac{1}{\omega_t - \omega_\tau + i\eta_2 - 2E} \right) \right. \\ + \frac{1}{\omega_\tau + i\eta_1 - 2E} \left(\frac{1}{\omega + \omega_\tau + i\eta_2 - 2E} + \frac{1}{\omega_t - \omega + i\eta_2 - 2E} \right) \\ \left. + \frac{1}{\omega_t - \omega_\tau - \omega + i\eta_1 - 2E} \left(\frac{1}{\omega_t - \omega_\tau + i\eta_2 - 2E} + \frac{1}{\omega_t - \omega + i\eta_2 - 2E} \right) \right] \\ - (E \to -E), \end{aligned} \tag{3.62}$$

from which we calculate, using again the symmetry $\omega \to \omega_t - \omega_\tau - \omega$,

$$\begin{aligned}\tilde{J}^{(3)}_{00\tau}(E,\omega_t,\omega_\tau) &= 2A(\omega_\tau)\left(\frac{1}{\omega_t + i\eta_3 - 2E} - \frac{1}{\omega_t + i\eta_3}\right)\times \\ &\times\left[\frac{F^{\mathrm{mix},1}_{00\tau}(2E)}{\omega_t - \omega_\tau + i\eta_2 - 2E} + \frac{F^{\mathrm{mix},2}_{00\tau}(2E)}{\omega_\tau + i\eta_1 - 2E}\right. \\ &+\left.\frac{F^{\mathrm{mix},1}_{00\tau}(2E) - F^{\mathrm{mix},2}_{00\tau}(2E)}{\omega_\tau + i\eta_1}\right] - (E \to -E).\end{aligned} \tag{3.63}$$

Here we introduced the two functions

$$F^{\mathrm{mix},1}_{00\tau}(2E) = \int d\omega\, \frac{A(\omega)A(\omega_t - \omega_\tau - \omega)}{\omega + i\eta_1 + 2E}, \tag{3.64}$$

and

$$F^{\mathrm{mix},2}_{00\tau}(2E) = \int d\omega\, \frac{A(\omega)A(\omega_t - \omega_\tau - \omega)}{\omega + \omega_\tau + i\eta_2 + 2E}. \tag{3.65}$$

In the impulsive limit one finally gets

$$\begin{aligned}\tilde{J}^{(3)}_{00\tau}(E,\omega_t,\omega_\tau) &= \left(\frac{1}{\omega_t + i\eta_3 - 2E} - \frac{1}{\omega_t + i\eta_3}\right)\times \\ &\times\left[\frac{1}{\omega_t - \omega_\tau + i\eta_2 - 2E} + \frac{1}{\omega_\tau + i\eta_1 - 2E}\right]\bar{A}^3 - (E \to -E).\end{aligned} \tag{3.66}$$

The calculation for the $\tilde{J}^{(3)}_{0\tau\tau}$ part is here omitted, but as in the previous cases the associated signal can be obtained by the exchange $\omega_\tau \leftrightarrow \omega_t - \omega_\tau$. Also in this case the enhancement of the 2D map fro $\omega_t > 0$ is obtained at the intercepts of the lines $\omega_t = 0, 2E$ with $\omega_\tau = 2E$ or $\omega_t - \omega_\tau = 2E$. While the spots at $(2E, 0)$ and $(2E, 2E)$ gain also contributions from the purely interband process described by K^{inter}, we stress that the two spots at $(0, 2E)$ and $(0, -2E)$ are only present if this mixed interband-intraband scattering is included, making then possible to identify regions in the 2D map that are selectively sensitive to this specific nonlinear pathway.

As we did in the previous section, we compare also here the non-dispersive and dispersive limits, by computing the 2D map in the $t \ll \Delta$ regime where $w(E) \sim \delta(E - \Delta)$ and in the $t \gg \Delta$ limit by taking into account all the prefactors to K^{inter} and K^{mix} of Eq. 3.45 in the integral over energy E. We observe that in the former two-level limit the prefactor of the mixed process is suppressed by a factor t^2/Δ^2, so that only the interband contribution survives. We show in Fig. 3.7a the obtained result, where one observes the transition from a 2D map witnessed by a broadband field to the situation where the field gets narrower and the spectral features associated with the pump are most prominent.

It is interesting to compare what we have just obtained with the two-level formalism usually presented in literature[94, 80], assuming in our case to have the resonance of the two-level system coinciding with the direct band gap of the semiconductor. Indeed, we would obtain exactly the previous result from a perturbative solution of the following hamiltonian coupled to a gauge field $A(t)$ via the standard dipole approximation,

$$H = -\Delta|{+1}\rangle\langle{+1}| + \Delta|{-1}\rangle\langle{-1}| + \mu A(t)|{+1}\rangle\langle{-1}| + \mathrm{h.c.}, \tag{3.67}$$

where the two states represent the valence ($|+1\rangle$) and conduction ($|-1\rangle$) bands of the system in the limit of negligible dispersion and μ is the dipole moment.

In Fig. 3.7b we show the results in the opposite $t \gg \Delta$ limit. As one can immediately notice, there is similarity between the two cases, at least at the four spots mentioned above where purely interband transitions play a major role. In addition to them, we also observe the other peaks along the line $\omega_t = 0$, which correspond to the terms involving also intraband scattering, i.e. the K^{mix}, which as explained before are suppressed in the $t \ll \Delta$ limit.

Comparing the two paramagnetic and diamagnetic contributions, it is evident the power of the 2D technique in distinguishing the two classes of processes shown here, that produce very different signals when a sufficiently broad incoming pulse is used. We remark that this is a crucial point: all the results above have been obtained by assuming that the spectral content of the field remains intact when entering the sample, a situation which occurs only in certain experimental realizations, as e.g. in Ref. [72]. We will then explicitly analyze in the next chapter a case where most of the features of the 2D map witnessed by the experiment are heavily influenced by the linear response of the system, making it challenging to distinguish among different nonlinear pathways.

To conclude the chapter, let us summarize in Fig. 3.8a and Fig. 3.8b the results that we have obtained so far, having for simplicity in mind the two-level limit. Fully-diamagnetic processes produce two-point response functions which only depend on the sum of two incoming frequencies. In the monochromatic limit, the four peaks corresponding to non-linearly generated first harmonic will then be weighted by the combination $K(2\Omega) + 2K(0)$, while the third harmonic will be weighted by $3K(2\Omega)$, according to Eq. 3.14, which can be resonantly enhanced only when $2\Omega = 2\Delta$. In the impulsive limit, the same kernel produces pair of stripes along the lines $\omega_t - \omega_\tau = \pm 2\Delta$ or $\omega_\tau = \pm 2\Delta$: the first pair is realized when only one photon is exchanged with the delayed pulse, the second one when two photons coming from it are involved.

Fully paramagnetic processes require to deal with four-point response functions, which naturally have a more complicated structure. When monochromatic pulses are used, the kernel is read out at different incoming frequencies, $K(\Omega, \Omega, -\Omega)$ for the first harmonic and $K(\Omega, \Omega, \Omega)$ for the third harmonic. In this case enhancement can occur in principle whenever one, two or three photons from the pump are resonant with the internal energy scale 2Δ, an argument which we will encounter again the next chapter when discussing the experimental results on NbN [72]. In the impulsive case, one gets four peaks instead of stripes at the intercepts between $\omega_t = \pm 2\Delta$ and $\omega_t - \omega_\tau = \pm 2\Delta$ or $\omega_\tau = \pm 2\Delta$, i.e. the maximum enhancement occurs when all the electronic propagators entering the nonlinear response are read out resonantly by the incoming pulses.

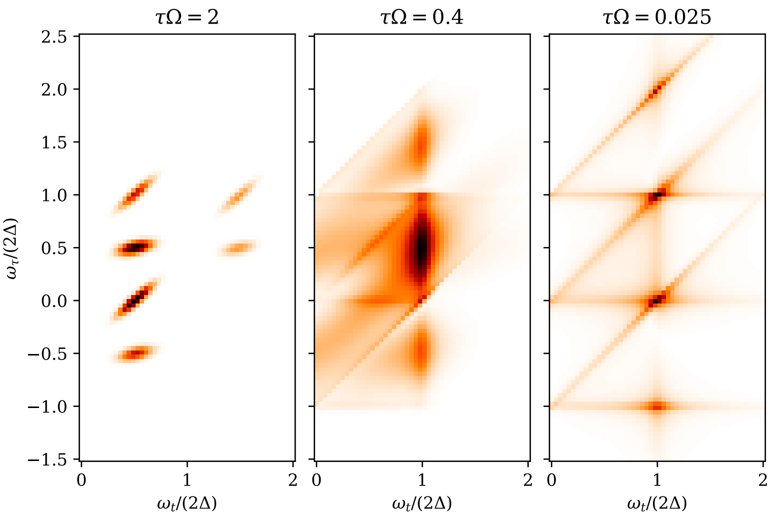

(a) The 2D map obtained in the two-level limit $t \ll \Delta$.

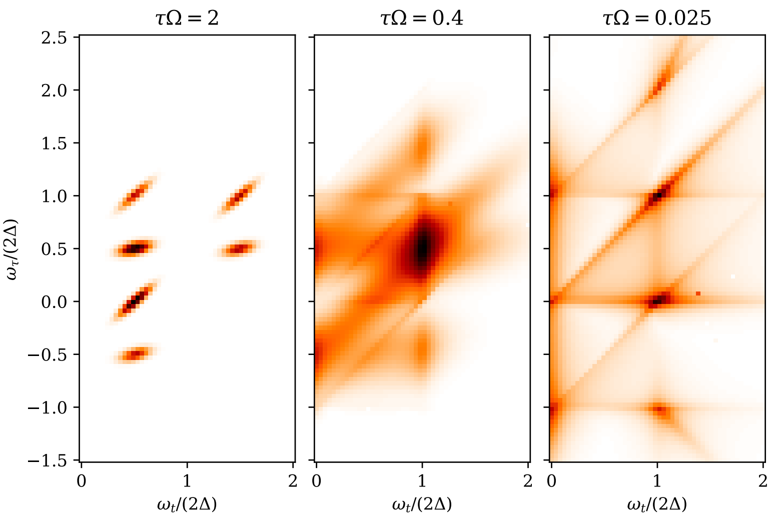

(b) The 2D map obtained for $t/\Delta = 100$.

Figure 3.7. Analgous of the previous Fig. 3.6a and Fig. 3.6b for the fully-paramagnetic process, computed integrating over energy E the sum of Eq. 3.57 and 3.59. In the upper panel we weight the sum by $w(E) \sim \delta(E - \Delta)$, corresponding to the two-level limit which is only sensitive to K^{inter}. In the lower panel we explicitly include the full form of $w(E)$ derived from Eq. 3.45. Also here we show the dependence on the time duration of the incoming pulse, defined by $A(t) = \bar{A}e^{-t^2/(2\tau^2)}\cos(\Omega t)$. We set $2\Omega = 2\Delta$, i.e. twice the central frequency of the pulse is resonant with the optical gap of the semiconductor.

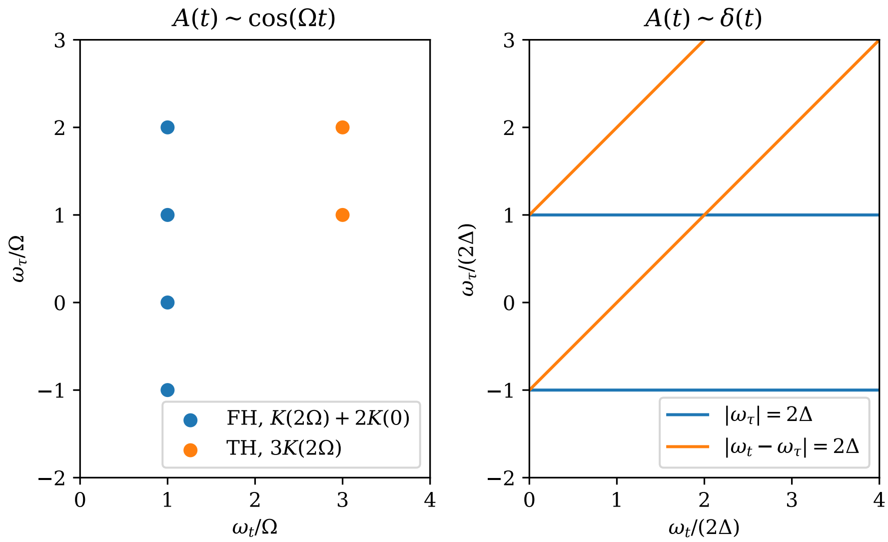

(a) Schematic 2D map for the diamagnetic process

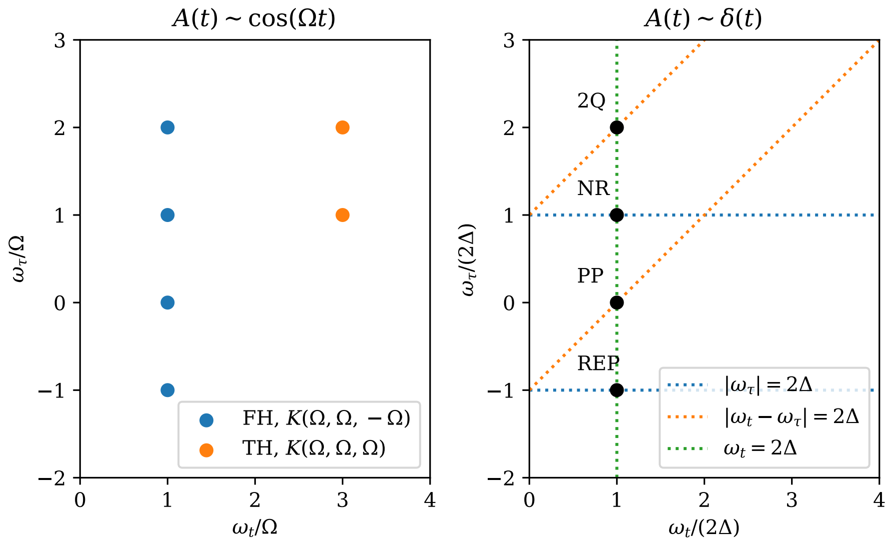

(b) Schematic 2D map for the paramagnetic process. We listed the names of the four peaks which are usually reported in the literature: 2Q (two-quantum), NR (non-rephasing), PP (pump-probe) and REP (rephasing).

Figure 3.8. Conclusive comparison between the appearance of diamagnetic and paramagnetic processes in the monochromatic (left column) and impulsive limit (right column).

Chapter 4

Applications of 2D-THz spectroscopy to superconductors

Part of this chapter has been published in Ref. [39]. The rest of the chapter will be submitted soon for publication.

4.1 Application to $c-$axis response of cuprates

In this section we want to analyze the $c-$axis response of nearly optimally-doped $La_{2-x}Sr_xCuO_4$ ($x = 0.17$), a single-layer superconducting cuprate, whose 2D-THz spectroscopy measurements have been presented in Ref. [89]. As described in Chapter 2, the $c-$axis polarized THz measurements are particularly sensitive to the presence of the Josephson plasma mode, at frequency ω_z. In particular, the experimental work focuses on the spectral features of the peak in frequency domain called Josephson Echo, at $(\omega_z, -\omega_z)$, with the aim to extract information on the role of the disorder in the interlayer tunneling of Cooper pairs.

Indeed, already at level of linear response, the presence of inhomogeneity in the superconducting phase is invoked to explain the modification of the form of the reflectivity edge, see Fig. 4.1 from Ref. [31], that in turns results in the appearance of an absorption peak in the real part of the conductivity. From the theoretically point of view, an effective model to explain this observation was proposed in Ref. [144], where a statistical distribution of the Josephson plasma frequency ω_z is introduced in place of a single value. However, a precise estimate of the importance of this type of spatially-related, inhomogeneous disorder from linear spectroscopy is difficult, since its effects are often mixed with the more standard broadening associated with homogeneous, Born-like scattering. Thus, the experiment aimed at exploiting the intrinsic richness of the 2D-THz signal in order to disentangle the two contributions.

Before briefly discussing the effects of this type of disorder on the 2D map, we want to understand the observed signal in the theoretical framework presented in the previous chapter. At low temperatures, the experimental 2D map is characterized by four spots located at frequencies $(\omega_z, -\omega_z)$, $(\omega_z, 0)$, (ω_z, ω_z) and $(\omega_z, 2\omega_z)$, with $\omega_z \sim 2$ THz for the doping level $x = 0.17$ of the studied sample. The experiments are performed in a reflection configuration by means of a relatively broadband pulse, so that in principle the observation can be reconciled with the impulsive-limit

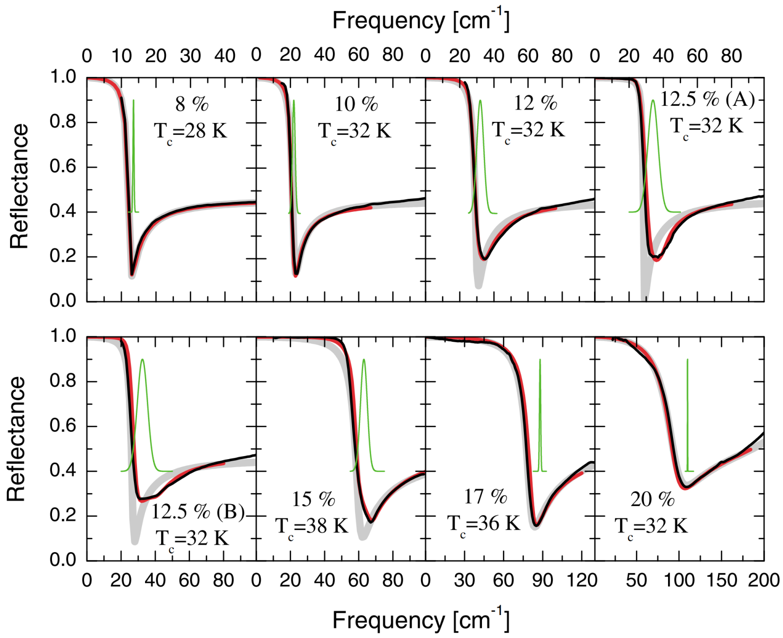

Figure 4.1. Reflectivity curves (black line) of LSCO samples at different doping levels (in percent) collected in Ref. from Ref. [31]. The experimental prophiles were fitted using the standard two-fluid model (bold gray line) or with the effective model to account for disorder proposed in Ref. [144] (red line), with a doping-dependent gaussian weight (green line).

picture displayed in Fig. 3.8b, where the internal energy scale is determined by the Josephson plasmon at ω_z. As we will see by explicit calculation, at least at low temperatures the internal screening of the incoming field is predominant, producing an effective narrowband pulse centered around ω_z. Consequently, it would be more appropriate to recast this peculiar case in the monochromatic-limit sketch in Fig. 3.2, where it is actually difficult to distinguish between the different nonlinear pathways contributing to the 2D response.

4.1.1 Fresnel effects in the 2D-THz case

Let us reconsider at first the result presented in the Chapter 1 for the reflected field from a bulk sample, which is the situation appropriate for the configuration used in Ref. [89]. The outgoing electric field reads, see Eq. 1.70,

$$\begin{aligned} E^{\text{out}}(\omega) = \frac{4\pi i}{c}\frac{1}{1+n(\omega)}\int d\omega_i\, K^{(3)}(\omega_1,\omega_2,\omega_3)A_{\text{ext}}(\omega_1)A_{\text{ext}}(\omega_2)A_{\text{ext}}(\omega_3)\times \\ \times\frac{t(\omega_1)t(\omega_2)t(\omega_3)}{n(\omega)\omega/c+\sum_i n(\omega_i)\omega_i/c}\delta\left(\omega-\sum_i\omega_i\right). \end{aligned} \tag{4.1}$$

In this expression we have separated on the first line inside the integral the result that one would obtain neglecting the propagation effects inside the material, where the external fields are convoluted with the nonlinear third order kernel. In the second line we see instead the contribution of internal screening, which has its own frequency dependence and can mask the genuine nonlinear effects included in $K^{(3)}$. In this way, we will see that even the simplest instantaneous kernel can show complicated signatures linked to the response due to the propagation of the generated signal at the interface between vacuum and material.

To proceed with the evaluation of the 2D map, we can apply here the same procedure presented in the previous sections, see e.g. Eq. 3.49. One gets for the piece with the double interaction with the $A_0(t)$ field and the single interaction with $A_\tau(t)$,

$$E^{\text{out}}_{00\tau}(\omega_t,\omega_\tau) = \int d\omega\, K^{(3)}_{\mathcal{S}}(\omega,\omega_\tau,\omega_t-\omega_\tau-\omega)\times \\ \times A_{\text{ext}}(\omega)A_{\text{ext}}(\omega_\tau)A_{\text{ext}}(\omega_t-\omega_\tau-\omega)\mathcal{F}_{00\tau}(\omega,\omega_t,\omega_\tau), \tag{4.2}$$

where the function $\mathcal{F}_{00\tau}$ takes into account all the factors related to propagation effects and reads

$$\mathcal{F}_{00\tau}(\omega,\omega_t,\omega_\tau) = \frac{2\pi i t(\omega_t)t(\omega)t(\omega_\tau)t(\omega_t-\omega_\tau-\omega)}{n(\omega_t)\omega_t + n(\omega)\omega + n(\omega_\tau)\omega_\tau + n(\omega_t-\omega_\tau-\omega)(\omega_t-\omega_\tau-\omega)}. \tag{4.3}$$

An analogous result for $E^{\text{out}}_{0\tau\tau}(\omega_t,\omega_\tau)$ is obtained by switching $\omega_\tau \leftrightarrow \omega_t-\omega_\tau$, corresponding to the system interacting once with the $A_0(t)$ field and twice with $A_\tau(t)$.

We now specialize this result to the case of the $c-$axis response of cuprate superconductors. We focus on two different processes which we have encountered in the previous Chapter 2, namely the instantaneous and the two-plasmon kernel, which are both finite in the effective cosine-model that we have adopted to describe the third-harmonic response, see Section 2.5.4. For our purposes, we just consider $K^{(3)} \sim$ const. in Eq. 4.2 to simulate the instantaneous contribution, while we use the results reported in Sections 2.5.2 and 2.5.3 for the two-plasmon part. We recall that the expression of the latter kernel as a function of the sum-frequency ω of the two incoming photons is given by Eq. 2.67, which we report here

$$K_{2\text{p}}(\omega) \sim \int dz\, \rho_{LL}(z)\frac{1}{z}\frac{\coth\left(\frac{\beta z}{2}\right)}{(2z)^2-(\omega+i\gamma)^2}, \tag{4.4}$$

where $\rho_{LL}(z)$ is the density of state associated with the two-plasmon process, see Eq. 2.81. In the region in proximity of the lower plasma edge, the latter density grows linearly as $\rho_{LL}(z)\sim z\theta(z-\omega_z)$. Moreover, nearby the critical temperature we can also approximate $\coth \beta z/2 \sim T/z$, so that the above kernel can be easily integrated and reads, neglecting constant prefactors,

$$K_{2\text{p}}(\omega) \sim \frac{T}{(\omega+i\gamma)^2}\log\left(1-\frac{(\omega+i\gamma)^2}{4\omega_z^2}\right), \tag{4.5}$$

which almost coincides with the so-called plasmon squeezing contribution in Ref. [52]. We stress that although near T_c the two derivations give the same result, the procedure followed in Ref. [52] is only valid in the region $T\sim T_c$, where plasmon fluctuations have thermal nature. For low temperatures, the latter would predict a suppression scaling with T which neglects quantum anharmonic effects, which are indeed taken into account in our framework by the $\coth \beta z/2 \to 1$ for $T \to 0$. At this point we can then express the contributions of the two-plasmon process to the 2D map by using the relation

$$K_{\mathcal{S}}^{(3)}(\omega, \omega_\tau, \omega_t - \omega_\tau - \omega) \sim K_{2\mathrm{p}}(\omega + \omega_\tau) + K_{2\mathrm{p}}(\omega_t - \omega) + K_{2\mathrm{p}}(\omega_t - \omega_\tau). \tag{4.6}$$

Using again the symmetry in Eq. 4.2 upon replacement $\omega \to \omega_t - \omega_\tau - \omega$ we can show that the first two terms of the previous sum are actually equal. As it happened before, the form of the kernel $K_{\mathcal{S}}^{(3)}$ for the $E_{0\tau\tau}^{\mathrm{out}}(\omega_t, \omega_\tau)$ is obtained by switching $\omega_\tau \leftrightarrow \omega_t - \omega_\tau$ in the previous expression.

In order to compute the effect of the function $\mathcal{F}$ in masking the spectral features of the kernels just introduced, we consider the usual dielectric function containing the superfluid response and the normal dissipative term, namely

$$\epsilon(\omega) = \epsilon_\infty \left(1 - \frac{\omega_z^2}{\omega^2} + i\frac{\gamma}{\omega}\right), \tag{4.7}$$

from which we can derive the refractive index as $n(\omega) = \sqrt{\epsilon(\omega)}$. We remark that in Ref. [31] an extensive analysis of the linear response from LSCO samples at different doping levels has been carried out, taking also into account the role of inhomogeneities. Following Ref. [144], the two-fluid dielectric function is weighted by a gaussian distribution of ω_z values, whose variance is fitted on the reflectivity curves collected from the various samples. The authors find that at doping $x = 0.17$, where the experiment of Ref. [89] is performed, the differences between the model of $\epsilon(\omega)$ obtained by taking into account the effect of inhomogeneities and the standard two-fluid reflectivity in Eq. 4.7 with finite γ are almost unperceptible, as can be seen from the very small value of the width of the gaussian distribution that they consider. For this reason, in this section we stick to the dielectric function presented in Eq. 4.7, since we are now mainly interested in understanding the filtering effect produced by such a sharp reflectivity edge.

In order to check the relevance of the screening effects, we then show in Fig. 4.2 the shape of the internal field $A_{\mathrm{in}}(\omega) = t(\omega)A_{\mathrm{ext}}(\omega)$. We considered for A_{ext} the experimental pulse spectrum of Ref. [89] and we modeled the parameters of the dielectric function fitting the experimental data measuring LSCO samples at doping levels $x = 0.16$ [137] and $x = 0.18$ [60] for several temperatures. The extracted values for ω_z and γ are then interpolated in order to get a reasonable estimation of the appropriate parameters for LSCO at $x = 0.17$, since we have not temperature dependent reflectivity spectra in Ref. [89]. As we can see from the right panel in Fig. 4.2, at the lowest temperature $T = 6$ K the field gets reshaped with the peak now shifting from the central frequency of the pump towards the value of ω_z.

We then show in Fig. 4.3a the resulting 2D map when the instantaneous kernel is considered. At $T = 6$ K we clearly observe the four spots located at the positions $(\omega_z, -\omega_z)$, $(\omega_z, 0)$, (ω_z, ω_z) and $(\omega_z, 2\omega_z)$, with $\omega_z \sim 2$ THz, consistent with the experiment. Rising the temperature the peaks redshift along the ω_t axis following the plasma edge and at $T = 25$ K there is more or less a coincidence between the position of the latter and the central frequency of the pulse, see the dashed guiding lines in the figure. At larger temperatures the plasma edge redshifts furtherly but

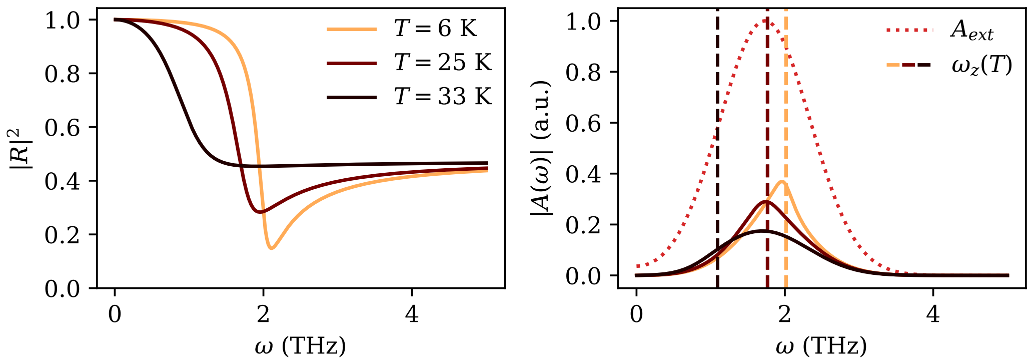

Figure 4.2. The simulated reflectance (left panel) of a LSCO sample at doping level $x = 0.17$ for three selected temperatures, using the interpolated parameters from Ref. [137] and Ref. [60] with the two-fluid model in Eq. 4.7. At low T the plasma edge (dashed vertical lines) produces a filtering effect on the incoming field (right panel), as we show comparing the external field used in Ref. [89] (dashed line) with the internal one $A_{\text{in}}(\omega) = t(\omega)A_{\text{ext}}(\omega)$ (solid line).

the broadening of the minimum is such that it is difficult to distinguish the spectral weight associated to the different spots. Nevertheless, one can still appreciate very near to T_c that along the ω_τ axis the maxima are still sensitive to the central frequency of the pump. This effect is more evident in Ref. [52], which is reported in Fig. 4.4 due to the smaller spectral width of the incoming pulse used in those simulations. The asymmetric behavior between the horizontal sliding of the peaks along the ω_t direction following the redshift of the plasma edge and their almost fixed position as a function of ω_τ can be understood inspecting Eq. 4.3. In the latter expression three $t(\omega_i)$ factors are multiplied by the pump spectrum in order to reconstruct the shape of the internal field that generates the nonlinear signal, whose behavior is determined by the interplay between A_{ext}, centered at Ω, and the frequency dependence of t, characterized by the plasma scale ω_z, as shown in Fig. 4.2. Nevertheless, there is a further factor $t(\omega_t)$ which is only related to the propagation of the outgoing radiation that reshapes along the horizontal direction the generated 2D signal, being eventually only sensitive to the scale of ω_z.

In Fig. 4.3b we show the results of the simulations with the two-plasmon kernel. For these we kept in Eq. 4.6 the same values of $\gamma(T)$ that we fitted for the linear response. As it can be noticed, it is very difficult to appreciate the difference between the instantaneous process and the diamagnetic-like one, since by assuming the same $\gamma(T)$ in refractive index entering the $\mathcal{F}$ factor and the damping in the two-plasmon process one softens both effects in the same way. There is a small difference in the relative intensities of the various peaks at low temperatures, in particular the two at $(\omega_z, -\omega_z)$ and $(\omega_z, 2\omega_z)$ that are placed on the lines of enhancement foreseen by Fig. 3.6a, i.e. $\omega_t - \omega_\tau = 2\omega_z$ and $\omega_\tau = 2\omega_z$, respectively. Nevertheless, since the experimental protocol of Ref. [89] requires to collect the four spots in a non-collinear geometry with the incoming and outgoing radiation inclined at different angles with respect to the sample surface, it is at the moment not possible to directly compare the relative intensities of the peaks.

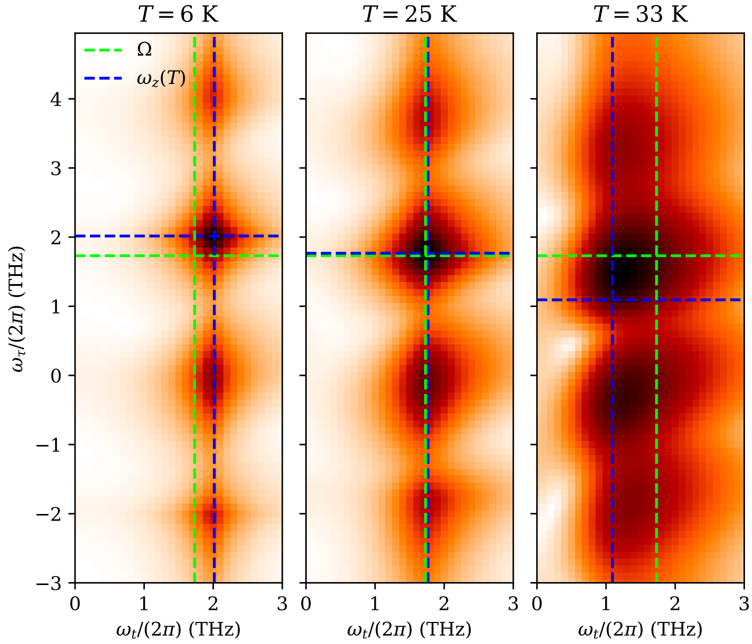

(a) The 2D map obtained considering the instantaneous process.

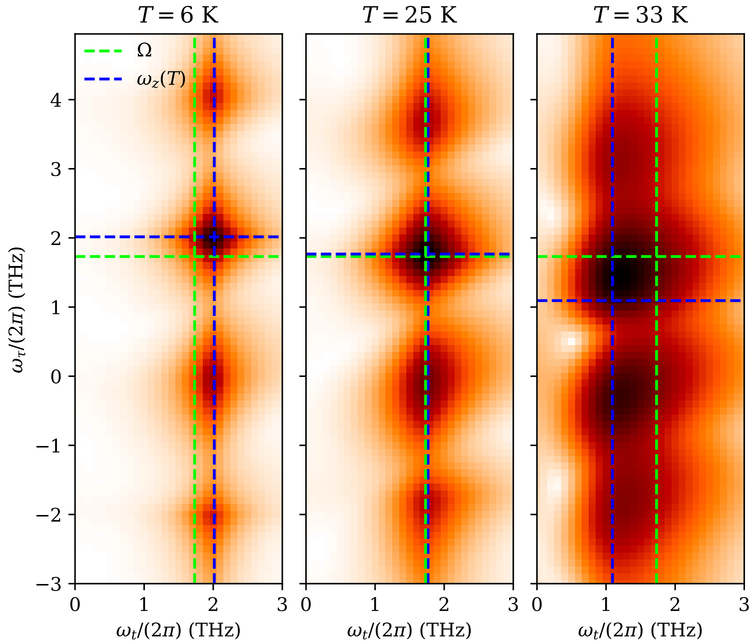

(b) The 2D map obtained considering the two-plasmon process.

Figure 4.3. The simulated 2D-THz response of LSCO ($x = 0.17$) probed with $c-$axis polarized electric field, with incoming spectrum similar to the one used in Ref. [89], for three different temperatures. In the upper panel we compute the signal resulting from an instantaneous kernel, in the lower one we consider the two-plasmon excitation mechanism presented in Chapter 2. We superimpose as guides to the eye the positions of the central frequency of the pump (green dashed line) and of the plasma frequency at the various temperatures (blue dashed line).

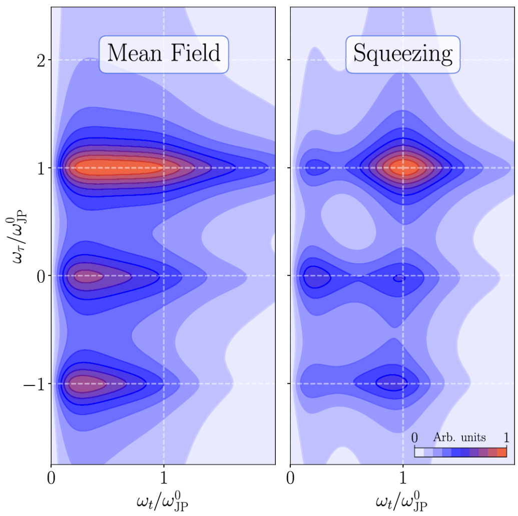

Figure 4.4. 2D maps obtained for the instantaneous (mean field) and two-plasmon (squeezing) contributions obtained in Ref. [52], where the difference in the two processes is more evident. In this case the incoming field is narrower than the one used in Fig. 4.3a and Fig. 4.3b and propagation effects are taken into account differently.

A similar simulation has been presented also in Ref. [52], where a different behavior between the instantaneous (named mean-field) and the two-plasmon (named squeezing) process is observed for $T \sim T_c$ as can be seen in Fig. 4.4. The differences between our results and those in Ref. [52] are most probably due to (i) the smaller spectral width of the pulse used in their simulation and (ii) the way in which linear-response effects are taken into account to generate Fig. 4.4, namely considering each internal driving field as screened by $1/\epsilon(\omega)$ in place of the functional form in 4.3.

4.1.2 Two-level model for inhomogeneity

In this section we want to take into account with a minimal model the role of inhomogeneity in the measured 2D-THz spectra, by applying the formalism developed for inhomogeneous line broadening in molecules [129] as suggested in Ref. [89]. The calculation that we present here allows one to study the variation of the lineshapes for all the four spots analyzed in the experimental data on LSCO. The starting point is the assumption that the system is characterized by a statistical distribution of plasma frequencies, which is taken as a gaussian [144, 31]

$$\rho(\omega_z) \sim e^{-(\omega_z-\bar{\omega}_z)^2/(2\sigma^2)}. \tag{4.8}$$

One then assumes that the 2D map can be obtained by considering

$$\langle E^{\rm out}\rangle = \int d\omega_z \rho(\omega_z) E^{\rm out}(\omega_z), \tag{4.9}$$

where the $E^{\rm out}(\omega_z)$ is simulated by considering a fixed $c-$axis plasma frequency. In order to make the contribution of inhomogeneities more transparent, we consider just the contribtution from the instantaneous third-order kernel. We also approximate the internal screening described by the $\mathcal{F}$ function introduced in Eq. 4.3 by considering $A_{\text{in}}(\omega) = A_{\text{ext}}(\omega)/\epsilon(\omega)$, i.e. $t(\omega) \sim 1/\epsilon(\omega)$, that for an impulsive field $A(\omega) = \bar{A}$ allows one to perform analytical calculations when the dielectric constant in Eq. 4.7 is considered. One can then show that for $\gamma \ll \omega_z$ the internal $A_{\text{in}}(t)$ can be approximated as

$$A_{\text{in}}(t) = \bar{A}\omega_z \theta(t) e^{-\gamma t} \sin(\omega_z t), \tag{4.10}$$

so that one can then express E^{out} in time domain

$$E^{\text{out}}(t,\tau) = A_{\text{in}}^2(t) A_{\text{in}}(t+\tau) + A_{\text{in}}(t) A_{\text{in}}^2(t+\tau). \tag{4.11}$$

By combining the various oscillating terms coming from the sine, one can selectively isolate the contributions to the 2D map located at the spots foreseen by the frequency vector scheme in Fig. 3.2, where now the internal field is narrowed by the presence of the well defined plasma edge at $\omega = \omega_z$. If one is for instance interested in the so-called Josephson Echo peak, it suffices to select terms containing $e^{-i\omega_z(t-\tau)}$ in Eq. 4.11, namely

$$E^{\text{out}}_{(1,-1)}(t,\tau) = \bar{A}^3 \omega_z^3 \theta(t)\theta(t+\tau) e^{-2\gamma t} e^{-\gamma(t+\tau)} e^{-i\omega_z(t-\tau)}. \tag{4.12}$$

We want to perform the Fourier transform $(t,\tau) \to (\omega_t, \omega_\tau)$, which in this simple case will produce Lorentzian lineshapes. Before proceeding with the inclusion of the inhomogeneities, we stress that the shape of the resulting peak is already strongly dependent on the way in which the signal is collected, due to presence of the homogeneous broadening γ. If one were able to explore both positive and negative time delays, i.e. the Fourier transform can be at least in theory extended for $\tau < 0$ to $\tau > 0$, one gets from Eq. 4.12

$$E^{\text{out}}_{(1,-1)}(\omega_t, \omega_\tau) = \bar{A}^3 \omega_z^3 \frac{1}{\omega_t - \omega_\tau - 2\omega_z + 2i\gamma} \frac{1}{\omega_\tau + \omega_z + i\gamma}. \tag{4.13}$$

The Josephson Echo peak is then stretched by a finite γ along the lines $\omega_\tau = -\omega_z$ and $\omega_\tau = \omega_t - 2\omega_z$, see upper row of Fig. 4.5a. Conversely, if one only collected the signal for $\tau > 0$, one must replace the $\theta(t+\tau)$ in Eq. 4.12 with a $\theta(\tau)$, i.e. the Fourier transform cannot run for $\tau < 0$. This will affect the 2D signal by modifying the previous expression into

$$E^{\text{out}}_{(1,-1)}(\omega_t, \omega_\tau) = \bar{A}^3 \omega_z^3 \frac{1}{\omega_t - \omega_z + 3i\gamma} \frac{1}{\omega_\tau + \omega_z + i\gamma}. \tag{4.14}$$

As it is evident, the stretching of the peak due to γ occurs in this case along the lines $\omega_\tau = -\omega_z$ and $\omega_t = \omega_z$. We remark here that in this simple model it is possible to analytically simulate the 2D map for both situations, i.e. when one collects data for both positive and negative time-delays or for $\tau > 0$ only. However, we have seen in the previous section that it is extremely useful to use the Fourier transform along the τ axis to saturate one frequency integral which determined the nonlinear third order current, which assumes to have a signal extending both for $\tau < 0$ and $\tau > 0$. For the purpose of comparing the simulated map with the experiments performed collecting only $\tau > 0$, it is then convenient to proceed in the following way. One first performs the simulation as we have illustrated previously, then we numerically anti-Fourier transform $(\omega_t, \omega_\tau) \to (t, \tau)$ and cut the signal for $\tau < 0$. As a last step, we go back to Fourier space by means of a last numerical Fourier transform. This is exactly the procedure that we have followed to obtain the simulations in Fig. 4.3a and Fig. 4.3b.

With this in mind, we now proceed to analyze the role of inhomogeneities in determining the spectral shape of the peaks in the model introduced above. Considering only $\tau > 0$ for a direct comparison with Ref. [89], we have to integrate over ω_z with a gaussian weight the expression in Eq. 4.14, namely

$$\langle E^{\text{out}}_{(1,-1)} \rangle(\omega_t, \omega_\tau) = \bar{A}^3 \int d\omega_z \, \frac{\omega_z^3 e^{-(\omega_z - \bar{\omega}_z)^2/(2\sigma^2)}}{(\omega_t - \omega_z + 3i\gamma)(\omega_\tau + \omega_z + i\gamma)}. \tag{4.15}$$

The integral can be analitically computed again in terms of Faddeeva functions, denoted here as $w(z)$ and the result reads, neglecting constant prefactors,

$$\langle E^{\text{out}}_{(1,-1)} \rangle(\omega_t, \omega_\tau) = \frac{w\left[(\omega_t - \bar{\omega}_z + 3i\gamma)\,/\left(\sqrt{2}\sigma\right)\right] + w\left[(\omega_\tau + \bar{\omega}_z + i\gamma)\,/\left(\sqrt{2}\sigma\right)\right]}{\omega_t + \omega_\tau + 4i\gamma}. \tag{4.16}$$

We remark here that we have approximated $\omega_z^3 \sim \bar{\omega}_z^3$ in the numerator of Eq. 4.15, which amounts to neglect corrections of order $\sigma^2/\bar{\omega}_z^2$ to the previous expression. We notice that there are different limiting cases according to the values of γ and σ, which represent homogeneous and inhomogeneous broadening, respectively. When homogeneous broadening is dominant, one observes the same linewidh that are obtained in the case where we neglect the distribution of plasma frequencies, i.e. replacing the gaussian in Eq. 4.15 with a delta centered at $\bar{\omega}_z$, getting back Eq. 4.14. When inhomogenous broadening is dominant, one can replace the same gaussian with a constant, and the integral over ω_z would produce the same pole in Eq. 4.16, which elongates the peak along the line connecting $(\bar{\omega}_z, -\bar{\omega}_z)$ with the origin. This result is somehow expected if one realizes that varying the value of ω_z one is simply shifting the position of the peak along the same line, as depicted in Fig. 4.5b. We also give here the results of the same procedure applied to the other three spots measured in Ref. [72]. For the $(\bar{\omega}_z, 0)$, so-called pump-probe peak, one has

$$\langle E^{\text{out}}_{(1,0)} \rangle(\omega_t, \omega_\tau) = \frac{w\left[(\omega_t - \bar{\omega}_z + 3i\gamma)\,/\left(\sqrt{2}\sigma\right)\right]}{\omega_\tau + 2i\gamma}, \tag{4.17}$$

where the stretching occurs along the ω_t axis. For the $(\bar{\omega}_z, \bar{\omega}_z)$ rephasing peak the expression reads

$$\langle E^{\text{out}}_{(1,1)} \rangle(\omega_t, \omega_\tau) = \frac{w\left[(\omega_\tau - \bar{\omega}_z + i\gamma)\,/\left(\sqrt{2}\sigma\right)\right] - w\left[(\omega_t - \bar{\omega}_z + 3i\gamma)\,/\left(\sqrt{2}\sigma\right)\right]}{\omega_\tau - \omega_t + 2i\gamma}, \tag{4.18}$$

while the two-quantum spot at $(\bar{\omega}_z, 2\bar{\omega}_z)$ can be simulated through

$$\langle E^{\text{out}}_{(1,2)} \rangle(\omega_t, \omega_\tau) = \frac{w\left[(\omega_\tau - 2\bar{\omega}_z + 2i\gamma)\,/\left(2\sqrt{2}\sigma\right)\right] - w\left[(\omega_t - \bar{\omega}_z + 3i\gamma)\,/\left(\sqrt{2}\sigma\right)\right]}{2\omega_t - \omega_\tau + 4i\gamma}. \tag{4.19}$$

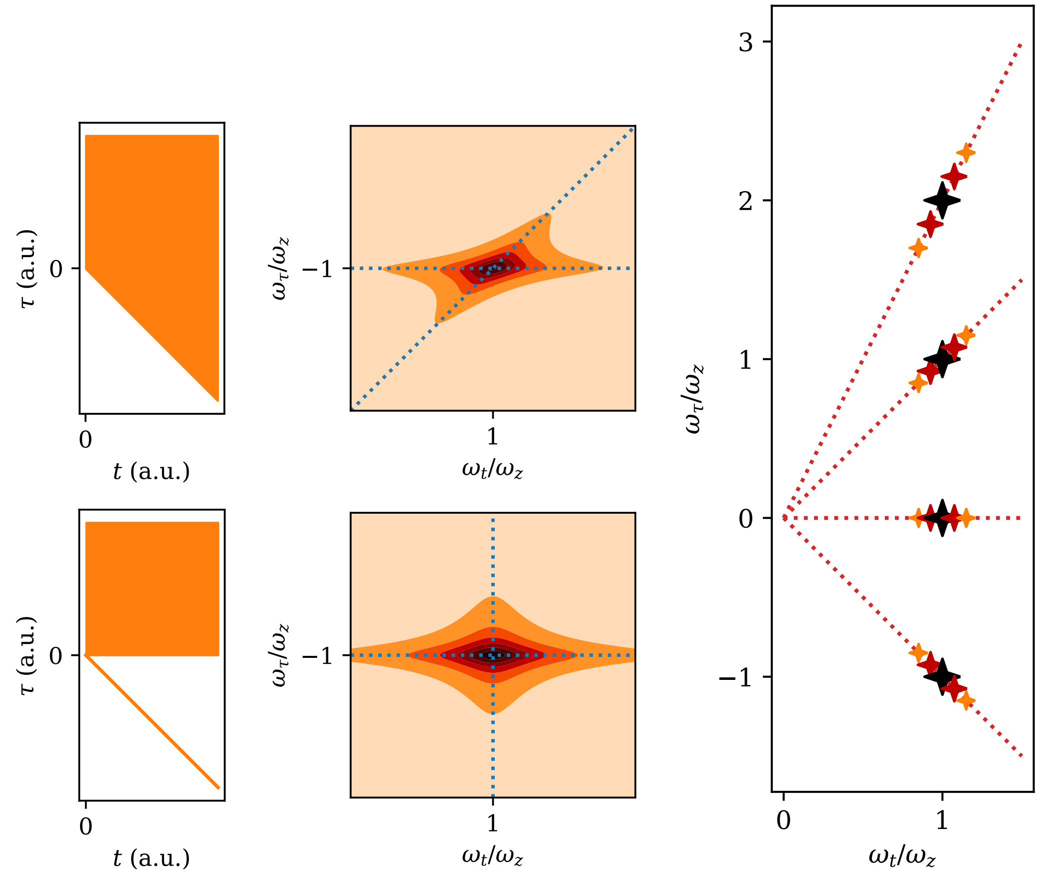

(a) Difference between the appearance of the Josephson Echo peak in the 2D map when the signal in time-domain is collected for both $\tau > 0$ and $\tau < 0$ (upper row), or for $\tau > 0$ only (lower row), as it happens for the data shown in Ref. [89]. Blue dotted lines denote the maxima of the two Lorentzian functions which are found from Eq. 4.13 (upper panel) and Eq. 4.14 (lower panel).

(b) Schematic picture of the effect of inhomogeneous broadening on the appearance of the 2D map. The statistical distribution of ω_z acts to shift the position of the four peaks towards the origin along the red dotted lines.

Figure 4.5. Schematic representation of two effects determining the shape and the orientation of the peaks measured in a 2D experiment, applied to the case of LSCO probed with $c-$axis polarized pulses.

In Fig. 4.6 we fit the full spectral profile in Eq. 4.16 on the 2D data collected in Ref. [89], leaving as free parameters the central value $\bar{\omega}_z$ and the variance σ of the gaussian distribution of plasma frequencies, as well as the homogeneous broadening. The values obtained are $\bar{\omega}_z = 2.01$ THz, $\gamma = 0.04$ THz and $\sigma = 0.15$ THz, which are however different from those reported in Ref. [89] because of the different fitting model used [129]. The same values are then used to simulated the other three peaks through Eq. 4.17, Eq. 4.18 and Eq. 4.19. The comparison between the obtained lineshapes and the experimental maps is qualitatively reasonable, given the set of approximations that we have made in order to get an analytical formula which can be used to fit the experimental peaks.

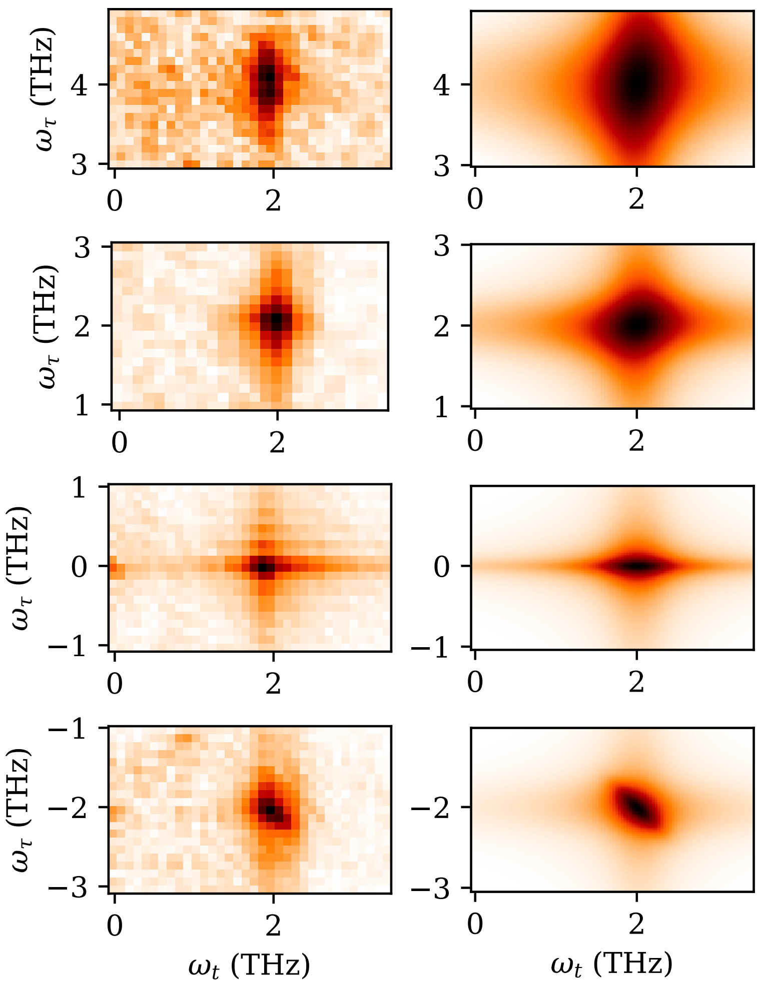

Figure 4.6. Comparison between the experimental peaks collected in Ref. [89] at $T = 6$ K (left column) and the simulations obtained by using the simple model for the inhomogeneities presented above (right column).We fitted the full map of the Josephson Echo peak using Eq. 4.16 and we kept the same $\bar{\omega}_z$, γ and σ to simulate the other three peaks through Eq. 4.17, Eq. 4.18 and Eq. 4.19.

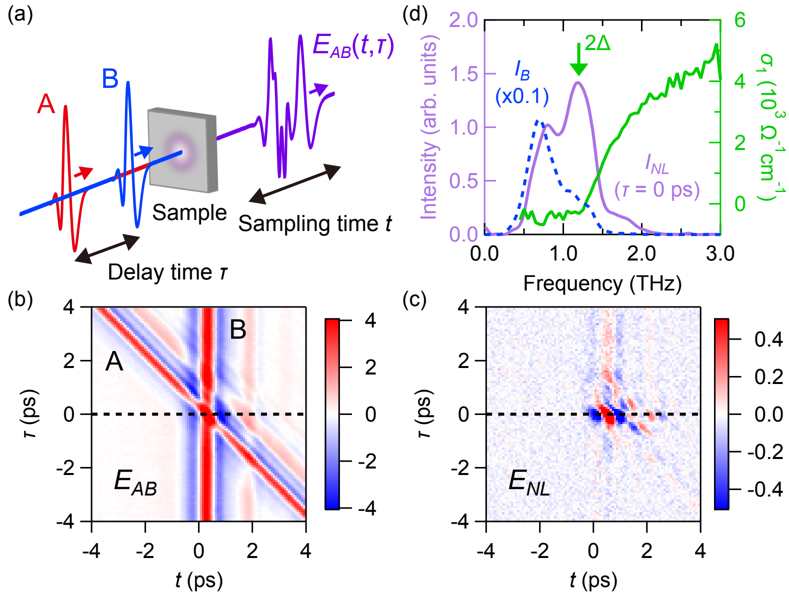

Figure 4.7. (a) A schematic of the THz 2DCS experiment. (b) Time traces of the A and B pulses together ($E_{AB}(t, \tau)$) transmitted after the NbN sample ($T_c = 14.9$ K) at 5 K as a function of the sampling time t and the delay time τ. (c) The same plot as (b) but for the nonlinear signal $E_{NL}(t, \tau)$. (d) Power spectrum of the THz nonlinear signal from NbN at 5 K measured at $\tau = 0$ ps with the broad-band THz pulses (purple, left axis). The blue dashed curve on the left axis is the power spectrum of the B-pulse. The green curve on the right axis shows the real part of the optical conductivity at 5 K.

4.2 Application to superconducting NbN

In this section, we present the THz nonlinear response of the conventional dirty-limit superconductor NbN, investigated using 2D-THz spectroscopy as reported in Ref. [72]. The experimental data were collected by N. Peter Armitage's research team, while the theoretical analysis, including numerical simulations, was conducted in collaboration with G. Seibold.

The schematic of the experiment is depicted in Fig. 4.7(a). Two intense single-cycle THz pulses are generated using the tilted-pulse front technique with $LiNbO_3$ [59, 148, 62]. We first performed 2D-THz spectroscopy on NbN ($T_c = 14.9$ K) using broadband THz pulses, whose peak E-field did not exceed 3 kV/cm. We measured the transmitted THz E-fields of two pulses ($E_A(t, \tau)$, $E_B(t)$) separately, and of both pulses ($E_{AB}(t, \tau)$) together as shown in Fig. 4.7(b). We swept the delay time τ of the A-pulse with respect to the arrival of the B-pulse. The E-field of the nonlinear signal is obtained as $E_{NL}(t, \tau) = E_{AB}(t, \tau) - E_A(t, \tau) - E_B(t)$, presented in Fig. 4.7(c). We perform a Fourier transform with respect both t and τ. Fig. 4.7(d) shows the power spectrum of the nonlinear signal at 5 K when $\tau = 0$ ps (the purple curve). The nonlinear signal exhibits two peaks: one matches twice the SC gap 2Δ identified in the THz optical conductivity measured at 5 K (the green curve on the right axis), and the other is located at slightly higher energy than the center frequency of the B-pulse.

In Fig. 4.8(a), we present the power spectrum of the nonlinear signal at $\tau = 0$ ps

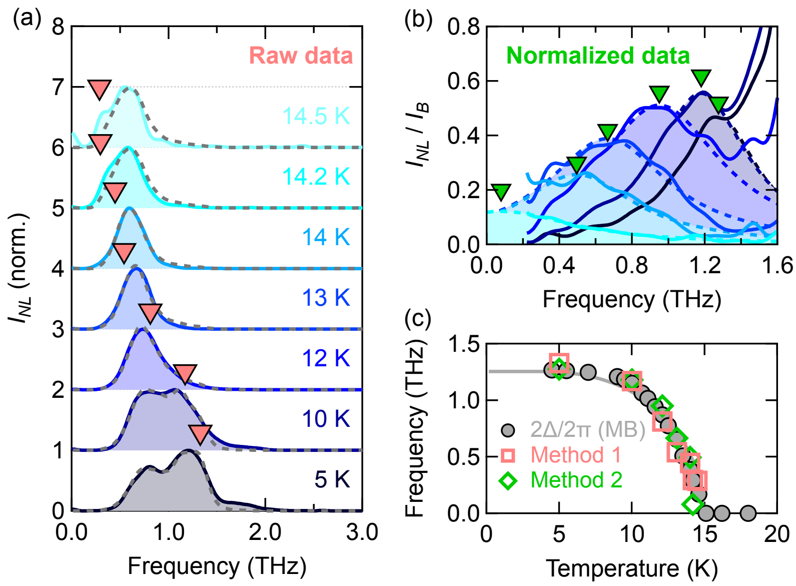

Figure 4.8. (a) Power spectrum of the nonlinear signal from NbN (T_c = 14.9 K) when τ = 0 ps at different temperatures with single-cycle THz pulses. The grey dashed curves denote the fit to the data using a Lorentzian multiplied by the B-pulse power spectra. The obtained peak energy is presented by the red arrows. (b) The nonlinear signal in (a) divided by the B-pulse power spectra as a function of temperature. The obtained peak energy with fitting is shown by the green arrows. The dashed curves are the fits to the data using a Lorentzian. (c) Peak energy of the nonlinear signal as a function of temperature obtained by fitting the raw data in (a) (red open squares) and the normalized data in (b) (green open diamonds). The grey circles are the temperature dependence of the gap evaluated using the Mattis-Bardeen model.

measured at different temperatures. The peak energy in the nonlinear signal shows a redshift with increasing temperature. We evaluated the energy of the peak in two ways. First, we fit the power spectra of the nonlinear signal using the power spectrum of the B-pulse multiplied by a Lorentzian. The fits reasonably reproduce the data as presented by the grey dashed curves in Fig. 4.8(a). The extracted peak energy is plotted as a function of temperature by red open squares in Fig. 4.8(c), in good agreement with the temperature dependence of 2Δ (the grey circles) as seen in the linear responses.

We also evaluated the peak energy by normalizing the nonlinear signal spectra with the B-pulse spectra, as shown in Fig. 4.8(b). While the normalized spectra display an increasing tendency toward higher frequency below 12 K, peaks are discerned in the frequency range from 0.3 to 1.4 THz. We fit the normalized spectrum with a Lorentzian and plot the obtained peak energy as a function of temperature by green open diamonds in Fig. 4.8(c), consistent with those in the first procedure. We note that the same result of the peak-energy shift is obtained using the A-pulse to normalize the nonlinear signal. This direct correspondence between the peak energy of the nonlinear signal and the SC gap energy was also found in other NbN samples with different T_c.

To obtain deeper insight into the spectrum of the nonlinear signal, we performed

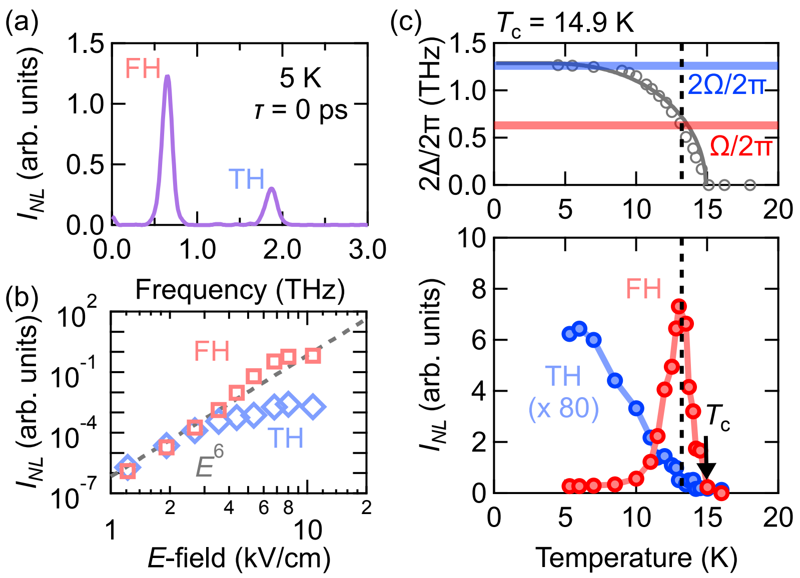

Figure 4.9. (a) Power spectrum of the THz nonlinear signal at 5 K measured at $\tau = 0$ ps with narrowband THz pulses. (b) The frequency-integrated intensity of the FH and TH contributions at 5 K when $\tau = 0$ ps as a function of the B-pulse peak E-field. The dashed grey curve is the guide to the eye with a slope of 6. (c) Temperature dependence of the frequency-integrated intensity of the FH (red) and TH (blue) contributions. The top presents the temperature dependence of 2Δ evaluated from the linear conductivity as compared to Ω (red) and 2Ω (blue). The solid grey curve is the gap computed by numerically solving the BCS equation. The black dashed line denotes the temperature that satisfies $\Omega = 2\Delta$.

THz 2DCS using narrowband THz pulses with the peak E-field of 3 kV/cm and a driving angular frequency of $\Omega = 0.63$ THz. Fig. 4.9(a) shows the nonlinear signal spectra for NbN with $T_c = 14.9$ K measured at 5 K when $\tau = 0$ ps. The power spectrum exhibits two peaks at 0.63 THz and 1.9 THz, corresponding to the FH and third harmonic (TH) contributions, respectively. Both FH and TH intensities follow E^6 as shown in Fig. 4.9(b) up to the THz peak E-field of 10 and 3 kV/cm, respectively, indicating that both are third-order nonlinear responses. As discussed in Chapter 1, a monochromatic field is able to generate through a third-order non linear process signals at Ω and 3Ω. The novelty of this setup as compared to standard THG experiments discussed in Chapter 1 is the possibility to directly extract the nonlinear FH contribution by subtracting the $E_A + E_B$ signal from the E_{AB} one, thus removing the linear-order contribution.

Fig. 4.9(c) shows the frequency-integrated intensity of the FH and TH signals as a function of temperature with the multi-cycle THz pulses when $\tau = 0$ ps. Here, we integrate from 0.3 to 1 THz for the FH signal, and from 1.6 to 2.2 THz for the TH signal. The temperature dependence of the TH signal is consistent with the previous reports where it takes its maximum intensity when twice the drive frequency matches twice the SC gap energy 2Δ (i.e. $2\Omega = 2\Delta$) as shown in the top panel [98, 139, 99, 128], see for comparison Fig. 1.1. By contrast, the FH signal displays a resonant enhancement when the driving frequency matches 2Δ (i.e. $\Omega = 2\Delta$).

4.2.1 Numerical simulations and phenomenological theory

To clarify the experimental observations, we analyze the different nonlinear processes following the diagrammatic approach presented in the chapters above and published in previous work [20, 130, 140, 123]. We recall that nonlinear processes in the superconducting state can be obtained by combining the diamagnetic (quadratic) and paramagnetic (linear) couplings between electronic excitation and the electromagnetic field, as reported in Eq. 1.27 and in Section 1.4. In the diagrammatic representation, the former is represented as a density-like electronic vertex with two-photon lines attached, while the latter appears as current-like electronic vertex with a single-photon line. We recall that the third-order nonlinear current is expressed as

$$J_{NL}(\omega) = \int d\omega_i \, K(\omega_1, \omega_2, \omega_3) A(\omega_1) A(\omega_2) A(\omega_3) \delta(\omega - \omega_1 - \omega_2 - \omega_3), \tag{4.20}$$

where $A(\omega)$ denotes the gauge field. When an incoming monochromatic field $A(\omega) = A_0 \left[\delta(\omega - \Omega) + \delta(\omega + \Omega)\right]$ is considered, the previous expression reads more simply,

$$\begin{aligned} J_{NL}(\omega) &= \delta(\omega - \Omega)[K(\Omega, \Omega, -\Omega) + K(\Omega, -\Omega, \Omega) + K(-\Omega, \Omega, \Omega)] A_0^3 \\ &\quad + \delta(\omega - 3\Omega) K(\Omega, \Omega, \Omega) A_0^3 + (\Omega \to -\Omega), \end{aligned} \tag{4.21}$$

which predicts the generation of two harmonics at frequencies Ω and 3Ω, both of which can be accessed by the technique described above and controlled by different combinations of frequencies entering the nonlinear kernel. As recalled in Chapter 1, the general expression Eq. 4.20 for a clean superconductor is greatly simplified because only a diamagnetic, Raman-like density interaction between fermions and gauge fields is allowed. The relevant diagram is shown for convenience in Fig. 4.10(a). Accordingly, one has only two-photon vertices and Eq. 4.20 becomes

$$\begin{aligned} J_{NL}^{\text{dia}}(\omega) &= \int d\omega_i \, K^{\text{dia}}(\omega_1 + \omega_2) A(\omega_1) A(\omega_2) A(\omega_3) \delta(\omega - \omega_1 - \omega_2 - \omega_3) \\ &= \int d\omega' \, K^{\text{dia}}(\omega') A(\omega - \omega') A^{(2)}(\omega'), \end{aligned} \tag{4.22}$$

having denoted

$$A^{(2)}(\omega) \equiv \int d\omega' \, A(\omega') A(\omega - \omega'). \tag{4.23}$$

Here, the only possible maxima in the nonlinear current occurs when the sum of two incoming photon frequencies match the energy at which the kernel is enhanced, i.e., for a superconductor $\omega_1 + \omega_2 = 2\Delta$. In the case of monochromatic incident pulses at frequency Ω, this condition is satisfied when $2\Omega = 2\Delta$, at which both the FH and TH responses are expected to be enhanced. By contrast, in our experiments, the nonlinear FH response in the disordered NbN is enhanced at $\Omega = 2\Delta$, indicating that the diamagnetic process cannot account for the observations presented above, leading us to consider other processes.

In the presence of disorder, coupling via paramagnetic current-like processes are also allowed, which includes both self-energy and vertex corrections induced by scattering with impurities. In previous theoretical works [123, 14, 140, 130], it has been shown that the most important contribution to the nonlinear current comes from the diagram on the left in Fig. 4.10 (b), where one has to retain the full generic

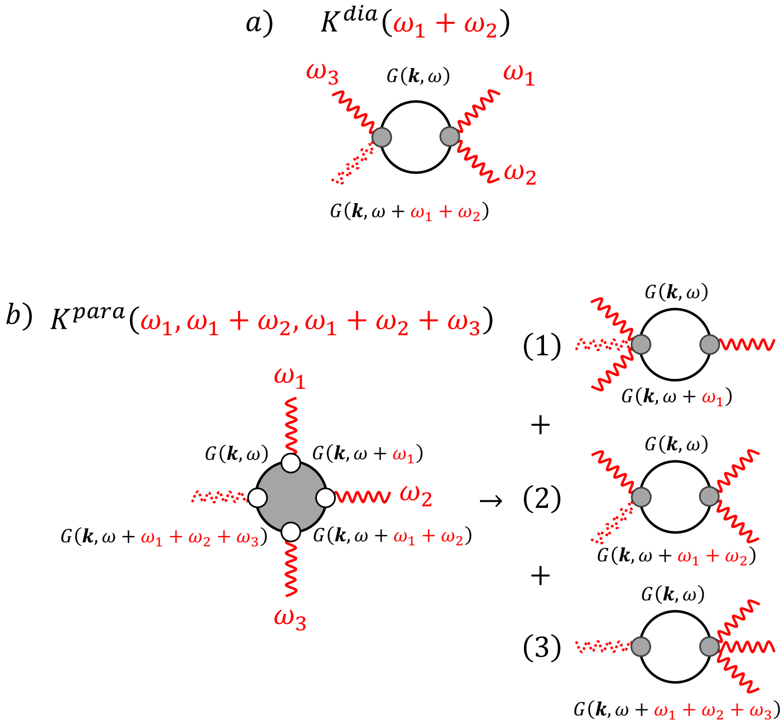

Figure 4.10. Diagrams that contribute to the purely BCS part of the nonlinear kernel. In the clean case (a), K^{dia} is the only important process, involving two diamagnetic interactions (grey bullets). This produces a response that explicitly depends only on the sum of two incoming photons (red wavy lines) entering a convolution of two fermionic propagators (black lines) $G(\mathbf{k}, \omega)$ where ω and $\mathbf{k}$ are the frequency and momentum, respectively, of the electronic Green's function, over which one integrates. In the disordered case (b), the paramagnetic process K^{para} dominates the nonlinear response, with four current-like vertices (white bullets) connecting four electron propagators and four-photon lines. In this case, one has different combinations of the external frequencies entering the fermionic propagators, which are convoluted. The grey-shaded area inside the bubble represents the self-energy and vertex corrections induced by impurities. The full frequency structure of K^{para} on the left is mapped through Eq. 4.26 into the sum of the three effective Kubo-like susceptibilities on the right.

	TH	FH
K^{dia}	$\Omega = \Delta$	$\Omega = \Delta$
K^{para}	$\Omega = 2\Delta/3, \Delta, 2\Delta$	$\Omega = \Delta, 2\Delta$

Table 4.1. Summary of the possible enhancements of the first and third harmonic signals allowed by the diamagnetic and paramagnetic kernels reported in the text and observed in the numerical simulations.

expression in Eq. 4.20, plus vertex corrections induced by amplitude and phase fluctuations, which dominate the signal at high disorder levels. By examining the structure of this diagram in the Lehmann representation, as done e.g. in Ref. [116], we can rewrite the nonlinear kernel in the form of $K^{\mathrm{para}}(\omega_1, \omega_1 + \omega_2, \omega_1 + \omega_2 + \omega_3)$, leading to

$$J^{\mathrm{para}}_{NL}(\omega) = \int d\omega_i \, K^{\mathrm{para}}(\omega_1, \omega_1{+}\omega_2, \omega_1{+}\omega_2{+}\omega_3) A(\omega_1) A(\omega_2) A(\omega_3) \delta(\omega{-}\omega_1{-}\omega_2{-}\omega_3). \tag{4.24}$$

From Eq. 4.24, one can find that for a monochromatic field with frequency Ω, the paramagnetic nonlinear current can in principle display resonances whenever any of the three combinations of external frequencies running into the fermionic kernel in K^{para} match 2Δ. Importantly, the resonances at $\Omega = 2\Delta/3$ and $\Omega = 2\Delta$ in the TH component and at $\Omega = 2\Delta$ in the FH component are unique to the paramagnetic process. In particular, the resonance of the FH paramagnetic contribution at $\Omega = 2\Delta$ coincides with our experimental observation, demonstrating that the observed FH nonlinear signal stems from paramagnetic processes.

Having established the theoretical framework, we simulated the time evolution of an attractive Hubbard model with local disorder

$$H = -t \sum_{\langle ij \rangle} c^{\dagger}_{i,\sigma} c_{j,\sigma} - |U| \sum_i n_{i,\uparrow} n_{i,\downarrow} + \sum_{i,\sigma} V_i n_{i,\sigma} \,. \tag{4.25}$$

Here, the first term describes the hopping of charge carriers between nearest neighbors, the second term is the on-site attractive interaction, and the last term introduces disorder via a site-dependent potential.The latter is taken from a flat distribution with $-V_0 \leq V_i \leq +V_0$. In addition, we coupled a monochromatic gauge field to Eq. 4.25 via the Peierls substitution and solved the model by evaluating the time-dependent Bogoliubov-De Gennes equations. Nonlinear FH and TH components of the nonlinear current were then computed from the resulting time-dependent density matrix. Results presented here were obtained for a 16×16 square lattice at zero temperature with charge carrier concentration and attractive interaction fixed to $n = 0.5$ and $U/t = 2$, respectively. The strength of the impurity potential V_0/t is converted to the dimensionless parameter $k_F l$ where k_F is the Fermi wave vector and l is the electronic mean free path. The details of the numerical implementation are described in previous works [123, 122, 14]. In the numerical simulations, we can separately evaluate the nonlinear current, which arises from only BCS quasiparticle excitations and that which also includes the amplitude mode, by constraining the time-dependence of the SC order parameter in the density matrix or not. In order to confirm the dependence of the results on the strength of the disorder, we performed

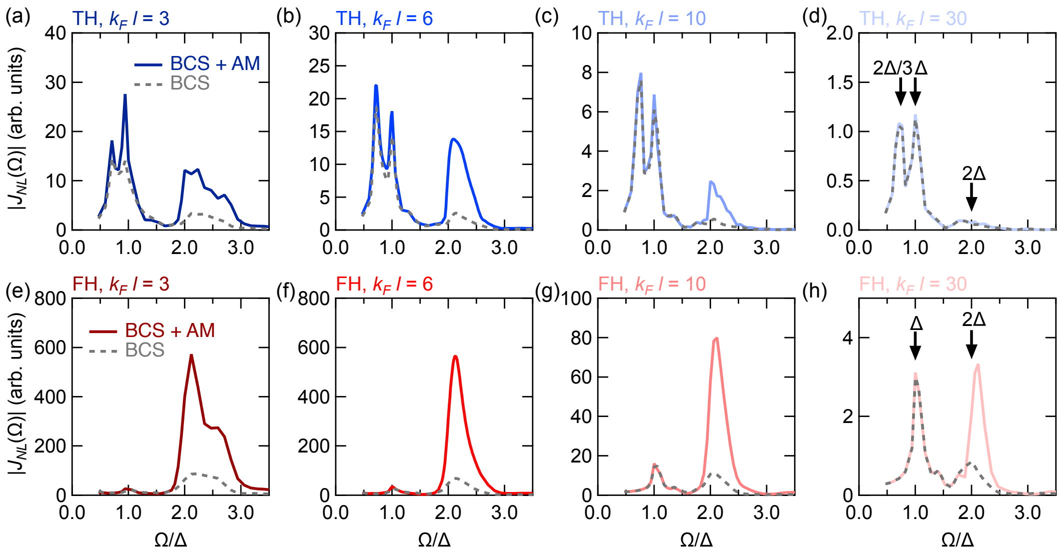

Figure 4.11. (a-d) The nonlinear current amplitude $|J_{NL}(\Omega)|$ for the TH components as a function of the driving frequency Ω normalized by the SC gap Δ, for $k_F l$ values of (a) 3, (b) 6, (c) 10, and (d) 30, respectively. The BCS contribution and the sum of the BCS and amplitude-mode (AM) contributions are denoted by the dashed and solid curves, respectively. (e-h) The same plots as (a-d), but for the FH components.

simulations for several disorder levels. Since we used the NbN samples with $T_c = 14.9$ K, 12.5 K, and 9.1 K, we chose $k_F l = 3$, 6, and 10 in the numerical simulations [22]. To further confirm the robustness of the amplitude-mode predominance at $\Omega = 2\Delta$, we also performed the numerical simulation for $k_F l = 30$.

We present the numerical results of the TH and FH nonlinear current amplitudes for different $k_F l$ in Fig. 4.11(a-d) and (e-h), respectively. The corresponding TH and FH nonlinear current intensities for $k_F l = 10$ are shown in Fig. 4.14(a) and (b) above, respectively. We find that (i) the nonlinear FH spectra hosts peaks at $\Omega = \Delta$ and $\Omega = 2\Delta$ and (ii) the TH contribution is peaked at $\Omega = 2\Delta/3$, $\Omega = \Delta$ and $\Omega = 2\Delta$, see Table 4.1. Remarkably, the $\Omega = 2\Delta$ resonance for the FH response is strongly enhanced by the amplitude mode regardless of the disorder level. In the following we will propose a theoretical explanation for this enhancement based on a perturbative treatment of disorder, for the moment we remark that these numerical results reveal that the experimentally observed resonance at $\Omega = 2\Delta$ in the FH nonlinear signal can be attributed to the amplitude mode in the entire investigated disorder range. In contrast, the other resonances are strongly influenced by the disorder level. For instance, Fig. 4.11(a)-(c) show that the amplitude-mode contribution at $\Omega = \Delta$ in the TH increases going from the $k_F l = 30$ case to the more disordered $k_F l = 3$ case, in agreement with the previous works [130, 123, 140].

In order to compute the spectral features at finite temperatures and for an arbitrary pulse shape, we modeled the nonlinear kernel as the sum of three Lorentzian functions as

$$K^{\text{para}}(\omega_1, \omega_1+\omega_2, \omega_1+\omega_2+\omega_3) = \alpha^{(1)}L(\omega_1) + \alpha^{(2)}L(\omega_1+\omega_2) + \alpha^{(3)}L(\omega_1+\omega_2+\omega_3), \tag{4.26}$$

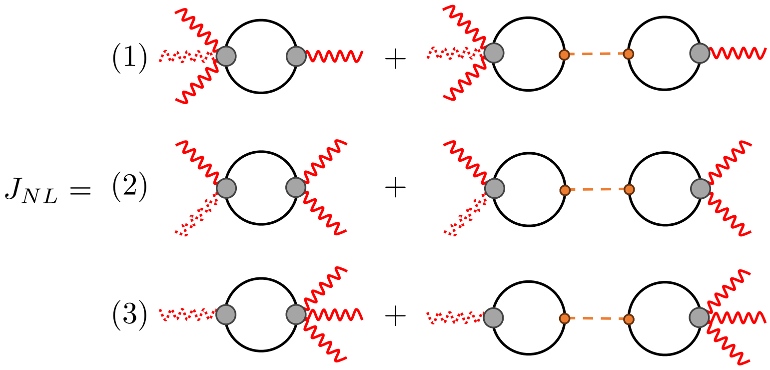

Figure 4.12. Diagrams contributing to the nonlinear kernel Eq. 4.26, with each row weighted by the corresponding $\alpha^{(i)}$. In the model, we effectively approximate both BCS and amplitude-mode contributions (first and second columns, respectively) as Lorentzian propagators at energy 2Δ.

where $\alpha^{(i)}$ is the weight for each contribution and

$$L(\omega) = \frac{\Delta(T)^2}{(\omega + i\delta)^2 - 4\Delta(T)^2}, \tag{4.27}$$

is a Lorentzian function peaked at 2Δ, i.e. the characteristic energy scale of both BCS and amplitude-mode contributions. In order to include the finite temperature effect, we included in the Lorentzian by the factor $\Delta(T)^2$, such that the kernel softens approaching T_c and mimics the temperature evolution of the nonlinear response in the clean case [20].

The kernel in Eq. 4.26 approximates the possible diagrammatic contributions to the nonlinear current shown in Fig. 4.12, which is the minimal model to account for the numerically observed positions of the resonances. It should be stressed that the diagrams of Fig. 4.12 must be interpreted as a mapping of the real paramagnetic diagram of Fig. 4.10 into effective Kubo-like diagrams, leading each one to a specific resonant combination of the incoming frequencies, in such a way that the resulting resonance is at the position foreseen by the numerical simulation. With this in mind, the three processes lead to

$$J^{(1)}_{NL}(\omega) = 3\alpha^{(1)} \int d\omega' \, A(\omega')A^{(2)}(\omega - \omega')L(\omega'), \tag{4.28}$$

$$J^{(2)}_{NL}(\omega) = 3\alpha^{(2)} \int d\omega' \, A(\omega - \omega')A^{(2)}(\omega')L(\omega'), \tag{4.29}$$

$$J^{(3)}_{NL}(\omega) = \alpha^{(3)} L(\omega) \int d\omega' \, A(\omega')A^{(2)}(\omega - \omega'). \tag{4.30}$$

We find that here $J^{(2)}_{NL}(\omega)$ has the same frequency dependence as diamagnetic processes, which have an intrinsic Kubo-like nature. One can now fit the parameters $\alpha^{(i)}$ by plugging Eq. 4.26 into the general expression Eq. 4.24 for monochromatic fields centered at Ω. The FH nonlinear current can be written as

$$J_{NL}(\Omega) = \alpha^{(1)}[2L(\Omega) + L(-\Omega)] + \alpha^{(2)}[2L(0) + L(2\Omega)] + 3\alpha^{(3)}L(\Omega), \tag{4.31}$$

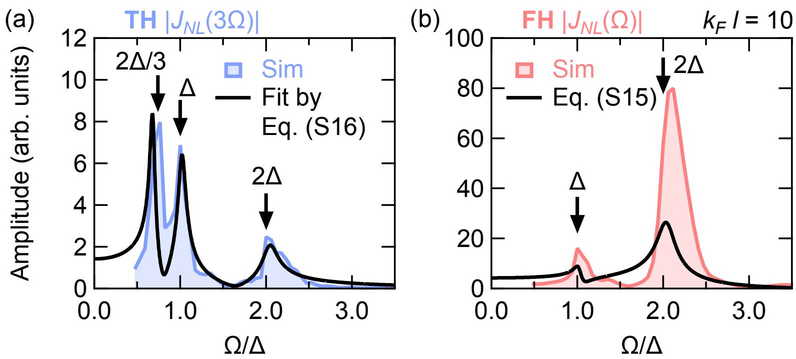

Figure 4.13. (a) Fitting to the numerical simulated amplitude of the TH nonlinear response as a function of the driving frequency Ω using Eq. 4.32. The (b) The FH nonlinear response computed by Eq. 4.31 with the weights $\alpha^{(i)}$ obtained from the fitting in (a). Here, the disorder level is $k_F l = 10$.

where we take into account the combinatorial prefactors, which stem from the different ways of choosing the arguments of the L functions among two positive Ω and one negative Ω frequencies to get an overall FH signal. Similarly, we can express the TH nonlinear current as

$$J_{NL}(3\Omega) = \alpha^{(1)}L(\Omega) + \alpha^{(2)}L(2\Omega) + \alpha^{(3)}L(3\Omega). \tag{4.32}$$

We determined the weights $\alpha^{(i)}$ in Eq. 4.31 and 4.32 by fitting the exact numerical results for the BCS and amplitude-mode contributions ($k_F l = 6$) with Eq. 4.32. In Fig. 4.13(a), we compare the numerical results for the TH nonlinear current with the fit using Eq. 4.32, while Fig. 4.13(b) shows the FH nonlinear current calculated by Eq. 4.31 with the same $\alpha^{(i)}$ fitted on the TH, compared with the corresponding numerical simulation. Despite the simplification of the model in Eq. 4.26, the previous relations qualitatively reproduce the numerical results for both the FH and TH.

With this model at hand we proceed to compute the temperature dependence of the FH and TH signals. We employed an incoming pulse with a Gaussian spectrum $E(t) = E_0 e^{-t^2/(2\tau^2)} \cos(\Omega t)$ with $\Omega = 0.63$ THz, the frequency of the experimental band-pass filter, and $\tau \sim 3$ ps. We modeled the scaling in temperature of the superconducting gap amplitude as in the experiments, with $2\Delta(0) = 1.2$ THz fitted from the optical conductivity at 5 K. The TH and FH intensities are proportional to $|J_{NL}(\Omega)|^2$ and $|J_{NL}(3\Omega)|^2$ respectively, evaluated through Eq. 4.26 keeping a finite broadening $\delta = 0.12$ THz. Fig. 4.14(a) compares the numerical results with the experimental data appropriately normalized by the incoming THz E-field for the FH and TH components, as prescribed in Eq. 1.62. The calculated result for the FH component displays a substantial agreement with experiments, indicating that the FH signal stems from the amplitude-mode contribution at $\Omega = 2\Delta$ mediated by the paramagnetic processes. The numerical result for the TH component displays a monotonic increase when the temperature is lowered, consistent with the experimental data. The increase in the TH intensity toward the lower temperature is due to the resonance of $\Omega = \Delta$ around at very low temperature, which is likely dominated by the amplitude mode in the high disorder level relevant for NbN. To check the internal consistency of our approach, we further simulate the nonlinear

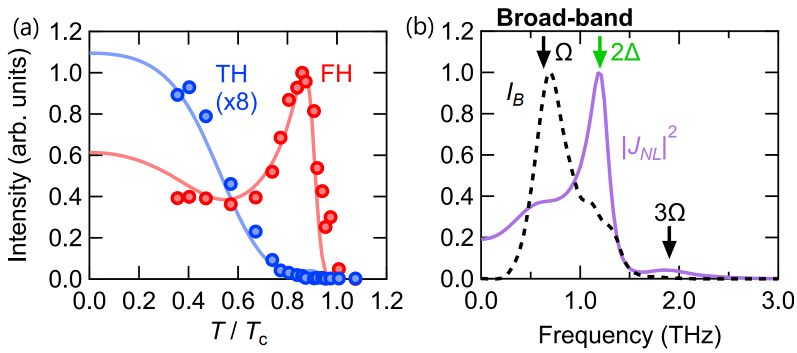

Figure 4.14. (a) Comparison between the experimental data (open circles) and the theoretical results (solid curves) for the temperature dependence of the FH (red) and TH (blue). The temperature T is normalized by T_c. To remove the temperature-dependent screening effects, the experimental nonlinear signal intensity ($|E_{NL}|^2$) is normalized by the internal B-pulse E-field (E_B^6). The theoretical results correspond to the nonlinear current intensity $|J_{NL}|^2$ at the driving frequency of 0.63 THz for a E-field constant in temperature.(b) The nonlinear current simulated using the broadband THz pulses. The black dashed curve shows the intensity of the driving THz E-field, obtained by simulating the experimental THz B-pulse.

current driven by broadband THz pulses. Fig. 4.14(b) presents the nonlinear current induced by the broad-band THz pulses for $2\Delta = 1.2$ THz, using the incoming pulse in the experiment. The computed nonlinear current exhibits three peaks at $\Omega = 0.63$ THz, $2\Delta = 1.2$ THz, and $3\Omega = 1.9$ THz, qualitatively reproducing the experimental observation in Fig. 4.7(b).

4.2.2 Analysis of the 2D-THz spectra

In the previous discussion we mainly focused on the information which can be extracted by analysing the $\tau = 0$ signal from the 2D-THz setup, which was used to access the non-linearly generated FH component in the narrowband measurements and the full $J_{NL}(\omega)$ for the broadband ones. Here we show how one can disentangle the various nonlinear optical processes that contribute to the full $\tau-$dependent response, each of which can give different information about excitations and their lifetimes. When two narrowband pulses are employed, the different contributions can be easily mapped onto the 2D spectrum in the space of (ω_t, ω_τ) using the so-called frequency-vector scheme [149, 94], as we have already analyzed in the previous chapter.

To check the difference between pump-probe experiments and 2D-THz response, we then performed measurements of the NbN sample ($T_c = 14.9$ K) at 5 K using narrow-band (centered at $\Omega = 0.63$ THz) and broad-band THz pulses for A and B pulses, respectively. This is essentially the same situation as conventional pump-probe experiments in Ref. [98, 97], except for the slightly more intense probe B E-field of 3 kV/cm. Fig. 4.15(a) and (b) show the time traces of the A and B pulses together ($E_{AB}(t, \tau)$) and the nonlinear signal ($E_{NL}(t, \tau)$) transmitted after the sample as a function of the sampling time t and the delay time τ. In Fig. 4.15(c), we present the nonlinear signal as a function of τ with the sampling time fixed at

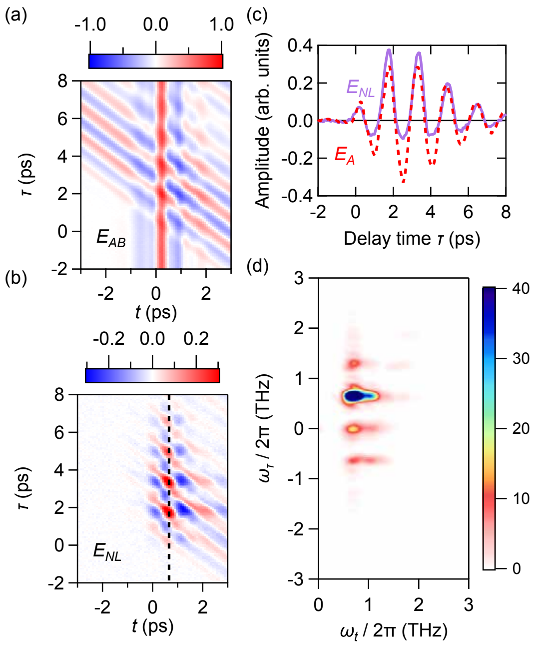

Figure 4.15. (a) Time traces of the narrow-band A and broad-band B pulses together ($E_{AB}(t, \tau)$) transmitted through the NbN sample ($T_c = 14.9$ K) at 5 K as a function of the sampling time t and the delay time τ. (b) The same plot as (a) but for the nonlinear signal ($E_{NL}(t, \tau)$). (c) Nonlinear signal as a function of τ measured at $t = 0.66$ ps (denoted by dashed vertical line in (b)). The red dashed curve shows the time trace of the A-pulse. (d) 2D power spectra of the nonlinear signal measured in (c) for $\tau \geq 0$ ps (the AB pulse sequence).

$t = 0.66$ ps together with the narrow-band A-pulse. Importantly, the nonlinear signal oscillates following the A-pulse, indicating the presence of the Ω-oscillatory component, which is not discerned in strong pump-weak probe setups. This is clearly seen in the 2D power spectra of the nonlinear signal for $\tau \geq 0$ ps displayed in Fig. 4.15(d). One can find peaks at $\omega_\tau = 2\Omega$, Ω, 0, and $-\Omega$, corresponding to the two-quantum, non-rephasing, pump-probe, and rephasing responses, respectively, as expected from the general consideration of the frequency-vector scheme.

We now analyse the 2D spectra when two THz pulses are broadband in light of the theoretical framework exposed above, which helps to understand where our approach necessarily needs refinement. The measurements can be reproduced by a phenomenological model which assumes two third-order nonlinear processes: (i) a coherent part associated with the effective nonlinear kernel due to quasiparticle and amplitude mode, given by the sum of Eq. 4.28, Eq. 4.29 and Eq. 4.30, (ii) an incoherent response modeled as the diamagnetic-like process in Eq. 4.29 with central resonance at zero frequency, which we assign to out-of-equilibrium quasiparticle recombination. The procedure to get the 2D-THz map from these expressions follows the steps presented in the Chapter 3, i.e. we replace $A(\omega) \to A(\omega)(1+e^{-i\omega\tau})$, keeping as $A(\omega)$ the spectrum of the transmitted broadband THz field, in the kernels recalled above. We show in Fig. 4.16(a) the experimental 2D power spectra of the nonlinear signal, together with the simulation in Fig. 4.16(b). While the intensities of some

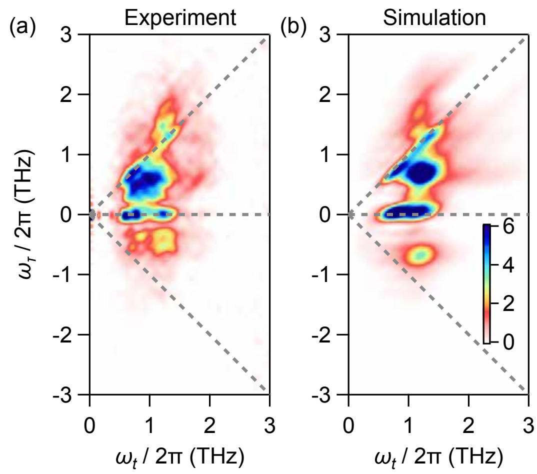

Figure 4.16. (a) 2D power spectra of the nonlinear signal measured at 5 K with the broad-band THz pulses. (b) The same plot as (a) but in the simulation.

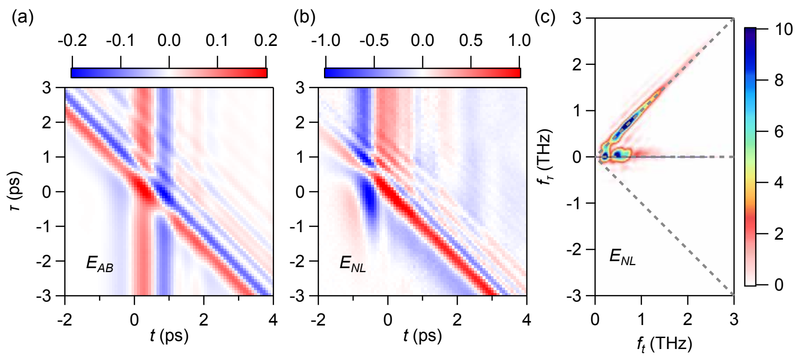

Figure 4.17. The THz 2D data for the A and B peak E-fields of 72 and 82 kV/cm. (a) Time traces of the A and B pulses together ($E_{AB}(t, \tau)$) transmitted after the NbN sample ($T_c = 14.9$ K) at 5 K as a function of the sampling time t and the delay time τ. (b) The same plot as (a) but for the nonlinear signal $E_{NL}(t, \tau)$. (c) 2D power spectra of the nonlinear signal shown in (b).

peaks are different, the positions and shapes of the peaks are reasonably reproduced.

Finally, we present the THz 2D spectra measured with the maximum A and B peak E-fields of 72 and 82 kV/cm, in Fig. 4.17(a) and (b), which show $E_{AB}(t, \tau)$ and $E_{NL}(t, \tau)$, respectively. When compared to Fig. 4.7(d) where A and B peak E-fields are 3 kV/cm, this high-field case displays prominent long-lasting oscillations, one along the τ direction for $\tau \geq 0$ ps and the other along the anti-diagonal direction for $\tau < 0$ ps. Accordingly, the power spectrum of $E_{NL}(t, \tau)$ in Fig. 4.17(c) displays streaks along $f_\tau = 0$ and $f_\tau = f_t$, as also measured by another group using extremely intense pulses [92], while losing all the coherent contribution (i) described above. If one wanted to reproduce with a minimal model the latter observation, we would again use the incoherent diamagnetic-like process (ii), which producess stripes as we showed in Fig. 3.8a in Chapter 3, with the resonance frequency centered at zero. At such high fields, then, our approach should necessarily be expanded in order to include beyond-equilibrium effects at a microscopic level.

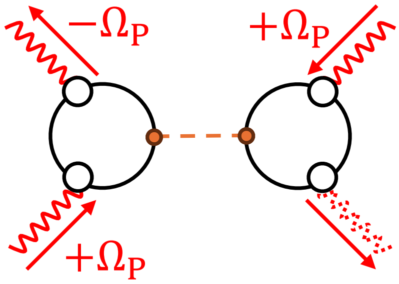

Figure 4.18. The relevant diagram contributing to the enhancement of the amplitude mode contribution to the non-linearly generated first harmonic current by a monochromatic incoming field (wavy lines) centered at $\pm\Omega_P$. Left and right polarization bubbles need to be calculated by effectively including disorder. The intermediate Higgs propagator (dashed line) is read out at zero frequency.

4.2.3 Analytical estimate of the amplitude-mode contribution to the FH

In the rest of the chapter we want to provide some analytical insight to justify the numerical observation reported in the previous section regarding the enhancement of the amplitude-mode contribution to the non-linearly generated first harmonic current. Indeed, an in-depth analysis of the time-dependent results simulated on the finite-size system allowed us to isolate the all important process providing the biggest contribution to the response mentioned above, shown in Fig. 4.18. As discussed in early works by Gorkov and Eliashberg [54, 55, 35], the process that we are considering here is actually the one giving birth to the so-called Eliashberg effect, namely a modification of the value of the order parameter upon irradiation with an electromagnetic field. As discussed in Ref. [29] through the quasiclassical formalism [76], the Eliashberg effect can provide relevant corrections to the linear conductivity of the system. Here we will show that this effect is also connected to the enhancement of the first harmonic of the gauge field. In particular, we will report here a calculation of the Eliashberg effect by means of the effective-action formalism in Matsubara frequency representation, which we then extend to real frequencies using the standard analytical continuation prescription [54, 76], reproducing a result which is fully equivalent to the one obtained through the Keldysh techinque in Ref. [29] but valid at various disorder level $\gamma/(2\Delta)$.

We start by building the contribution to the nonlinear response due to the intermediate Higgs propagator in Fig. 4.18 at general incoming frequencies, which will give rise to the Eliashberg effect when the amplitude fluctuations $\delta\Delta$ are evaluated at zero frequency. We collect in the effective action for the Hubbard-Stratonovich fields and the gauge field the relevant terms involving the amplitude channel, which reads in a sketchy expression

$$\begin{aligned} S[A,\Delta] = &\sum_{i\Omega_1, i\Omega_2} \chi_{001}(i\Omega_1, i\Omega_{12}) A(i\Omega_1) A(i\Omega_2) \delta\Delta(-i\Omega_{12}) \\ &+ \sum_{i\Omega} \left(\frac{1}{U} + \chi_{11}(i\Omega) \right) |\delta\Delta(i\Omega)|^2. \end{aligned} \tag{4.33}$$

The first term describes the coupling at second order between the gauge field A via paramagnetic insertions, mediated by σ_0, and the amplitude fluctuation $\delta\Delta$ of the order parameter, mediated by σ_1. Here χ_{001} then encodes the Higgs-light coupling, and the subscripts denote insertion of the corresponding σ_0 or σ_1 Pauli matrices. The second term instead reproduces the RPA-level resummation of the interaction U, which gives rise to the well-known amplitude mode [20]. For instance, introducing the shorthand notation $i\Omega_{12} = i\Omega_1 + i\Omega_2$, one has in the clean limit

$$\chi_{001}(i\Omega_1, i\Omega_2) = \sum_{i\omega_n,\mathbf{k}} \left(\frac{\partial \xi_{\mathbf{k}}}{\partial k}\right)^2 \mathrm{Tr}\,[G(i\omega_n + i\Omega_1, \mathbf{k})G(i\omega_n + i\Omega_{12}, \mathbf{k})\sigma_1 G(i\omega_n, \mathbf{k})], \tag{4.34}$$

which is exactly zero [20]. The expression, as we will see, can be nonetheless generalized to the disordered case, where it becomes instead relevant. After integration of the amplitude fluctuations in Eq. 4.33, we obtain the fourth order term in the gauge field which contributes to the nonlinear first harmonic. Defining as usual the inverse Higgs propagator [20] as

$$\chi_{\Delta\Delta} = \frac{1}{U} + \chi_{11}(i\Omega), \tag{4.35}$$

the action reads

$$\begin{aligned} S[A^4] = \sum_{i\Omega_1, i\Omega_2, i\Omega_3} & \chi_{001}(i\Omega_1, i\Omega_2)\chi_{001}(i\Omega_3, -i\Omega_{123})\chi^{-1}_{\Delta\Delta}(i\Omega_{12})\times \\ & \times A(i\Omega_1)A(i\Omega_2)A(i\Omega_3)A(-i\Omega_{123}). \end{aligned} \tag{4.36}$$

In Fig. 4.19a and 4.19b we show in more detail the structure of the two diagrams $\chi_{001}(i\Omega_1, i\Omega_2)$ and $\chi_{001}(i\Omega_3, -i\Omega_{123})$, respectively. As we will discuss below, even though the two diagrams look similar in Matsubara formalism, the analytical continuation to real frequencies will lead to different results. This has to do with the fact that the A and Δ insertions in the bubble play different roles as *perturbation* and *detection* fields.

After analytical continuation to real frequencies, the nonlinear current due to the Higgs contribution reads

$$J^{(3)}(\Omega) = \int [d\Omega_i]\, \chi^L_{001}(\Omega_1, \Omega_2)\chi^R_{001}(\Omega_3, -\Omega)\chi^{-1}_{\Delta\Delta}(\Omega_{12})A(\Omega_1)A(\Omega_2)A(\Omega_3)\delta(\Omega - \Omega_{123}), \tag{4.37}$$

where we denoted with apices L and R the crucially different functions obtained from the analytical contituations of the two diagrams in Fig. 4.19a and 4.19b, respectively. In presence of a monochromatic field at frequency Ω_P, i.e. $A(\Omega) = A_P\delta(\Omega - \Omega_P) + A_P^*\delta(\Omega + \Omega_P)$, we will show that the left part of the diagram is related to the the Eliashberg effect, i.e. to a finite value of the time-averaged, zero-frequency fluctuation of the order parameter, reading

$$\langle\delta\Delta(0)\rangle_{\Omega_P} \equiv \chi^L_{001}(\Omega_P, -\Omega_P)\chi^{-1}_{\Delta\Delta}(0)|A_P|^2. \tag{4.38}$$

The Eliashberg effect will give a signature in the non-linearly generated first harmonic current thanks to its connection to the right side of the diagram, that we will show to

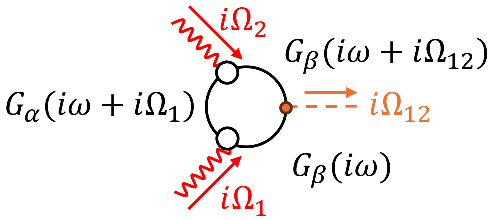

(a) Left part of the relevant diagram for the excitation of the amplitude mode, $\chi_{001}(i\Omega_1, i\Omega_2)$.

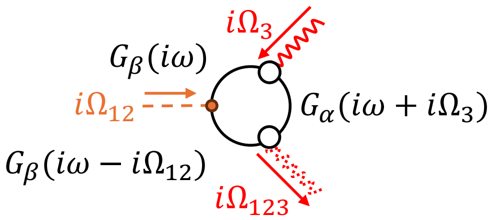

(b) Right part of the relevant diagram for the excitation of the amplitude mode, $\chi_{001}(i\Omega_3, -i\Omega_{123})$.

Figure 4.19. The Feynman diagrams determining the contribution of the amplitude fluctuations to the nonlinear response. Filled dots represent σ_0 vertices for the paramagnetic light-matter interaction, photons are represented as wavy lines; crossed dots represent σ_1 vertices for the interaction with the amplitude mode (dashed line).

be equivalent to the derivative of the current-current response $\chi_{00}(\Omega_P)$ with respect to the order parameter, namely

$$J^{(3)}(\Omega_P) = \chi^R_{001}(\Omega_P, -\Omega_P)\langle\delta\Delta(0)\rangle_{\Omega_P} A_P = \frac{\partial\chi_{00}(\Omega_P)}{\partial\Delta}\langle\delta\Delta(0)\rangle_{\Omega_P} A_P. \tag{4.39}$$

In order to show explicitly these results we need to compute the χ_{001} functions when disorder is present. Before proceeding with this computation, we briefly recall the procedure within the context of the linear conductivity, which leads to the well-known expressions deduced by Mattis and Bardeen [100]. The corresponsing results will also be needed to prove the relation in Eq. 4.39 above.

4.2.4 Linear response in presence of disorder

Let us begin from the procedure to obtain the Mattis-Bardeen [100] expression for the long-wavelength current-current response function $\chi_{00}(|\mathbf{q}| = 0, i\Omega)$. In the clean limit this would read

$$\chi_{00}(i\Omega) = \sum_{i\omega_n,\mathbf{k}} \left(\frac{\partial\xi_\mathbf{k}}{\partial k}\right)^2 \mathrm{Tr}\,[G(i\omega_n, \mathbf{k})G(i\omega_n + i\Omega, \mathbf{k})], \tag{4.40}$$

where the matrix Green function is as always $G(i\omega_n, \mathbf{k}) = (i\omega_n\sigma_0 + \xi_\mathbf{k}\sigma_3 - \Delta\sigma_1)^{-1}$, see Fig. 4.20a. In presence of disorder the momentum $\mathbf{k}$ is not anymore a good quantum number, and one should in principle revert to the following expression

$$\chi_{00}(i\Omega) = \sum_{\alpha\beta}\sum_{i\omega_n} v^2_{\alpha\beta}\,\mathrm{Tr}\,[G_\alpha(i\omega_n)G_\beta(i\omega_n + i\Omega)], \tag{4.41}$$

where now α labels the set of new eigenstates obtained by diagonalizing the Bogoliubov-De Gennes hamiltonian [47] and $v_{\alpha\beta}$ is the matrix element of the velocity operator associated with the paramagnetic-like coupling. If one remains in the limit of validity of Anderson's theorem [6], one can show that the new Green function still retains the form $G_\alpha(i\omega_n) = (i\omega_n\sigma_0 + \xi_\alpha\sigma_3 - \Delta\sigma_1)^{-1}$, where ξ_α is now the eigenvalue associated with the eigenstate α of the hamiltonian which includes the disorder potential but without the pairing interaction, i.e. in the disordered normal state. One can then rewrite

$$\chi_{00}(i\Omega) = \sum_{i\omega_n} \int d\xi d\xi' \, W_\gamma(\xi, \xi') \, \mathrm{Tr} \left[G(i\omega_n, \xi) G(i\omega_n + i\Omega, \xi') \right], \tag{4.42}$$

where we define

$$W_\gamma(\xi, \xi') = \sum_{\alpha\beta} v_{\alpha\beta}^2 \delta(\xi - \xi_\alpha) \delta(\xi' - \xi_\beta). \tag{4.43}$$

Now, one is left with the problem of finding the function $W_\gamma(\xi, \xi')$, which depends on matrix elements $v_{\alpha\beta}$. It is important to notice that in this approximation one can immediately extend the result derived for a dirty metal to the case of a dirty superconductor, that was indeed the original viewpoint adopted in Mattis and Bardeen's work [100]. For a detailed discussion regarding the function $W(\xi, \xi')$ we then refer to the above mentioned work or to Ref. [105], we just mention the result

$$W_\gamma(\xi, \xi') \sim v_F^2 \frac{\gamma}{(\xi - \xi')^2 + \gamma^2}, \tag{4.44}$$

which can be understood if one thinks that disorder mixes up momentum eigenstates, that are used to define the current operator from the kinetic part of the non-interacting hamiltonian, within an energy shell of width $\gamma = v_F l$, with l the mean free path, around the Fermi surface. In the strong disorder limit $\gamma \gg \Delta$, one can actually replace $W(\xi, \xi')$ with a constant and extend the integral over ξ, ξ' across the whole energy range. This procedure is actually equivalent to completely relax momentum conservation between the two electronic propagators entering the current-current response in the clean-limit expression, separately integrating over different momenta in the two Green's functions, as described in Mahan's book [93]. Since one has

$$\int d\xi \, G(i\omega_n, \xi) = \int d\xi \, \frac{i\omega_n \sigma_0 - \xi \sigma_3 + \Delta \sigma_1}{(i\omega_n)^2 - \xi^2 - \Delta^2} = -\pi \frac{i\omega_n \sigma_0 + \Delta \sigma_1}{\sqrt{\Delta^2 - (i\omega_n)^2}}, \tag{4.45}$$

then the current-current response reads, omitting overall v_F, N_F factors that are not relevant for the present discussion,

$$\begin{aligned} \chi_{00}(i\Omega) &= \sum_{i\omega_n} \mathrm{Tr} \left[\frac{i\omega_n \sigma_0 + \Delta \sigma_1}{\sqrt{\Delta^2 - (i\omega_n)^2}} \frac{(i\omega_n + i\Omega)\sigma_0 + \Delta \sigma_1}{\sqrt{\Delta^2 - (i\omega_n + i\Omega)^2}} \right] \\ &= \sum_{i\omega_n} \frac{i\omega_n (i\omega_n + i\Omega) + \Delta^2}{\sqrt{\Delta^2 - (i\omega_n)^2} \sqrt{\Delta^2 - (i\omega_n + i\Omega)^2}}. \end{aligned} \tag{4.46}$$

We now need to compute the Matsubara summation and perform the analytical continuation to real frequency. The sum over the Matsubara frequency is transformed into an integral in the complex plane over the contour $\mathcal{C}$ depicted in Fig. 4.20b as follows [76, 1]

$$\chi_{00}(i\Omega) = \frac{1}{2\pi i} \int_{\mathcal{C}} dz \, n(z) \frac{z(z + i\Omega) + \Delta^2}{\sqrt{\Delta^2 - z^2} \sqrt{\Delta^2 - (z + i\Omega)^2}}, \tag{4.47}$$

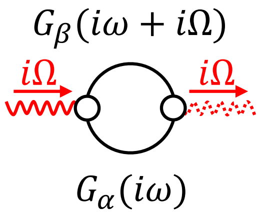

(a) Diagram for the current-current response function $\chi_{00}(i\Omega)$. Filled dots represent σ_0 vertices for the paramagnetic light-matter interaction, photons are represented as wavy lines.

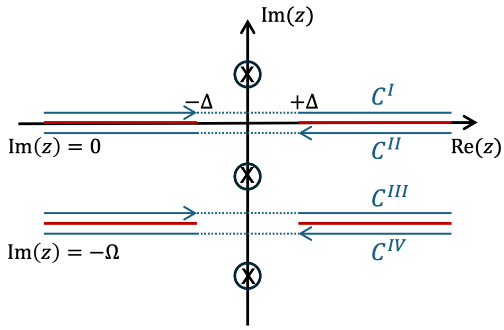

(b) The sum over resides at $i\omega_n$ in Eq. 4.46 is transformed in the integration over the contour $\mathcal{C}$, composed by the four pieces $\mathcal{C}^I$,$\mathcal{C}^{II}$,$\mathcal{C}^{III}$,$\mathcal{C}^{IV}$ chosen to circumvent the branch cuts (red lines).

Figure 4.20. The current-current response χ_{00} in Matsubara frequency space (left) and its analytical structure when it is continued to the complex-frequency plane (right).

where we denoted as $n(z)$ the Fermi function. The contour $\mathcal{C}$ is chosen to circumvent the branch cuts of the square roots at the denominator, which are located along the lines $\mathrm{Im}(z) = 0$ and $\mathrm{Im}(z) = -\Omega$ in the interval $|\mathrm{Re}(z)| > \Delta$. The four pieces read, using $n(\epsilon + i\Omega) = n(\epsilon)$,

$$\int_{\mathcal{C}^I} dz\,(\cdots) = \int_{-\infty}^{+\infty} d\epsilon\, n(\epsilon) \frac{(\epsilon + i\eta)(\epsilon + i\Omega) + \Delta^2}{\sqrt{\Delta^2 - (\epsilon + i\eta)^2}\sqrt{\Delta^2 - (\epsilon + i\Omega)^2}} \tag{4.48}$$

$$\int_{\mathcal{C}^{II}} dz\,(\cdots) = -\int_{-\infty}^{+\infty} d\epsilon\, n(\epsilon) \frac{(\epsilon - i\eta)(\epsilon + i\Omega) + \Delta^2}{\sqrt{\Delta^2 - (\epsilon - i\eta)^2}\sqrt{\Delta^2 - (\epsilon + i\Omega)^2}} \tag{4.49}$$

$$\int_{\mathcal{C}^{III}} dz\,(\cdots) = \int_{-\infty}^{+\infty} d\epsilon\, n(\epsilon) \frac{(\epsilon - i\Omega)(\epsilon + i\eta) + \Delta^2}{\sqrt{\Delta^2 - (\epsilon - i\Omega)^2}\sqrt{\Delta^2 - (\epsilon + i\eta)^2}} \tag{4.50}$$

$$\int_{\mathcal{C}^{IV}} dz\,(\cdots) = -\int_{-\infty}^{+\infty} d\epsilon\, n(\epsilon) \frac{(\epsilon - i\Omega)(\epsilon - i\eta) + \Delta^2}{\sqrt{\Delta^2 - (\epsilon - i\Omega)^2}\sqrt{\Delta^2 - (\epsilon - i\eta)^2}} \tag{4.51}$$

where η, lifting the contour above and below the branch cuts, can be interpreted as the Dynes parameter [34]. The analytical continuation can be then immediately performed, with special attention to the sign of $i\eta$ in the pieces $\mathcal{C}^{II}$ and $\mathcal{C}^{III}$ in order to select the correct branch of the square root shifted by $i\Omega$. One obtains

$$\begin{aligned}\int_{\mathcal{C}^I} dz\,(\cdots) &= \int_{-\infty}^{+\infty} d\epsilon\, n(\epsilon) \frac{(\epsilon + i\eta)(\epsilon + \Omega + i\eta) + \Delta^2}{\sqrt{\Delta^2 - (\epsilon + i\eta)^2}\sqrt{\Delta^2 - (\epsilon + \Omega + i\eta)^2}} \\ &\equiv \int_{-\infty}^{+\infty} d\epsilon\, n(\epsilon) \left(g_\epsilon^R g_{\epsilon+\Omega}^R + f_\epsilon^R f_{\epsilon+\Omega}^R\right)\end{aligned} \tag{4.52}$$

$$\begin{aligned}\int_{\mathcal{C}^{II}} dz\,(\cdots) &= -\int_{-\infty}^{+\infty} d\epsilon\, n(\epsilon) \frac{(\epsilon - i\eta)(\epsilon + \Omega + i\eta) + \Delta^2}{\sqrt{\Delta^2 - (\epsilon - i\eta)^2}\sqrt{\Delta^2 - (\epsilon + \Omega + i\eta)^2}} \\ &\equiv -\int_{-\infty}^{+\infty} d\epsilon\, n(\epsilon) \left(g_\epsilon^A g_{\epsilon+\Omega}^R + f_\epsilon^A f_{\epsilon+\Omega}^R\right)\end{aligned} \tag{4.53}$$

$$\begin{aligned}\int_{\mathcal{C}^{III}} dz\,(\cdots) &= \int_{-\infty}^{+\infty} d\epsilon\, n(\epsilon) \frac{(\epsilon-\Omega-i\eta)(\epsilon+i\eta)+\Delta^2}{\sqrt{\Delta^2-(\epsilon-\Omega-i\eta)^2}\sqrt{\Delta^2-(\epsilon+i\eta)^2}} \\ &\equiv \int_{-\infty}^{+\infty} d\epsilon\, n(\epsilon+\Omega)\left(g^A_\epsilon g^R_{\epsilon+\Omega} + f^A_\epsilon f^R_{\epsilon+\Omega}\right)\end{aligned} \tag{4.54}$$

$$\begin{aligned}\int_{\mathcal{C}^{IV}} dz\,(\cdots) &= -\int_{-\infty}^{+\infty} d\epsilon\, n(\epsilon) \frac{(\epsilon-\Omega-i\eta)(\epsilon-i\eta)+\Delta^2}{\sqrt{\Delta^2-(\epsilon-\Omega-i\eta)^2}\sqrt{\Delta^2-(\epsilon-i\eta)^2}} \\ &\equiv -\int_{-\infty}^{+\infty} d\epsilon\, n(\epsilon+\Omega)\left(g^A_\epsilon g^A_{\epsilon+\Omega} + f^A_\epsilon f^A_{\epsilon+\Omega}\right)\end{aligned} \tag{4.55}$$

Here we defined the functions

$$g^{R,A}_\epsilon = \frac{\epsilon \pm i\eta}{\zeta^{R,A}_\epsilon} = \frac{\epsilon \pm i\eta}{\sqrt{\Delta^2-(\epsilon\pm i\eta)^2}}, \tag{4.56}$$

and

$$f^{R,A}_\epsilon = \frac{\Delta}{\zeta^{R,A}_\epsilon} = \frac{\Delta}{\sqrt{\Delta^2-(\epsilon\pm i\eta)^2}}, \tag{4.57}$$

which are related to the normal and anomalous part of the Green's function in the superconducting state [29, 76]. Since the relations $g^{R,A}_{-\epsilon} = -g^{A,R}_\epsilon$ and $f^{R,A}_{-\epsilon} = f^{A,R}_\epsilon$ hold, one can rewrite the $\chi_{00}(\Omega)$ as

$$\begin{aligned}\chi_{00}(\Omega) = \frac{1}{4\pi i}\int_{-\infty}^{+\infty} d\epsilon\, \Big[&\tanh(\beta\epsilon/2)\left(g^R_\epsilon g^R_{\epsilon+\Omega} + f^R_\epsilon f^R_{\epsilon+\Omega}\right) \\ &- \tanh(\beta(\epsilon+\Omega)/2)\left(g^A_\epsilon g^A_{\epsilon+\Omega} + f^A_\epsilon f^A_{\epsilon+\Omega}\right) \\ &+ \left(\tanh(\beta(\epsilon+\Omega)/2) - \tanh(\beta\epsilon/2)\right)\left(g^A_\epsilon g^R_{\epsilon+\Omega} + f^A_\epsilon f^R_{\epsilon+\Omega}\right)\Big],\end{aligned} \tag{4.58}$$

which coincide with the usual Mattis-Bardeen expressions when the limit $\eta \to 0$ is taken, where the following relations hold

$$g^R_\epsilon = \frac{i|\epsilon|}{\sqrt{\epsilon^2-\Delta^2}}\theta(|\epsilon|-\Delta) + \frac{\epsilon}{\sqrt{\Delta^2-\epsilon^2}}\theta(\Delta-|\epsilon|) \tag{4.59}$$

$$f^R_\epsilon = \frac{i\Delta \mathrm{sgn}(\epsilon)}{\sqrt{\epsilon^2-\Delta^2}}\theta(|\epsilon|-\Delta) + \frac{\Delta}{\sqrt{\Delta^2-\epsilon^2}}\theta(\Delta-|\epsilon|) \tag{4.60}$$

and corresponding ones for g^A_ϵ and f^A_ϵ. One gets the analytical expressions for the conductivity in the superconducting state σ_{sc} obtained by Mattis and Bardeen at $T=0$ [100], that read, defining the normal state conductivity as $\sigma_N = ne^2/(m\gamma)$,

$$\frac{\sigma'_{sc}}{\sigma_N} = \theta(\omega-2\Delta)\left[\left(1+\frac{2\Delta}{\omega}\right)E\left(\frac{\omega-2\Delta}{\omega+2\Delta}\right) - \frac{4\Delta}{\omega}K\left(\frac{\omega-2\Delta}{\omega+2\Delta}\right)\right], \tag{4.61}$$

and

$$\begin{aligned}\frac{\sigma''_{sc}}{\sigma_N} = \frac{1}{2}\Bigg[&\left(1+\frac{2\Delta}{\omega}\right)E\left(\sqrt{1-\left(\frac{\omega-2\Delta}{\omega+2\Delta}\right)^2}\right) \\ &+\left(\frac{2\Delta}{\omega}-1\right)K\left(\sqrt{1-\left(\frac{\omega-2\Delta}{\omega+2\Delta}\right)^2}\right)\Bigg].\end{aligned} \tag{4.62}$$

Here $K(k)$ is the complete elliptic integral of the first kind

$$K(k) = \int_0^{\frac{\pi}{2}} \frac{1}{\sqrt{1-k^2\sin^2\theta}}\,d\theta, \tag{4.63}$$

while $E(k)$ is the complete elliptic integral of the second kind

$$E(k) = \int_0^{\frac{\pi}{2}} \sqrt{1-k^2\sin^2\theta}\,d\theta. \tag{4.64}$$

If one keeps the full frequency dependence of the function $W_\gamma(\xi,\xi')$ in Eq. 4.42 it is possible to obtain the expression for the linear conductivity valid at arbtrary $\gamma/(2\Delta)$ value, see Zimmermann [156]. One has, omitting overall v_F, N_F factors,

$$\begin{aligned}\chi_{00}(i\Omega) = \sum_{i\omega_n}\int d\xi d\xi'\,W_\gamma(\xi,\xi')\times \\ \times\,\mathrm{Tr}\left[\frac{i\omega_n\sigma_0-\xi\sigma_3+\Delta\sigma_1}{(i\omega_n)^2-\xi^2-\Delta^2}\frac{(i\omega_n+i\Omega)\sigma_0-\xi'\sigma_3+\Delta\sigma_1}{(i\omega_n+i\Omega)^2-\xi'^2-\Delta^2}\right].\end{aligned} \tag{4.65}$$

By residues one can show that

$$\int d\xi d\xi'\,W_\gamma(\xi,\xi')\frac{1}{\xi^2+\alpha^2}\frac{1}{\xi'^2+\beta^2} = \frac{\pi^2}{\alpha\beta(\alpha+\beta+\gamma)} \tag{4.66}$$

$$\int d\xi d\xi'\,W_\gamma(\xi,\xi')\frac{\xi}{\xi^2+\alpha^2}\frac{\xi'}{\xi'^2+\beta^2} = \frac{\pi^2}{\alpha+\beta+\gamma}, \tag{4.67}$$

which can be used to obtain the resulting current-current response in Matsubara representation as

$$\begin{aligned}\chi_{00}(i\Omega) = \sum_{i\omega_n}\left(\frac{i\omega_n(i\omega_n+i\Omega)+\Delta^2}{\sqrt{\Delta^2-(i\omega_n)^2}\sqrt{\Delta^2-(i\omega_n+i\Omega)^2}}+1\right)\times \\ \times\,\frac{1}{\sqrt{\Delta^2-(i\omega_n)^2}+\sqrt{\Delta^2-(i\omega_n+i\Omega)^2}+\gamma}.\end{aligned} \tag{4.68}$$

The analytical continuation proceeds from now on following the same steps presented before.

4.2.5 Evaluation of the χ^L_{001} diagram - Eliashberg effect

We now move towards the evaluation of the χ_{001} diagram in presence of disorder, reamining in the same framework that we have recalled for the calculation of the linear conductivity. The all important difference is the presence of a further σ_1 vertex associated with the amplitude fluctuations. As mentioned above, the bubble can be written as a trace over the Green's function G_α computed over the exact eigenstates ξ_α. If the pairing interaction still connects time-reversed states and the order parameter is s-wave like, one can easily realize that the amplitude vertex does not mix eigenstates in the basis α. This means that one has to evaluate

$$\chi_{001}(i\Omega_1,i\Omega_2) = \sum_{\alpha\beta}\sum_{i\omega_n} v^2_{\alpha\beta}\,\mathrm{Tr}\left[G_\alpha(i\omega_n+i\Omega_1)G_\beta(i\omega_n+i\Omega_{12})\sigma_1 G_\beta(i\omega_n)\right], \tag{4.69}$$

where the eigenstate index β is conserved at the σ_1 (amplitude) insertion. Taking into account disorder in the same Mattis-Bardeen spirit, one could separately integrate over energy the single propagator between the two gauge field lines and the two propagators that sandwich the σ_1 vertex connected to the excitation of the Higgs mode, see Fig. 4.19a. Noticing that

$$\begin{aligned} G(i\omega_n + i\Omega_{12}, \xi)\sigma_1 G(i\omega_n, \xi) = & \frac{(i\omega_n + i\Omega_{12})\sigma_0 - \xi\sigma_3 + \Delta\sigma_1}{(i\omega_n + i\Omega_{12})^2 - \xi^2 - \Delta^2} \times \\ & \times \sigma_1 \frac{i\omega_n\sigma_0 - \xi\sigma_3 + \Delta\sigma_1}{(i\omega_n)^2 - \xi^2 - \Delta^2}, \end{aligned} \tag{4.70}$$

the corresponding integration over energy yields

$$\begin{aligned} \int d\xi\, G(i\omega_n + i\Omega_{12}, \xi)\sigma_1 G(i\omega_n, \xi) = & \frac{\pi}{\sqrt{\Delta^2 - (i\omega_n)^2} + \sqrt{\Delta^2 - (i\omega_n + i\Omega_{12})^2}} \times \\ \times \left[-\sigma_1 + \frac{\left(i\omega_n(i\omega_n + i\Omega_{12}) + \Delta^2\right)\sigma_1 + \Delta(2i\omega + i\Omega_{12})\sigma_0}{\sqrt{\Delta^2 - (i\omega_n)^2}\sqrt{\Delta^2 - (i\omega_n + i\Omega_{12})^2}} \right]. & \end{aligned} \tag{4.71}$$

Then, the diagram reads, omitting again v_F, N_F factors,

$$\begin{aligned} \chi_{001}(i\Omega_1, i\Omega_2) = & \sum_{i\omega_n} \frac{1}{\sqrt{\Delta^2 - (i\omega_n)^2} + \sqrt{\Delta^2 - (i\omega_n + i\Omega_{12})^2}} \frac{\Delta}{\sqrt{\Delta^2 - (i\omega_n + i\Omega_1)^2}} \\ & \times \left[-1 + \frac{i\omega_n(i\omega_n + i\Omega_{12}) + \Delta^2 + (2i\omega_n + i\Omega_{12})(i\omega_n + i\Omega_1)}{\sqrt{\Delta^2 - (i\omega_n)^2}\sqrt{\Delta^2 - (i\omega_n + i\Omega_{12})^2}} \right]. \end{aligned} \tag{4.72}$$

Even though the same χ_{001} bubble appears in the L and R part of the diagram in Fig. 4.19a and Fig. 4.19b, respectively, the analyitical continuation makes the two different. The reason, as we shall see, is connected to the fact that the L diagram describes the Δ response to a A^2 perturbation, while the R part describes a J (i.e. A) response to a ΔA perturbation. Notice that if instead one at this point sets $i\Omega_1 = \pm i\Omega$ and $i\Omega_2 = \mp i\Omega$, i.e. one treats the Matsubara frequency as the external frequencies of the monochromatic pump, one would get from the previous expression

$$\chi_{001}(i\Omega, -i\Omega) = \sum_{i\omega_n} \frac{i\omega_n(2i\omega_n + i\Omega)\Delta}{\left(\sqrt{\Delta^2 - (i\omega_n)^2}\right)^3 \sqrt{\Delta^2 - (i\omega_n + i\Omega)^2}} + (i\Omega \to -i\Omega), \tag{4.73}$$

which can be immediately verified to be the derivative with respect to the order parameter Δ of the current-current response function

$$\frac{\partial\chi_{00}(i\Omega)}{\partial\Delta} = \frac{\partial}{\partial\Delta} \sum_{i\omega_n} \frac{i\omega_n(i\omega_n + i\Omega) + \Delta^2}{\sqrt{\Delta^2 - (i\omega_n)^2}\sqrt{\Delta^2 - (i\omega_n + i\Omega)^2}}. \tag{4.74}$$

If the previous expression is now analytically continued to real frequencies after the summation over $i\omega_n$, the result is simply the derivative with respect to Δ of Eq. 4.58. A different result is obtained if, on the other hand, one firstly computes the Matsubara summation over $i\omega_n$ directly in Eq. 4.72 and, as a second step,

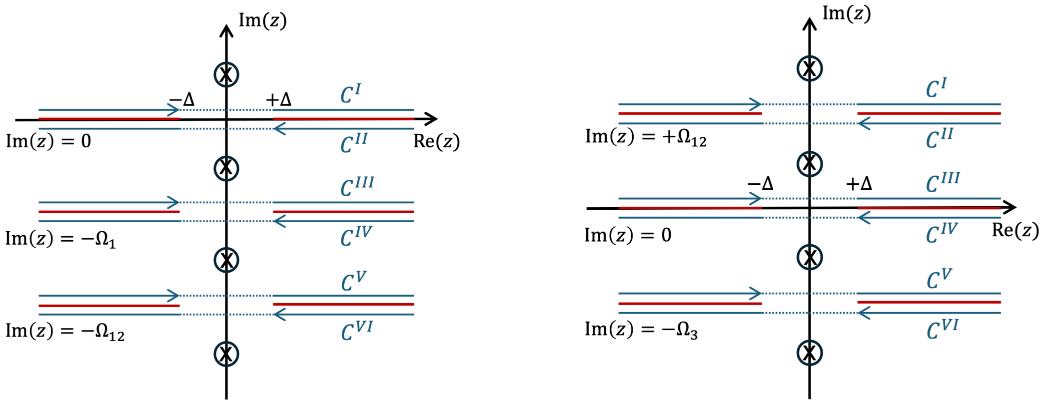

(a) Contour for Eq. 4.72. **(b)** Contour for Eq. 4.91.

Figure 4.21. The sums in Eq. 4.72 and Eq. 4.91 are evalueted through the integral over the two contours $\mathcal{C}$ composed by the six pieces $\mathcal{C}^I$,$\mathcal{C}^{II}$,$\mathcal{C}^{III}$,$\mathcal{C}^{IV}$,$\mathcal{C}^V$,$\mathcal{C}^{VI}$. Notice the different topology of the contours in the two cases when $\Omega_{12} \to 0$, which is the origin of the different form of the analitically continued χ^L_{001} and χ^R_{001}.

analytically continues the result over real frequencies $(i\Omega_1, i\Omega_2) \to (\Omega_1, \Omega_2)$ with the same technique presented for the current-current response. Only after analytical continuation one then sets $(\Omega_1, \Omega_2) \to (\Omega, -\Omega)$.

Let us then start from the L diagram, and let us recall that we are interested to $i\Omega_{1,2} = i2\pi n_{1,2}T$ Matsubara frequencies for $n_{1,2} > 0$ [54, 76], that will be later on analytically continued to (positive or negative) real frequencies. The sum over the Matsubara frequencies in Eq. 4.72 is transformed into an integral in the complex plane over the contour $\mathcal{C}$ depicted in Fig. 4.21a as follows

$$\begin{aligned}\chi_{001}(i\Omega_1, i\Omega_2) = \frac{1}{2\pi i}\int_{\mathcal{C}} dz\, n(z)&\frac{1}{\sqrt{\Delta^2 - z^2} + \sqrt{\Delta^2 - (z + i\Omega_{12})^2}}\times \\ &\times\frac{\Delta}{\sqrt{\Delta^2 - (z + i\Omega_1)^2}}\times \\ &\times\left[-1 + \frac{z(z + i\Omega_{12}) + \Delta^2 + (2z + i\Omega_{12})(z + i\Omega_1)}{\sqrt{\Delta^2 - z^2}\sqrt{\Delta^2 - (z + i\Omega_{12})^2}}\right].\end{aligned} \tag{4.75}$$

The contour $\mathcal{C}$ is chosen to circumvent the current three branch cuts of the square roots at the denominator, which are located along the lines $\mathrm{Im}(z) = 0$, $\mathrm{Im}(z) = -\Omega_1$ and $\mathrm{Im}(z) = -\Omega_{12}$ in the interval $|\mathrm{Re}(z)| > \Delta$. Since $\Omega_{12} > \Omega_1$ the contours $\mathcal{C}_{III}, \mathcal{C}_{IV}, \mathcal{C}_V, \mathcal{C}_{VI}$ are all on the same side with respect to the branch cut at $\mathrm{Im}(z) = 0$. Let us now write explicitly the six contributions, paying again attention to the sign of $i\eta$ in $\mathcal{C}^{II}, \mathcal{C}^{III}, \mathcal{C}^{IV}, \mathcal{C}^V$,

$$\begin{aligned}\mathcal{I}_1 = \int_{-\infty}^{+\infty} d\epsilon\, n(\epsilon)&\frac{1}{\sqrt{\Delta^2 - (\epsilon + i\eta)^2} + \sqrt{\Delta^2 - (\epsilon + \Omega_{12} + i\eta)^2}}\frac{\Delta}{\sqrt{\Delta^2 - (\epsilon + \Omega_1 + i\eta)^2}} \\ \times&\left[-1 + \frac{(\epsilon + i\eta)(\epsilon + \Omega_{12} + i\eta) + \Delta^2 + (2(\epsilon + i\eta) + \Omega_{12})\,(\epsilon + \Omega_1 + i\eta)}{\sqrt{\Delta^2 - (\epsilon + i\eta)^2}\sqrt{\Delta^2 - (\epsilon + \Omega_{12} + i\eta)^2}}\right]\end{aligned} \tag{4.76}$$

$$\mathcal{I}_2 = \int_{+\infty}^{-\infty} d\epsilon\, n(\epsilon) \frac{1}{\sqrt{\Delta^2-(\epsilon-i\eta)^2}+\sqrt{\Delta^2-(\epsilon+\Omega_{12}+i\eta)^2}} \frac{\Delta}{\sqrt{\Delta^2-(\epsilon+\Omega_1+i\eta)^2}} \times \left[-1+\frac{(\epsilon-i\eta)(\epsilon+\Omega_{12}+i\eta)+\Delta^2+(2\epsilon+\Omega_{12})(\epsilon+\Omega_1+i\eta)}{\sqrt{\Delta^2-(\epsilon-i\eta)^2}\sqrt{\Delta^2-(\epsilon+\Omega_{12}+i\eta)^2}}\right] \tag{4.77}$$

$$\mathcal{I}_3 = \int_{-\infty}^{+\infty} d\epsilon\, n(\epsilon) \frac{1}{\sqrt{\Delta^2-(\epsilon-\Omega_1-i\eta)^2}+\sqrt{\Delta^2-(\epsilon+\Omega_2+i\eta)^2}} \frac{\Delta}{\sqrt{\Delta^2-(\epsilon+i\eta)^2}} \times \left[-1+\frac{(\epsilon-\Omega_1-i\eta)(\epsilon+\Omega_2+i\eta)+\Delta^2+(2\epsilon-\Omega_1+\Omega_2)(\epsilon+i\eta)}{\sqrt{\Delta^2-(\epsilon-\Omega_1-i\eta)^2}\sqrt{\Delta^2-(\epsilon+\Omega_2+i\eta)^2}}\right] \tag{4.78}$$

$$\mathcal{I}_4 = \int_{+\infty}^{-\infty} d\epsilon\, n(\epsilon) \frac{1}{\sqrt{\Delta^2-(\epsilon-\Omega_1-i\eta)^2}+\sqrt{\Delta^2-(\epsilon+\Omega_2+i\eta)^2}} \frac{\Delta}{\sqrt{\Delta^2-(\epsilon-i\eta)^2}} \times \left[-1+\frac{(\epsilon-\Omega_1-i\eta)(\epsilon+\Omega_2+i\eta)+\Delta^2+(2\epsilon-\Omega_1+\Omega_2)(\epsilon-i\eta)}{\sqrt{\Delta^2-(\epsilon-\Omega_1-i\eta)^2}\sqrt{\Delta^2-(\epsilon+\Omega_2+i\eta)^2}}\right] \tag{4.79}$$

$$\mathcal{I}_5 = \int_{-\infty}^{+\infty} d\epsilon\, n(\epsilon) \frac{1}{\sqrt{\Delta^2-(\epsilon-\Omega_{12}-i\eta)^2}+\sqrt{\Delta^2-(\epsilon+i\eta)^2}} \frac{\Delta}{\sqrt{\Delta^2-(\epsilon-\Omega_2-i\eta)^2}} \times \left[-1+\frac{(\epsilon-\Omega_{12}-i\eta)(\epsilon+i\eta)+\Delta^2+(2\epsilon-\Omega_{12})(\epsilon-\Omega_2-i\eta)}{\sqrt{\Delta^2-(\epsilon-\Omega_{12}-i\eta)^2}\sqrt{\Delta^2-(\epsilon+i\eta)^2}}\right] \tag{4.80}$$

$$\mathcal{I}_6 = \int_{+\infty}^{-\infty} d\epsilon\, n(\epsilon) \frac{1}{\sqrt{\Delta^2-(\epsilon-\Omega_{12}-i\eta)^2}+\sqrt{\Delta^2-(\epsilon-i\eta)^2}} \frac{\Delta}{\sqrt{\Delta^2-(\epsilon-\Omega_2-i\eta)^2}} \times \left[-1+\frac{(\epsilon-\Omega_{12}-i\eta)(\epsilon-i\eta)+\Delta^2+\left(2(\epsilon-i\eta)-\Omega_{12}\right)(\epsilon-\Omega_2-i\eta)}{\sqrt{\Delta^2-(\epsilon-\Omega_{12}-i\eta)^2}\sqrt{\Delta^2-(\epsilon-i\eta)^2}}\right]. \tag{4.81}$$

At this point, we make the replacement $(\Omega_1, \Omega_2) \to (\Omega, -\Omega)$ and we use the same notation for $g_\epsilon^{R,A}$,$f_\epsilon^{R,A}$ and $\zeta_\epsilon^{R,A}$ introduced before. We get for the sum of the four integrals along $\mathcal{C}^{II}$,$\mathcal{C}^{III}$,$\mathcal{C}^{IV}$,$\mathcal{C}^{V}$ the result

$$\mathcal{I}_2+\cdots+\mathcal{I}_5 = \int_{-\infty}^{+\infty} d\epsilon\, \left(\tanh\left(\beta(\epsilon+\Omega)/2\right)-\tanh\left(\beta\epsilon/2\right)\right) \times \times \left[\frac{g_\epsilon^R f_\epsilon^A + g_\epsilon^A f_\epsilon^R}{\zeta_\epsilon^R+\zeta_\epsilon^A}(g_{\epsilon+\Omega}^R - g_{\epsilon+\Omega}^A) + \frac{g_\epsilon^R g_\epsilon^A + f_\epsilon^R f_\epsilon^A - 1}{\zeta_\epsilon^R+\zeta_\epsilon^A}(f_{\epsilon+\Omega}^R - f_{\epsilon+\Omega}^A)\right], \tag{4.82}$$

which corresponds to what is called the anomalous contribution in Ref. [29], while the contributions integrating along $\mathcal{C}^{I}$,$\mathcal{C}^{VI}$ read

$$\mathcal{I}_1+\mathcal{I}_6 = \int_{-\infty}^{+\infty} d\epsilon\, \tanh\left(\beta\epsilon/2\right)\left[\frac{g_\epsilon^R}{\zeta_\epsilon^R}(g_{\epsilon+\Omega}^R f_\epsilon^R + g_\epsilon^R f_{\epsilon+\Omega}^R) - \frac{g_\epsilon^A}{\zeta_\epsilon^A}(g_{\epsilon+\Omega}^A f_\epsilon^A + g_\epsilon^A f_{\epsilon+\Omega}^A)\right]. \tag{4.83}$$

The resulting $\chi_{001}^L(\Omega,-\Omega)$ is shown in Fig. 4.22a, where we actually plot $\langle\delta\Delta\rangle_{\Omega_P}$ including the $\chi_{\Delta\Delta}^{-1}$ according to Eq. 4.38, which is comparable with the result of

Ref. [29], showing in particular an enhancement of the order parameter in the region $\Omega < 2\Delta(T)$, maximised for temperatures close to the critical one. We remark here that strictly speaking the combination at the denominator of the anomalous contribution,

$$\zeta_\epsilon^R + \zeta_\epsilon^A \sim i\sqrt{\epsilon^2 - \Delta^2} - i\sqrt{\epsilon^2 - \Delta^2} \sim 0, \tag{4.84}$$

is actually zero in the limit $\eta \to 0$ in the region $|\epsilon| > \Delta$. Since the consequent divergence in the integrand is neither canceled nor regularized by any zero at the numerator, one should keep a finite value of the Dynes parameter η in order to actually simulate the Eliashberg effect, whose overall scale will be then controlled by the value of $1/\eta$. This is actually a crucial point which was also noticed in the original works by Gorkov and Eliashberg [55, 35], who assumed that a finite η represented a finite lifetime due to further scattering mechanisms than the elastic one with impurities, such as electron-electron or electron-phonon interaction. One can then approximate

$$\frac{1}{\zeta_\epsilon^R + \zeta_\epsilon^A} \sim \frac{\sqrt{\epsilon^2 - \Delta^2}}{2|\epsilon|\eta}\theta(|\epsilon| - \Delta), \tag{4.85}$$

and collect the relevant terms in $\chi^L_{001}(\Omega, -\Omega)$. If one focuses on the enhancement of the gap near the critical temperature, where $\Delta \ll T$, one can also approximate

$$\tanh\left(\beta(\epsilon + \Omega)/2\right) - \tanh\left(\beta\epsilon/2\right) \sim \frac{\Omega}{2T}. \tag{4.86}$$

Finally one has

$$\chi^L_{001}(\Omega, -\Omega) \sim \frac{\Omega\Delta}{2T\eta}P(\Omega), \tag{4.87}$$

where the function $P(\Omega)$ is the same function defined in Kopnin's treatment of Eliashberg effect [78]

$$\begin{aligned} P(\Omega) = \Omega \int_\Delta^{+\infty} d\epsilon\, &\frac{\epsilon(\epsilon + \Omega) + \Delta^2}{\epsilon(\epsilon + \Omega)\sqrt{\epsilon^2 - \Delta^2}\sqrt{(\epsilon + \Omega)^2 - \Delta^2}} \\ - \theta(\Omega - 2\Delta) \int_\Delta^{\Omega - \Delta} & d\epsilon\, \frac{\epsilon(\Omega - \epsilon) - \Delta^2}{\epsilon\sqrt{\epsilon^2 - \Delta^2}\sqrt{(\Omega - \epsilon)^2 - \Delta^2}}, \end{aligned} \tag{4.88}$$

and correspond to the non-thermal distribution f originally derived by Eliashberg [35, 55].

If one wants to include the effect of a finite $\gamma/(2\Delta)$ value it is sufficient to keep the matrix element $W(\xi, \xi')$ in the evaluation of χ^L_{001}. By following a procedure similar to the one adopted for the linear conductivity, starting from Eq. 4.69 one can write

$$\begin{aligned} \chi_{001}(i\Omega_1, i\Omega_2) = &\sum_{i\omega_n} \int d\xi d\xi'\, W_\gamma(\xi, \xi') \\ &\times \mathrm{Tr}\left[\frac{i\omega_n\sigma_0 - \xi\sigma_3 + \Delta\sigma_1}{(i\omega_n)^2 - \xi^2 - \Delta^2}\frac{(i\omega_n + i\Omega_1)\sigma_0 - \xi'\sigma_3 + \Delta\sigma_1}{(i\omega_n + i\Omega_1)^2 - \xi'^2 - \Delta^2} \times \right. \\ &\times \left. \frac{(i\omega_n + i\Omega_{12})\sigma_0 - \xi\sigma_3 + \Delta\sigma_1}{(i\omega_n + i\Omega_{12})^2 - \xi^2 - \Delta^2}\sigma_1\right], \end{aligned} \tag{4.89}$$

where, in analogy with what we have done before, the two Green's functions (those sorrounding the order parameter vertex σ_1) are taken at the same energy and one (that between the two gauge field vertices σ_0) at a different one. Using the same integrals presented before one obtains, denoting for clarity $\zeta_{i\omega_n} = \sqrt{\Delta^2 - (i\omega_n)^2}$ and $\Theta = i\omega_n(i\omega_n + i\Omega_{12}) + \Delta^2 + (2i\omega_n + i\Omega_{12})(i\omega_n + i\Omega_1)$,

$$\chi_{001}(i\Omega_1, i\Omega_2) = \sum_{i\omega_n} \frac{1}{\zeta_{i\omega_n} + \zeta_{i\omega_n+i\Omega_1} + \gamma} \frac{1}{\zeta_{i\omega_n+i\Omega_{12}} + \zeta_{i\omega_n+i\Omega_1} + \gamma} \frac{\Delta}{\zeta_{i\omega_n} + \zeta_{i\omega_n+i\Omega_{12}}} \\ \times \left[1 + \frac{\zeta_{i\omega_n} + \zeta_{i\omega_n+i\Omega_1} + \zeta_{i\omega_n+i\Omega_{12}}}{\zeta_{i\omega_n}\zeta_{i\omega_n+i\Omega_1}\zeta_{i\omega_n+i\Omega_{12}}}\Theta \right. \\ \left. + \frac{\gamma}{\zeta_{i\omega_n+i\Omega_1}}\left(-1 + \frac{\Theta}{\zeta_{i\omega_n}\zeta_{i\omega_n+i\Omega_{12}}}\right)\right]. \tag{4.90}$$

In the limit where γ is large, one recovers the diffusive result presented before in Eq. 4.72. We stress that even in presence of finite γ the combination $1/(\zeta_{i\omega_n} + \zeta_{i\omega_n+i\Omega_{12}})$ still gives divergent contributions when the Dynes parameter is sent to zero. The analytical continuation procedure is analogous to the one presented above and we present the resulting $\chi^L_{001}(\Omega_P, -\Omega_P)$ in Fig. 4.22b, where we focused on the effect of different disorder levels at $T = 0$. In this case one can appreciate the presence of a cutoff scale of order γ above which the effect on $\langle\delta\Delta\rangle_{\Omega_P}$ is suppressed.

4.2.6 Evaluation of the χ^R_{001} diagram - Derivative of the conductivity

Let us now repeat the computation for the other diagram, χ^R_{001}. In this case, as we have recalled, the diagram represents the current response to a mixed gauge field and Higgs perturbation. For positive Matsubara frequencies this leads to a different relative position of the branch cuts in the complex plane, as shown in Fig. 4.21b. Let us first rewrite is explicitly as

$$\chi_{001}(i\Omega_3, -i\Omega_{123}) = \sum_{i\omega_n} \frac{1}{\sqrt{\Delta^2 - (i\omega_n)^2} + \sqrt{\Delta^2 - (i\omega_n - i\Omega_{12})^2}} \frac{\Delta}{\sqrt{\Delta^2 - (i\omega_n + i\Omega_3)^2}} \\ \times \left[-1 + \frac{i\omega_n(i\omega_n - i\Omega_{12}) + \Delta^2 + (2i\omega_n - i\Omega_{12})(i\omega_n + i\Omega_3)}{\sqrt{\Delta^2 - (i\omega_n)^2}\sqrt{\Delta^2 - (i\omega_n - i\Omega_{12})^2}}\right]. \tag{4.91}$$

The sum over the Matsubara frequencies here is again transformed into an integral in the complex plane over the contour $\mathcal{C}$ depicted in Fig. 4.21b as follows

$$\chi_{001}(i\Omega_3, -i\Omega_{123}) = \frac{1}{2\pi i}\int_{\mathcal{C}} dz\, n(z) \frac{1}{\sqrt{\Delta^2 - z^2} + \sqrt{\Delta^2 - (z - i\Omega_{12})^2}} \times \\ \times \frac{\Delta}{\sqrt{\Delta^2 - (z + i\Omega_3)^2}} \times \\ \times \left[-1 + \frac{z(z - i\Omega_{12}) + \Delta^2 + (2z - i\Omega_{12})(z + i\Omega_3)}{\sqrt{\Delta^2 - z^2}\sqrt{\Delta^2 - (z - i\Omega_{12})^2}}\right]. \tag{4.92}$$

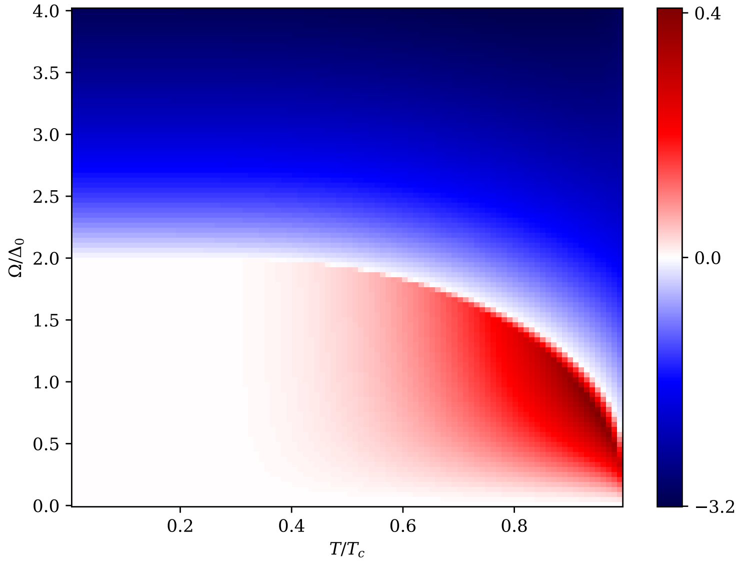

(a) Plot of the function $\langle\delta\Delta\rangle_{\Omega_P}$ computed through Eq. 4.38 using the expression for $\chi^L_{001}(\Omega, -\Omega)$ presented above, as a function of temperature and frequency. Notice that we included also the $\chi_{\Delta\Delta}$ factor which is not present in the corresponding Figure in Ref. [29].

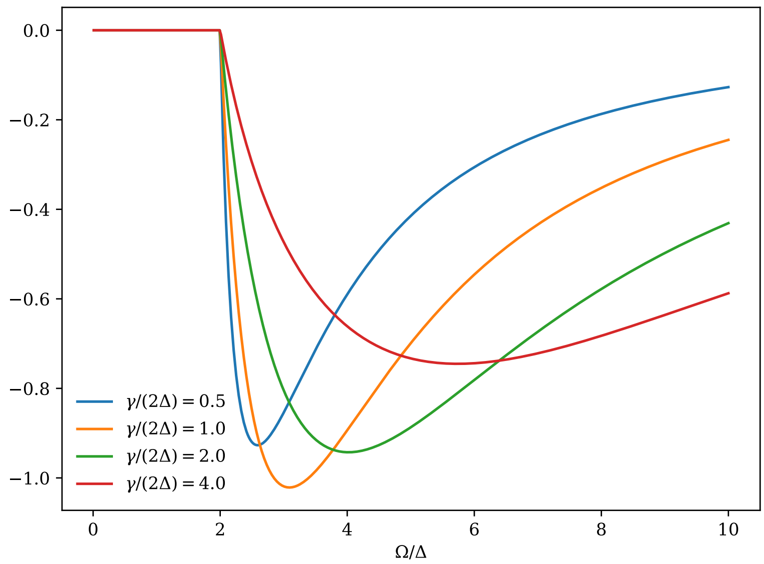

(b) Plot of the function $\langle\delta\Delta\rangle_{\Omega_P}$ at $T = 0$ with different $\gamma/(2\Delta)$ parameters, which correspond to different disorder levels, using Eq. 4.90. We notice that differently from the panel above there is a cutoff energy of order γ at which the effect is suppressed.

Figure 4.22. Comparison between the $\langle\delta\Delta\rangle_{\Omega_P}$ in the strong disorder limit (upper limit), corresponding to Ref. [29], and including the effect of the Mattis-Bardeen matrix element W as in Eq. 4.90.

Also here the contour $\mathcal{C}$ is chosen to circumvent the current three branch cuts of the square roots at the denominator, which are in this case located along the lines $\mathrm{Im}(z) = +\Omega_{12}$, $\mathrm{Im}(z) = 0$ and $\mathrm{Im}(z) = -\Omega_3$ in the interval $|\mathrm{Re}(z)| > \Delta$. Let us now write explicitly the six contributions, paying again attention to the sign of $i\eta$ in $\mathcal{C}^{II}, \mathcal{C}^{III}, \mathcal{C}^{IV}, \mathcal{C}^{V}$,

$$\begin{aligned}\mathcal{I}_1 = &\int_{-\infty}^{+\infty} d\epsilon\, n(\epsilon) \frac{1}{\sqrt{\Delta^2 - (\epsilon + i\eta)^2} + \sqrt{\Delta^2 - (\epsilon + \Omega_{12} + i\eta)^2}} \times \\ &\times \frac{\Delta}{\sqrt{\Delta^2 - (\epsilon + \Omega_{123} + i\eta)^2}} \times \\ &\times \left[-1 + \frac{(\epsilon + i\eta)(\epsilon + \Omega_{12} + i\eta) + \Delta^2 + (2(\epsilon + i\eta) + \Omega_{12})(\epsilon + \Omega_{123} + i\eta)}{\sqrt{\Delta^2 - (\epsilon + i\eta)^2}\sqrt{\Delta^2 - (\epsilon + \Omega_{12} + i\eta)^2}}\right]\end{aligned} \tag{4.93}$$

$$\begin{aligned}\mathcal{I}_2 = &\int_{+\infty}^{-\infty} d\epsilon\, n(\epsilon) \frac{1}{\sqrt{\Delta^2 - (\epsilon - i\eta)^2} + \sqrt{\Delta^2 - (\epsilon + \Omega_{12} + i\eta)^2}} \times \\ &\times \frac{\Delta}{\sqrt{\Delta^2 - (\epsilon + \Omega_{123} + i\eta)^2}} \times \\ &\times \left[-1 + \frac{(\epsilon - i\eta)(\epsilon + \Omega_{12} + i\eta) + \Delta^2 + (2\epsilon + \Omega_{12})(\epsilon + \Omega_{123} + i\eta)}{\sqrt{\Delta^2 - (\epsilon - i\eta)^2}\sqrt{\Delta^2 - (\epsilon + \Omega_{12} + i\eta)^2}}\right]\end{aligned} \tag{4.94}$$

$$\begin{aligned}\mathcal{I}_3 = &\int_{-\infty}^{+\infty} d\epsilon\, n(\epsilon) \frac{1}{\sqrt{\Delta^2 - (\epsilon - \Omega_{12} - i\eta)^2} + \sqrt{\Delta^2 - (\epsilon + i\eta)^2}} \times \\ &\times \frac{\Delta}{\sqrt{\Delta^2 - (\epsilon + \Omega_3 + i\eta)^2}} \times \\ &\times \left[-1 + \frac{(\epsilon - \Omega_{12} - i\eta)(\epsilon + i\eta) + \Delta^2 + (2\epsilon - \Omega_{12})(\epsilon + \Omega_3 + i\eta)}{\sqrt{\Delta^2 - (\epsilon - \Omega_{12} - i\eta)^2}\sqrt{\Delta^2 - (\epsilon + i\eta)^2}}\right]\end{aligned} \tag{4.95}$$

$$\begin{aligned}\mathcal{I}_4 = &\int_{+\infty}^{-\infty} d\epsilon\, n(\epsilon) \frac{1}{\sqrt{\Delta^2 - (\epsilon - \Omega_{12} - i\eta)^2} + \sqrt{\Delta^2 - (\epsilon - i\eta)^2}} \times \\ &\times \frac{\Delta}{\sqrt{\Delta^2 - (\epsilon + \Omega_3 + i\eta)^2}} \times \\ &\times \left[-1 + \frac{(\epsilon - \Omega_{12} - i\eta)(\epsilon - i\eta) + \Delta^2 + (2(\epsilon - i\eta) - \Omega_{12})(\epsilon + \Omega_3 + i\eta)}{\sqrt{\Delta^2 - (\epsilon - \Omega_{12} - i\eta)^2}\sqrt{\Delta^2 - (\epsilon - i\eta)^2}}\right]\end{aligned} \tag{4.96}$$

$$\begin{aligned}\mathcal{I}_5 = &\int_{-\infty}^{+\infty} d\epsilon\, n(\epsilon) \frac{1}{\sqrt{\Delta^2 - (\epsilon - \Omega_{123} - i\eta)^2} + \sqrt{\Delta^2 - (\epsilon - \Omega_3 - i\eta)^2}} \times \\ &\times \frac{\Delta}{\sqrt{\Delta^2 - (\epsilon + i\eta)^2}} \times \\ &\times \left[-1 + \frac{(\epsilon - \Omega_{123} - i\eta)(\epsilon - \Omega_3 - i\eta) + \Delta^2 + (2(\epsilon - \Omega_3 - i\eta) - \Omega_{12})(\epsilon + i\eta)}{\sqrt{\Delta^2 - (\epsilon - \Omega_{123} - i\eta)^2}\sqrt{\Delta^2 - (\epsilon - \Omega_3 - i\eta)^2}}\right]\end{aligned} \tag{4.97}$$

$$
\begin{aligned}
\mathcal{I}_6 = &\int_{+\infty}^{-\infty} d\epsilon\, n(\epsilon) \frac{1}{\sqrt{\Delta^2-(\epsilon-\Omega_{123}-i\eta)^2}+\sqrt{\Delta^2-(\epsilon-\Omega_3-i\eta)^2}} \times \\
&\times \frac{\Delta}{\sqrt{\Delta^2-(\epsilon-i\eta)^2}} \times \\
&\times \left[-1+\frac{(\epsilon-\Omega_{123}-i\eta)(\epsilon-\Omega_3-i\eta)+\Delta^2+\left(2(\epsilon-\Omega_3-i\eta)-\Omega_{12}\right)(\epsilon-i\eta)}{\sqrt{\Delta^2-(\epsilon-\Omega_{123}-i\eta)^2}\sqrt{\Delta^2-(\epsilon-\Omega_3-i\eta)^2}}\right].
\end{aligned} \tag{4.98}
$$

Making the replacement $(\Omega_3, -\Omega_{123}) \to (\Omega, -\Omega)$, one immediately notices that in this case, due to the different relative positions of the branch cuts, the integrations along $\mathcal{C}^{II}$ and $\mathcal{C}^{III}$ cancel with each other, leaving the sum of four pieces. Writing them explicitly, one immediately realizes that they build up the derivative with respect to Δ of the current-current response function χ_{00} computed above, namely

$$
\begin{aligned}
\chi^R_{001}(\Omega,-\Omega) = &\frac{1}{4\pi i}\int_{-\infty}^{+\infty} d\epsilon\, \tanh\left(\beta\epsilon/2\right)\left(g^R_\epsilon f^R_{\epsilon+\Omega}+f^R_\epsilon g^R_{\epsilon+\Omega}\right)\left(\frac{g^R_\epsilon}{\zeta^R_\epsilon}+\frac{g^R_{\epsilon+\Omega}}{\zeta^R_{\epsilon+\Omega}}\right) \\
&-\frac{1}{4\pi i}\int_{-\infty}^{+\infty} d\epsilon\, \tanh\left(\beta(\epsilon+\Omega)/2\right)\left(g^A_\epsilon f^A_{\epsilon+\Omega}+f^A_\epsilon g^A_{\epsilon+\Omega}\right)\left(\frac{g^A_\epsilon}{\zeta^A_\epsilon}+\frac{g^A_{\epsilon+\Omega}}{\zeta^A_{\epsilon+\Omega}}\right) \\
&+\frac{1}{4\pi i}\int_{-\infty}^{+\infty} d\epsilon\, \left[\left(\tanh\left(\beta(\epsilon+\Omega)/2\right)-\tanh\left(\beta\epsilon/2\right)\right)\times\right. \\
&\left.\times\left(g^A_\epsilon f^R_{\epsilon+\Omega}+f^A_\epsilon g^R_{\epsilon+\Omega}\right)\left(\frac{g^A_\epsilon}{\zeta^A_\epsilon}+\frac{g^R_{\epsilon+\Omega}}{\zeta^R_{\epsilon+\Omega}}\right)\right].
\end{aligned} \tag{4.99}
$$

At $T = 0$, we can as well express the derivative of the current-current response with respect to Δ using the relations between the elliptic integrals and their derivatives with respect to the arguments. We get for the imaginary part

$$
\frac{\partial\chi''_{00}}{\partial\Delta} = \theta(\omega-2\Delta)\frac{8\Delta}{\omega+2\Delta}K\left(\frac{\omega-2\Delta}{\omega+2\Delta}\right), \tag{4.100}
$$

and for the real part

$$
\frac{\partial\chi'_{00}}{\partial\Delta} = \frac{4\Delta}{\omega+2\Delta}K\left(\sqrt{1-\left(\frac{\omega-2\Delta}{\omega+2\Delta}\right)^2}\right). \tag{4.101}
$$

Notice that the derivative of the imaginary part is always finite, with a step discontinuity at $\omega = 2\Delta$. The derivative of the real part, being its Kramers-Kronig transform, shows consequently a log-like singularity at $\omega = 2\Delta$, as confirmed by the fact that for $\omega \to 2\Delta$ the argument of the K function tends to one, where the elliptic integral of the first kind diverges logarithmically. These findings are shown in Fig. 4.23a and 4.23b, where we show the real and imaginary part of the χ^R_{001} as a function of temperature and frequency for the strong disorder limit and at $T = 0$ for various values of $\gamma/(2\Delta)$ parameter, as done for χ^L_{001}. As one can see, the singularity at $\Omega = 2\Delta(T)$ remains evident as a function of temperature.

Finally, taking the results shown in Fig. 4.22a and 4.22b for $\langle\delta\Delta\rangle_{\Omega_P}$ together with those in Fig. 4.23a and 4.23b for the derivative of the current-current response,

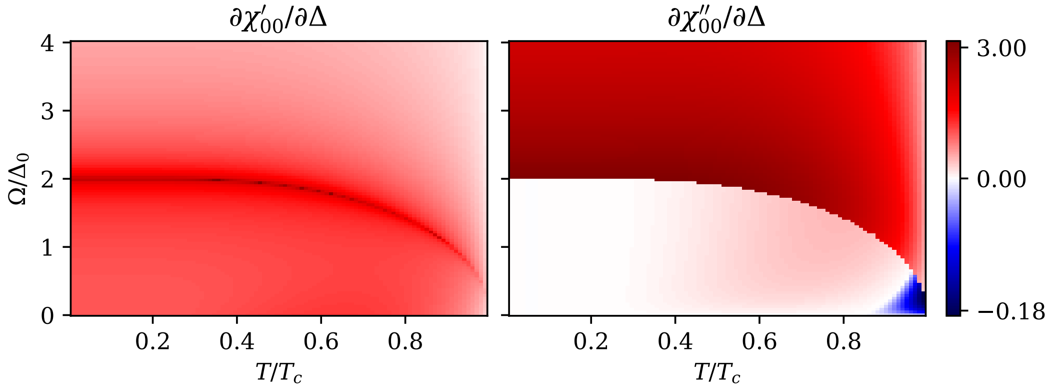

(a) Frequency and temperature dependent colormap of the derivative of the real (left panel) and imaginary part (right panel) of the current-current response, where red (blue) regions indicate positive (negative) values.

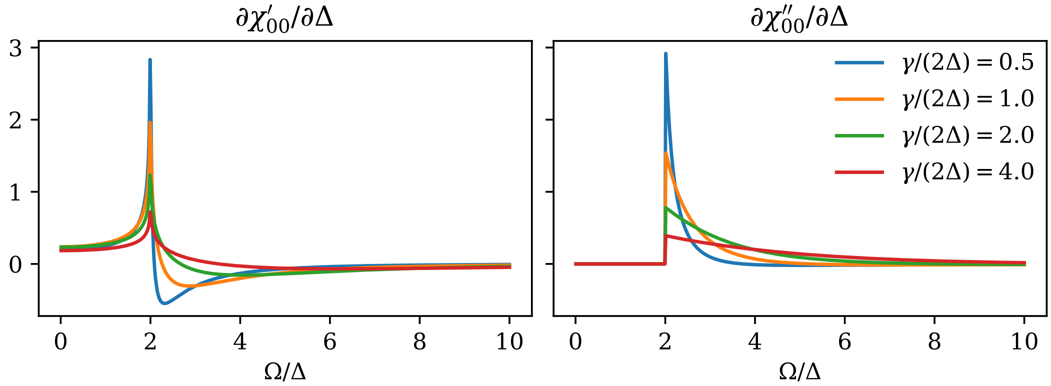

(b) Real (left panel) and imaginary part (right panel) at $T = 0$ of the derivative of the current-current response, including the effect of the Mattis-Bardeen matrix element W, with different $\gamma/(2\Delta)$ parameters.

Figure 4.23. Comparison between the $\chi^R_{001}(\Omega, -\Omega)$ functions which correspond to the derivative of the current-current response in the strong disorder limit (upper panels) and at various disorder levels (lower panels). Notice that to compare the upper and lower panels at large $\gamma/(2\Delta)$ one has to multiply the upper one by $1/\gamma$, i.e. the overall scale of W_γ at large disorder.

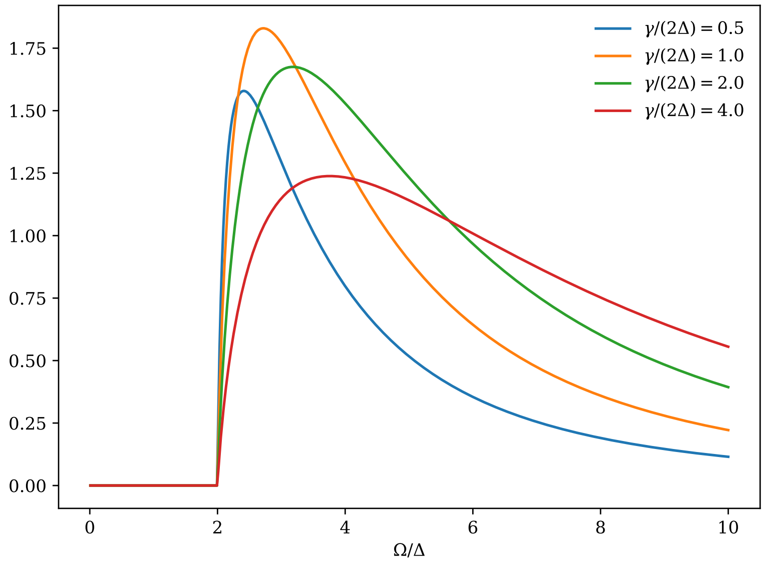

Figure 4.24. Plot of $|J^{(3)}(\Omega)|$ according to Eq. 4.102 at various disorder levels.

one realizes that there is actually the possibility of enhancement of the nonlinear first harmonic current given by

$$J^{(3)}(\Omega_P) = \frac{\partial \chi_{00}(\Omega_P)}{\partial \Delta} \langle \delta\Delta \rangle_{\Omega_P}. \tag{4.102}$$

As we have just seen, the first factor is singular along the curve $\Omega = 2\Delta(T)$, while the second one is enhanced i) in the subgap region, with a maximum in proximity of the critical temperature, or ii) in the above gap region inside an energy scale of order γ. Preliminary results in the finite-size system at $T = 0$ show indeed a substantial agreement between the full numerical solution for the nonlinear first harmonic $J^{(3)}(\Omega_P)$ and the analytical result presented in the previous expression, which is reported in Fig. 4.24, that one can compare with the analogous numerical simulation in Fig. 4.11 above. We stress that the numerical simulations report the contribution of the purely-quasiparticle diagram $\langle jjjj \rangle$ plus the one including the amplitude fluctuations, i.e. $\langle jj\Delta \rangle \langle \Delta jj \rangle \chi_{\Delta\Delta}$. We need then to compute in the same framework presented in this last section the $\langle jjjj \rangle$ part in order to complete the comparison, a task which we leave for the immediate future. As a final remark, we stress here that although we do not observe here a resonant enhancement of the amplitude fluctuations, since there is not a tunable frequency argument inside the corresponding propagator $\chi_{\Delta\Delta}$, one still gets a enhanced contribution from the fermionic bubble coupling light with the amplitude vertex. Again, this is a crucial consequence of computing the light-matter interaction in a microscopic model which includes the effect of disorder.

Conclusions

In this thesis, we developed a theoretical framework that captures several experimental findings in nonlinear THz spectroscopy on superconducting systems across various geometries and protocols.

We began by introducing a general procedure to connect non-linearly generated electric fields with a microscopically derived response function. This derivation relies on a perturbative solution of inhomogeneous Maxwell's equations, enabling consistent inclusion of screening effects that occur at linear order. Our method is flexible and has been specialized for various time-resolved protocols, as discussed in the remainder of this thesis. Notably, the solution assumes a one-dimensional propagation of light, where field propagation effects are governed by Maxwell-like propagation of four-wave mixing within the material through a spatially-independent third-order kernel. A possible extension of this work could generalize this framework to non-normal incidence experimental geometries, as used, for instance, in two-dimensional spectroscopies of superconducting cuprates. Additionally, it is worth noting that in our study on the linear response effects due to the off-axis growth of anisotropic materials (Ref. [124]), not included here for brevity, highlighted interesting results from the mixing of in-plane and out-of-plane refractive indices, which could also prove relevant in nonlinear protocols.

In the second chapter, we present a unified treatment of third harmonic generation in single-layer and bilayer cuprate superconductors probed along their $c-$axis, as detailed in our publication (Ref. [39]). We demonstrate that in bilayer systems, the combined effects of plasmon dispersion and light polarization can shift the two-plasmon resonance away from the plasma edge observed in linear spectroscopy. To model this behavior, we employ an effective Josephson-like framework, where intrinsic anharmonicity enables a natural exploration of nonlinear response functions driven by phase-fluctuation dynamics—an essential factor in the $c-$axis response of cuprate superconductors. While effective, this model lacks a microscopic description of the light-matter vertex, which instead appears as a parameter modulated by the superfluid stiffness. Future studies could benefit from a more microscopic approach that captures the coupling between fermionic degrees of freedom and phase excitations. This approach is challenging due to the pronounced anisotropy between in-plane and out-of-plane tunneling mechanisms and the unconventional nature of electron-electron interactions in the superconducting state, which are distinctive to cuprate systems.

We then focused on the application of two-dimensional THz spectroscopy for studying fermionic systems. In the third chapter, we introduced a comprehensive description of the technique, emphasizing the connection between the experimental outcomes and the underlying microscopic response function. Using a simple semiconductor model, we analyzed how paramagnetic and diamagnetic processes manifest in the 2D map, drawing parallels with prior studies that demonstrate the technique's capacity to distinguish various nonlinear pathways. We also examined how the spectral composition of the incoming pulses reshapes the response, aiming to clarify the interplay between the intrinsic spectrum of internal degrees of freedom and the actual waveforms used in experiments. Although the semiconductor model may initially seem unrelated to superconducting systems, we established connections between the two based on (i) similarities in their density of states and (ii) the impact of disorder on unbalancing the electron-like and hole-like contributions to the superconducting paramagnetic current, which exactly cancel in the clean limit. Moving forward, we hope to extend the non-interacting model, currently focused solely on electronic degrees of freedom, to scenarios that also incorporate phonons or other collective electronic excitations.

In the final chapter, we applied two-dimensional spectroscopy to two prototypical materials: NbN thin films and single-layer cuprates probed with $c-$axis polarized electric fields. For the cuprates, we built on the findings from the first and second chapters to demonstrate the challenges of isolating distinct nonlinear pathways associated with superconducting phase fluctuations, such as the two-plasmon process. The linear response of the system introduces prominent signatures that can obscure the true frequency structure of the nonlinear kernel. In addition, we used an effective model, initially developed for the $c-$axis linear response of cuprates, to describe the effects of disorder on the 2D spectrum, which however requires further validation and refinement at a more microscopic level. A publication on the contents of chapter three and its application to Josephson plasmons will be submitted soon.

For NbN, the results of this investigation, as published in Ref. [72], focus particularly on the non-linearly generated first harmonic signal, which was naturally captured using a two-pulse setup. Through this work, we interpreted the experimental findings using numerical simulations on a finite-size system, which revealed a predominant contribution from paramagnetic processes that mediate the coupling with amplitude fluctuations. To analytically understand the mechanism driving this enhancement, we calculated the primary paramagnetic diagram that, according to the numerics, is chiefly responsible for the observed effect, using a Mattis-Bardeen-like approximation to incorporate disorder. This result is potentially linked to the Eliashberg effect, which involves a field-induced renormalization of the zero-frequency amplitude fluctuation of the order parameter, thereby impacting the nonlinear optical properties of the superconductor. The computation provided here is valid for monochromatic pulses, but it could be extended to account for finite spectral pulse widths, allowing for theoretical predictions in the context of two-dimensional measurements. In addition, it can also be extended to the case of two-bands superconductors, such as MgB_2, whose THG spectrum has been analyzed in another publication not included here for brevity (Ref. [40]).

Bibliography

[1] A. A. Abrikosov and L. P. Gorkov. On the theory of superconducting alloys, I. The electrodynamics of alloys at absolute zero. *Sov. Phys. JETP*, 8(6):1090–1098, 1959.

[2] A. A. Abrikosov, L. P. Gorkov, and I. E. Dzyaloshinski. *Methods of Quantum Field Theory in Statistical Physics*. Courier Corporation, May 2012.

[3] F. Alpeggiani and L. C. Andreani. Josephson surface plasmons in spatially confined cuprate superconductors. *Physical Review B*, 88(17):174513, Nov. 2013.

[4] A. Altland and B. D. Simons. *Condensed Matter Field Theory*. Cambridge University Press, Cambridge, 2 edition, 2010.

[5] L. J. P. Ament, M. van Veenendaal, T. P. Devereaux, J. P. Hill, and J. van den Brink. Resonant inelastic x-ray scattering studies of elementary excitations. *Reviews of Modern Physics*, 83(2):705–767, June 2011.

[6] P. W. Anderson. Theory of dirty superconductors. *Journal of Physics and Chemistry of Solids*, 11(1):26–30, Sept. 1959.

[7] Y. Ando and K. Segawa. Magnetoresistance of Untwinned $YBa_2Cu_3O_y$ Single Crystals in a Wide Range of Doping: Anomalous Hole-Doping Dependence of the Coherence Length. *Physical Review Letters*, 88(16):167005, Apr. 2002.

[8] H. Aoki, N. Tsuji, M. Eckstein, M. Kollar, T. Oka, and P. Werner. Nonequilibrium dynamical mean-field theory and its applications. *Reviews of Modern Physics*, 86(2):779–837, June 2014.

[9] J. Bardeen, L. N. Cooper, and J. R. Schrieffer. Theory of Superconductivity. *Physical Review*, 108(5):1175–1204, Dec. 1957.

[10] M. Basini, M. Udina, M. Pancaldi, V. Unikandanunni, S. Bonetti, and L. Benfatto. Terahertz ionic Kerr effect: Two-phonon contribution to the nonlinear optical response in insulators. *Physical Review B*, 109(2):024309, Jan. 2024.

[11] D. N. Basov, R. D. Averitt, and D. Hsieh. Towards properties on demand in quantum materials. *Nature Materials*, 16(11):1077–1088, Nov. 2017.

[12] D. N. Basov, T. Timusk, B. Dabrowski, and J. D. Jorgensen. C-axis response of $YBa_2Cu_4O_8$: A pseudogap and possibility of Josephson coupling of CuO_2 planes. *Physical Review B*, 50(5):3511–3514, Aug. 1994.

[13] M. Bejas, V. Zimmermann, D. Betto, T. D. Boyko, R. J. Green, T. Loew, N. B. Brookes, G. Cristiani, G. Logvenov, M. Minola, B. Keimer, H. Yamase, A. Greco, and M. Hepting. Plasmon dispersion in bilayer cuprate superconductors. *Physical Review B*, 109(14):144516, Apr. 2024.

[14] L. Benfatto, C. Castellani, and G. Seibold. Linear and nonlinear current response in disordered d-wave superconductors. *Physical Review B*, 108(13):134508, Oct. 2023.

[15] L. Benfatto, A. Toschi, and S. Caprara. Low-energy phase-only action in a superconductor: A comparison with the XY model. *Physical Review B*, 69(18):184510, May 2004.

[16] T. G. H. Blank, K. A. Grishunin, K. A. Zvezdin, N. T. Hai, J. C. Wu, S.-H. Su, J.-C. A. Huang, A. K. Zvezdin, and A. V. Kimel. Two-Dimensional Terahertz Spectroscopy of Nonlinear Phononics in the Topological Insulator $MnBi_2Te_4$. *Physical Review Letters*, 131(2):026902, July 2023.

[17] N. Bloembergen and P. S. Pershan. Light Waves at the Boundary of Nonlinear Media. *Physical Review*, 128(2):606–622, Oct. 1962.

[18] M. Born and K. Huang. *Dynamical Theory of Crystal Lattices*. Oxford university press, 1996.

[19] T. Cea, P. Barone, C. Castellani, and L. Benfatto. Polarization dependence of the third-harmonic generation in multiband superconductors. *Physical Review B*, 97(9):094516, Mar. 2018.

[20] T. Cea, C. Castellani, and L. Benfatto. Nonlinear optical effects and third-harmonic generation in superconductors: Cooper pairs versus Higgs mode contribution. *Physical Review B*, 93(18):180507, May 2016.

[21] T. Cea, C. Castellani, G. Seibold, and L. Benfatto. Nonrelativistic Dynamics of the Amplitude (Higgs) Mode in Superconductors. *Physical Review Letters*, 115(15):157002, Oct. 2015.

[22] B. Cheng, L. Wu, N. J. Laurita, H. Singh, M. Chand, P. Raychaudhuri, and N. P. Armitage. Anomalous gap-edge dissipation in disordered superconductors on the brink of localization. *Physical Review B*, 93(18):180511, May 2016.

[23] H. Chu, M.-J. Kim, K. Katsumi, S. Kovalev, R. D. Dawson, L. Schwarz, N. Yoshikawa, G. Kim, D. Putzky, Z. Z. Li, H. Raffy, S. Germanskiy, J.-C. Deinert, N. Awari, I. Ilyakov, B. Green, M. Chen, M. Bawatna, G. Cristiani, G. Logvenov, Y. Gallais, A. V. Boris, B. Keimer, A. P. Schnyder, D. Manske, M. Gensch, Z. Wang, R. Shimano, and S. Kaiser. Phase-resolved Higgs response in superconducting cuprates. *Nature Communications*, 11(1):1793, Apr. 2020.

[24] H. Chu, S. Kovalev, Z. X. Wang, L. Schwarz, T. Dong, L. Feng, R. Haenel, M.-J. Kim, P. Shabestari, L. P. Hoang, K. Honasoge, R. D. Dawson, D. Putzky, G. Kim, M. Puviani, M. Chen, N. Awari, A. N. Ponomaryov, I. Ilyakov, M. Bluschke, F. Boschini, M. Zonno, S. Zhdanovich, M. Na, G. Christiani,

G. Logvenov, D. J. Jones, A. Damascelli, M. Minola, B. Keimer, D. Manske, N. Wang, J.-C. Deinert, and S. Kaiser. Fano interference between collective modes in cuprate high-Tc superconductors. *Nature Communications*, 14(1):1343, Mar. 2023.

[25] P. Coleman. *Introduction to Many-Body Physics*. Cambridge University Press, Cambridge, 2015.

[26] S. T. Cundiff and S. Mukamel. Optical multidimensional coherent spectroscopy. *Physics Today*, 66(7):44–49, July 2013.

[27] A. de la Torre, D. M. Kennes, M. Claassen, S. Gerber, J. W. McIver, and M. A. Sentef. Colloquium: Nonthermal pathways to ultrafast control in quantum materials. *Reviews of Modern Physics*, 93(4):041002, Oct. 2021.

[28] S. De Palo, C. Castellani, C. Di Castro, and B. K. Chakraverty. Effective action for superconductors and BCS-Bose crossover. *Physical Review B*, 60(1):564–573, July 1999.

[29] P. Derendorf, A. F. Volkov, and I. M. Eremin. Nonlinear response of diffusive superconductors to ac electromagnetic fields. *Physical Review B*, 109(2):024510, Jan. 2024.

[30] F. Ding and M. T. Zanni. Heterodyned 3D IR spectroscopy. *Chemical Physics*, 341(1):95–105, Nov. 2007.

[31] S. V. Dordevic, S. Komiya, Y. Ando, and D. N. Basov. Josephson Plasmon and Inhomogeneous Superconducting State in $La_{2-x}Sr_xCuO_4$. *Physical Review Letters*, 91(16):167401, Oct. 2003.

[32] M. Dressel. Electrodynamics of Metallic Superconductors. *Advances in Condensed Matter Physics*, 2013(1):104379, 2013.

[33] D. Dulić, A. Pimenov, D. van der Marel, D. M. Broun, S. Kamal, W. N. Hardy, A. A. Tsvetkov, I. M. Sutjaha, R. Liang, A. A. Menovsky, A. Loidl, and S. S. Saxena. Observation of the Transverse Optical Plasmon in $SmLa_{0.8}Sr_{0.2}CuO_{4\text{-}\delta}$. *Physical Review Letters*, 86(18):4144–4147, Apr. 2001.

[34] R. C. Dynes, V. Narayanamurti, and J. P. Garno. Direct Measurement of Quasiparticle-Lifetime Broadening in a Strong-Coupled Superconductor. *Physical Review Letters*, 41(21):1509–1512, Nov. 1978.

[35] G. M. Eliashberg. Film superconductivity stimulated by a high-frequency field. *JETP Letters*, 11, 1970.

[36] W. A. B. Evans. A general analytic continuation response formalism for large quantum systems. *Proceedings of the Physical Society*, 88(3):723–751, July 1966.

[37] D. Fausti, R. I. Tobey, N. Dean, S. Kaiser, A. Dienst, M. C. Hoffmann, S. Pyon, T. Takayama, H. Takagi, and A. Cavalleri. Light-Induced Superconductivity in a Stripe-Ordered Cuprate. *Science*, 331(6014):189–191, Jan. 2011.

[38] L. Feng, J. Cao, T. Priessnitz, Y. Dai, T. de Oliveira, J. Yuan, R. Oka, M.-J. Kim, M. Chen, A. N. Ponomaryov, I. Ilyakov, H. Zhang, Y. Lv, V. Mazzotti, G. Kim, G. Christiani, G. Logvenov, D. Wu, Y. Huang, J.-C. Deinert, S. Kovalev, S. Kaiser, T. Dong, N. Wang, and H. Chu. Dynamical interplay between superconductivity and charge density waves: A nonlinear terahertz study of coherently driven $2H-\mathrm{NbSe}_2$. *Physical Review B*, 108(10):L100504, Sept. 2023.

[39] J. Fiore, N. Sellati, F. Gabriele, C. Castellani, G. Seibold, M. Udina, and L. Benfatto. Investigating Josephson plasmons in layered cuprates via nonlinear terahertz spectroscopy. *Physical Review B*, 110(6):L060504, Aug. 2024.

[40] J. Fiore, M. Udina, M. Marciani, G. Seibold, and L. Benfatto. Contribution of collective excitations to third harmonic generation in two-band superconductors: The case of MgB_2. *Physical Review B*, 106(9):094515, Sept. 2022.

[41] M. Först, C. Manzoni, S. Kaiser, Y. Tomioka, Y. Tokura, R. Merlin, and A. Cavalleri. Nonlinear phononics as an ultrafast route to lattice control. *Nature Physics*, 7(11):854–856, Nov. 2011.

[42] D. Fu, D. Nicoletti, M. Fechner, M. Buzzi, G. D. Gu, and A. Cavalleri. Terahertz phase slips in striped $\mathrm{La}_{2-x}\mathrm{Ba}_x\mathrm{CuO}_4$. *Physical Review B*, 105(2):L020502, Jan. 2022.

[43] F. Gabriele, C. Castellani, and L. Benfatto. Generalized plasma waves in layered superconductors: A unified approach. *Physical Review Research*, 4(2):023112, May 2022.

[44] F. Gabriele, R. Senese, C. Castellani, and L. Benfatto. Charge-density response in layered metals: Retardation effects, generalized plasma waves, and their spectroscopic signatures. *Physical Review B*, 109(4):045137, Jan. 2024.

[45] F. Gabriele, M. Udina, and L. Benfatto. Non-linear Terahertz driving of plasma waves in layered cuprates. *Nature Communications*, 12(1):752, Feb. 2021.

[46] F. J. García de Abajo. Optical excitations in electron microscopy. *Reviews of Modern Physics*, 82(1):209–275, Feb. 2010.

[47] P. G. D. Gennes. *Superconductivity Of Metals And Alloys*. CRC Press, Boca Raton, May 2019.

[48] C. Giannetti, M. Capone, D. Fausti, M. Fabrizio, F. Parmigiani, and D. Mihailovic. Ultrafast optical spectroscopy of strongly correlated materials and high-temperature superconductors: A non-equilibrium approach. *Advances in Physics*, 65(2):58–238, Mar. 2016.

[49] V. L. Ginzburg and L. D. Landau. On the Theory of Superconductivity. In V. L. Ginzburg, editor, *On Superconductivity and Superfluidity: A Scientific Autobiography*, pages 113–137. Springer, Berlin, Heidelberg, 2009.

[50] F. Giorgianni, T. Cea, C. Vicario, C. P. Hauri, W. K. Withanage, X. Xi, and L. Benfatto. Leggett mode controlled by light pulses. *Nature Physics*, 15(4):341–346, Apr. 2019.

[51] F. Giustino, J. H. Lee, F. Trier, M. Bibes, S. M. Winter, R. Valentí, Y.-W. Son, L. Taillefer, C. Heil, A. I. Figueroa, B. Plaçais, Q. Wu, O. V. Yazyev, E. P. A. M. Bakkers, J. Nygård, P. Forn-Díaz, S. D. Franceschi, J. W. McIver, L. E. F. F. Torres, T. Low, A. Kumar, R. Galceran, S. O. Valenzuela, M. V. Costache, A. Manchon, E.-A. Kim, G. R. Schleder, A. Fazzio, and S. Roche. The 2021 quantum materials roadmap. *Journal of Physics: Materials*, 3(4):042006, Jan. 2021.

[52] A. Gómez Salvador, P. E. Dolgirev, M. H. Michael, A. Liu, D. Pavicevic, M. Fechner, A. Cavalleri, and E. Demler. Principles of two-dimensional terahertz spectroscopy of collective excitations: The case of Josephson plasmons in layered superconductors. *Physical Review B*, 110(9):094514, Sept. 2024.

[53] L. P. Gorkov. Microscopic derivation of the Ginzburg-Landau equations in the theory of superconductivity. *Sov. Phys. JETP*, 9(6):1364–1367, 1959.

[54] L. P. Gorkov and G. M. Eliashberg. Generalization of the Ginzburg-Landau Equations for Non-stationary Problems in the Case of Alloys with Paramagnetic Impurities. *Sov. Phys. JETP*, 27:328, 1968.

[55] L. P. Gorkov and G. M. Eliashberg. Superconducting alloys in a strong alternating field. *Sov. Phys. JETP*, 29(4):698–703, 1969.

[56] R. Grasset, K. Katsumi, P. Massat, H.-H. Wen, X.-H. Chen, Y. Gallais, and R. Shimano. Terahertz pulse-driven collective mode in the nematic superconducting state of $Ba_{1-x}K_xFe_2As_2$. *npj Quantum Materials*, 7(1):1–6, Jan. 2022.

[57] R. Haenel, P. Froese, D. Manske, and L. Schwarz. Time-resolved optical conductivity and Higgs oscillations in two-band dirty superconductors. *Physical Review B*, 104(13):134504, Oct. 2021.

[58] O. Hart and R. Nandkishore. Extracting spinon self-energies from two-dimensional coherent spectroscopy. *Physical Review B*, 107(20):205143, May 2023.

[59] J. Hebling, G. Almási, I. Z. Kozma, and J. Kuhl. Velocity matching by pulse front tilting for large-area THz-pulse generation. *Optics Express*, 10(21):1161–1166, Oct. 2002.

[60] R. Henn, C. Bernhard, A. Wittlin, M. Cardona, and S. Uchida. Far infrared ellipsometry using synchrotron radiation: The out-of-plane response of $La_{2-x}Sr_xCuO_4$. *Thin Solid Films*, 313–314:642–648, Feb. 1998.

[61] M. Hepting, L. Chaix, E. W. Huang, R. Fumagalli, Y. Y. Peng, B. Moritz, K. Kummer, N. B. Brookes, W. C. Lee, M. Hashimoto, T. Sarkar, J.-F. He, C. R. Rotundu, Y. S. Lee, R. L. Greene, L. Braicovich, G. Ghiringhelli,

Z. X. Shen, T. P. Devereaux, and W. S. Lee. Three-dimensional collective charge excitations in electron-doped copper oxide superconductors. *Nature*, 563(7731):374–378, Nov. 2018.

[62] H. Hirori, A. Doi, F. Blanchard, and K. Tanaka. Single-cycle terahertz pulses with amplitudes exceeding 1MV/cm generated by optical rectification in $LiNbO_3$. *Applied Physics Letters*, 98(9):091106, Mar. 2011.

[63] C. C. Homes, T. Timusk, R. Liang, D. A. Bonn, and W. N. Hardy. Optical conductivity of c axis oriented $YBa_2Cu_3O_{6.70}$: Evidence for a pseudogap. *Physical Review Letters*, 71(10):1645–1648, Sept. 1993.

[64] W. Hu, S. Kaiser, D. Nicoletti, C. R. Hunt, I. Gierz, M. C. Hoffmann, M. Le Tacon, T. Loew, B. Keimer, and A. Cavalleri. Optically enhanced coherent transport in $YBa_2Cu_3O_{6.5}$ by ultrafast redistribution of interlayer coupling. *Nature Materials*, 13(7):705–711, July 2014.

[65] L. Huber, S. F. Maehrlein, F. Wang, Y. Liu, and X.-Y. Zhu. The ultrafast Kerr effect in anisotropic and dispersive media. *The Journal of Chemical Physics*, 154(9):094202, Mar. 2021.

[66] C. L. Johnson, B. E. Knighton, and J. A. Johnson. Distinguishing nonlinear Terahertz excitation pathways with two-dimensional spectroscopy. *Physical Review Letters*, 122(7):073901, Feb. 2019.

[67] D. M. Juraschek and S. F. Maehrlein. Sum-frequency ionic Raman scattering. *Physical Review B*, 97(17):174302, May 2018.

[68] K. Kaj, K. A. Cremin, I. Hammock, J. Schalch, D. N. Basov, and R. D. Averitt. Terahertz third harmonic generation in c-axis $La_{1.85}Sr_{0.15}CuO_4$. *Physical Review B*, 107(14):L140504, Apr. 2023.

[69] T. Kakeshita, S. Uchida, K. M. Kojima, S. Adachi, S. Tajima, B. Gorshunov, and M. Dressel. Transverse Josephson Plasma Mode in T^* Cuprate Superconductors. *Physical Review Letters*, 86(18):4140–4143, Apr. 2001.

[70] T. Kampfrath, K. Tanaka, and K. A. Nelson. Resonant and nonresonant control over matter and light by intense terahertz transients. *Nature Photonics*, 7(9):680–690, Sept. 2013.

[71] D. Karaiskaj, A. D. Bristow, L. Yang, X. Dai, R. P. Mirin, S. Mukamel, and S. T. Cundiff. Two-Quantum Many-Body Coherences in Two-Dimensional Fourier-Transform Spectra of Exciton Resonances in Semiconductor Quantum Wells. *Physical Review Letters*, 104(11):117401, Mar. 2010.

[72] K. Katsumi, J. Fiore, M. Udina, R. Romero, D. Barbalas, J. Jesudasan, P. Raychaudhuri, G. Seibold, L. Benfatto, and N. P. Armitage. Revealing Novel Aspects of Light-Matter Coupling by Terahertz Two-Dimensional Coherent Spectroscopy: The Case of the Amplitude Mode in Superconductors. *Physical Review Letters*, 132(25):256903, June 2024.

[73] K. Katsumi, M. Nishida, S. Kaiser, S. Miyasaka, S. Tajima, and R. Shimano. Near-infrared light-induced superconducting-like state in underdoped $YBa_2Cu_3O_y$ studied by c-axis terahertz third-harmonic generation. *Physical Review B*, 107(21):214506, June 2023.

[74] J. H. Kim, H. S. Somal, M. T. Czyzyk, D. van der Marel, A. Wittlin, A. M. Gerrits, V. H. M. Duijn, N. T. Hien, and A. A. Menovsky. Strong damping of the c-axis plasmon in high-T_c cuprate superconductors. *Physica C: Superconductivity*, 247(3):297–308, June 1995.

[75] M.-J. Kim, S. Kovalev, M. Udina, R. Haenel, G. Kim, M. Puviani, G. Cristiani, I. Ilyakov, T. V. A. G. de Oliveira, A. Ponomaryov, J.-C. Deinert, G. Logvenov, B. Keimer, D. Manske, L. Benfatto, and S. Kaiser. Tracing the dynamics of superconducting order via transient terahertz third-harmonic generation. *Science Advances*, 10(11):eadi7598, Mar. 2024.

[76] N. B. Kopnin. *Theory of Nonequilibrium Superconductivity*, volume 110. Oxford University Press, 2001.

[77] S. Kovalev, T. Dong, L.-Y. Shi, C. Reinhoffer, T.-Q. Xu, H.-Z. Wang, Y. Wang, Z.-Z. Gan, S. Germanskiy, J.-C. Deinert, I. Ilyakov, P. H. M. van Loosdrecht, D. Wu, N.-L. Wang, J. Demsar, and Z. Wang. Band-selective third-harmonic generation in superconducting MgB_2: Possible evidence for the Higgs amplitude mode in the dirty limit. *Physical Review B*, 104(14):L140505, Oct. 2021.

[78] M. Kozina, M. Fechner, P. Marsik, T. van Driel, J. M. Glownia, C. Bernhard, M. Radovic, D. Zhu, S. Bonetti, U. Staub, and M. C. Hoffmann. Terahertz-driven phonon upconversion in $SrTiO_3$. *Nature Physics*, 15(4):387–392, Apr. 2019.

[79] R. Kubo. Statistical-Mechanical Theory of Irreversible Processes. I. General Theory and Simple Applications to Magnetic and Conduction Problems. *Journal of the Physical Society of Japan*, 12(6):570–586, June 1957.

[80] W. Kuehn, K. Reimann, M. Woerner, T. Elsaesser, and R. Hey. Two-Dimensional Terahertz Correlation Spectra of Electronic Excitations in Semiconductor Quantum Wells. *The Journal of Physical Chemistry B*, 115(18):5448–5455, May 2011.

[81] Y. Laplace and A. Cavalleri. Josephson plasmonics in layered superconductors. *Advances in Physics: X*, 1(3):387–411, May 2016.

[82] Y. Lee, M. Martini, T. Confalone, S. Shokri, C. N. Saggau, D. Wolf, G. Gu, K. Watanabe, T. Taniguchi, D. Montemurro, V. M. Vinokur, K. Nielsch, and N. Poccia. Encapsulating High-Temperature Superconducting Twisted van der Waals Heterostructures Blocks Detrimental Effects of Disorder. *Advanced Materials*, 35(15):2209135, 2023.

[83] A. Leitenstorfer, A. S. Moskalenko, T. Kampfrath, J. Kono, E. Castro-Camus, K. Peng, N. Qureshi, D. Turchinovich, K. Tanaka, A. G. Markelz, M. Havenith,

C. Hough, H. J. Joyce, W. J. Padilla, B. Zhou, K.-Y. Kim, X.-C. Zhang, P. U. Jepsen, S. Dhillon, M. Vitiello, E. Linfield, A. G. Davies, M. C. Hoffmann, R. Lewis, M. Tonouchi, P. Klarskov, T. S. Seifert, Y. A. Gerasimenko, D. Mihailovic, R. Huber, J. L. Boland, O. Mitrofanov, P. Dean, B. N. Ellison, P. G. Huggard, S. P. Rea, C. Walker, D. T. Leisawitz, J. R. Gao, C. Li, Q. Chen, G. Valušis, V. P. Wallace, E. Pickwell-MacPherson, X. Shang, J. Hesler, N. Ridler, C. C. Renaud, I. Kallfass, T. Nagatsuma, J. A. Zeitler, D. Arnone, M. B. Johnston, and J. Cunningham. The 2023 terahertz science and technology roadmap. *Journal of Physics D: Applied Physics*, 56(22):223001, Apr. 2023.

[84] X. Li, T. Qiu, J. Zhang, E. Baldini, J. Lu, A. M. Rappe, and K. A. Nelson. Terahertz field–induced ferroelectricity in quantum paraelectric $SrTiO_3$. *Science*, 364(6445):1079–1082, June 2019.

[85] H.-W. Lin, G. Mead, and G. A. Blake. Mapping $LiNbO_3$ Phonon-Polariton Nonlinearities with 2D THz-THz-Raman Spectroscopy. *Physical Review Letters*, 129(20):207401, Nov. 2022.

[86] J. Lin, J. Yuan, K. Jin, Z. Yin, G. Li, K.-J. Zhou, X. Lu, M. Dantz, T. Schmitt, H. Ding, H. Guo, M. P. M. Dean, and X. Liu. Doping evolution of the charge excitations and electron correlations in electron-doped superconducting $La_{2-x}Ce_xCuO_4$. *npj Quantum Materials*, 5(1):1–8, Jan. 2020.

[87] P. B. Littlewood and C. M. Varma. Gauge-Invariant Theory of the Dynamical Interaction of Charge Density Waves and Superconductivity. *Physical Review Letters*, 47(11):811–814, Sept. 1981.

[88] P. B. Littlewood and C. M. Varma. Amplitude collective modes in superconductors and their coupling to charge-density waves. *Physical Review B*, 26(9):4883–4893, Nov. 1982.

[89] A. Liu, D. Pavićević, M. H. Michael, A. G. Salvador, P. E. Dolgirev, M. Fechner, A. S. Disa, P. M. Lozano, Q. Li, G. D. Gu, E. Demler, and A. Cavalleri. Probing inhomogeneous cuprate superconductivity by terahertz Josephson echo spectroscopy. *Nature Physics*, pages 1–6, Sept. 2024.

[90] D. A. B. Lopez, W. Hu, and D. M. Juraschek. Electro-phononic and magneto-phononic frequency conversion, Apr. 2024.

[91] J. Lu, X. Li, H. Y. Hwang, B. K. Ofori-Okai, T. Kurihara, T. Suemoto, and K. A. Nelson. Coherent Two-Dimensional Terahertz Magnetic Resonance Spectroscopy of Collective Spin Waves. *Physical Review Letters*, 118(20):207204, May 2017.

[92] L. Luo, M. Mootz, J. H. Kang, C. Huang, K. Eom, J. W. Lee, C. Vaswani, Y. G. Collantes, E. E. Hellstrom, I. E. Perakis, C. B. Eom, and J. Wang. Quantum coherence tomography of light-controlled superconductivity. *Nature Physics*, 19(2):201–209, Feb. 2023.

[93] G. D. Mahan. *Many-Particle Physics*. Springer US, Boston, MA, 2000.

[94] F. Mahmood, D. Chaudhuri, S. Gopalakrishnan, R. Nandkishore, and N. P. Armitage. Observation of a marginal Fermi glass. *Nature Physics*, 17(5):627–631, May 2021.

[95] M. Martini, Y. Lee, T. Confalone, S. Shokri, C. N. Saggau, D. Wolf, G. Gu, K. Watanabe, T. Taniguchi, D. Montemurro, V. M. Vinokur, K. Nielsch, and N. Poccia. Twisted cuprate van der Waals heterostructures with controlled Josephson coupling. *Materials Today*, 67:106–112, July 2023.

[96] E. A. Mashkovich, K. A. Grishunin, R. M. Dubrovin, A. K. Zvezdin, R. V. Pisarev, and A. V. Kimel. Terahertz light–driven coupling of antiferromagnetic spins to lattice. *Science*, 374(6575):1608–1611, Dec. 2021.

[97] R. Matsunaga and R. Shimano. Higgs amplitude mode in s-wave superconductors revealed by terahertz pump-terahertz probe spectroscopy. In *Ultrafast Phenomena and Nanophotonics XIX*, volume 9361, pages 150–157. SPIE, Mar. 2015.

[98] R. Matsunaga, N. Tsuji, H. Fujita, A. Sugioka, K. Makise, Y. Uzawa, H. Terai, Z. Wang, H. Aoki, and R. Shimano. Light-induced collective pseudospin precession resonating with Higgs mode in a superconductor. *Science*, 345(6201):1145–1149, Sept. 2014.

[99] R. Matsunaga, N. Tsuji, K. Makise, H. Terai, H. Aoki, and R. Shimano. Polarization-resolved terahertz third-harmonic generation in a single-crystal superconductor NbN: Dominance of the Higgs mode beyond the BCS approximation. *Physical Review B*, 96(2):020505, July 2017.

[100] D. C. Mattis and J. Bardeen. Theory of the Anomalous Skin Effect in Normal and Superconducting Metals. *Physical Review*, 111(2):412–417, July 1958.

[101] M. Mitrano, A. Cantaluppi, D. Nicoletti, S. Kaiser, A. Perucchi, S. Lupi, P. Di Pietro, D. Pontiroli, M. Riccò, S. R. Clark, D. Jaksch, and A. Cavalleri. Possible light-induced superconductivity in K_3C_{60} at high temperature. *Nature*, 530(7591):461–464, Feb. 2016.

[102] M. Mootz, L. Luo, J. Wang, and l. E. Perakis. Visualization and quantum control of light-accelerated condensates by terahertz multi-dimensional coherent spectroscopy. *Communications Physics*, 5(1):1–10, Mar. 2022.

[103] M. Mootz, J. Wang, and I. E. Perakis. Lightwave terahertz quantum manipulation of nonequilibrium superconductor phases and their collective modes. *Physical Review B*, 102(5):054517, Aug. 2020.

[104] D. Munzar, C. Bernhard, A. Golnik, J. Humlíček, and M. Cardona. Anomalies of the infrared-active phonons in underdoped $YBa_2Cu_3O_y$ as evidence for the intra-bilayer Josephson effect. *Solid State Communications*, 112(7):365–369, Oct. 1999.

[105] Y. Murotani and R. Shimano. Nonlinear optical response of collective modes in multiband superconductors assisted by nonmagnetic impurities. *Physical Review B*, 99(22):224510, June 2019.

[106] Y. Murotani, N. Tsuji, and H. Aoki. Theory of light-induced resonances with collective Higgs and Leggett modes in multiband superconductors. *Physical Review B*, 95(10):104503, Mar. 2017.

[107] A. Nag, M. Zhu, M. Bejas, J. Li, H. C. Robarts, H. Yamase, A. N. Petsch, D. Song, H. Eisaki, A. C. Walters, M. García-Fernández, A. Greco, S. M. Hayden, and K.-J. Zhou. Detection of acoustic plasmons in hole-doped lanthanum and bismuth cuprate superconductors using resonant inelastic X-ray scattering. *Physical Review Letters*, 125(25):257002, Dec. 2020.

[108] N. Nagaosa. *Quantum Field Theory in Condensed Matter Physics*. Springer, Berlin, Heidelberg, 1999.

[109] D. Nicoletti and A. Cavalleri. Nonlinear light–matter interaction at terahertz frequencies. *Advances in Optics and Photonics*, 8(3):401–464, Sept. 2016.

[110] A. Paramekanti, M. Randeria, T. V. Ramakrishnan, and S. S. Mandal. Effective actions and phase fluctuations in d-wave superconductors. *Physical Review B*, 62(10):6786–6799, Sept. 2000.

[111] N. Poccia, S. Y. F. Zhao, H. Yoo, X. Huang, H. Yan, Y. S. Chu, R. Zhong, G. Gu, C. Mazzoli, K. Watanabe, T. Taniguchi, G. Campi, V. M. Vinokur, and P. Kim. Spatially correlated incommensurate lattice modulations in an atomically thin high-temperature $Bi_{2.1}Sr_{1.9}CaCu_{2.0}O_{8+y}$ superconductor. *Physical Review Materials*, 4(11):114007, Nov. 2020.

[112] M. Puviani, R. Haenel, and D. Manske. Quench-drive spectroscopy and high-harmonic generation in BCS superconductors. *Physical Review B*, 107(9):094501, Mar. 2023.

[113] S. Rajasekaran, E. Casandruc, Y. Laplace, D. Nicoletti, G. D. Gu, S. R. Clark, D. Jaksch, and A. Cavalleri. Parametric amplification of a superconducting plasma wave. *Nature Physics*, 12(11):1012–1016, Nov. 2016.

[114] S. Rajasekaran, J. Okamoto, L. Mathey, M. Fechner, V. Thampy, G. D. Gu, and A. Cavalleri. Probing optically silent superfluid stripes in cuprates. *Science*, 359(6375):575–579, Feb. 2018.

[115] C. Reinhoffer, P. Pilch, A. Reinold, P. Derendorf, S. Kovalev, J.-C. Deinert, I. Ilyakov, A. Ponomaryov, M. Chen, T.-Q. Xu, Y. Wang, Z.-Z. Gan, D.-S. Wu, J.-L. Luo, S. Germanskiy, E. A. Mashkovich, P. H. M. van Loosdrecht, I. M. Eremin, and Z. Wang. High-order nonlinear terahertz probing of the two-band superconductor MgB_2: Third- and fifth-order harmonic generation. *Physical Review B*, 106(21):214514, Dec. 2022.

[116] H. Rostami, M. I. Katsnelson, G. Vignale, and M. Polini. Gauge invariance and Ward identities in nonlinear response theory. *Annals of Physics*, 431:168523, Aug. 2021.

[117] S. Savel'ev, A. L. Rakhmanov, V. A. Yampol'skii, and F. Nori. Analogues of nonlinear optics using terahertz Josephson plasma waves in layered superconductors. *Nature Physics*, 2(8):521–525, Aug. 2006.

[118] S. Savel'ev, V. A. Yampol'skii, A. L. Rakhmanov, and F. Nori. Terahertz Josephson plasma waves in layered superconductors: Spectrum, generation, nonlinear and quantum phenomena. *Reports on Progress in Physics*, 73(2):026501, Jan. 2010.

[119] L. Schwarz, B. Fauseweh, N. Tsuji, N. Cheng, N. Bittner, H. Krull, M. Berciu, G. S. Uhrig, A. P. Schnyder, S. Kaiser, and D. Manske. Classification and characterization of nonequilibrium Higgs modes in unconventional superconductors. *Nature Communications*, 11(1):287, Jan. 2020.

[120] L. Schwarz, R. Haenel, and D. Manske. Phase signatures in the third-harmonic response of Higgs and coexisting modes in superconductors. *Physical Review B*, 104(17):174508, Nov. 2021.

[121] L. Schwarz and D. Manske. Theory of driven Higgs oscillations and third-harmonic generation in unconventional superconductors. *Physical Review B*, 101(18):184519, May 2020.

[122] G. Seibold. On the Evaluation of Higher-Harmonic-Current Responses for High-Field Spectroscopies in Disordered Superconductors. *Condensed Matter*, 8(4):95, Dec. 2023.

[123] G. Seibold, M. Udina, C. Castellani, and L. Benfatto. Third harmonic generation from collective modes in disordered superconductors. *Physical Review B*, 103(1):014512, Jan. 2021.

[124] N. Sellati, J. Fiore, C. Castellani, and L. Benfatto. Optical Absorption in Tilted Geometries as an Indirect Measurement of Longitudinal Plasma Waves in Layered Cuprates. *Nanomaterials*, 14(12):1021, Jan. 2024.

[125] N. Sellati, J. Fiore, S. P. Villani, L. Benfatto, and M. Udina. Phonon-Polaritons in Non-Centrosymmetric Systems: Theory of Terahertz Pump-Optical Probe Spectroscopy, Nov. 2024.

[126] N. Sellati, F. Gabriele, C. Castellani, and L. Benfatto. Generalized Josephson plasmons in bilayer superconductors. *Physical Review B*, 108(1):014503, July 2023.

[127] T. Shibauchi, H. Kitano, K. Uchinokura, A. Maeda, T. Kimura, and K. Kishio. Anisotropic penetration depth in $La_{2-x}Sr_xCuO_4$. *Physical Review Letters*, 72(14):2263–2266, Apr. 1994.

[128] R. Shimano and N. Tsuji. Higgs Mode in Superconductors. *Annual Review of Condensed Matter Physics*, 11(Volume 11, 2020):103–124, Mar. 2020.

[129] M. E. Siemens, G. Moody, H. Li, A. D. Bristow, and S. T. Cundiff. Resonance lineshapes in two-dimensional Fourier transform spectroscopy. *Optics Express*, 18(17):17699–17708, Aug. 2010.

[130] M. Silaev. Nonlinear electromagnetic response and Higgs-mode excitation in BCS superconductors with impurities. *Physical Review B*, 99(22):224511, June 2019.

[131] C. L. Smallwood and S. T. Cundiff. Coherent Spectroscopy: Multidimensional Coherent Spectroscopy of Semiconductors. *Laser & Photonics Reviews*, 12(12):1870052, 2018.

[132] G. Stefanucci and R. van Leeuwen. *Nonequilibrium Many-Body Theory of Quantum Systems: A Modern Introduction*. Cambridge University Press, Mar. 2013.

[133] A. Subedi, A. Cavalleri, and A. Georges. Theory of nonlinear phononics for coherent light control of solids. *Physical Review B*, 89(22):220301, June 2014.

[134] Z. Sun, M. M. Fogler, D. N. Basov, and A. J. Millis. Collective modes and terahertz near-field response of superconductors. *Physical Review Research*, 2(2):023413, June 2020.

[135] M. Suzuki and M. Hikita. Resistive transition, magnetoresistance, and anisotropy in $La_{2\text{-}x}Sr_xCuO_4$ single-crystal thin films. *Physical Review B*, 44(1):249–261, July 1991.

[136] N. Taherian, M. Först, A. Liu, M. Fechner, D. Pavicevic, A. von Hoegen, E. Rowe, Y. Liu, S. Nakata, B. Keimer, E. Demler, M. H. Michael, and A. Cavalleri. Squeezed Josephson plasmons in driven $YBa_2Cu_3O_{6+x}$, Jan. 2024.

[137] K. Tamasaku, Y. Nakamura, and S. Uchida. Charge dynamics across the CuO_2 planes in $La_{2-x}Sr_xCuO_4$. *Physical Review Letters*, 69(9):1455–1458, Aug. 1992.

[138] Y. Tokura, M. Kawasaki, and N. Nagaosa. Emergent functions of quantum materials. *Nature Physics*, 13(11):1056–1068, Nov. 2017.

[139] N. Tsuji and H. Aoki. Theory of Anderson pseudospin resonance with Higgs mode in superconductors. *Physical Review B*, 92(6):064508, Aug. 2015.

[140] N. Tsuji and Y. Nomura. Higgs-mode resonance in third harmonic generation in NbN superconductors: Multiband electron-phonon coupling, impurity scattering, and polarization-angle dependence. *Physical Review Research*, 2(4):043029, Oct. 2020.

[141] D. B. Turner, K. W. Stone, K. Gundogdu, and K. A. Nelson. Three-dimensional electronic spectroscopy of excitons in GaAs quantum wells. *The Journal of Chemical Physics*, 131(14):144510, Oct. 2009.

[142] M. Udina, T. Cea, and L. Benfatto. Theory of coherent-oscillations generation in Terahertz pump-probe spectroscopy: From phonons to electronic collective modes. *Physical Review B*, 100(16):165131, Oct. 2019.

[143] M. Udina, J. Fiore, T. Cea, C. Castellani, G. Seibold, and L. Benfatto. THz non-linear optical response in cuprates: Predominance of the BCS response over the Higgs mode. *Faraday Discussions*, 237(0):168–185, Sept. 2022.

[144] D. van der Marel and A. Tsvetkov. Transverse optical plasmons in layered superconductors. *Czechoslovak Journal of Physics*, 46(6):3165–3168, June 1996.

[145] C. Vaswani, J. H. Kang, M. Mootz, L. Luo, X. Yang, C. Sundahl, D. Cheng, C. Huang, R. H. J. Kim, Z. Liu, Y. G. Collantes, E. E. Hellstrom, I. E. Perakis, C. B. Eom, and J. Wang. Light quantum control of persisting Higgs modes in iron-based superconductors. *Nature Communications*, 12(1):258, Jan. 2021.

[146] A. von Hoegen, R. Mankowsky, M. Fechner, M. Först, and A. Cavalleri. Probing the interatomic potential of solids with strong-field nonlinear phononics. *Nature*, 555(7694):79–82, Mar. 2018.

[147] Z.-X. Wang, J.-R. Xue, H.-K. Shi, X.-Q. Jia, T. Lin, L.-Y. Shi, T. Dong, F. Wang, and N.-L. Wang. Transient Higgs oscillations and high-order nonlinear light-Higgs coupling in a terahertz wave driven NbN superconductor. *Physical Review B*, 105(10):L100508, Mar. 2022.

[148] S. Watanabe, N. Minami, and R. Shimano. Intense terahertz pulse induced exciton generation in carbon nanotubes. *Optics Express*, 19(2):1528–1538, Jan. 2011.

[149] M. Woerner, W. Kuehn, P. Bowlan, K. Reimann, and T. Elsaesser. Ultrafast two-dimensional terahertz spectroscopy of elementary excitations in solids. *New Journal of Physics*, 15(2):025039, Feb. 2013.

[150] C.-J. Yang, J. Li, M. Fiebig, and S. Pal. Terahertz control of many-body dynamics in quantum materials. *Nature Reviews Materials*, 8(8):518–532, Aug. 2023.

[151] Y. Yu, L. Ma, P. Cai, R. Zhong, C. Ye, J. Shen, G. D. Gu, X. H. Chen, and Y. Zhang. High-temperature superconductivity in monolayer Bi2Sr2CaCu2O8+δ. *Nature*, 575(7781):156–163, Nov. 2019.

[152] J. Yuan, L. Shi, L. Yue, B. Li, Z. Wang, S. Xu, T. Xu, Y. Wang, Z. Gan, F. Chen, Z. Lin, X. Wang, K. Jin, X. Wang, J. Luo, S. Zhang, Q. Wu, Q. Liu, T. Hu, R. Li, X. Zhou, D. Wu, T. Dong, and N. Wang. Dynamical interplay between superconductivity and pseudogap in cuprates as revealed by terahertz third-harmonic generation spectroscopy. *Science Advances*, 10(6):eadg9211, Feb. 2024.

[153] S. Zhang, Z. Sun, Q. Liu, Z. Wang, Q. Wu, L. Yue, S. Xu, T. Hu, R. Li, X. Zhou, J. Yuan, G. Gu, T. Dong, and N. Wang. Revealing the frequency-dependent oscillations in nonlinear Terahertz response induced by Josephson current. *National Science Review*, page nwad163, June 2023.

[154] S. Y. F. Zhao, X. Cui, P. A. Volkov, H. Yoo, S. Lee, J. A. Gardener, A. J. Akey, R. Engelke, Y. Ronen, R. Zhong, G. Gu, S. Plugge, T. Tummuru, M. Kim, M. Franz, J. H. Pixley, N. Poccia, and P. Kim. Time-reversal symmetry breaking superconductivity between twisted cuprate superconductors. *Science*, 382(6677):1422–1427, Dec. 2023.

[155] S. Y. F. Zhao, N. Poccia, M. G. Panetta, C. Yu, J. W. Johnson, H. Yoo, R. Zhong, G. D. Gu, K. Watanabe, T. Taniguchi, S. V. Postolova, V. M. Vinokur, and P. Kim. Sign-Reversing Hall Effect in Atomically Thin High-Temperature $Bi_{2.1}Sr_{1.9}CaCu_{2.0}O_{8+\delta}$ Superconductors. *Physical Review Letters*, 122(24):247001, June 2019.

[156] W. Zimmermann, E. H. Brandt, M. Bauer, E. Seider, and L. Genzel. Optical conductivity of BCS superconductors with arbitrary purity. *Physica C: Superconductivity*, 183(1):99–104, Nov. 1991.